1 2 9 0

UNIVERSIDADE D
COIMBRA

Sara Diana Cabete Diogo de Oliveira

Component Method for Predicting the Cyclic Behaviour of Dissipative Steel Beam-to-column Joints

Tese no âmbito do Doutoramento em Construção Metálica e Mista orientada pelo Professor Doutor Luís Alberto Proença Simões da Silva, pelo Professor Doutor Ricardo Joel Teixeira Costa e pelo Professor Doutor Yukihiro Harada apresentada ao Departamento de Engenharia Civil da Faculdade de Ciências e Tecnologia da Universidade de Coimbra

Outubro de 2023

Faculdade de Ciências e Tecnologia da Universidade de Coimbra
Departamento de Engenharia Civil

Sara Diana Cabete Diogo de Oliveira

COMPONENT METHOD FOR PREDICTING THE CYCLIC BEHAVIOUR OF DISSIPATIVE STEEL BEAM-TO-COLUMN JOINTS

MÉTODO DAS COMPONENTES PARA A PREVISÃO DO COMPORTAMENTO CÍCLICO DE JUNTAS VIGA-COLUNA METÁLICAS DISSIPATIVAS

Tese de Doutoramento em Construção Metálica e Mista,

orientada pelo Professor Doutor Luís Alberto Proença Simões da Silva, pelo Professor Doutor Ricardo Joel Teixeira Costa e pelo Professor Doutor Yukihiro Harada.

Outubro de 2023

1 2 90

UNIVERSIDADE D
COIMBRA

INSTITUITONS AND SUPPORT

1290
FACULDADE DE CIÊNCIAS E TECNOLOGIA
UNIVERSIDADE D COIMBRA

isise
Institute for Sustainability and Innovation in Structural Engineering

fct
Fundação para a Ciência e a Tecnologia

REPÚBLICA PORTUGUESA
CIÊNCIA, TECNOLOGIA E ENSINO SUPERIOR

UNIÃO EUROPEIA
Fundo Social Europeu

Research Fund for Coal & Steel

ABSTRACT

The cyclic behaviour of beam-to-column joints has a crucial role on the overall seismic response of steel frames and recent studies highlighted the influence of joint rotation capacity on the seismic response of mid-rise MR frames designed according to EN 1998-1.

For seismic actions, EN 1998-1 allows the formation of plastic hinges (dissipative zones) in the joints when partial-strength and/or semi-rigid joints are considered, provided that a set of requirements are verified. These requirements include (i) the rotation capacity of joints being consistent with the global deformations demands, (ii) members framing into the connections being stable at the ultimate limit state (ULS) and (iii) the effect of joint deformation on global drift being considered using nonlinear static global analysis or non-linear time history analysis. On the other hand, EN 1993-1-8 provides models to compute the strength and the stiffness of joints but no reliable analytical tools are available to predict their cyclic behaviour.

The main goal of this study is to contribute for developing a simplified design method that takes into a count the cyclic behaviour of the joint. In order to do so, a procedure is being developed based on the component method coded in EN 1993-1-8, named cyclic component method (CCM) aimed to predict cyclic moment-rotation behaviour of the joints, suitable for application for a wide range of joint configurations. The development of the CCM required not only the conceptual definition and mathematical implementation of the model but also the development and calibration of the constitutive laws for the components making use of experimental tests, with emphasis on the T-stub component.

KEYWORDS

steel beam-to-column joints | component method | cyclic behaviour | finite element method | T-stub

RESUMO

O comportamento cíclico de juntas viga-coluna tem um papel crucial no desempenho estrutural de pórticos metálicos, sendo que estudos recentes destacam a influência da capacidade de rotação das juntas na resposta sísmica de pórticos simples de altura média dimensionados de acordo com a EN 1998-1.

Para zonas dissipativas, a EN 1998-1 permite a formação de rótulas plásticas (zonas dissipativas) nas juntas nas juntas de resistência parcial e/ou juntas semirrígidas desde que um conjunto de requisitos sejam verificados. Estes requisitos incluem (i) a necessidade de capacidade de rotação das juntas ser superior às deformações requeridas, (ii) os membros ligados apresentarem um comportamento estável para Estado Limite Último (ELU) e (iii) o efeito da deformação das juntas no comportamento global da estrutura ser levado em consideração por intermédio de uma análise global estática não-linear ou de uma análise temporal não-linear. Por outro lado, a EN 1993-1-8 fornece modelos para o cálculo da resistência e da rigidez inicial de juntas, no entanto não existem ferramentas analíticas viáveis para prever o comportamento cíclico de juntas.

O principal objetivo deste estudo é contribuir para o desenvolvimento de um método de dimensionamento simples que tem em consideração o comportamento cíclico de juntas. Para fazer face a esta lacuna, está a ser desenvolvido um procedimento baseado no método das componentes preconizado na EN 1993-1-8, designado por método das componentes cíclico

(CCM), adequado para uma vasta gama de configurações de juntas. O desenvolvimento do CCM requer, não só a definição conceptual e matemática da implementação de modelos, mas também o desenvolvimento e calibração de leis constitutivas para as componentes através de ensaios experimentais, em particular, na componente T-stub.

PALAVRAS-CHAVE

juntas viga-coluna metálicas | método das componentes | comportamento cíclico | método dos elementos finitos | T-stub

ACKNOWLEDGEMENTS

Há quem diga que a realização de um Doutoramento é um percurso solitário, mas eu nunca estive sozinha. Pelo caminho contei com o apoio de inúmeras pessoas que foram cruciais para o desenvolvimento desta Tese de Doutoramento.

Aos meus orientadores científicos, Professor Doutor Luís Alberto Proença Simões da Silva (Universidade de Coimbra), Professor Doutor Ricardo Joel Teixeira Costa (Universidade de Coimbra) e Professor Doutor Yukihiro Harada (Universidade de Chiba), por aceitarem orientar-me, pelo empenho e disponibilidade com que acompanharam este trabalho.

Ao Professor Doutor Carlos Rebelo Alberto da Silva Rebelo (Universidade de Coimbra) pela orientação científica durante a participação nos projetos Europeus *European pre-QUALified steel JOINTS* (EQUALJOINTS) e *Valorisation of knowledge for European pre-QUALified steel JOINTS* (EQUALJOINTS+) e por me ter dado a oportunidade de participar nas reuniões de projeto e *workshops* internacionais.

À Fundação para a Ciência e a Tecnologia (FCT), pelo apoio financeiro através da Bolsa de Investigação para Doutoramento com a referência 2020.04437.BD e à minha instituição de acolhimento Sustainability and Innovation in Structural Engineering (ISISE), com a referência UIDB / 04029/2020, e de Associate Laboratory Advanced Production and Intelligent Systems (ARISE), com a referência LA/P/0112/2020.

Aos antigos e atuais colaboradores do Laboratório de Construções, Estruturas e Mecânica Estrutural do Departamento de Engenharia Civil (DEC), em particular ao Engenheiro Ilídio Santos e ao Cláudio Martins pela preciosa ajuda e assistência na realização dos ensaios experimentais.

Aos demais funcionários do DEC e da Associação para o Desenvolvimento da Engenharia Civil (ACIV), que de alguma forma contribuíram para o meu percurso académico e dia-a-dia no departamento, em particular ao Ricardo Oliveira, ao Nuno Almeida e à Maria José.

Aos meus colegas de gabinete, Mohammad Reza Mohammadi, Trayana Tankova, Luís Laím e Francisca Santos, pela camaradagem, pelos conselhos e por terem sempre uma palavra amiga. Um especial agradecimento também ao Hélder Craveiro e ao Hugo Caetano, que apesar de não terem sido meus colegas de gabinete, foram igualmente importantes no dia-a-dia do Piso 5.

À equipa de disseminação do ISISE, Francisca Santos, Eliana Inca, Laura Sousa, Miguel Pereira e Trayana Tankova, pelo espírito de equipa e por todo o dinamismo na organização de atividades e na gestão de redes sociais, que apesar de todo o trabalho e tempo extracurricular que assim o exigiu, permitiu-me desenvolver outras competências.

À equipa do Clube de Programação do DEC, em especial ao Professor Doutor António Alberto Correia (Universidade de Coimbra) pelos ensinamentos de programação, pela orientação na organização das atividades, pelos conselhos e pelo interesse no desenvolvimento da Tese.

À minha amiga de infância, Raquel Marques, que me apoia independentemente do tempo ou da distância que nos separe. Aos amigos que Coimbra me deu e que levo comigo para a vida, em

especial à minha amiga Rita Malaguerra e à sua mãe Célia Pedro, que me apoiaram e que se tornaram na minha família de Coimbra.

Ao Bruno Pedrosa, um agradecimento muito especial, por todo o carinho e compreensão, por ser o meu farol e o meu porto de abrigo, por me encorajar e por ter sempre acreditado em mim.

Finalmente à minha família, em especial aos meus pais, Deolinda e Paulo, agradeço os sacrifícios, o apoio, a compreensão e amor incondicional. Aos meus avós, Virgílio e Jusita, e à minha tia Cami que me apoiaram ao longo de todo o meu percurso académico.

Coimbra, 28 de outubro de 2023 Sara Diogo de Oliveira

CONTENTS

5 Cyclic modelling of T-stubs: decoupled component model........165

NOTATIONS

Lowercase Latin letters

a	coefficient (Piluso and Rizzano model)
a_0	original thickness of a flat test piece (coupon)
a_f	thickness of a flat test piece after fracture (coupon)
b	width of the T-stub; coefficient (Piluso and Rizzano model); width of the shank of the bolt (Augusto’s procedure); total number of blocks (refined mechanical model)
b_0	original width of the parallel length of a flat test piece (coupon)
b_c	width of the column flange
b_eff	effective width of a T-stub flange
b'_eff	effective width of a T-stub flange (Faella *et al.* model)
b_f	width of the parallel length of a flat test piece after fracture (coupon)
d	deformation; distance between the web and the bolt axis (T-stub); centreline gap between the T parts of the T-stub caused by F (T-stub experimental tests); distance between the loading cell and the column flange (Augusto’s procedure)
$d_\mathrm{1,lbf}$	distance of the bolt row 1 to the lower beam flange (Augusto’s procedure)
$d_\mathrm{2,lbf}$	distance of the bolt row 2 to the lower beam flange (Augusto’s procedure)
$d_\mathrm{1,ubf}$	distance of the bolt row 1 to the upper beam flange (Augusto’s procedure)
$d_\mathrm{2,ubf}$	distance of the bolt row 2 to the upper beam flange (Augusto’s procedure)
$d_{\mathrm{all},i}$	Sum of the deformations of the components CFB, BT and EPB for each bolt row i, disregarding flip deformation (Augusto’s procedure)
$d_\mathrm{all,lbf}$	sum of the deformations of the components CFB, BT and EPB at the lower beam flange level, disregarding flip deformation (Augusto’s procedure)
$d_\mathrm{all,ubf}$	sum of the deformations of the components CFB, BT and EPB at the upper beam flange level, disregarding flip deformation (Augusto’s procedure)

d_b	diameter of the bolt
d_{bh}	diameter of the bolt head
$d_{b,i}$	diameter of the bolt of the bolt row i (Augusto's procedure)
$d_{\mathrm{B},i}$	deformation of the component bolts in tension for each bolt row i (Augusto's procedure)
d_c	cap deformation (IMK model)
$d_{\mathrm{CF},i}$	deformation of the component column flange in bending for each bolt row i (Augusto's procedure)
d_{cw}	deformation of the column web is obtained from the displacement fields (Augusto's procedure)
d_{CWS}	deformation of the column web component
$d_{\mathrm{CF},i}$	deformation of the component end-plate in bending for each bolt row i (Augusto's procedure)
d_{EP}	interpolated deformation of the end-plate at the beam flanges level (Augusto's procedure)
$d_{\mathrm{EP},i}$	deformation of the component end-plate in bending for each bolt row i (Augusto's procedure)
$d_{\mathrm{flip_{EP}},\mathrm{lbf}}$	flip deformation of the extended part of the end-plate at the lower beam flange level (Augusto's procedure)
$d_{\mathrm{flip_{EP}},\mathrm{ubf}}$	flip deformation of the extended part of the end-plate at the upper beam flange level (Augusto's procedure)
d_{lim}	deformation limit for the reloading branch when the component becomes active (characterization of tension-only and compression only components)
d_m	deformation for the attainment of the of the stress σ_u (PFR model)
$d_{m,n}$	deformation of the component n located in row m
d_{max}	deformation amplitude (Piluso and Rizzano model)
$d_n^{i,j}$	deformation of component n in iteration j of increment i (iterative incremental procedure)
d_h	deformation at the beginning of strain hardening (attainment of the strain level ε_h) (PFR model)
d_p	ultimate plastic deformation under monotonic loading conditions (Piluso and Rizzano model)

d_r	deformation at residual strength (IMK model)
d_{slip}	horizontal slip (Piluso and Rizzano model)
d_{start}	deformation corresponding to the starting point of a generic branch (MRA model)
d_u	deformation at ultimate conditions
d_w	diameter of the washer, or the width across points of the bolt head or nut, as relevant
d_{wsh}	diameter of the washer
d_y	yield deformation
e	edge distance of the T-stub flange, i.e. distance (measured perpendicularly to the T-stub web) from the axis of a bolt hole to the adjacent edge
e_1	edge distance of the T-stub flange, i.e. distance (measured parallel to the T-stub web) from the axis of a bolt hole to the adjacent edge
f	internal force
$f_{\mathrm{CWS}}^{i,j}$	internal force in component column web panel in shear
f_f	stress at fracture
$f_{m,n}$	internal force in component n located in row m (mechanical model)
$f_n^{i,j}$	internal force component n in iteration j of increment i (iterative incremental procedure)
$f_{m,l\mathrm{eft}}^{i,j}$	internal forces of components in the left side on the node where the DOF is assigned to
$f_{m,r\mathrm{ight}}^{i,j}$	internal forces of components in the right side on the node where the DOF is assigned to
$f_{m,l\mathrm{eftmost}}^{i,j}$	internal forces of leftmost components in row m
$f_{m,r\mathrm{ightmost}}^{i,j}$	internal forces of rightmost components in row m
$f_{t,m,\mathrm{left}}^{i,j}$	internal forces of components in the left on the node where the DOF
$f_{t,m,\mathrm{leftmost}}^{i,j}$	the internal forces of leftmost components in row m of block t
$f_{t,m,\mathrm{right}}^{i,j}$	internal forces of components in the right side on the node where the DOF
$f_{t,m,\mathrm{rightmost}}^{i,j}$	the internal forces of rightmost components in row m of block t

f_u	ultimate stress
f_{ub}	ultimate strength of the bolt
f_y	yield strength; yield stress
h_b	height of the beam
h_c	height of the column cross section; integration length of the compression stresses (Augusto's procedure)
h_t	lever arm (Krawinkler's model); integration length of the tension stresses (Augusto's procedure)
h_wc	height of the column web
i	increment; bolt row (Augusto's procedure)
i_F	empiric parameter related with the level of strength degradation (MRA model)
i_K	empiric parameter related with the level of stiffness degradation (MRA model)
i_M	empiric parameter related with the level of strength degradation (MRA model)
j	iteration
l	bolt length
l_s	bolt shank length
l_t	bolt thread length
k	stiffness coefficient; coefficient of proportionality (coupon)
k_2	empirical parameter equal to 0.9
k_left	tangent stiffness of the components which are immediately in the left side of the node where the DOF is assigned (mechanical model)
$k_{m,\mathrm{leftmost}}$	tangent stiffness for the first (the leftmost) spring in row m (mechanical model)
$k_{m,\mathrm{rightmost}}$	tangent stiffness for the last (the rightmost) spring in row m (mechanical model)
$k_n^{i,j}$	tangent stiffness of component n in iteration j of increment i (iterative incremental procedure)

k_{right}	tangent stiffness of the components which are immediately in the right side of the node where the DOF is assigned (mechanical model)
$k_{t,m,\mathrm{left}}$	tangent stiffness of the components, which are immediately in the left side of the node where the DOF is assigned, of row m in block t
$k_{t,m,\mathrm{leftmost}}$	tangent stiffness of the leftmost component of row m in block t
$k_{t,m,\mathrm{single}}$	tangent stiffness of the single component of row m in block t
$k_{t,m,\mathrm{right}}$	tangent stiffness of the components, which are immediately in the right side of the node where the DOF is assigned, of row m in block t (refined mechanical model)
$k_{t,m,\mathrm{rightmost}}$	tangent stiffness of the rightmost component of row m in block t (refined mechanical model)
m	location of the restraining line, i.e. distance between location of critical sections where plastic hinges can develop (T-stub); row number (mechanical model)
m'	location of the restraining line (Faella *et al.* model)
n	location of the prying forces (T-stub); component number (mechanical model)
n_d	total number of nodes (mechanical model)
n_f	total number of degrees of freedom number (mechanical model)
r	root radius of an I or H section; total number of rows (mechanical model)
r^2	coefficient of determination
r_t	total number of rows in block t (refined mechanical model)
t	transition law from the lower bound to the upper bound curve (MRA model); block number (refined mechanical model)
t_1	empirical parameter related to pinching (MRA model)
t_2	empirical parameter related to pinching (MRA model)
t_{bh}	thickness of the bolt head
t_{bn}	thickness of the bolt nut
t_{f}	thickness of the T-stub flange
$t_{\mathrm{f,l}}$	flange thickness of the lower T-sub flange

$t_{\mathrm{f,u}}$	flange thickness of the upper T-sub flange
t_{fc}	thickness of the column flange
t_{w}	thickness of the T-stub web
t_{wc}	thickness of the column web
t_{wsh}	thickness of the washer
t_{s}	thickness of the transverse stiffeners; thickness of the rigid support (T-stub test on rigid support)
$\boldsymbol{u}$	vector of nodal displacements
u	displacement
v	total number of vertical rigid elements (refined mechanical model)
x	beam length from the column flange to the measured beam section (Augusto’s procedure)
y_m	y coordinate of components of row m (mechanical model)
y_{CWS}	y coordinate of the CWS (mechanical model)
y_{GC}	y coordinate of beam geometric centre
$y_{t,m}$	local y coordinate of the row m in block t
z	lever arm

Uppercase Latin letters

A	area
$\boldsymbol{A}$	Jacobean matrix
A_0	original cross-sectional area of the parallel length
A_s	tensile stress area of the bolt
B	T-stub width
$B_{t,Rd}$	design tension resistance of a bolt

B_u	ultimate axial resistance of a single bolt
C	calibration parameter related to pinching (MRA model); constant depending on the true stress-true strain curve of the material (PFR model)
CF_i	pre-defined nodes in the FE mesh for the column flange holes for the bolt row i (Augusto's procedure)
$\mathrm{DT}i$	application point of the displacement transducer or pre-defined node in the FE mesh (Augusto's procedure)
E	Young's modulus
E_0	energy dissipated under monotonic conditions
E_{ci}	energy dissipated up to the i-th cycle
E_{cc}	cyclic energy dissipation capacity (calibrated for constant amplitude cyclic tests) (Piluso and Rizzano model)
E_h	hysteretic energy dissipation
E_p	plastic modulus (RA model)
$E_{\mathrm{red},i}$	correction of the Young's modulus for mechanism type-i (Coelho *et al.* model)
E_t	set of row numbers with only one spring in block t
EP_i	pre-defined nodes in the FE mesh for the end-plate holes for the bolt row i (Augusto's procedure)
F	Force; applied force (experimental test)
$\boldsymbol{F}$	vector of external nodal forces
F_0	reference strength (MRA model)
$F_{0\mathrm{a}}$	reference strength of the ascending branch (MRA model)
$F_{0\mathrm{d}}$	reference strength of the descending branch (MRA model)
$F_{0,\mathrm{l}}$	reference strength of the lower bound curve (MRA model)
$F_{0,\mathrm{u}}$	reference strength of the upper bound curve (MRA model)
F_c	peak strength (IMK model)
F_f	load recorded at fracture (coupon tensile test)
F_h	strength at the beginning of strain hardening branch (attainment of the strain level ε_h) (PFR model)

F_i	load at cycle i
$\bar{F}_{i,Rd,0}$	ratio between the design resistance of mechanism type-i accounting for shear and that corresponding to the basic formulation (Coelho *et al.* model)
F_m	strength for the attainment of the stress level σ_u (PFR model)
$F_{\max}$	force corresponding on the force-deformation curve to the deformation amplitude $d_{\max}$ of the imposed cyclic action (Piluso and Rizzano model)
$F_{p,C}$	nominal minimum preloading force
F_r	residual strength (IMK model)
F_{Rd}	design resistance
F_{start}	force corresponding to the starting point of a generic branch (MRA model)
$F_{\text{t,b}}$	force in the bolt cross section (Augusto's procedure)
$F_{T,Rd}$	design tension resistance of a T-stub flange
F_u	strength at ultimate conditions
F_y	yield strength
H	support reaction
H_{h}	empirical coefficient defining the level of isotropic hardening (MRA model)
$\boldsymbol{IntF}_{\text{DOF}}^{i,j}$	internal forces vector for increment i and iteration j (iterative incremental procedure)
$I_{y,\text{b}}$	second moment of area of the section around the stronger axis of the beam
$I_{y,\text{c}}$	second moment of area of the section around the stronger axis of the column
$\boldsymbol{K}$	stiffness matrix
K	stiffness
K_{ini}	initial stiffness
K_0	initial stiffness (MRA model)
K_{0a}	initial stiffness of an ascending branch (MRA model)
$K_{0,C}$	initial stiffness of non-dissipative components with compression-only behaviour
K_{0d}	initial stiffness of a descending branch (MRA model)

$K_{0,\mathrm{l}}$	initial stiffness of the lower bound curve (MRA model)
$K_{0,\mathrm{red}}$	reduced initial stiffness due to stiffness degradation (MRA model)
$K_{0,\mathrm{t}}$	initial stiffness of the transition curve (MRA model)
$K_{0,T}$	initial stiffness of non-dissipative components with tension-only behaviour
$K_{0,\mathrm{u}}$	initial stiffness of the upper bound curve (MRA model)
K_{b}	stiffness of a single bolt-row with two bolts
K_{beam}	stiffness of the T-stub computed making use of the beam model analogy
K_{CWS}	initial stiffness of the column web panel in shear (Krawinkler’s model)
$K_{\mathrm{CWS,h}}$	residual stiffness resulting from the strain hardening (Krawinkler’s model)
$K_{\mathrm{CWS,p}}$	post-limit stiffness of the column web panel in shear (Krawinkler’s model)
K_{eq}	equivalent stiffness of a T-stub
K_{f}	stiffness of the T-stub flange for a single bolt-row with two bolts
$K_{\mathrm{f,l}}$	stiffness of the lower T-stub flange
$K_{\mathrm{f,spring}}$	initial stiffness of the flange in the decoupled component component (mechanical model)
$K_{\mathrm{f,u}}$	stiffness of the upper T-stub flange
$\boldsymbol{K_g}$	global stiffness matrix
K_i	slope of the first part of the reloading branch in the i-h cycle (Piluso and Rizzano model)
K_{pb}	stiffness of a single bolt-row with two preloaded bolts
K_{pl}	post-limit stiffness
$K_{pl,\mathrm{l}}$	post-limit stiffness of the lower bound curve (MRA model)
$K_{pl,\mathrm{t}}$	post-limit stiffness of the transition curve (MRA model)
$K_{pl,\mathrm{u}}$	post-limit stiffness of the upper bound curve (MRA model)
K_W	stiffness of the soil (Winkler foundation)
L	length; length of the column between the supports (Augusto’s procedure)
L_0	original gauge length (coupon)

L_2	distance between the beam axis and the bottom support (Augusto's procedure)
L_b	bolt elongation length; length of the beam
L_c	length of the column; parallel length (coupon)
L_t	total length of test piece (coupon)
M	bending moment
M_0	reference bending moment
$M_{0,\mathrm{inc}}$	increased value of the strength due to strain hardening (MRA model)
$M_{0,\mathrm{l}}$	bending moment of the lower bound curve (MRA model)
$M_{0,\mathrm{red}}$	reduced bending moment due to strength degradation (MRA model)
$M_{0,\mathrm{t}}$	bending moment of the transition curve (MRA model)
$M_{0,\mathrm{u}}$	bending moment of the upper bound curve (MRA model)
M_b	beam bending force at the joint core periphery
M_c	column bending force at the joint core periphery
$M_{connection}$	bending moment of the connection
M_CWS	bending moment of the column web panel in shear component
M_Ed	design bending moment
M_fc	bending moment of the column flange (Augusto's procedure)
M_{joint}	bending moment of the joint
$M_{pl,Rd}$	design value of the plastic resistance to bending moment
M_start	bending moment corresponding to the starting point of a generic branch (MRA model)
M_u	ultimate bending moment
M_y	yield bending moment
N	axial force; shape parameter
N_a	shape parameter of the ascending branch (MRA model)
N_d	shape parameter of the descending branch (MRA model)

N_l	shape parameter of the lower bound curve (MRA model)
N_t	shape parameter of the transition curve (MRA model)
N_u	shape parameter of the upper bound curve (MRA model)
P	vertical load
$\boldsymbol{Q}$	unbalanced forces vector; prying forces (T-stub)
$\boldsymbol{R}$	reference external load vector
R	support reaction
R_eH	upper yield strength, i.e. the maximum value of stress prior to the first decrease in force (coupon tensile test)
$RF2$	reaction force at nodes according to the axes yy (Augusto's procedure)
R_m	tensile strength, i.e. the stress corresponding to the maximum force, F_m (coupon tensile test)
S_0	original cross-sectional area (coupon)
S_f	minimum cross-sectional area measured after fracture (coupon tensile test)
S_m	total number of components in row m (mechanical model)
U	displacement
$\boldsymbol{U}$	vector of nodal displacements
$U2$	displacement according to the axes yy (Agugusto's procedure)
$U3$	displacement according to the axes zz (Augusto's procedure)
V	shear force
V_b	beam shear force at the joint core periphery
V_c	shear strength due to the transverse web stiffeners (Augusto's procedure); column shear force at the joint core periphery
V_n	shear force in the column web panel in shear (Augusto's procedure)
V_p	shear force corresponding to the post-yielding of the panel zone (Krawinkler's model); shear when the column flange yields (Krawinkler's model)
V_y	shear force corresponding to the first yielding of the panel zone (Krawinkler's model)

WC_i	pre-defined nodes in the column flange web for the bolt row i (Augusto's procedure)
WP_i	pre-defined nodes in the end-plate web for the bolt row i (Augusto's procedure)

Lowercase Greek letters

α	angle (Piluso and Rizzano model); coefficient (Winkler foundation)
β	percentage of the component's initial stiffness in tension; coefficient (Winkler foundation)
β_{lim}	limit value for plastic/ultimate mode classification (T-stub)
β_{Rd}	non-dimensional parameter related to the plastic mode classification (T-stub)
β_u	non-dimensional parameter related to the failure mode classification (T-stub)
γ	shear strain; shear deformation
γ	shear strain
γ_y	shear strain when the column shear panel yields (Krawinkler's model)
δ	variation
δd	variation of deformation
δu	variation of displacement
δF	variation of force
$\delta \boldsymbol{U}^{i,j}$	total variation of the nodal displacement vector in the iteration
$\delta \boldsymbol{U'}^{i,j}$	variation of nodal displacements caused by reference external load vector
$\delta \boldsymbol{U''}^{i,j}$	variation of nodal displacement due to unbalance load vector
ε	strain
ε_{eng}	engineering strain
ε_f	strain at fracture

ε_{h}	strain at the beginning of hardening branch
ε_{true}	true strain
ε_{u}	ultimate strain
ε_{y}	yield strain
ζ	coefficient (Faella *et al.* model)
θ	rotation angle
λ	$= n/m$
$\lambda^{i,j}$	external load vector multiplier
μ	average
v_{CWS}	odal displacement of the right end of the component column web panel in shear
v_{left}	nodal displacements on the left nodes of that component
v_{leftmost}	nodal displacements in implicit nodes at the beginning of each row (leftmost nodes)
v_{middle}	nodal displacements in actual nodes (with a DOF assign to), which are located between two components
v_{right}	nodal displacements on the right nodes of that component
$v_{\mathrm{rightmost}}$	nodal displacements in implicit nodes at the end of each row (rightmost nodes)
σ	stress; standard deviation
σ_{0}	reference plastic stress (yield stress)
σ_{11}	normal stresses according to the axes xx
σ_{22}	normal stresses according to the axes yy
σ_{33}	normal stresses according to the axes zz
σ_{eng}	engineering stress
σ_{f}	stress at fracture
σ_{true}	true stress
σ_{u}	ultimate stress

σ_y	yield stress
τ	shear stress
τ_{23}	shear stress according to the axes yz
ϕ	rotation
ϕ_0	rotation corresponding to the reference bending moment
$\lvert\phi_0\rvert$	absolute value of the deformation corresponding to the starting point of the current excursion (MRA model)
$\phi_{connection}$	rotation of the connection
ϕ_{CWS}	rotation of the column web panel in shear component
ϕ_{cw}	column web panel contribution to the global rotation of the joint (Augusto's procedure)
$\phi_{\mathrm{el,b}}$	contribution of the elastic deformation of the beam to the global rotation of the joint (Augusto's procedure)
$\phi_{\mathrm{el,c}}$	contribution of the elastic deformation of the column to the global rotation of the joint (Augusto's procedure)
ϕ_{ep}	end-plate contribution to the global rotation of the joint (Augusto's procedure)
ϕ_{joint}	joint rotation
ϕ_{lim}	parameter related to the maximum previously experienced deformation in the direction of the loading branch (MRA model)
ϕ_{max}	maximum absolute value of deformation experienced in the previous loading history, in the direction of lading branch to be described (MRA model)
ϕ_{start}	deformation corresponding to the starting point of a generic branch (MRA model)
ϕ_{total}	global rotation of the joint (Augusto's procedure)
$\bar{\phi}_{\mathrm{u,0}}$	ultimate value in the case of monotonic loading (MRA model)
ϕ_y	conventional yielding value of deformation
ψ	empirical parameter (Piluso and Rizzano model)

Uppercase Greek letters

Δ	increment (incremental iterative procedure)
Ψ	coefficient (Faella *et al.* model)
Ω_t	set of row numbers of block t

Abbreviations

0D	non-dimensional
1D	one-dimensional
2D	two-dimensional
3D	three-dimensional
BFC	beam flange in compression
BT	bolts in tension
BWT	beam web in tension
CCM	cyclic component model
CFB	column flange in bending
CFT	curve fitting type
CTCM	coupled tension-compression model
CWC	column web in transverse compression
CWS	column web panel in shear
CWT	column web in transverse tension
DOF	degree of freedom
DTCM	decoupled tension-compression model
EC	Eurocode

EPB	end-plate in bending
FE	finite element
FEA	finite element analysis
FEM	finite element method
MRA	modified Richard-Abbot
SBCJ	steel beam-to-column joint
SDOF	single degree of freedom
SHM	smooth hysteretic model
TS-CCM	T-stub decoupled cyclic component model

PART I: INTRODUCTION AND LITERATURE REVIEW

1 INTRODUCTION

1.1. Research relevance and scope

Currently, European code for seismic design of structures, EN 1998-1 (EC8-1) (CEN, 2005d), prescribes design assisted by tests for the design of dissipative steel beam-to-column joints (SBCJs). This is owing to the lack of reliable models for predicting their behaviour under cyclic conditions, resulting in expensive and time-consuming design, unsuitable for real-life projects. The analysis of joint behaviour is complex because of several phenomena, such as material and geometrical non-linearity, contact, and slip (Simões da Silva, Santiago and Vila Real, 2002). These complexities can be dealt with using refined three-dimensional (3D) finite element method (FEM) models. However, the use of a 3D FEM requires relevant expertise, is computationally expensive, and produces results that may depend on the user (Simões da Silva, 2008). An alternative simplified method that deals with the complexity of joints is the component method (CM) coded in European code EN1993-1-8 (EC3-1-8) (CEN, 2005c) for the design of steel structures under quasi-static conditions. This method evolved from the study by Zoetemeijer (1974) on bolted SBCJs in the 1970s, which was subsequently extended by Tschemmernegg's research group (1987; 1998), Jaspart (2000), Weynand *et al.* (1995), and several others. A thorough review of these developments may be found in Jaspart and Weynand (2016).

The CM provides simple procedures to evaluate the moment–rotation response of a wide range of steel joint configurations, and it is based on a simplified mechanical model composed of extensional springs (0D elements) and rigid links. The behaviour of a joint is determined based on the equilibrium and compatibility relations between springs arranged in an appropriate layout considering the constitutive relation of each spring. Each spring element, also known as a component, represents a specific region of the joint (e.g. column web) subjected to a specific type of loading (e.g. tension). The components to be considered in a model are only those relevant for the overall joint structural behaviour (Weynand, Jaspart and Steenhuis, 1995). In general, each component is characterised by a non-linear force–deformation relation, although simpler idealisations are possible.

Earthquakes induce internal cyclic actions on structural elements and may introduce high amplitude rotations in joints, causing the material to repeatedly experience plastic strains, and consequently, undergo failure driven by a low-cycle fatigue (Landolfo *et al.*, 2017). The typical approach to simulate the moment–rotation response of steel joints under these conditions has been to develop multi-parameter mathematical expressions that can reproduce the observed experimental cyclic moment–rotation behaviour for a few steel joints with a few typologies. Subsequently, the values of the parameters are calibrated to satisfactorily correlate to a small range of section sizes for joints having the same typologies (Nogueiro, 2009). This approach relies purely on statistical calibration, without a solid physical background, and thus, cannot be generalized.

To overcome the lack of design guidelines and following the same strategy used in Japan and USA after the 1994 Northridge and 1995 Kobe earthquakes, the European projects, EQUALJOINTS (Landolfo, 2017a) and EQUALJOINTS+ (Landolfo, 2017b), led to the development of the pre-qualification criteria for SBCJs suitable for seismic regions. This project also resulted in the development of detailed rules for (i) the characterization and modelling of the cyclic behaviour of components, and (ii) the development of a cyclic analysis procedure called as the cyclic component method (CCM). In this thesis, the CCM is specifically addressed.

Among the various components of a beam-to-column steel joint, the T-stub is probably the most complex and presents specific challenges related to the prediction of its cyclic behaviour. On the other hand, the T-stub is one of the main dissipation energy sources of a joint. Hence, a deep understanding of the cyclic behaviour of bolted T-stubs is required to identify their governing parameters and the best strategy to account for it in the scope of the CCM. The experimental cyclic tests in isolated T-stubs are the most reliable source of information for the analysis of the cyclic behaviour of T-stubs.

1.2. Research objectives and methodology

The research study presented has the fundamental objective to develop analytical and numerical tools able to increase the efficiency of the modelling and design of steel beam-to-column joints for cyclic actions. The main goal is to contribute to the development of an analytical design method, based on the component method. More specifically, there is the intention to:

(i) characterization and modelling of the quasi-static cyclic behaviour of one of the most dissipative components of a SBCJ, i.e. the components that can be modelled though the T-stub analogy

  - characterize the cyclic behaviour of components through experimental tests on isolated components, namely on T-stubs;
  - develop analytical hysteretic models for dissipative components to be incorporated in the CCM;

(ii) development and implementation of a tool aimed for the assessment of quasi-static cyclic of SBCJs

  - conceptualization, mathematical formulation and numerical implementation of the Cyclic Component Method (CCM), a generic and simple procedure to compute the cyclic behaviour of SBCJs through a mechanical model of the joint based in the component method coded in EC3-1-8 (CEN, 2005c);
  - develop a software that embodies the CCM.

1.3. Organization of the document

This document is divided into three parts:

Part I encloses the introduction and the literature review and is composed by two chapters.

Chapter 1 – *Introduction*, presents a brief description of research scope, objectives and plan.

Chapter 2 – *Literature review*, presents the background material and the relevant theoretical bases for the research on SBCJs. A detail review of past analytical and numerical work, to characterize the steel joints behaviour is performed. At the component level, with special emphasis in the T-stub, methods to characterize their hysteretic behaviour are reviewed. It is also included in this chapter the data collection and treatment of the available experimental tests on isolated T-stubs, found in the literature, used later in Part II.

Part II contains three chapters and includes developments on the characterization of the cyclic behaviour of T-stubs.

Chapter 3 – *Experimental assessment of the cyclic behaviour of T-stubs*, describes the experimental program on isolated T-stubs under monotonic and cyclic loading performed in the scope of the current thesis and the detailing and discussion of tests results. Experimental results are used later in Chapters 4 and 5.

Chapter 4 – *Cyclic modelling of T-stubs: global models*, an assessment of two approaches available in technical literature to model the cyclic behaviour of T-stubs by adjusting models to its global behaviour is conducted. The performance of each modelling procedures is compared against experimental results.

Chapter 5 – *Cyclic modelling of T-stubs: decoupled component model*, a rationale for decoupling the T-stub is presented and a framework and the implementation of a compatible decoupled component model for the T-stub under seismic loading is proposed. The accuracy of the proposed model is validated by comparison with experimental test results.

Part III encloses four chapters and further developments on the component method for cyclic loadings.

Chapter 6 – *Cyclic component model*, where the development of the CCM for predicting the cyclic response of SBCJs is presented.

Chapter 7 – *Computational implementation*, devoted to the computational implementation of the CCM.

Chapter 8 – *Illustrative example*, a case study is presented in order to illustrate the applicability of the previous tools and methodologies. Available procedures found in the literature to extract the cyclic behaviour of a SBCJ and its components from refined 3D FEM models are applied. The accuracy of the proposed CCM is validated by comparison with numerical results.

Chapter 9 – *Conclusions and future work*, a summary of the main findings and contributions of the thesis is provided together with some suggestions for future research.

2 LITERATURE REVIEW

2.1. Introduction

The quasi-static monotonic behaviour of SBCJs is hard to predict due their material and geometric non-linear behaviour. The prediction of their cyclic behaviour is even more complex because of several additional phenomena such as hysteresis, pinching and the degradation of the mechanical properties.

The background material and the relevant theoretical bases for the research on SBCJs is presented focusing the two main topics: the behaviour of steel joints under cyclic loading and the analysis and design methods. A brief description of the available mathematical models for non-linear hysteric behaviour of steel joints and the current design methods for SBCJs analysis and design, including the component method adopted by EN 1993-1-8 (CEN, 2005c) and refined three-dimensional (3D) finite element method (FEM) modelling, are also presented.

In order to extend the component method to the prediction of the seismic response of SBCJs, the modelling of the cyclic response of the joint components is necessary. Accordingly, procedures to characterize the cyclic behaviour of the T-stubs – one of the most important components of bolted connections – are addressed in three ways: experimental, analytical and numerical (refined 3D FEM modelling).

2.2. Terms and definitions

A strong beam-to-column joint between I/H cross sections consists of a web panel and a connection. The web panel is the portion of the column web within the height of the connected member. The connection is the location at which two or more elements meet. These parts of a generic SBCJ configuration are illustrated in Figure 2.1.

The connection presented in Figure 2.1, named double extended end-plate connection, is very common in contemporary construction due to their high capacity to transfer the internal forces between beams and columns, namely bending moment, shear force and axial force, and because it allows symmetric behaviour under cyclic loading (sagging and hogging). The connection consists of an end-plate welded to the beam and bolted to the column flange. It is also common to add transverse stiffeners or supplementary web plates in the column – a generic configuration of a double extended end-plate joint is illustrated in Figure 2.2. The reference case of SBCJ considered in the current thesis is the double extended end-plate connection.

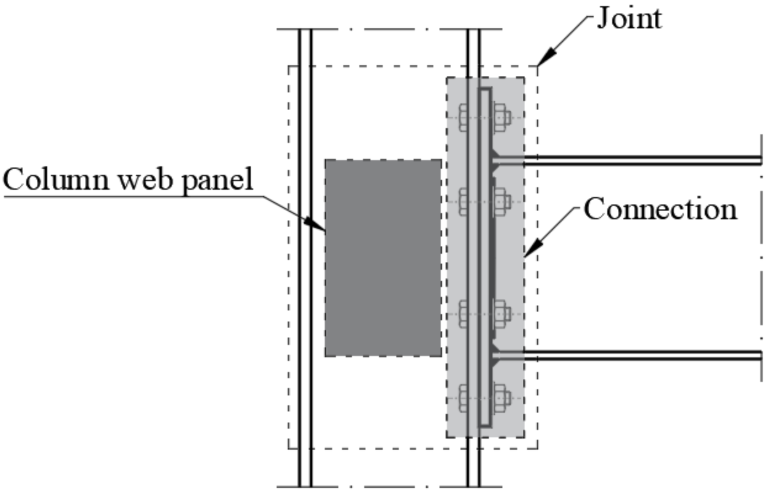

Figure 2.1 – Parts of a beam-to-column joint configuration.

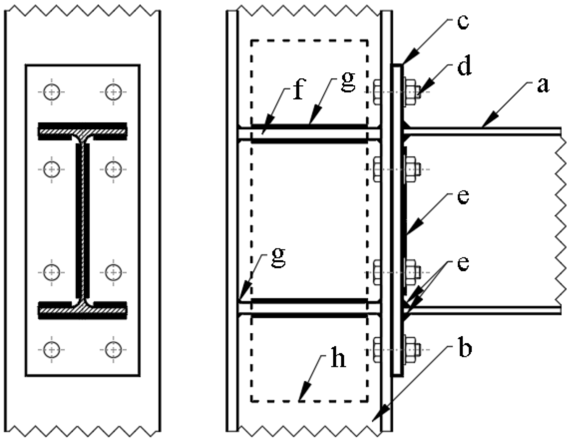

a – beam
b – column
c – end-plate
d – bolts
e – beam to end-plate welds
f – transverse stiffeners
g – column to stiffeners welds
h – supplementary web plates

Figure 2.2 – Generic configuration of double-extended end-plate joints.

2.3. Behaviour of steel joints and its components under cyclic loading

2.3.1. Global behaviour

The structural behaviour of steel joints under cyclic loading is characterised by hysteretic loops with progressive degradation of the strength and the stiffness, which are frequently combined with pinching effects. As an example, Figure 2.3 presents two extreme behaviours of steel joints: a stable behaviour – see Figure 2.3(a) – for a double extended end-plate SBCJ (Bursi and Ferrario, 2003), where degradation is barely noticed, and extensive pinching – see Figure 2.3(b) – for a flush end-plate SBCJ (Bernuzzi, Zandonini and Zanon, 1996).

Independently of the type of cyclic behaviour, usually the quasi-static monotonic curve is a good approximation for the upper/lower bound of the cyclic curve (envelope/backbone curve) up to the maximum/minimum bending moment, as illustrated in Figure 2.4. It should be mentioned that the behaviour of a joint is also dependent on the loading velocity due to rate-dependent hardening (Ribeiro *et al.*, 2015), however, in this study, only quasi-static cyclic behaviour is addressed.

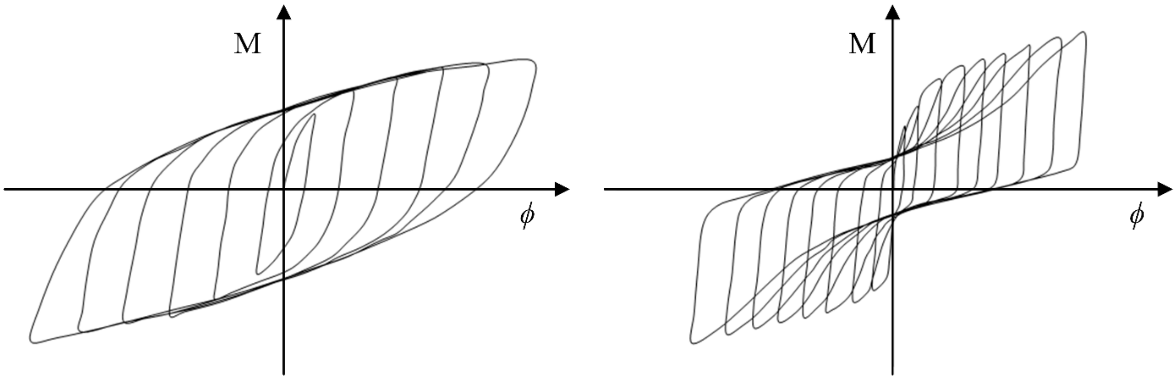

(a) (b)

Figure 2.3 – Extreme steel joint behaviours: (a) stable and (b) extensive pinching.

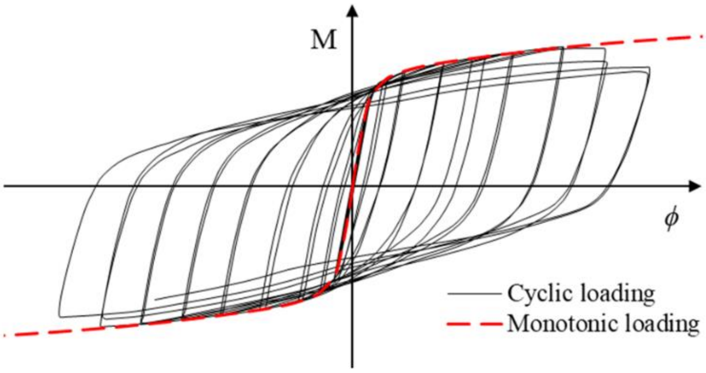

Figure 2.4 – Monotonic and cyclic response.

For exemplification, Figure 2.5 depicts a simplified multi-linear force-deformation envelope/ backbone curve used for hysteretic models of structural elements (Ibarra, Medina and Krawinkler, 2005). Typically, the envelope shows an initial linear branch characterised by elastic stiffness until the yielding strength is reached, followed by a hardening branch. When the maximum force/moment is reached, a softened branch produced by the cyclic degradation is observed, characterised by a post-capping stiffness, followed by a constant branch corresponding to the residual strength.

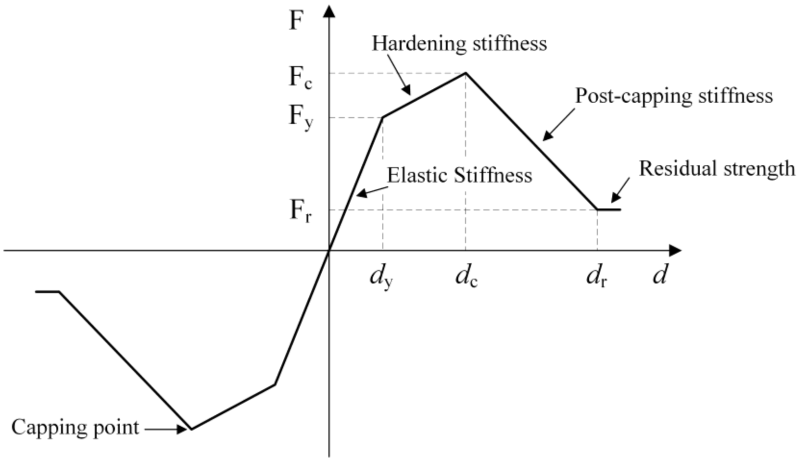

Figure 2.5 – Simplified multi-linear backbone curve.

Figure 2.6 illustrates the three common hysteresis loops types usually observed in the bending moment-rotation response of steel joints subjected to cyclic loading.

First, Figure 2.6(a) shows a degradation of stiffness corresponding to the progressive reduction in the stiffness in the loading and unloading branches resulting from accumulation of plastic deformations and the deterioration of the mechanical properties of the joint components.

Similarly, Figure 2.6(b) depicts the degradation of strength, which also results from accumulation of plastic deformations and the deterioration of the mechanical properties of the joint components.

Finally, Figure 2.6(c) illustrates the pinching phenomenon, that may be caused by slip and loss of contact between different parts of a joint.

The failure of the steel joint eventually occurs after a certain number of loading and unloading cycles, depending on the level of plastic strain that is achieved in each cycle.

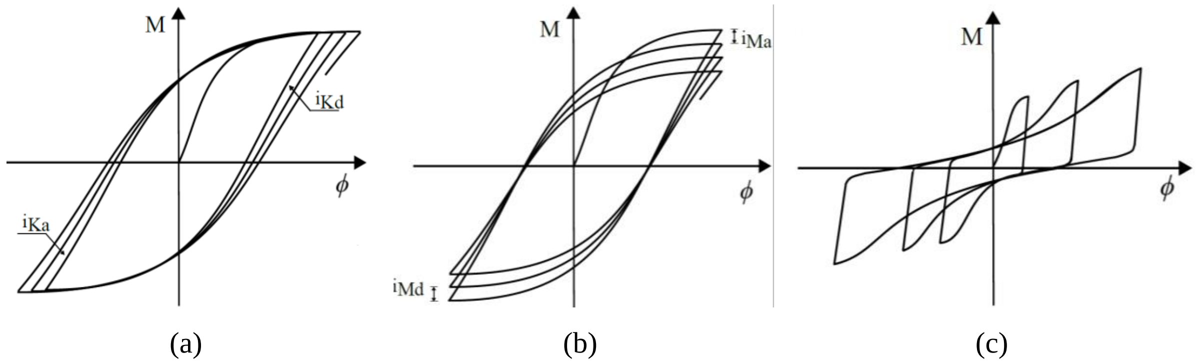

(a) (b) (c)

Figure 2.6 – Typical hysteretic moment-rotation behaviour of steel joints: (a) stiffness degradation, (b) strength degradation and (c) pinching.

2.3.2. Influence of the components in the overall cyclic behaviour of a joint

The typology of the hysteretic behaviour of a SBCJ is directly related to the behaviour of the components involved in the dissipation phenomena, mainly the weakest components. As an example, Figures 2.7(a) and 2.8(a) illustrate the behaviour of two extended end-plate SBCJ: (i) without column web panel stiffeners, whereby the panel zone is the weakest component (Iannone *et al.*, 2011) and (ii) with column web panel stiffeners (doubler and continuity plates), whereby the end-plate in bending is the weakest component (Iannone *et al.*, 2011).

The column web panel in shear of the SBCJ without stiffeners (Figure 2.7) is the component mainly responsible for the energy dissipation capacity of the joint, Figure 2.7(b), showing a stable behaviour. On the other hand, in the SBCJ with column web panel stiffeners (Figure 2.8), the component with the highest energy dissipation is the T-stub, whose behaviour shows extensive pinching, Figure 2.8(c), which is reflected in the joint global behaviour, Figure 2.8(a). As this example shows, the understanding and the characterization of the behaviour of the components under cyclic loading is crucial for the modelling of the cyclic behaviour of a joint and, consequently, to extend the component method for cyclic loading.

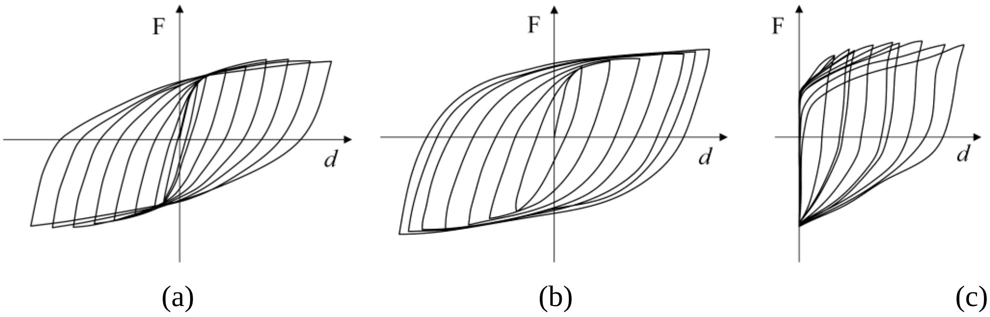

(a) (b) (c)

Figure 2.7 – Cyclic behaviour of an extended end-plate SBCJ without stiffeners: (a) joint, (b) column web panel in shear and (c) end-plate equivalent T-stub (adapted from (Iannone *et al.*, 2011)).

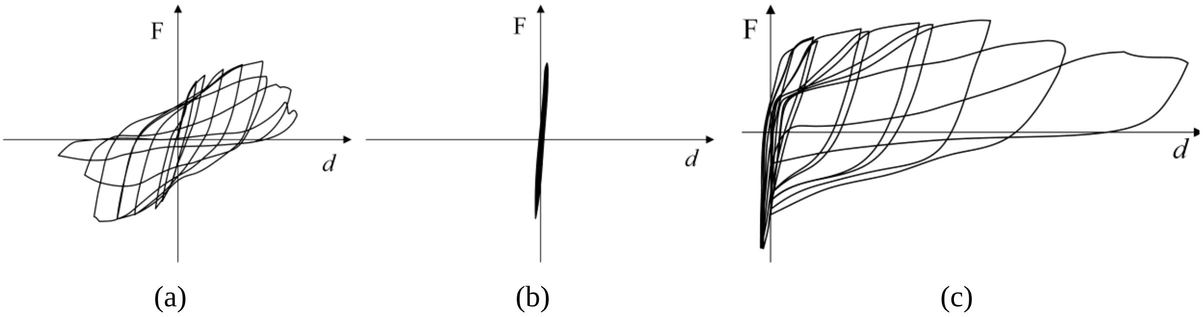

(a) (b) (c)

Figure 2.8 – Cyclic behaviour of an extended end-plate SBCJ with column web panel stiffeners: (a) joint, (b) column web panel in shear and (c) end-plate equivalent T-stub (adapted from Iannone *et al.* (2011)).

2.4. Multi-parameter mathematical models for the cyclic moment−rotation curves of joints

EC3-1-8 (CEN, 2005c) provides codified information to determine the force–deformation behaviour of numerous components for quasi-static monotonic conditions. For cyclic loading EC3-1-8 does not provide any guidance and thus a possible approach is to use multi-parameter mathematical models fitted with experimental results to simulate the behaviour of single components used in the scope of the components method. This approach was followed in the course of this thesis and thus a brief summary of this topic is presented to clarify the reasons for the models used.

2.4.1. Continuous models

The typical cyclic behaviour of steel joints explained in the previous section requires an adequate mathematical description for practical applications. Historically, two mathematical formulas provide the basis for most of the models that have been proposed in the literature: (i) Ramberg–Osgood-type mathematical model (Ramberg and Osgood, 1943) and (ii) Richard–Abbott-type mathematical model (Richard and Abbott, 1975; Della Corte, De Matteis and Landolfo, 2000; Nogueiro, Simões and Bento, 2006; Nogueiro *et al.*, 2007), but other alternatives were also developed.

2.4.1.1. Ramberg-Osgood type models

Ramberg and Osgood (1943) proposed a three-parameter model for the non-linear relationship between the stress (or generalised deformation) and strain (or generalised internal force) of ductile materials/elements. This model is extensively used in FE software packages and is appropriate for steel elements with strain hardening and a smooth transition from the elastic to the plastic region. The main limitation of this model is its inability to simulate the behaviour of materials/elements with softening. The Ramberg-Osgood model is expressed by the mathematical expression given by Eq. (2.1).

$$\varepsilon = \frac{\sigma}{E} + K \cdot \left(\frac{\sigma}{E}\right)^N \tag{2.1}$$

where ε is strain, σ is stress, E is Young’s Modulus, K and N are constants that define the shape of the curve in the hardening part and depend on the material being considered. The first term in Eq. (2.1) accounts for the elastic part of the constitutive relations and the second term accounts for the inelastic part.

The use of the Ramberg–Osgood model to represent the nonlinear $M-\phi$ behaviour of joints was suggested for the first time by Ang and Morris (1984), see Eq. (2.2)

$$\frac{\phi}{\phi_0}=\frac{M}{M_0}\left(1+\left(\frac{M}{M_0}\right)^{N-1}\right) \tag{2.2}$$

where ϕ is the rotation and M is the bending moment, M_0 is a reference bending moment and ϕ_0 is the corresponding rotation and N is a shape parameter.

2.4.1.2. Colson-Louveau type models

Colson and Louveau (1983) and Kishi and Chen (1990), proposed a three-parameter power model for the bending moment-rotation given by

$$\phi=\frac{M}{K_0\cdot\left(1-\left(\frac{M}{M_{\mathrm{u}}}\right)^{N}\right)^{\frac{1}{N}}} \tag{2.3}$$

where K_0 is the initial stiffness, M_{u} is the ultimate moment capacity, both evaluated analytically, and N is the shape parameter. The first two parameters are the limit values of the moment-rotation curve and the shape parameter allows to adjust the curvature between the initial stiffness branch and the post-elastic moment-rotation branch of the $M-\phi$ curve. This model was calibrated for the three types of connections: single/double web angle connections, top and seat angle connections, and top and seat angle connections with double web angles (Cruz *et al.*, 1998) however is not suitable for curves which do not tend to follow a post-elastic flat branch (Chen and Lui, 1991).

2.4.1.3. Bouc-Wen type models

The Bouc-Wen model, was originally proposed by Bouc (1967), later was generalized by Wen (1976) and was further modified by several others (Baber and Wen, 1981; Baber and Noori, 1985, 1986). The final model, known as the Bouc-Wen-Baber-Noori model (Baber and Noori, 1986), is a smooth hysteretic dynamic model for single-degree-of-freedom (SDOF) mechanical system under forced vibration, including strength and stiffness degradation, comprising a continuous change of stiffness due to yielding and sharp changes due to unloading, and pinching. Sivaselvan and Reinhorn (2000), proposed a variation of the Wen-Bouc model to a versatile smooth hysteretic model (SHM) that includes, in addition to stiffness and strength degradation, the pinching effect, derived from inelastic material behaviour. However, it does not include a negative backbone curve tangent stiffness. The modelling of asymmetric hysteresis have been proposed by Dobson *et al.* (1997) and Song and Kiureghian (2006).

2.4.1.4. Richard-Abbott type models

Richard and Abbott (1975) proposed a three-parameter mathematical model to represent the generalised deformation versus the generalised internal forces of non-linear structural systems. The new model has the advantage of representing stress explicitly in terms of the strain according to the expression

$$\sigma = \frac{\left(E - E_p\right)\cdot\varepsilon}{\left(1 + \left|\frac{\left(E - E_p\right)\cdot\varepsilon}{\sigma_0}\right|^{N}\right)^{\frac{1}{N}}} + E_p\cdot\varepsilon, \tag{2.4}$$

where E_p is the plastic modulus, N is the shape parameter of the curve, σ_0 is the reference plastic stress (yield stress), and ε is the strain. In addition to provide the same degree of accuracy as the Ramberg–Osgood model, the Richard–Abbott model can represent materials with strain softening, which is a major limitation of the former.

The Richard–Abbott model was first applied to the cyclic moment rotation of joints by De Martino *et al.* (1984) and then extended by Della Corte *et al.* (2000) to deal with pinching, strength and stiffness deterioration, and hardening effects. Eq. (2.5) presents the mathematical expression for a generic branch of the moment–rotation curve of a joint for a simpler case without pinching, stiffness or strength degradation, and strain hardening effect where K_0 and K_{pl} are the initial and post-limit stiffness, respectively, N is the shape parameter of the curve, and M_0 is the reference plastic moment, M_{start} and ϕ_{start} are the coordinates of the first point of a generic branch. Including the pinching effect, damage, and cyclic hardening requires additional parameters.

$$M = M_{\mathrm{start}} - \frac{\left(K_0 - K_{pl}\right)\left(\phi_{\mathrm{start}} - \phi\right)}{\left(1 + \left|\frac{\left(K_0 - K_{pl}\right)\left(\phi_{\mathrm{start}} - \phi\right)}{\left|M_{\mathrm{start}}\right| + M_0}\right|^{N}\right)^{\frac{1}{N}}} - K_{pl}\cdot\left(\phi_{\mathrm{start}} - \phi\right) \tag{2.5}$$

Nogueiro *et al.* (2006; 2007) developed a modified Richard–Abbott (MRA) model for asymmetric cyclic behaviour and showed that this model accurately reproduces the cyclic moment–rotation response of steel joints provided all the relevant model parameters are appropriately calibrated. In the next paragraphs, the relevant expressions for the MRA model will be presented.

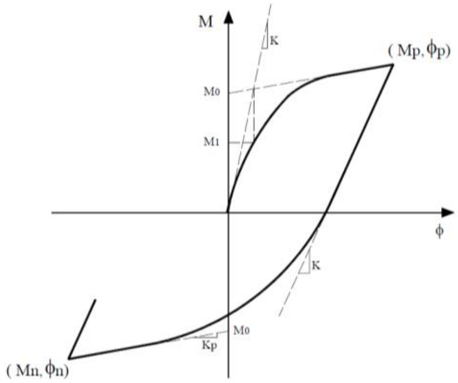

Figure 2.9 – Richard-Abbott model (Nogueiro *et al.*, 2005).

(i) Pinching effect

The Richard-Abbot model was extended by Della Corte *et al.* (2000) to include the pinching effect introducing two asymptotic lines that bound each branch of the model, as shown in Figure 2.10(a). These lines required the parameters $K_{0,\mathrm{l}}$, $M_{0,\mathrm{l}}$, $K_{pl,\mathrm{l}}$, N_l (lower bound curve) and $K_{0,\mathrm{u}}$, $M_{0,\mathrm{u}}$, $K_{pl,\mathrm{u}}$, N_u (upper bound curve). The parameters for transition curve between the bound lines ($K_{0,\mathrm{t}}$, $M_{0,\mathrm{t}}$, $K_{pl,\mathrm{t}}$, N_t), which reproduces the pinching effect – see Figure 2.10(a) – are incorporated in the MRA by replacing K_0, M_0, K_{pl}, N in Eq. (2.5) and should be determined as follows:

$$K_{0,\mathrm{t}} = K_{0,\mathrm{l}} + \left(K_{0,\mathrm{u}} - K_{0,\mathrm{l}}\right) \cdot t \tag{2.6}$$

$$M_{0,\mathrm{t}} = M_{0,\mathrm{l}} + \left(M_{0,\mathrm{u}} - M_{0,\mathrm{l}}\right) \cdot t \tag{2.7}$$

$$K_{pl,\mathrm{t}} = K_{pl,\mathrm{l}} + \left(K_{pl,\mathrm{u}} - K_{pl,\mathrm{l}}\right) \cdot t \tag{2.8}$$

$$N_{\mathrm{t}} = N_{\mathrm{l}} + (N_{\mathrm{u}} - N_{\mathrm{l}}) \cdot t \tag{2.9}$$

where t represents transition law from the lower bound to the upper bound line given by

$$t = \left(\frac{\left(\frac{\phi}{\phi_{\mathrm{lim}}}\right)^{t_1}}{\left(\frac{\phi}{\phi_{\mathrm{lim}}}\right)^{t_1} + 1} \right)^{t_2} \tag{2.10}$$

where t_1 and t_2 are parameters defined on the basis of experimental data. Note that no pinching implies $t = 1$.

The parameter ϕ_{lim} is related to the maximum previously experienced deformation in the direction of the loading branch to be described and it is given by

$$\phi_{\mathrm{lim}} = C \cdot (|\phi_0| + \phi_{\mathrm{max}}) \tag{2.11}$$

where C is a calibration parameter – see Figure 2.10(b), $|\phi_0|$ is the absolute value of the deformation corresponding to the starting point of the current excursion and ϕ_{max} is the maximum absolute value of deformation experienced in the previous loading history, in the direction of the branch to be described.

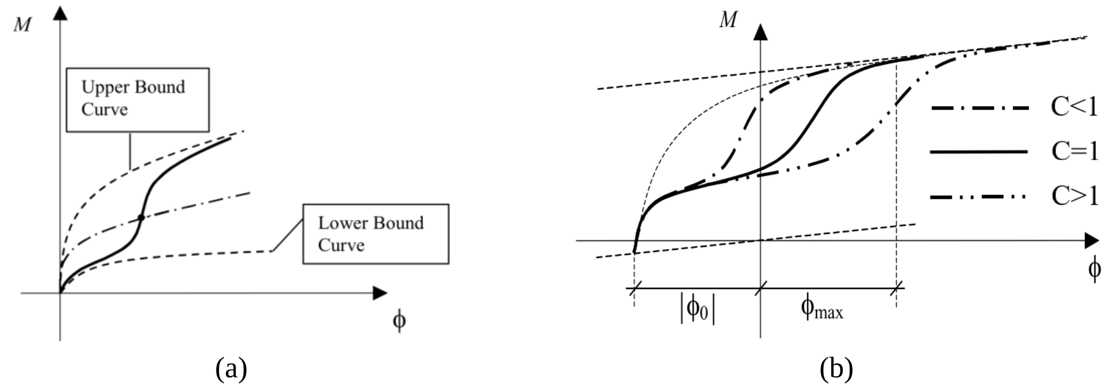

(a) (b)

Figure 2.10 – Loading branch with pinching: (a) upper and lower bound curve and (b) effect of parameter C (Della Corte, De Matteis and Landolfo, 2000).

(ii) Unloading branch

The unloading branch is assumed to be linear with a slope equal to the initial stiffness K_0 up to the intersection with the straight line obtained drawing the parallel to the hardening line going through the origin, see Figure 2.11. This allows the Bauschinger effect to be considered.

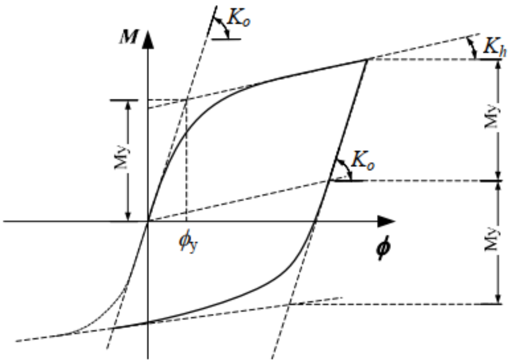

Figure 2.11 – Definition of the unloading branch (Nogueiro *et al.*, 2007).

(iii) Degradation

Cyclic behaviour leads to the accumulation of plastic deformation in the joint until failure occurs due to fracture. Accordingly, the cyclic load will lead to a deterioration of the stiffness $K_{0,\mathrm{red}}$ and strength $M_{0,\mathrm{red}}$ of the joint which can be incorporated in the MRA model in two ways: (i) degradation – replace K_0 and/or M_0 by $K_{0,\mathrm{red}}$ and/or $M_{0,\mathrm{red}}$, respectively, in Eq. (2.5); (ii) pinching combined with degradation – replace $K_{0,\mathrm{u}}$, $K_{0,\mathrm{l}}$, $M_{0,\mathrm{u}}$ and/or $M_{0,\mathrm{l}}$ by $K_{0,\mathrm{red}}$ and/or $M_{0,\mathrm{red}}$, when appropriate, in Eqs. (2.6) and/or (2.7); where $K_{0,\mathrm{red}}$ and $M_{0,\mathrm{red}}$ are computed according to the following expressions

$$K_{0,\mathrm{red}} = K_0 \cdot \left(1 - i_{\mathrm{K}} \cdot \frac{E_{\mathrm{h}}}{K_0 \cdot \bar{\phi}_{\mathrm{u},0}}\right) \tag{2.12}$$

$$M_{0,\mathrm{red}} = M_0 \cdot \left(1 - i_{\mathrm{M}} \cdot \frac{E_{\mathrm{h}}}{M_y \cdot \bar{\phi}_{\mathrm{u},0}}\right) \tag{2.13}$$

and where i_{K} and i_{M} are empiric parameters related with the level of degradation, E_{h} is the hysteretic energy dissipation accumulated in all previous cycles, M_y represents the conventional value of the joint plastic strength, $M_y = M_0/1 - K_{pl}/K_0$, and $\bar{\phi}_{\mathrm{u},0}$ corresponds to the ultimate value in the case of monotonic loading.

(iv) Strain hardening

Experimental results of constant deformation amplitude tests for joints not exhibiting strength deterioration show that cyclic hardening grows up in few cycles and then becomes stable. Isotropic hardening can be incorporated in the MRA model in three ways: (i) hardening – replace M_0 by $M_{0,\mathrm{inc}}$ in Eq. (2.5); (ii) pinching combined with hardening – replace $M_{0,\mathrm{u}}$ and/or $M_{0,\mathrm{l}}$ by $M_{0,\mathrm{inc}}$ in Eq. (2.7); and (iii) degradation combined with hardening – replace M_0 by $M_{0,\mathrm{inc}}$ in Eq. (2.13); where $M_{0,\mathrm{inc}}$ is computed according to the following expression

$$M_{0,inc} = \begin{cases} M_0, & \phi_{\max} < \phi_y \\ M_0 \cdot \left(1 + H_{\mathrm{h}} \cdot \dfrac{|\phi_{\max}| - \phi_y}{\phi_y}\right), & \phi_{\max} \geq \phi_y \end{cases} \tag{2.14}$$

where M_0 and $M_{0,\mathrm{inc}}$ are the initial and increased value of the strength, respectively, $\phi_{\max}$ is the maximum value of deformation reached in the loading history (in either positive or negative direction), ϕ_y is the conventional yielding value of deformation and H_{h} is an empirical coefficient defining the level of isotropic hardening (Filippou, Popov and Bertero, 1983). The above formulation practically corresponds to translate the asymptotic line of the original Richard-Abbott equation (De Martino, Faella and Mazzolani, 1984), as a function of the extent of the plastic deformation.

2.4.2. Multi-linear models

Multi-linear models are also commonly used to represent the behaviour of SBCJs and form the basis of simplified representations of design moment–rotation idealisations, e.g. in EC3-1-8 (CEN, 2005c). However, these models have the major drawback of being discontinuous and thus not continuously differentiable. In the following sections the main types of multi-linear models will be briefly resumed.

2.4.2.1. Krawinkler models

The Krawinkler model (Krawinkler, 1978), also known as the trilinear model, is one of the most commonly used multi-linear models for representing the shear behaviour of SBCJs with transverse stiffeners.

Krawinkler's trilinear model includes explicitly the contributions of the (i) deformation of the column web panel zone, (ii) the formation and deformation of plastic hinges in column flanges, and (iii) strain hardening (Downs, 2002), as shown in Figure 2.12. The Krawinkler model can also be seen as a mechanical model made of a hinged frame with rigid beams/columns placed along the joint periphery and with three angular 1D elements in the hinges with the constitutive relations shown in Figure 2.12(a).

In Figure 2.12(b) $V_y h_\mathrm{t}$ is the bending moment and γ_y is the shear strain when the column web panel in shear yields, $K_\mathrm{CWS} h_\mathrm{t}^2$ is the initial stiffness of the column web panel in shear, $K_\mathrm{CWS,p} h_\mathrm{t}^2$ is the post-limit stiffness after yielding of the column web panel, $V_\mathrm{p} h_\mathrm{t}$ is the shear when the column flanges yield and $K_\mathrm{CWS,h}$ is the residual stiffness resulting from the strain hardening.

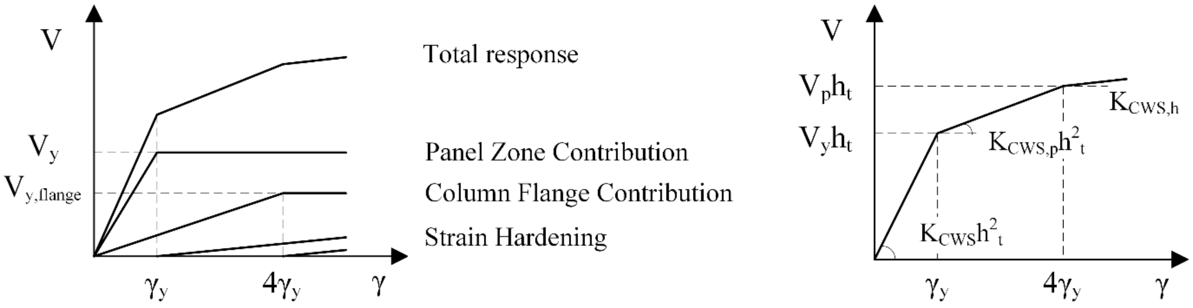

Figure 2.12 – Krawinkler's (a) shear force-shear strain relationship and (b) trilinear model.

2.4.2.2. IMK type models

Ibarra *et al.* (2005) proposed a hysteretic model including strength and stiffness degradation for both monotonic and cyclic loading, referred to in the literature as the Ibarra–Medina–Krawinkler (IMK) model.

The IMK model was developed based on a monotonic backbone curve – see Figure 2.5 – and captures the most important contributions to strength and stiffness deterioration by modifying basic hysteretic models (bilinear, peak-oriented, and pinching). The IMK model accounts for several sources of deterioration, e.g. cyclic deterioration, softening of post-yielding stiffness, and accounts for the residual strength after deterioration but does not account for cyclic hardening.

Lignos and Krawinkler (2011) performed numerical studies to calibrate deterioration parameters using previous data from more than 300 experimental tests and developed relationships to associate these parameters with geometric and material properties. The deterioration model used was a modified version of the IMK model, the modified Ibarra–Krawinkler (IK) model by Lignos and Krawinkler (Lignos, 2008; Lignos and Krawinkler, 2011), which was updated to include asymmetric component hysteretic behaviour, residual strength and incorporation of an ultimate deformation (Lignos, 2008).

2.4.3. Adopted mathematical model for cyclic behaviour

The models presented in the previous sections can reproduce the cyclic behaviour of a very narrow scope of joints.

The generalization of these models for a wider scope requires the calibration of several parameters supported by experimental and numerical analysis to account for the possible variations of the details of SBCJs, mechanical properties and load histories. This would require a significant amount of test in SBCJs and a complex calibration process.

These limitations were overcome for quasi-static monotonic loads using the CM, wherein a systematic identification and mechanical characterisation of the components allows the creation of a library of components that can be assembled to obtain the full behaviour of a large range of joints. In this study, a similar procedure was adopted to model the cyclic behaviour of joints. However, for the cyclic behaviour of components, the simple bilinear law which works well for the assessment of the strength and stiffness of steel joints under quasi-static monotonic loading is inadequate. Hence, without the loss of generality, the MRA model (section 2.4.1.4) was subsequently adopted as the mathematical framework for the cyclic modelling of components.

The main reasons for choosing the MRA were the advantages of a continuous and differentiable function within each ascending or descending branch and its capability to reproduce the main phenomena that characterize the cyclic behaviour of joints/components.

2.5. Mechanical models for joints

2.5.1. Generality

The component method (CM) nowadays is the reference method for the analysis and design of SBCJs under static monotonic conditions (Jaspart and Weynand, 2016). The behaviour of a joint is determined based on the equilibrium and compatibility relations between spring elements arranged in order to build a mechanical model together with rigid elements. Each spring element has a constitutive relation that represents a specific region of the joint under a specific type of loading, denoted as component.

However, as already stated in the Introduction Chapter, for cyclic conditions, limited research work is available on the CM (Hu, Leon and Park, 2011; Latour, Piluso and Rizzano, 2011) and there is no codified analytical method to predict the behaviour of steel joints mainly because components are subject to load reversal (i.e. tension to compression and vice-versa), i.e. different types of loading, for every load cycle.

This difficulty is recognized in codes of practice (FEMA, 2000a; Jaspart, 2000; CEN, 2004), suggesting that experimental demonstration of the suitability of steel joints should be used in seismic conditions. This led, in the US and Europe, to the pre-qualification of steel joints (Mahin, Malley and Hamburguer, 2002; AISC, 2016a, 2016b; Landolfo, 2017b, 2022), which is an efficient and pragmatic solution to overcome this problem but that presents the drawback of imposing a limited selection of available joint configurations and geometries. In addition, the aim of pre-qualification is mainly the assessment of the plastic rotation capacity, so that no modelling of the joint cyclic behaviour is provided by codes dealing with connection pre-qualification.

2.5.2. Monotonic modelling

2.5.2.1. Component method overview

To obtain the moment-rotation curve of a SBCJ through the component method, according to EC3-1-8 (CEN, 2005c), the following steps should be performed:

(i) identification of the active components among the components described in Table 6.1 of EC3-1-8 (CEN, 2005c);

(ii) characterization of each individual component in terms of strength, initial stiffness and rotation capacity to obtain the force-deformation response;

(iii) assembly of the components into a mechanical model composed of springs and rigid links;

(iv) assessment of the global $M - \phi$ of the joint making use of equilibrium, compatibility and constitutive relations.

The component method is illustrated in Figure 2.13 for a bolted extended end-plate connection with two bolt rows in tension. The active components to take into account in the joint rotational stiffness are: column web panel in shear (CWS), column web in transverse compression (CWC), column web in transverse tension (CWT), column flange in bending (CFB), end-plate in bending (EPB) and bolts in tension (BT).

The individual components are characterized by force-deformation curves, which can be obtained through experimental tests, numerical models or analytical models. Following, the basic components are assembled into the mechanical model to evaluate the bending moment-rotation response of the joint. Since the response of the joint is governed by the weakest component, the characterization of each individual component is of the outmost importance. An inadequate characterization of a component can jeopardise the results provided by the mechanical model.

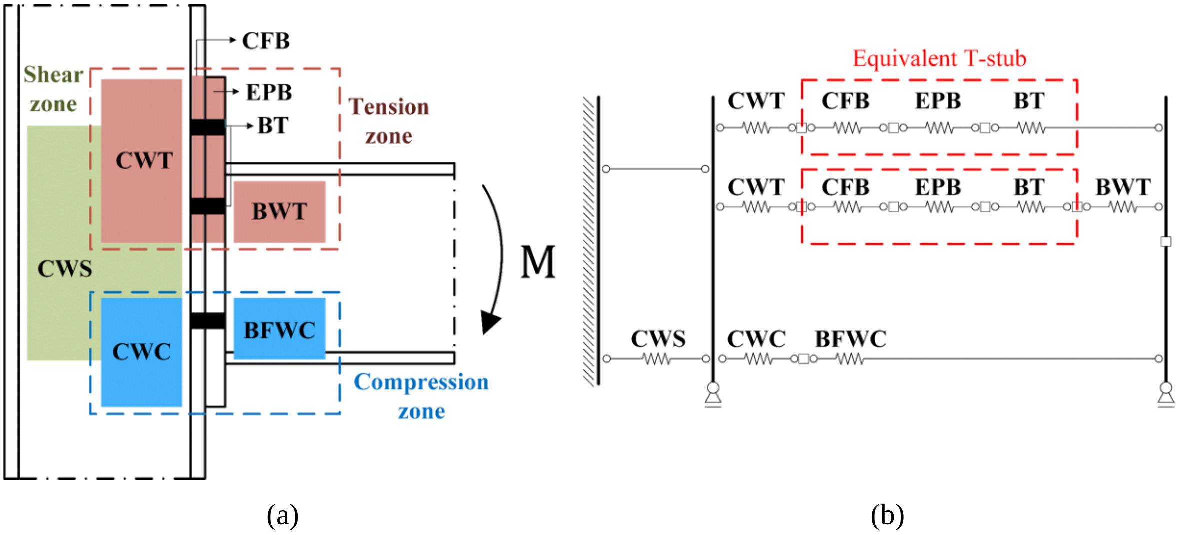

Figure 2.13 – Component method: (a) active components identification and (b) idealized mechanical model.

2.5.2.2. Equivalent T-stub

The highlighted components in Figure 2.13 – CFB, EPB and BT – can be modelled by means of the equivalent T-stub, which is a simplified geometrical idealization of the region prescribed in EC3-1-8 (CEN, 2005c). A T-stub is, as the name suggests, a T-shaped profile connected through the flanges by bolts whose geometry is defined so that it has the same behaviour of the real region of the joint that it represents.

Figures 2.14 and 2.15 identify the T-stub which accounts for the deformation of the column flange and the end-plate in bending in the particular case of an unstiffened and stiffened extended end-plate SBCJ, respectively – the T-stub models for the column flange and the end-plate sides are different. The presence of stiffeners (horizontal stiffeners in the column web or rib stiffeners in the end-plate) is also accounted for in the configuration of the T-stub.

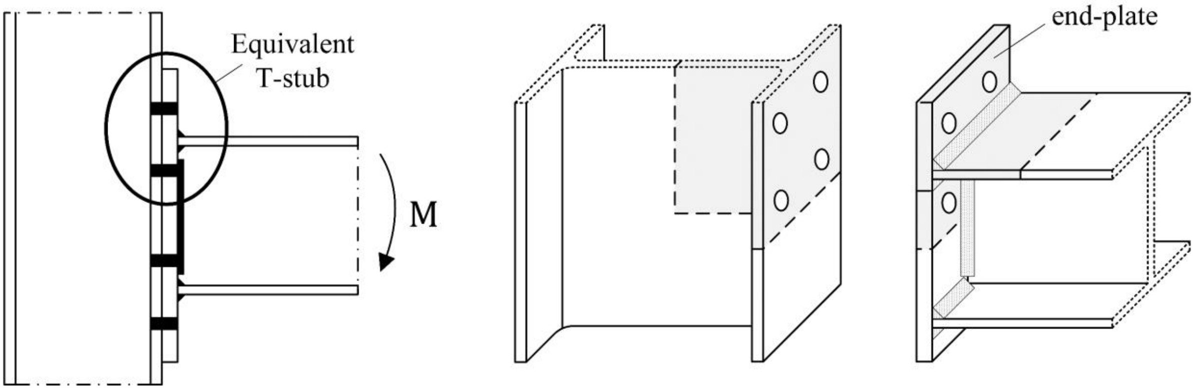

(a) joint (b) column flange side (c) end-plate side

Figure 2.14 – Unstiffened SBCJ: T-stub identification.

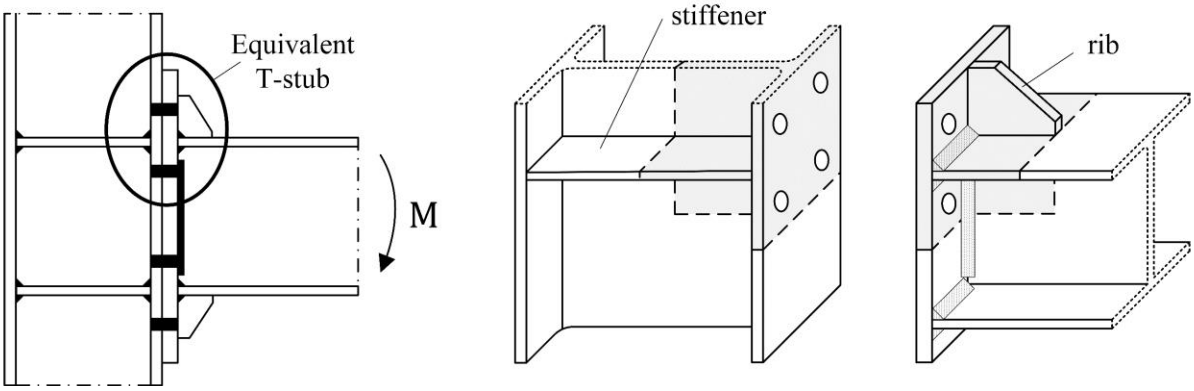

(a) joint (b) column flange side (c) end-plate side

Figure 2.15 – Stiffened SBCJ: T-stub identification.

2.5.3. Cyclic modelling

Some authors have recently studied and proposed the application of mechanical models for cyclic conditions based on the extension of the CM (Hu, Leon and Park, 2011, 2012; Iannone *et al.*, 2011; Latour, Piluso and Rizzano, 2011; Latour and Rizzano, 2019).

Latour *et al.* (2011) proposed a mechanical model, developed within the framework of the CM to predict the cyclic response of SBCJs suitable for (a) bolted extended end-plate connections and (b) double T connections, see Figure 2.16. Four sources of energy dissipation are considered: column flange in bending (CFB), column web in tension and compression (CWT-C), column web in shear (CWS), and end-plate in bending (EPB). The mechanical model is aimed for bolted connections having two bolt rows in tension and the behaviour of the two bolt rows in tension is modelled by means of only one spring element for each component. The use of the mechanical model requires three steps: (i) modelling of the cyclic behaviour of each component; (ii) assembling of the joint components; (iii) evaluation of joint cyclic moment-rotation curve. The end-plate in bending and the column flange in bending are modelled by means of the semi-analytical model for T-stubs proposed by Piluso and Rizzano (2008), see Section 2.7.3.1. A model was developed to characterize the column web panel in shear by enhancing the existing models of Kim and Engelhardt (1996, 2002). The model adopted to characterize the column web panel in tension and in compression is the one proposed by Krawinkler *et al.* (1983; 1985).

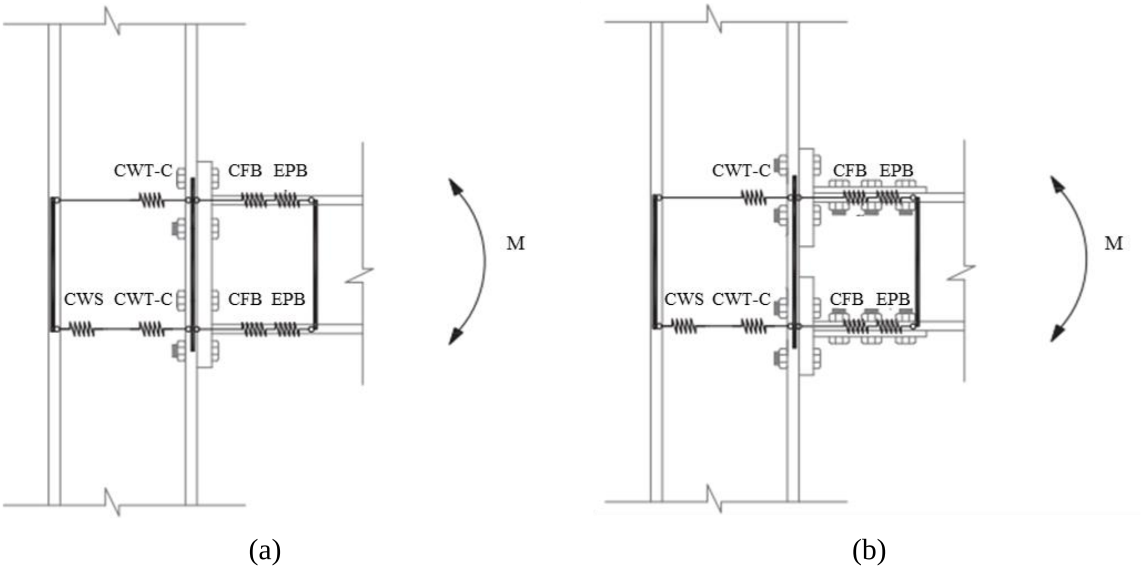

(a) (b)

Figure 2.16 – Mechanical model for (a) bolted extended endplate connections and (b) double T connections (Latour, Piluso and Rizzano, 2011).

Hu *et al.* (2011, 2012) developed a mechanical model to predict the cyclic moment-rotation curve of double T connections. Figure 2.17 shows the idealization of the force-distribution at the double T connections and the mechanical model developed, respectively. The mechanical model has the following components: (i) equivalent T-stub component, see Figure 2.36; (ii) axial deformation of the column; (ii) shear deformations of the beam and column and (iv) shear deformation of the column web panel. The T-stub is modelled by means of a refined component model developed by the same authors, see Section 2.7.3.2. The panel zone was modelled following the equations based on the AISC seismic provisions (FEMA, 2000b; AISC, 2005). The mechanical model was implemented in OpenSees (McKenna, Fenves and Scott, 2000).

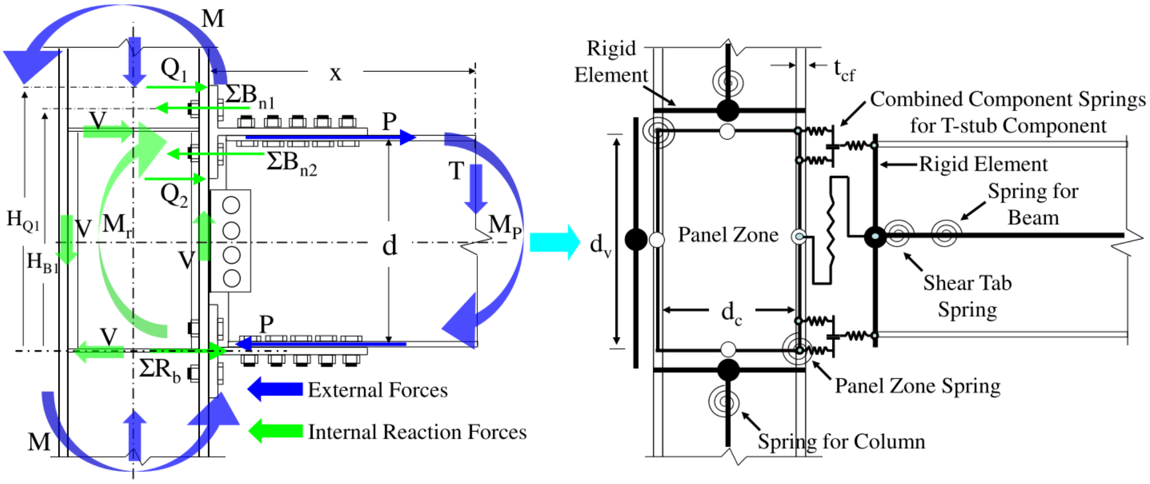

(a) (b)

Figure 2.17 – Spring model for the full-scale double T connection (Hu, Leon and Park, 2011).

2.5.4. Critical analysis of available mechanical models

Among the several authors who have addressed the development of models to simulate the cyclic behaviour of steel joints, Latour *et al.* (2011) showed that the CM approach can accurately reproduce the cyclic moment–rotation response of steel joints. However, the model developed by Latour *et al.* (2011) does not provide a general framework consistent with the well-proven CM for static monotonic responses, e.g. the T-stub components (column flange and end-plate in bending) are lumped in a global T-stub component. In addition, it cannot address directly joint configurations with a number of bolt rows in tension different from two. On the other hand, Hu *et al.* (2011, 2012), showed that a refined T-stub component model can be incorporated in a joint mechanical model to predict the cyclic response of double T connections, however, the proposed model is specific for the referred joint type.

2.6. Characterization of T-stub behaviour by experimental tests

2.6.1. Generality

Full-scale experimental tests are the most reliable method for characterization of the structural behaviour of joints. However, they do not provide insight into the behaviour of their basic components. To face this lack of granularity of information, the mechanical characteristics of the components of a SBCJ can be obtained from experimental small-scale tests over specimens representative of isolated components. These small-scale tests are also a convenient and economical way to assess the components behaviour. Accordingly, a large number of tests can be done, making possible experimental parametric and statistical analysis.

Among the various components of a SBCJ, the T-stub is probably the most complex and presents specific challenges particularly related to the prediction of its monotonic and cyclic behaviour. Hence, several specific studies regarding the cyclic behaviour of bolted T-stubs are available in the literature aimed to identify the parameters that govern their structural behaviour.

The governing parameters of the T-stub have been widely investigated for quasi-static monotonic loading. On the contrary, previous research on T-stub behaviour under cyclic loading is scarce. The monotonic tests usually aim to assess the initial stiffness, yielding load and ductility. On the other hand, cyclic tests aim to assess the degradation of those properties, as well as to characterize other phenomena that only arise in cyclic conditions.

It should also be noted that, to mimic the behaviour of the joint regions that can be modelled through the T-stub, a variety of isolated T-stub configurations are available in the literature.

In this section, the available experimental research is briefly address for monotonic loading, whereas detailed insight on the cyclic assessment is presented.

From this literature review presented in the following sections, a multitude of tests campaigns available were gathered to build a database. The collected data is presented in the current section and in Annex C, for both monotonic and cyclic loading. However, the list of experimental tests presented in Annex C includes only the documented tests with sufficient data to compare experimental results with analytical methods.

2.6.2. Monotonic behaviour

A considerable amount of experimental work was carried out in the past to characterize the quasi-static monotonic behaviour of isolated bolted T-stubs. Historically, Douty and McGuire

(1964) and Zoetemeijer (1974) were among the first to study such connections, followed by Agerskov (1976) and Packer and Morris (1977). Through the years, several researchers extended these preliminary works through the assessment of the influence of several geometric and mechanical properties on the behaviour of the T-stubs. The main goal of most of these tests on isolated T-stubs was to assess the suitability of the design codes and, for the specific cases that are not addressed in the design codes, to fulfil the gap through experimental evidence. This led to a great number of specimens tested. Following, some references are indicated for each parameter addressed through experimental tests over isolated T-stubs.

With reference to an end-plate SBCJ, the T-stub elements on the column side are generally hot-rolled profiles, whilst on the end-plate side such elements comprise two welded plates (the end-plate and the beam web/flange), see Figure 2.14. Therefore two T-stub configurations are available in the bibliography: welded specimens (Girão Coelho *et al.*, 2004; Guo *et al.*, 2017) and rolled specimens (Bursi and Jaspart, 1997; Gebbenken, Wanzek and Petersen, 1997; Piluso, Faella and Rizzano, 2001b).

In practice, not all T-stubs connect steel members with the same stiffness – e.g. small beams may be connected to very large and stiff columns. Therefore, two test set up on isolated T-stubs are used to reproduce those situations: coupled (Bursi and Jaspart, 1997; Gebbenken, Wanzek and Petersen, 1997; Girão Coelho *et al.*, 2004) and on rigid support (Bezerra *et al.*, 2020, 2022; Faralli *et al.*, 2021; Zhang *et al.*, 2022).

The idealization of the tension zone of a SBCJ by means of the equivalent T-stubs, may comprise one or more bolt rows. In the case of multiple bolt rows, depending on the pitch of the bolts, they may behave as a single bolt row or as a bolt group. Thus, the effective width, yield line patterns and group effects are key parameters to investigate. Accordingly, specimens with one or more bolt rows are available: one (Piluso, Faella and Rizzano, 2001a; Bezerra *et al.*, 2020; Tartaglia, D'Aniello and Zimbru, 2020), two (Girão Coelho *et al.*, 2004; Guo *et al.*, 2017; Zhao, He and Yan, 2021) and three bolt rows (Zhao, Lee and Chiew, 2016; Bezerra *et al.*, 2022).

Most of experimental tests are dedicated to T-stubs with two bolts per row. However, in actual structural joints, more than two bolts per row is often applied. The analytical model for T-stubs with more than two bolts per row is not currently covered by the codes. Limited research is available of specimens with four bolts per row (Latour *et al.*, 2014).

In an unstiffened SBCJ, the equivalent T-stub from the end-plate side may account for the additional stiffener that corresponds to the beam web, see Figure 2.14. On the other hand, in stiffened SBCJ, the equivalent T-stub from the column side includes the column web and the column stiffener, and the T-stub from the end-plate side includes ribs and the beam web, see Figure 2.15. Those situations are covered in the literature for specimens with one-sided transverse stiffeners (Girão Coelho *et al.*, 2004; Guo *et al.*, 2017) and two-sided transverse stiffeners (Özkılıç, 2021; S. Chen *et al.*, 2023).

The prediction of the axial stiffness of bolted T-stub according to EC3-1-8 does not account for the influence of bolt preloading. The same rules are applied for preloaded and non-preloaded bolts. However, experimental evidence has verified the beneficial gain of bolt preloading in T-stubs (Bursi and Jaspart, 1997; Faella, Piluso and Rizzano, 1998b; Zhang *et al.*, 2022).

EC3-1-8 allows using two types of high resistance bolts, namely the German HV and the British/French HR, without making any distinction. However, the tensile failure modes of these bolts are distinct (i.e. nut stripping for HV and shank necking for HR). On the other hand, connections to hollow section columns are usually done by means of hollo-bolts (one-side bolts). Specimens covering these bolts types are available: HV and HR bolts (Tartaglia, D'Aniello and Zimbru, 2020) and thread-fixed one-side bolts (Wulan *et al.*, 2020).

The use of high strength steel (HSS) in construction possesses great advantages but some challenges. Minimising the cross-section dimensions as the material provides higher strength, brings great economic benefits. However, HSS exhibit high yield ratios and limited deformation capacity when compared to mild steel grades. This topic is also addressed by experimental investigation on HSS T-stubs (Girão Coelho *et al.*, 2004; Zhao, Lee and Chiew, 2016; Guo *et al.*, 2017).

2.6.3. Cyclic behaviour

Since the 1990's, some research projects addressed the behaviour of T-stubs under cyclic loading using experimental tests. The list of documented experimental tests on T-stubs found in the literature comprises a total of 201 tests – listed in Table 2.1 – including coupled or with rigid support tests set up, and welded or rolled profiles, always including reference tests under monotonic loading. The importance of these tests relies in the fact that usually the components that can be analysed through T-stubs play a crucial role in the deformation and energy dissipation capacities of SBCJs.

Table 2.1 – List of experimental tests on T-stubs under monotonic and cyclic loading.

author	total no of tests	loading protocol	test set up	composition
Bursi *et al.* (1997)	10	monotonic and cyclic (increased amplitude)	rigid support	welded
Faella *et al.* (1999)	12	monotonic and cyclic (constant amplitude)	coupled	rolled
Leon (1999)	48	monotonic and cyclic (gradually increased amplitude)	rigid support	rolled with stem
Kasai and Xu (2002)	42	monotonic and cyclic (constant, shifted, reversed, gradually decreased and gradually increased amplitude)	rigid support	rolled
Piluso and Rizzano (2008)	28	monotonic and cyclic (constant and increased amplitude)	coupled	rolled and welded
Latour and Rizzano (2012)	11	monotonic and cyclic (constant amplitude)	rigid support and coupled	welded
Oliveira *et al.* (2021)	14	monotonic and cyclic (increased amplitude)	coupled	rolled
Yuan *et al.* (2021)	25	monotonic and cyclic (constant and increased amplitude)	rigid support	welded
Chen *et al.* (2023)	11	monotonic and cyclic (increased amplitude)	rigid support	welded

Within the research program at the University of Trento, Bursi *et al.* (1997) performed experimental tests on ten isolated T-stubs. The tested specimens had two bolt rows. Specimens subjected to cyclic loading experienced premature plate fractures at a hot spot of plastic strain concentration located at weld toes, see Figure 2.18. A clear pinching effect was seen for cyclic conditions, see Figure 2.19. The monotonic response lies very close to the envelope of the cyclic response before strength decay. Progressive strength degradation is then occurring associated to the increase of plastic deformations and damage at the weld toe. The effect of the loading history was also assessed showing that decreasing the number of cycles repetitions at each displacement level increases the maximum and ultimate displacements. Zandonini and Bursi (2002) compared the strength and the initial stiffness of the T-stubs obtained according to the EC3-1-8 model with the envelope of their experimental cyclic response and concluded that the initial stiffness predictions by the design code were not satisfactory.

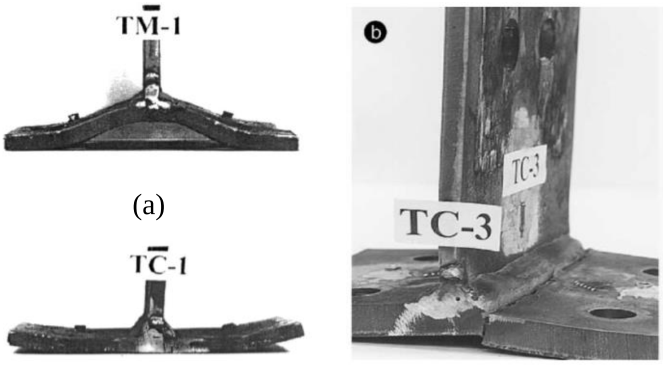

(a)

(b) (c)

Figure 2.18 – Deformed shape of specimens at the end of (a) TM-1, (b) TC-1, and (b) TC-3 tests (Nemati, Le Houedec and Zandonini, 2000; Bursi, Ferrario and Fontanari, 2002).

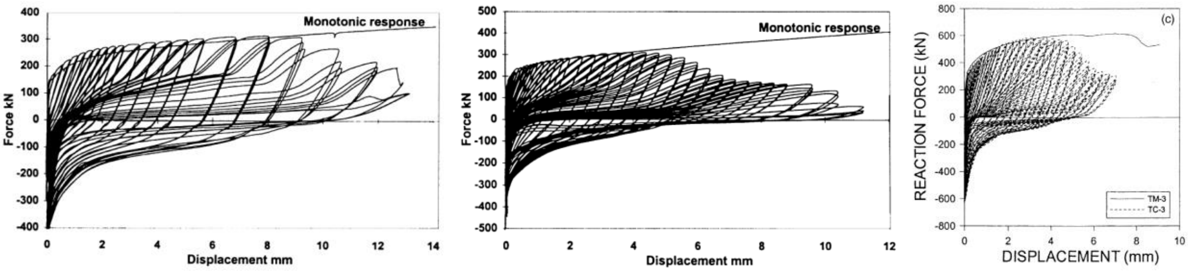

(a) (b) (c)

Figure 2.19 – Monotonic and cyclic responses: (a) TM-1 and TC-1, (b) TM-2 and TC-2, and (c) TM-3 and TC-3 (Nemati, Le Houedec and Zandonini, 2000; Bursi, Ferrario and Fontanari, 2002).

At the University of Salerno, Faella *et al.* (1999) conducted an experimental program on twelve bolted T-stubs obtained from hot-rolled profiles. Monotonic and cyclic tests under constant amplitude were carried out showing that the failure mode under monotonic loading can be different from the one occurring under cyclic loads. It was also observed that all cyclic tests exhibit the same failure mode independently of the load history. Degradation of strength, stiffness and energy dissipation capacity, and pinching was observed. Later, Piluso and Rizzano (2008) tested another batch of 28 bolted T-stub, divided in two groups: derived from rolled profiles and composed by welding. Monotonic and cyclic tests with constant and variable amplitude were carried out. Apart from degradation of strength and stiffness, and pinching they also observed that specimens with relevant plastic deformations of the bolts exhibit, under cyclic loading pronounced slip before reloading to applied forces equal to zero up to the recovery of bolt plastic deformation – note that the slip can also be seen as part of the pinching effect but will be treated in detail in this thesis because of their pronounced effect. More detail is discussed in Section 3.3. Recently, Latour and Rizzano (2012), performed a third experimental campaign of experimental tests comprising twenty-one welded T-stubs, eleven with rectangular plates and ten with hourglass plates, see Figure 2.20. The main focus was to quantify the increase of energy dissipation capacity of the classical T-stub (rectangular) provided by the proposed hourglass T-stub. Low-cycle fatigue loading histories were imposed to compare the energy dissipation capacities. The tested specimens had two bolt rows each and two distinct set ups were evaluated: coupled T-stubs and T-stubs on rigid support, see Figure 2.21. A thermal camera was used to detect propagation of heat along the flange, showing that the cyclic behaviour of hourglass T-stubs is very different from rectangular T-stubs in terms of the spread of plasticity and, as a consequence, energy dissipation capacity is also different.

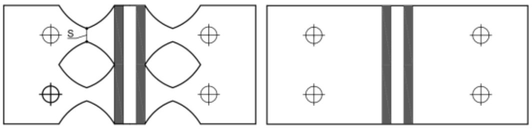

(a) (b)

Figure 2.20 – Typologies of tested specimens by Latour and Rizzano (2012): (a) hourglass and (b) rectangular.

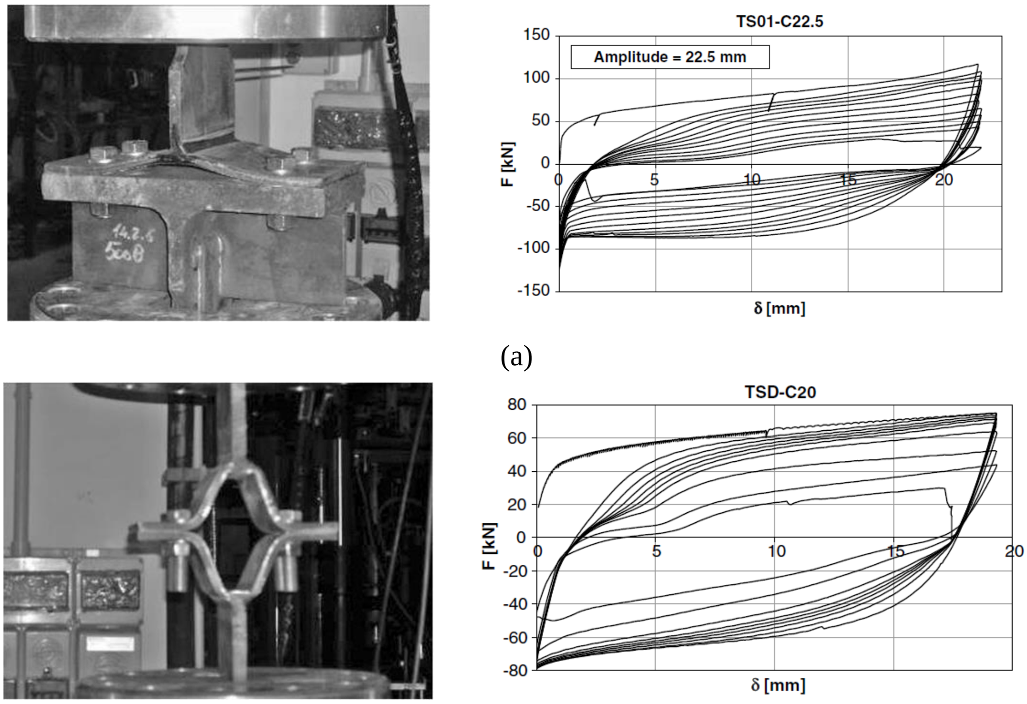

(a)

(b)

Figure 2.21 – Test set up and cyclic response of rectangular T-stubs: (a) rigid support and (b) coupled (Latour and Rizzano, 2012).

Leon (1999) tested 48 isolated T-stubs with the intention to provide the necessary data to develop a component spring model for a T-stub connection. The T-stubs tested were produced from hot-rolled profiles with stem, typically used in full-scale T-stub connections, see Figure 2.22(a). The T-stubs were tested in cyclic conditions with a load history comprising sequences of two steps: (i) during the tension phase, the T-stub was pulled to a given displacement and the load was recorded; after that (ii) the specimen was pushed in compression until a compressive force with the same magnitude of the previous tensile force was reached. The previous procedure lead to deformations larger in tension than in compression, see Figure 2.22(b).

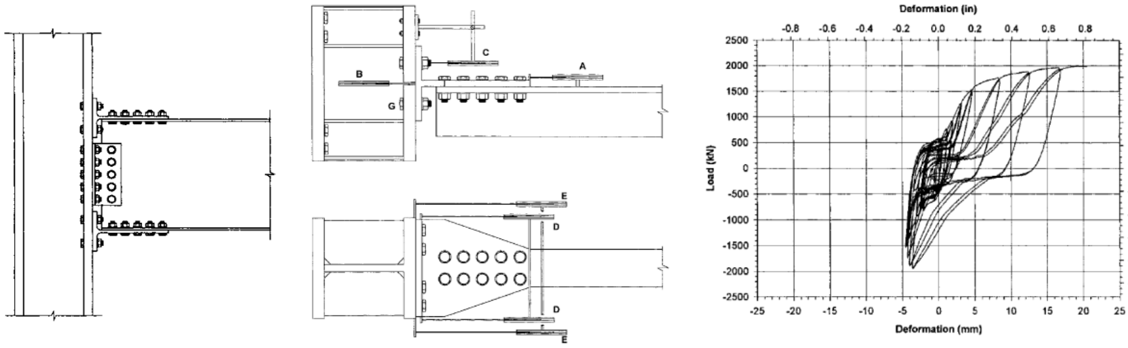

(a) (b) (c)

Figure 2.22 – (a) full-scale T-stub connection, (b) instrumentation scheme for isolated T-stub on rigid support and (c) cyclic force-deformation curve (Swanson and Leon, 2000).

Kasai and Xu (2002) carried out a test program on 34 isolated T-stubs focusing their attention mainly on the influence of the low-cycle fatigue loading history on the effectiveness of the application of the Miner’s rule (Miner, 1945). The authors categorized two deformation modes under cyclic loading by whether the bolt yields or not, mode Y and E, respectively – see Figure 2.23. It was concluded that the deformation modes and the hysteresis shape were affected by the relative stiffness and strength of the bolt and flange, and pinching was caused by yielding of the bolt and slipping between the flange and the rigid support.

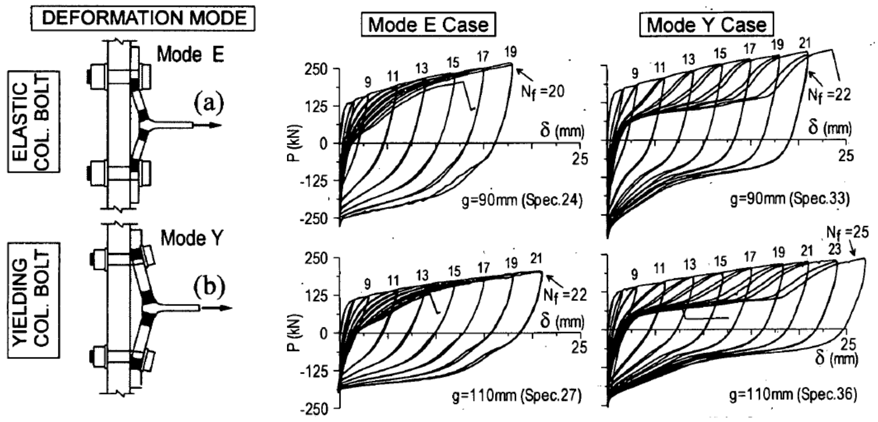

(a) (b)

Figure 2.23 – (a) deformation modes and (b) cyclic loading with increased peak displacement (Kasai and Xu, 2002).

Yuan *et al.* (2021) have conducted and experimental campaign comprising three carbon steel and twenty-two stainless steel T-stubs with the primary goal of developing a hysteretic model to predict the behaviour of stainless steel T-stubs. Two different failure modes were observed for T-stubs under variable amplitude: bolt fracture and flange fracture, see Figures 2.24 and 2.25. On the other hand, under constant amplitude three failure modes were observed: no visible surface cracking on flange, surface cracks initiated but no flange fracture occurred, and complete flange fracture developed through the plate thickness and across the flange width. In constant amplitude tests, noticeable slippage occurred for specimens failing according to static failure mode 2 (CEN, 2005c) when the force reaches zero. This slippage was attributed to the bolt elongation that result in separation between the T-stub flange and the rigid connector. The authors concluded that the stainless-steel T-stubs can achieve more favourable hysteretic performances and higher cumulative energy dissipation capacity than their carbon steel counterparts.

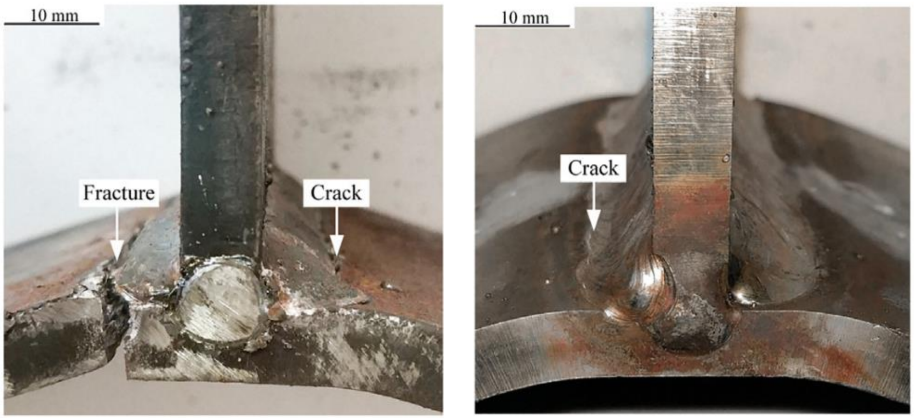

(a) carbon steel (b) stainless steel

Figure 2.24 – Failures in the vicinity of weld toe from variable amplitude tests (Yuan *et al.*, 2021).

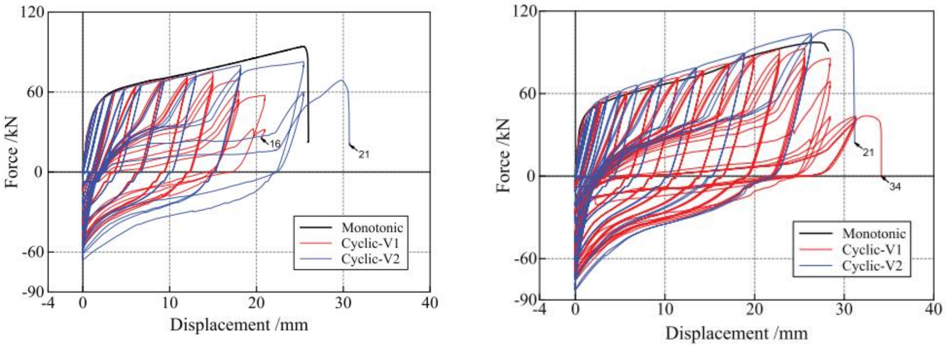

(a) carbon steel (b) stainless steel

Figure 2.25 – Hysteresis curves of variable amplitude tests (Yuan *et al.*, 2021).

Chen *et al.* (2023) investigated the performance of high strength steel T-stubs by testing eleven specimens. The effects of flange thickness, edge distance, bolt size and material grade were addressed. Specimens failed due to the fracture of the flanges near the weld toes or because of fracture of the bolts, corresponding to failure modes 1 and 2, respectively, according to EC3. Slip was observed immediately after reloading in the hysteretic response of the T-stubs, see Figure 2.26(b). Experimental results were compared to EC3 predictions only in terms of the design plastic resistance providing accurate predictions. The authors concluded that using a high strength material grade results in an improvement of ultimate load and energy dissipation.

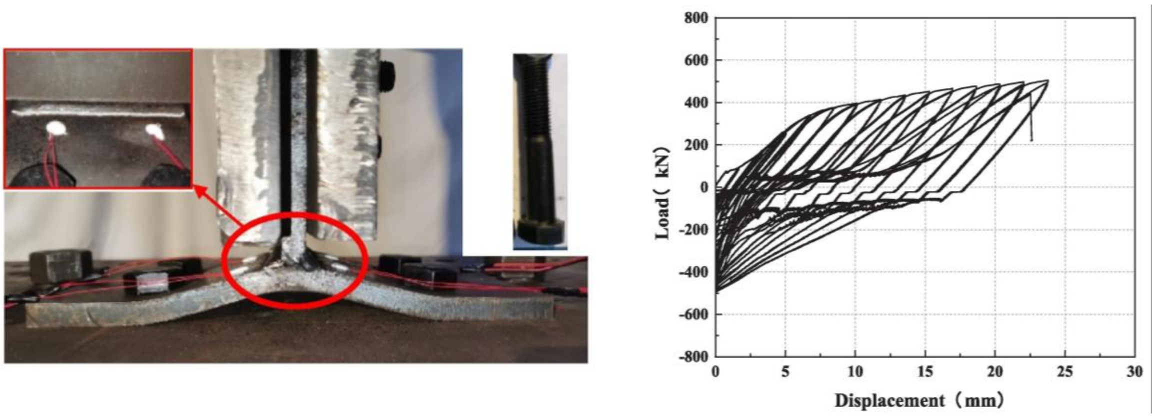

(a) (b)

Figure 2.26 – (a) failure mode of tested specimen and (b) hysteretic response (Z. Chen *et al.*, 2023).

2.7. Modelling of T-stubs using analytical models

2.7.1. Generality

From a practical point of view, neither experimental tests nor sophisticated 3D FEM models are appropriate to assess the mechanical properties of T-stubs for current design. On the other hand, analytical models may become relatively simple design models so that they can be used in practice. Accordingly, some efforts have been placed in the past in the development of analytical methods capable of predicting accurately the mechanical behaviour of the T-stubs and some of these models were included in design codes.

In this section, analytical models found in the literature for prediction of the monotonic and cyclic behaviour of T-stubs are described.

2.7.2. Monotonic behaviour

2.7.2.1. T-stub failure modes

Two categories of failure modes are considered relevant for T-stubs: (i) plastic mechanisms modes associated to yielding, named plastic failure mechanisms, and (ii) failure modes associated to ultimate conditions, named ultimate failure mechanism. Plastic failure mechanisms are usually used for design purposes whereas ultimate failure mechanism is associated to the actual failure.

(i) Plastic mechanism modes

Following the EC3-1-8 (CEN, 2005c) approach, the design (plastic) resistance $F_{T,Rd}$ of a T-stub is the lowest of three kinematically admissible failure modes considered (see Figure 2.27):

- Mode 1 (complete yielding of the flange) – formation of a plastic yield mechanism in the flange due to development of four plastic hinges;
- Mode 2 (bolt failure with yielding of the flange) – mixed failure through formation of two plastic hinges in the flange and failure of the bolts in tension;
- Mode 3 (bolt failure) – failure of the bolts without yielding of the flanges.

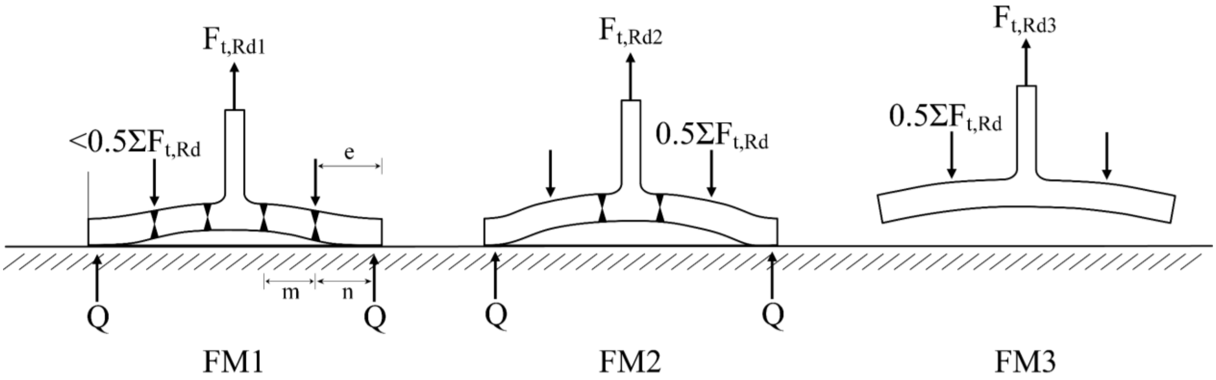

Figure 2.27 – Failure modes of bolted T-stubs.

Each mode is characterized by a value of the non-dimensional parameter β_{Rd} defined by the ratio between the design resistance of the T-stub flanges and design tension resistance of the bolts

$$\beta_{Rd} = \frac{4M_{pl,Rd}}{2B_{t,Rd}m} \tag{2.15}$$

where $M_{pl,Rd} = 0.25 b_{\mathrm{eff}} t_{\mathrm{f}}^2 f_y$, b_{eff} is the effective width, t_{f} is the flange thickness, f_y is the yield strength of the flange material, $B_{t,Rd} = k_2 f_{ub} A_s$ with $k_2 = 0.9$, A_s is the tensile stress area of the bolt, f_{ub} is the ultimate strength of the bolt, and m is the location of the restraining line.

(ii) Failure mechanism modes

Piluso *et al.* (2001a, 2001b) extended the failure plastic mechanism classification to include material strain-hardening, and thus ultimate failure prediction. Ultimate failure is assumed that occurs according one of three different modes similar to the ones described for the plastic mechanic formation, when the ultimate material strain is reached in either the T-stub flange or the bolt. Each failure mode is characterized by a value of the non-dimensional parameter β_u

$$\beta_u = \frac{4M_u}{2B_u m} \tag{2.16}$$

where M_u is the bending moment at ultimate conditions computed according to Piluso *et al.* (2001a, 2001b) and $B_u = f_{ub} A_s$ is the ultimate axial resistance of a single bolt.

(iii) Ranges for β_{Rd} and β_u

The failure mode type is defined through the following conditions:

(i) mode 1: $\beta \leq \beta_{\mathrm{lim}}$;

(ii) mode 2: $\beta_{\mathrm{lim}} < \beta \leq 2$ and

(iii) mode 3: $\beta > 2$.

Where β can be β_{Rd} and/or β_u. The limit values $\beta_{Rd,\mathrm{lim}}$ and $\beta_{u,\mathrm{lim}}$ are given by

$$\beta_{Rd,\mathrm{lim}} = \frac{2\lambda}{1+2\lambda} \tag{2.17}$$

$$\beta_{u,\mathrm{lim}} = \frac{2\lambda}{1+2\lambda}\left[1-(1+\lambda)\frac{d_w}{8n}\right] \tag{2.18}$$

where $\lambda = n/m$, n is the location of the prying forces and d_w is the diameter of the washer, or the width across points of the bolt head or nut, as relevant.

2.7.2.2. Initial stiffness of T-stubs

Extensive research work on the evaluation of the initial stiffness of a T-stub can be found in the literature. Three selected works are briefly addressed: (i) Jaspart proposal (1991, 1997) that led to the stiffness calculation model prescribed by EC3-1-8, (ii) Faella and co-workers model (1998a, 2000), since is also the baseline for the semi-empirical model to predict the cyclic behaviour of bolted T-stubs proposed by the same authors, and (iii) Coelho's (2004) proposal developed at University of Coimbra.

(i) Jaspart proposal (1991 – 1997)

Jaspart (1991) proposed expressions to evaluate the elastic initial stiffness of a single T-stub, which incorporate the compatibility between the deformability of the T-stub flanges and of the bolts. The T-stub element is modelled using a beam analogy prevented from rotation in the part corresponding to the web of the column (column flange in bending) or beam web/flange (end plate in bending) and with a simply support in the location of the prying forces. The expressions computed with this model follow the same approach as Yee and Melchers (1986) but with some modifications. Yee and Melchers (1986) assume that the prying forces are located at the edge of the flange ($n = e$) and Jaspart (1991) adopts the proposal by Douty and McGuire (1965) where the prying forces are assumed to be located closer to the bolts in the elastic range ($n = 0.75e$), see Figure 2.28. The bolts deformation is modelled according to Agerskov (1976).

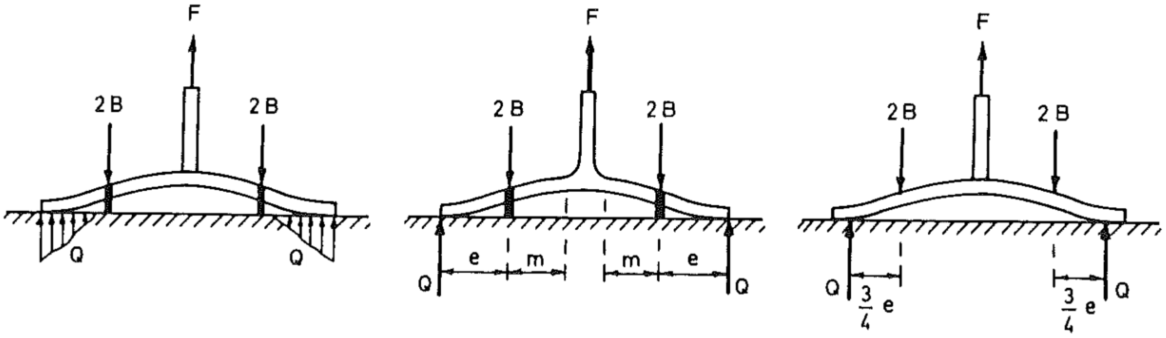

(a) actual distribution (b) idealisation by Yee and Melchers (c) idealisation by Douty and McGuire

Figure 2.28 – Location of the prying forces (Jaspart, 1997).

The former model, although simple, led to long analytical expressions for the stiffness of the T-stub and thus not suitable for everyday design. For this reason, Jaspart (1991) proposed a simplified approach for the prediction of the stiffness of bolted T-stubs to be included in EC3 with the following simplifications: (i) the location of the prying forces, n, is considered equal to $1.25m$ and (ii) the bolt deformability is dissociated from that of the T-stub, see Figure 2.29.

Assuming that (i) the bolts are no more deforming in tension, i.e. $A_s \approx \infty$, (ii) the T-stub is attached to a rigid foundation, and (iii) $0.75e = 1.25m$, the stiffness of a T-stub flange for a single bolt-row, K_{f}, is given by Eq. (2.19). The stiffness of a single bolt-row with two bolts, non-preloaded K_b and preloaded K_pb is given by Eqs. (2.20) and (2.21), respectively, where $b^*_\mathrm{eff} = 0.9b_\mathrm{eff}$ is the effective width of the T-stub flange for stiffness calculation, whereas b_eff represents the width of the flange that contributes to load transmission, and A_s is the tensile stress area of the bolt. The equation related to preloaded bolts is not prescribed in EC3-1-8.

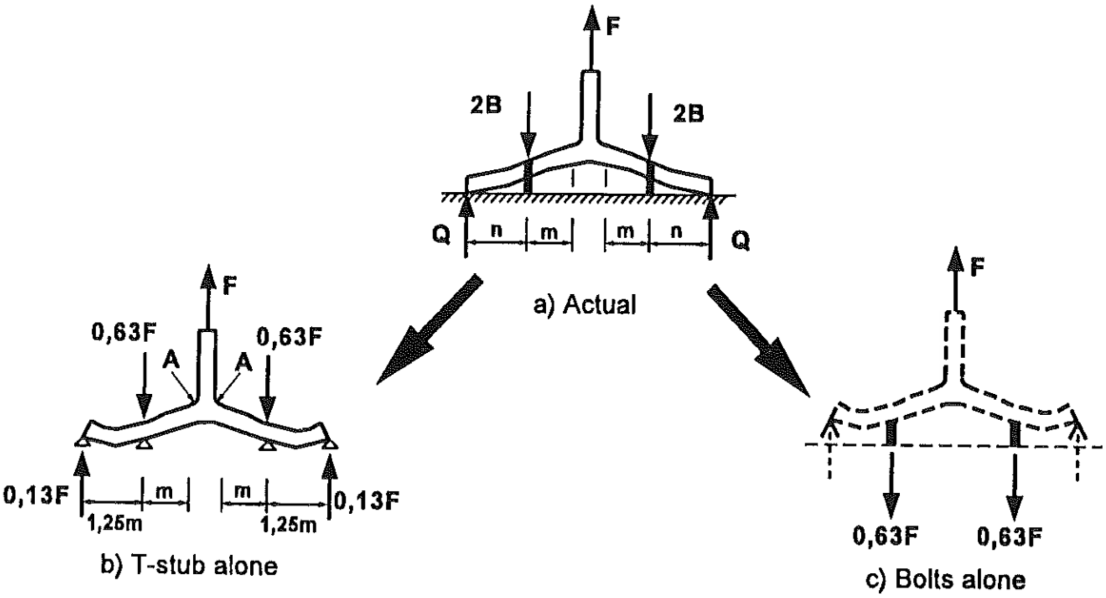

Figure 2.29 – Elastic deformation of the T-stub (Jaspart, 1997).

$$K_\mathrm{f} = 1.063\frac{Eb^*_\mathrm{eff}t^3}{m^3} \approx \frac{Eb^*_\mathrm{eff}t^3}{m^3} \tag{2.19}$$

$$K_\mathrm{b} = 1.6\frac{EA_s}{L_\mathrm{b}} \tag{2.20}$$

$$K_\mathrm{pb} = 9.5\frac{EA_s}{L_\mathrm{b}} \tag{2.21}$$

The bolt elongation length, L_b, is taken as

$$L_\mathrm{b} = t_\mathrm{f,u} + t_\mathrm{f,l} + t_\mathrm{wsh} + \frac{t_\mathrm{bh}}{2} + \frac{t_\mathrm{bn}}{2} \tag{2.22}$$

where $t_{\mathrm{f,u}}$ and $t_{\mathrm{f,l}}$ are the flange thickness of the upper and lower T-sub flange, respectively – to account the possibility of a test with two T-stubs in a row – t_{wsh} is the thickness of the washer, t_{bh} is the thickness of the bolt head and t_{bn} is the thickness of the bolt nut.

The initial stiffness of the overall T-stub connections K_{eq} for a single bolt-row is then computed by means of the following equation

$$K_{eq} = \frac{1}{\frac{1}{K_{\mathrm{f,u}}} + \frac{1}{K_{\mathrm{f,l}}} + \frac{1}{K_{\mathrm{b}}}} \tag{2.23}$$

where $K_{\mathrm{f,u}}$ and $K_{\mathrm{f,l}}$ are the stiffness of the upper and lower T-sub flange, again to account the possibility of a test with two T-stubs in a row.

(ii) Faella and co-workers' model (1998 – 2000)

To evaluate the initial stiffness of bolted T-stub connections, Faella et. al (1998a, 2000) analysed three distinct behavioural schemes related to the ratio between the flexural stiffness of the flanges and the axial stiffness of the bolts, as well as the location and degree of restraint provided by the bolts, see Figure 2.30. In the case of very thick T-stub flanges, the bolts are not able to prevent detachment of the connected flanges, thus it can be modelled by means of a flexible model, i.e., the bolt restraining action is modelled as simple supports located at the bolt axis, see Figure 2.30(a). In the case of very thin plates, the bolt preloading acts as a fixed edge, preventing the detachment of the T-stub flanges at the edge of the bolt head, therefore it can be modelled by means of the rigid beam approach, see Figure 2.30(c). However, the actual behaviour of the T-stub lays between these two limit cases, see Figure 2.30(b).

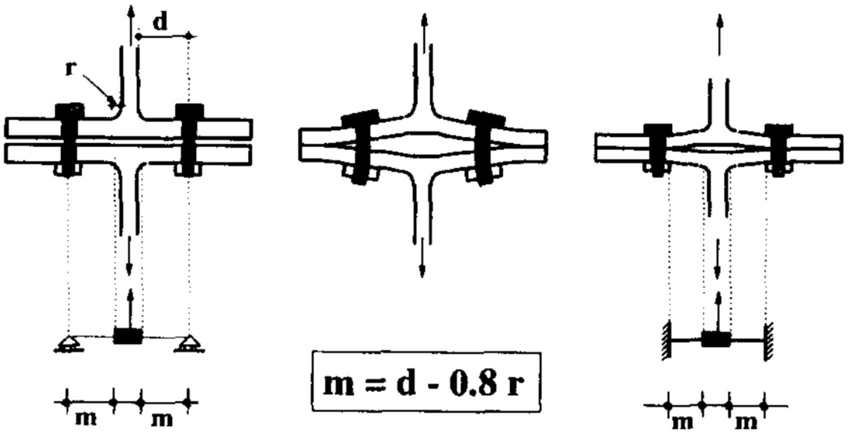

(a) (b) (c)

Figure 2.30 – Behavioural schemes of the T-stub connection (Faella, Piluso and Rizzano, 1998b).

Table 2.2 summarizes the expressions to compute the stiffness of the flanges and bolts according to each behavioural scheme, where the overall stiffness of a T-stub connection is computed according to Eq. (2.23).

In the first limit case, Figure 2.30(a), the influence of the prying forces is disregarded and the initial stiffness of a T-stub flange for a single bolt-row can be computed by Eq. (2.24) – for the initial stiffness of a bolt-row with a couple of non-preloaded bolts, K_{b}, the authors adopted for the stiffness of the bolts the equation present in EN 1993-1-8, see Eq. (2.25).

In the second limit case, Figure 2.30(c), the initial stiffness of a T-stub flange for a single bolt-row can be computed by Eq. (2.30).

In the intermediate case, see Figure 2.30(b), the initial stiffness of a T-stub flange for a single bolt-row can be computed by Eq. (2.26).

For preloaded bolts the authors point out two effects: (i) gives rise to an increase in the axial stiffness of the bolt-plate system, which is related to the decompression of the connected plates (Jaspart and Maquoi, 1995), and (ii) modifies the overall behaviour of the T-stub affecting both the flange span and its restraining conditions, which depends on the ratio between the flexural stiffness of the connected plates and the bolt axial stiffness. The plate-to-bolt stiffness ratio is given by the Eq. (2.27). In the case of preloaded bolts, the contribution of a single bolt in tension, K_bp, is given by Eq. (2.29).

Table 2.2 – Initial stiffness of bolted T-stubs according to Faella et. al (1998a, 2000).

flexible model		non-preloaded bolts	
$K_\mathrm{f} = \frac{0.5Eb'_\mathrm{eff}t_\mathrm{f}^3}{m^3}$	(2.24)	$K_\mathrm{b} = 1.6\frac{EA_s}{L_\mathrm{b}}$	(2.25)
intermediate model		preloaded bolts	
$K_\mathrm{f} = \Psi\frac{0.5Eb'_\mathrm{eff}t_\mathrm{f}^3}{m^3}$	(2.26)	$\frac{K_\mathrm{p}}{K_\mathrm{b}} = 4.10 + 3.25\frac{t_\mathrm{f}}{d_\mathrm{b}}$	(2.27)
$\Psi = 0.57\left(\frac{t_f}{d_b\sqrt{m/d_b}}\right)^{-1.28}$	(2.28)	$K_\mathrm{bp} = K_\mathrm{b} + K_\mathrm{p}$	(2.29)
rigid model			
$K_\mathrm{f} = \frac{2Eb'_\mathrm{eff}t_\mathrm{f}^3}{\left(m - \frac{d_\mathrm{bh}}{2}\right)^3}$	(2.30)		

In Table 2.2 the coefficient Ψ accounts both for the modification of the type of restraint, varying from the simple support to the full restraint, and for the reduction of m due to the bolt head restraining action. The expression for Ψ was obtained by means of a regression analysis with reference to the secant stiffness corresponding to 2/3 times the T-stub design resistance and considering a bolt preloading level equal to 80%.

In addition, the authors proposed corrections to the effective width b_{eff} and the location of the restraining line m for stiffness calculations.

The effective width b'_{eff} is computed by assuming a 45º spreading of the bolt action starting from the bolt head edge, see Figure 2.31. Therefore, with reference to the single bolt-row, the effective width can be computed as

$$b'_{\mathrm{eff}} = 2m + d_{\mathrm{bh}} \leq b \tag{2.31}$$

where d_{bh} is the bolt head diameter and b is the actual width of the T-stub.

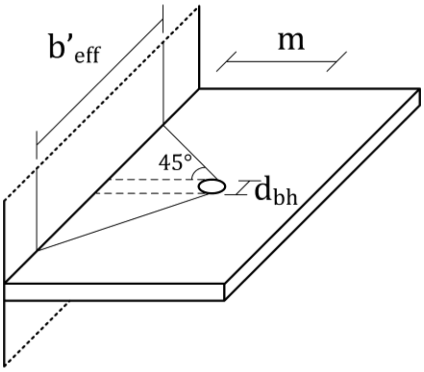

Figure 2.31 – Effective width according to Faella *et al.* (1998b).

The restraining line, m, as it has been shown through experimental results, has to be considered closer to the T-stub web as the ratio d/t_{f} decreases. Therefore, the authors proposed the following equation

$$m' = d - \zeta r \tag{2.32}$$

$$\zeta = 0.16\frac{d}{t_{\mathrm{f}}} - 0.08 \tag{2.33}$$

where ζ is function of the ratio d/t_f and has been obtained by means of a regression analysis.

(iii) Coelho et al. proposal (2004)

Coelho *et al.* (2004) proposed two beam model that uses geometrical and mechanical properties consistent with the EN 1993-1-8 prying model: (i) a simplified beam model, where the bolt is modelled as an extensional spring with similar characteristics to the Swanson bolt model (1999), see Figure 2.32(a), and (ii) a sophisticated beam model, where the bolt is modelled as a spring assembly in parallel within the bolt diameter, see Figure 2.32(b). The flange material constitutive law is modelled by means of a multilinear curve, that accounts for the strain hardening effects.

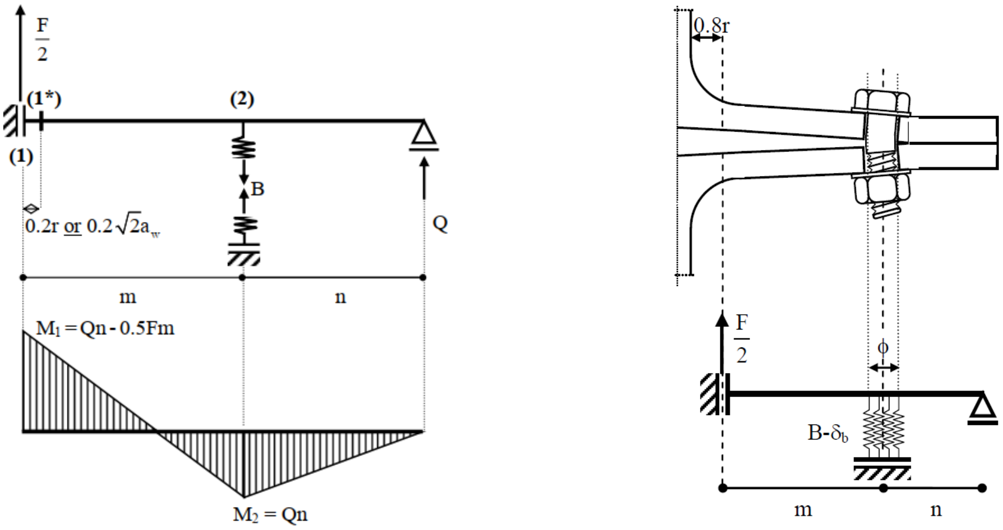

(a) (b)

Figure 2.32 – Beam models proposed by adopted by Coelho *et al.* (2004): (a) simplified and (b) sophisticated.

In addition, Coelho *et al.* (2004) proposed a correction of the Young's modulus to be introduced by means of a simple formula to employ in the beam model

$$E_{\mathrm{red},i} = 0.5E \cdot \bar{F}_{i,Rd,0} \tag{2.34}$$

where $\bar{F}_{i,Rd,0}$ is the ratio between the design resistance of mechanism type-i accounting for shear and that corresponding to the basic formulation is given by

- mechanism type-1

$$\bar{F}_{1,Rd,0} = \frac{2}{3}\left(\frac{m}{t_{\mathrm{f}}}\right)^2 \left(\sqrt{1 + \frac{3}{\left(\frac{m}{t_{\mathrm{f}}}\right)^2}} - 1 \right) \tag{2.35}$$

- mechanism type-2

$$\bar{F}_{2,Rd,0} = \frac{8}{3}\left(\frac{m}{t_{\mathrm{f}}}\right)^2 \frac{(1+\lambda)^2 \beta_{Rd}}{2\lambda + \beta_{Rd}} \left(\sqrt{1 + \frac{3}{4} \frac{\frac{2\lambda}{\beta_{Rd}} + 1}{\left(\frac{m}{t_{\mathrm{f}}}\right)^2 (1+\lambda)^2}} - 1 \right) \tag{2.36}$$

where $\lambda = n/m$ and β_{Rd} is the relation between the flexural resistance of the flanges and the axial resistance of the bolt and governs the occurrence of a given failure mode type, see Eq. (2.15).

2.7.2.3. Monotonic constitutive relation of bolted T-stubs

Piluso *et al.* (2001a, 2001b) developed an analytical model for predicting the plastic deformation capacity of bolted T-stubs. This model is addressed in this section since is also the baseline for a model to predict the cyclic behaviour of bolted T-stubs proposed by the same authors, see section 2.7.3.

Piluso *et al.* (2001a, 2001b) assumed the following simplifications: (i) 3D effects are not accounted for – the approach is based on a 2D model; (ii) geometrical nonlinearity is neglected; (iii) compatibility between bolt and flange deformations is not considered; (iv) the influence of the shear action is disregarded; (v) prying forces are located at the edges of the T-stub flanges; (vi) bending of the bolts is neglected; (vii) cracking of the material is approximately modelled by assuming the cracking condition as the occurrence of the ultimate strain in the extreme fibres of the T-stub flanges. The model is based in a beam analogy and addresses the following steps: (i) material constitutive law; (ii) moment-curvature relationship; (iii) failure modes; (iv) computing of plastic rotations and prediction of force-deformation curve.

The true stress – true strain relationship is represented by means of a multilinear model having four branches as illustrated in Figure 2.33(a). The force-deformation of a single T-stub can be modelled through four characteristic points, see Figure 2.33(b), which correspond to: (d_y, F_y) first yielding condition; (d_h, F_h) beginning of strain hardening; (d_m, F_m) achievement of the stress σ_u; (d_u, F_u) ultimate conditions. The characteristic coordinates of this curve are determinate according to the potential failure mode. The load levels corresponding to the mentioned characteristic points are determined according to the potential failure mode, whose expressions are coincident with the ones proposed in EC3-1-8 (CEN, 2005c), but with reference to the ultimate conditions instead of the design resistance. The evaluation of the deformations corresponding to the each load level can be found in (Piluso, Faella and Rizzano, 2001a).

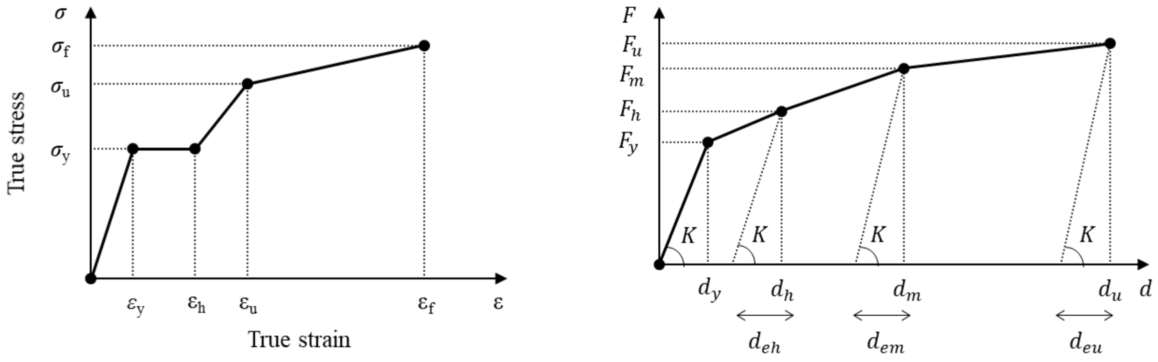

(a) (b)

Figure 2.33 – Multilinear modelling of (a) true stress – true strain curve and (b) force-deformation curve.

2.7.3. Cyclic behaviour

The prediction of cyclic response of basic components is a relatively recent research topic. Studying the cyclic behaviour of T-stubs is of the most importance as its modelling is required to extend the applicability of the design codes to seismic design and it represents a very important source of energy dissipation in a connection. However, only a few authors have proposed models to predict the cyclic behaviour of T-stubs.

Two major types of analytical models are available in bibliography for the cyclic behaviour of T-stubs (i) global models (Faella, Piluso and Rizzano, 1999; Piluso and Rizzano, 2008; Latour and Rizzano, 2019; Yuan *et al.*, 2021) and (ii) refined models (Hu, Leon and Park, 2011, 2012). Piluso and Rizzano (2008) model is described in detail, since is the only model, from the available models in the literature, which is applicable to predict the cyclic response of the T-stubs tested at University of Coimbra, see Sections 3.2 and 4.3.

2.7.3.1. T-stub global models

Model by Piluso and Rizzano (2008)

Faella *et al.* (1999) conducted an experimental program on T-stubs obtained from rolled profiles subjected to cyclic loading with constant amplitude and proposed an analytical model to predict its cyclic behaviour starting from the knowledge of theirs geometrical and mechanical properties. Later, Piluso and Rizzano (2008) performed experimental cyclic tests (constant and variable amplitude) on T-stubs obtained from rolled profiles and welded T-stubs and extended the model proposed by Faella *et al.* (1999) to welded T-stubs. Latour and Rizzano (2019), presented a mechanical model for exposed base plate connections based on the analytical models proposed by their co-workers (2001a, 2001b; 2008).

Piluso and Rizzano (2008) semi-analytical model to predict the cyclic force-deformation curve of bolted T-stubs, is based on the monotonic model proposed by the same authors, see Section 2.7.2.2, which includes stiffness and strength degradation rules taking into account the energy dissipation. According to the authors, there is no direct relation between the energy dissipation capacity under cyclic loading and monotonic behaviour since different failure modes can occur. Therefore, Eq. (2.37) was suggested to evaluate the cyclic energy dissipation capacity (calibrated for constant amplitude cyclic tests), E_{cc}, taking into consideration the energy dissipated under monotonic conditions, E_0, for the same displacement amplitude corresponding to that of the cyclic test.

$$\frac{E_{cc}}{E_0} = \psi_1 \left(\frac{t_\mathrm{f} d_p}{2Cm^2}\right)^{\psi_2} \tag{2.37}$$

where d_p is the ultimate plastic deformation under monotonic loading conditions, t_f is the flange thickness, C is a constant depending on the true stress-true strain curve of the material (Piluso, Faella and Rizzano, 2001a) and the coefficients ψ_1 and ψ_2 are equal to 2.081 and 1.212 and were obtained by means of a regression analysis of the experimental results.

The degradation laws of resistance and stiffness and the model were defined for each failure mode, as follow:

(i) Failure mode 1 (FM1)

For each cycle i the applied load F_i is related to the dissipated energy and deformation amplitude, through the expression

$$\frac{F_i}{F_\mathrm{max}} = 1 - a_1 \left(\frac{d_\mathrm{max}}{2d_y}\right)^{a_2} \left(\frac{E_{ci}}{E_{cc}}\right)^{a_3} \tag{2.38}$$

where E_{ci} is the energy dissipated up to the i-th cycle, d_max is the deformation amplitude, $d_y = F_y/K_0$ and K_0 is the initial stiffness for monotonic behaviour according to the model proposed by the same authors (Piluso, Faella and Rizzano, 2001a), see Section 2.7.2.2. The coefficients a_1, a_2 and a_3, presented in Table 2.3, were obtained by minimizing the scatter between the values of F_i/F_max and the corresponding experimental values.

Additionally, for each cycle, the slope of the first part of the reloading branch, K_i, is also related to the corresponding dissipated energy and deformation amplitude in the previous cycles though the expression

$$\frac{K_i}{K_0} = 1 - b_1 \left(\frac{d_{\max}}{2d_y}\right)^{b_2} \left(\frac{E_{ci}}{E_{cc}}\right)^{b_3} \tag{2.39}$$

where the coefficients b_1, b_2 and b_3, presented in Table 2.3, were obtained by minimizing the scatter between the values of K_i/K_0 and the corresponding experimental values.

Table 2.3 – Degradation laws parameters for FM1 (Piluso and Rizzano, 2008).

	a_1	a_2	a_3	b_1	b_2	b_3
rolled	0.086	0.716	3.029	0.693	0.126	0.099
welded	0.345	0.158	3.595	0.849	0.053	0.137

Figure 2.34(a) depicts the proposed model to predict the cyclic force-deformation curve. Point A corresponds to the inversion of the load sign and is lined up with $F_{\max}$ with a slope equal to K_0. The reloading phase can be reproduced by mean of two straight branches with different slope. Point C is the intersection point of the two straight branches and is assumed lined up with point A and B. The slope of the straight-line connecting points A, B and C is given by Eq. (2.40). Point D corresponds to the inversion of the load sign in the reloading phase and is determined through the geometric relations presented in the Figure 2.34(a).

$$\tan\alpha = \frac{F_{\max}}{d_{\max} - 2\frac{F_{\max}}{K_0}} \tag{2.40}$$

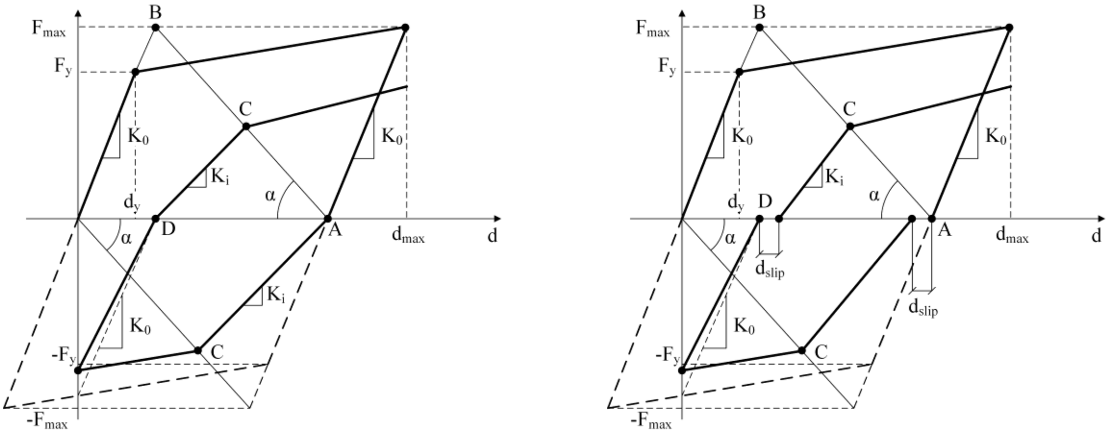

(a) (b)

Figure 2.34 – Cyclic model for (a) FM1 and (b) FM2 and FM3 (Piluso and Rizzano, 2008).

The main steps for the application of the model for predicting the cyclic behaviour of bolted T-stubs can be summarized as follows (Piluso and Rizzano, 2008):

1) prediction of the monotonic force-deformation curve (Piluso, Faella and Rizzano, 2001a);
2) computation of the energy dissipated under monotonic loading E_0 up to the deformation $d_{\max}$;
3) computation of the energy dissipation under cyclic loading E_{cc} for the imposed deformation amplitude $d_{\max}$ by means of Eq. (2.37);
4) computation of the force $F_{\max}$ corresponding on the force-deformation curve to the deformation amplitude $d_{\max}$ of the imposed cyclic action;
5) definition of the strength degradation rule by means of Eq. (2.38);
6) definition of the stiffness degradation rule and of the pinching phenomena by means of Eq. (2.39) and of the parameter α given by Eq. (2.40).

(ii) Failure modes 2 (FM2) and 3 (FM3)

The proposed model for FM2 and FM3 is similar to the one presented for FM1 but with the particularity of considering horizontal slips for near null loads – typical for these failure modes under cyclic loading – see Figure 2.34(b).

Regarding the strength and stiffness degradation, Eq. (2.38) and Eq. (2.39) can still be adopted to compute F_i and K_i but considering the coefficients a_1, a_2, a_3, b_1, b_2 and b_3 shown in Table 2.4.

Table 2.4 – Degradation laws parameters for FM2 and FM3 (Piluso and Rizzano, 2008).

	a_1	a_2	a_3	b_1	b_2	b_3
rolled	0.380	0.025	1.867	0.872	0.008	0.037
welded	0.483	-0.168	1.089	0.805	0.098	0.020

The horizontal slip is defined by

$$d_{\text{slip}} = a + b\left(\frac{E_{ci}}{E_{cc}}\right) \tag{2.41}$$

where the coefficients a and b are given by Table 2.5.

Table 2.5 – Coefficients a and b (Piluso and Rizzano, 2008).

unloading range		loading range	
$a = 0.143 d_{\text{max}}^{1.008}$	(2.42)	$a = 0.0075 d_{\text{max}}^2 - 0.0306 d_{\text{max}} - 0.0069$	(2.43)
$b = 0.001 d_{\text{max}}^{2.549}$	(2.44)	$b = 0.0079 d_{\text{max}}^2 - 0.0989 d_{\text{max}} - 0.3374$	(2.45)

Model by Yuan et al. (2021)

Yuan *et al.* (2021) proposed an analytical hysteretic model for austenitic stainless steel bolted T-stubs. Based on experimental results, namely the observed failure modes and the hysteretic loops shape, the hysteretic response curves were classified into two categories: type 1 for those without slippage during loading and type 2 for those with such slippage where types 1 and 2 also refer to the static failures defined by EC3-1-8 provisions. The proposed hysteretic models, shown in Figure 2.35, consists of three stages: (i) tri-linear loading branch, (ii) the unloading branch and (iii) the reloading branch (with possible slippage). The method adopted to predict the initial stiffness is the one proposed by Faella *et al.* (1998b) accounting for the bolt pre-loading effect. The post-limit stiffness model is the one proposed by Jaspart (1991). The model also embodies some features of the Piluso and Rizzano (2008) model, in particular the strength degradation rule and the slippage phenomenon, but new values are suggested for the empirical parameters.

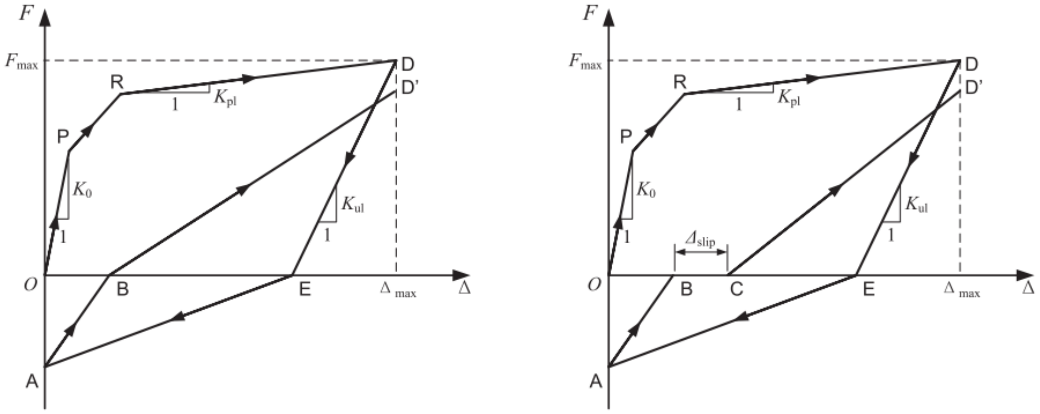

(a) (b)

Figure 2.35 – Simplified hysteretic models for stainless steel T-stubs by Yuan *et al.* (2021).

2.7.3.2. T-stub refined models

Hu *et al.* (2011, 2012) proposed a refined T-stub component model composed by multiple sub-components, see Figure 2.17. The overall T-stub deformation arises from the deformability contributions of the sub-components tension bolts, the T-stub flange, the T-stem, the shear bolts, the combined bearing and slip deformations, and the bearing compression.

The multi-linear cyclic models for individual T-stub sub-components are shown in Figure 2.37 for (a) bolt in tension, (b) bending of the T-stub flange due to the prying action, (c) bearing deformation of the T-stub flange surface, and in Figure 2.38 for (a) T-stem elongation, and (b) combining slip and bolt bearing deformation.

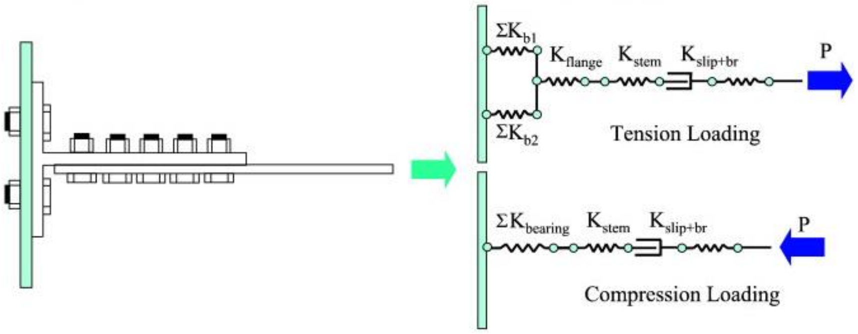

(a) T-stub (b) component model

Figure 2.36 – Spring model for individual T-stub components (Hu, Leon and Park, 2011, 2012).

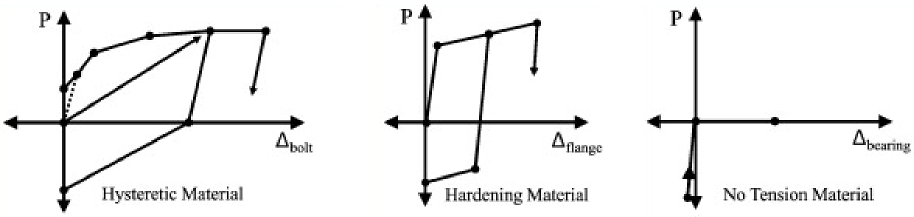

(a) tension bolt (b) T-stub flange (c) bearing compression

Figure 2.37 – Models for individual T-stub sub-components (Hu, Leon and Park, 2011, 2012).

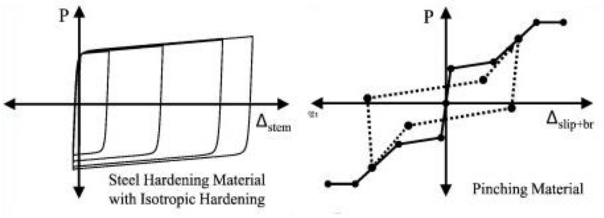

(a) T-stem (b) slip and bolt bearing

Figure 2.38 – Models for individual T-stub sub-components (Hu, Leon and Park, 2011, 2012).

2.7.3.3. Critical analysis of available hysteretic models

The models presented in the previous sections were specifically developed to predict the cyclic behaviour of bolted T-stubs. Two types of modelling were found: (i) global models and (ii) refined models (assemblage of basic sub-components). The latter follows the EC3-1-8 philosophy for mechanical modelling of SBCJs, based on the characterization of individual sub-components, however the number of components involved is clearly excessive to be accounted for in the framework of a model for a full SBCJ. Available models are able to reproduce important phenomena such as pinching, strength and stiffness degradation and slip. However, they cannot detect failure and consequently cannot assess the ultimate deformation capacity in cyclic conditions.

2.8. Characterization of joints and components behaviour by refined 3D FEM models

2.8.1. Generality

The finite element method (FEM), is an extremely powerful tool, which may require large computational resources, used to obtain approximate solutions of boundary value problems in engineering (Hutton, 2003).

Finite element analysis (FEA), with the available computer resources nowadays, has an important role in research as an alternative tool for investigation and understanding of the joint behaviour. In addition, is a tool commonly used for parametric analysis.

However, the use of a 3D FEM requires relevant expertise, is computationally expensive, and produces results that may depend on the user (Simões da Silva, 2008). In addition, sophisticated FE models may present convergence and calibration difficulties, especially in cyclic loading analysis.

The experimental tests are the most trustworthy procedure to assess the bending moment–rotation behaviour of a SBCJ. However, the characterization of the behaviour of individual components directly from experimental test is difficult. The refined 3D FEM modelling allows a deep insight of the components behaviour that is not possible to assess in a full-scale experimental test.

In this section, previous research of 3D FEM modelling of SBCJs and isolated T-stub is presented.

2.8.2. Review of refined 3D FE modelling

2.8.2.1. Steel joints

In 1976, Krishnamurthy and Graddy (1976) presented the first attempts in the field of 3D FEM modelling of bolted end-plate connections and proposed equations to predict the general rotational behaviour. Following their work, Kukreti, Murray and Ablmaali (1987) proposed a methodology based on FE modelling to characterize the $M - \phi$ relationship for the same type of connections.

In order to overcome the limitations of 2D analysis, several researcher followed using 3D FE modelling, namely Sherbourne and Bahaari (1994), Bursi and Jaspart (1997), Maggi *et al.* (2005) and Shi *et al.* (2008), etc.

Although extensive work can be found in the literature in the field of 3D modelling of bolted connections, the studies are mainly related to prediction of the joint global behaviour. Only in 2017 was proposed a procedure to characterize the individual components behaviour from refined 3D FE models by Augusto (2017). Section 2.8.4, summarizes this procedure for extracting the behaviour of a SBCJ and the individual components.

2.8.2.2. Isolated T-stubs

Extensive numerical modelling to predict the response of isolated T-stubs using refined FEM models can be found in the literature for monotonic loading (Bursi *et al.*, 1997; Bursi and Jaspart, 1998; Girão Coelho, Simões da Silva and Bijlaard, 2006; Faralli *et al.*, 2018; Gödrich *et al.*, 2019; Bezerra *et al.*, 2020; Tartaglia, D’Aniello and Zimbru, 2020; Zhao, He and Yan, 2021).

Refined 3D FEM modelling requires experimental data to be available to calibrate the models. As seen in Section 2.6.3, only a few experimental campaigns on isolated T-stub under cyclic conditions were found in the literature. Consequently, only a few FEM numerical studies dedicated to the cyclic response of T-stubs are also available (Nemati, Le Houedec and

Zandonini, 2000; Bursi, Ferrario and Fontanari, 2002; Sebbagh *et al.*, 2021; Z. Chen *et al.*, 2023).

Within the research program at the University of Trento, Nemati *et al.* (2000) presented a refined 3D FEM model to simulate the cyclic response of isolated T-stubs using the SAMCEF software. To reduce computational effort, only $1/4$ of the specimen was modelled (the specimens had two bolt rows). The numerical model, validated with experimental results, provided information about the deformed shape, reactions, stress rate and plasticity propagation. The deformed shape and the related reactions were analysed step-by-step through each loading and unloading phase of a complete cycle.

Later, Bursi *et al.* (2002) presented numerical work on the analysis of low-cycle fracture behaviour of isolated T-stubs. The inelastic cyclic behaviour of materials was calibrated based on refined 3D model of the coupons specimens with the non-linear isotropic/kinematic hardening model available in the ABAQUS FEM package. On the other hand, refined 2D models were adopted to simulate the cyclic response of isolated T-stubs due to demanding computational effort. The model was able to simulate the monotonic force-deformation behaviour, but failed to reproduce the cyclic behaviour. A parametric study was conducted to assess the fracture resistance at the welded flange-to-web connection.

Recently, Sebbagh *et al.* (2021) conducted a numerical study on isolated T-stubs with two and four bolts per row under monotonic and cyclic conditions. The refined 3D FEM model was done using the CAST3M software (CEA, 2017). The main goal was to obtain the evolution of the prying forces and bolt forces. Constant and variable amplitude cyclic loading was considered. The numerical model could not predict the degradation of strength and stiffness in constant amplitude tests.

Chen *et al.* (2023) performed a numerical study on high-strength steel isolated T-stubs. The refined 3D FEM model was developed with ABAQUS software. Two types of hardening models were employed in the constitutive relation of steel, namely the kinematic hardening model and combined hardening model (Chaboche model). The authors concluded that the models using Chaboche constitutive relationship are more reliable. The model was not able to reproduce the slip observed in the force-deformation experimental curves, see Figure 2.26.

2.8.3. Modelling overview and main options

In FEM modelling several aspects may have an important effect in the outputs, e.g. the type of elements, mesh, boundary conditions, material models, interactions and constraints. The modelling overview and FE options addressed in this sections are related with the numerical models developed in ABAQUS (2014c) by Augusto (2017) used in Chapter 8 of this thesis.

2.8.3.1. Element types and mesh

One of the most important aspects of FE modelling is the choice of the elements type and the mesh size and type. The finite element process deals with a large number of equations that must be solved. Having into account that the number of differential equations is related to the element shape and its number of nodes, the accuracy of the results as well as the computational effort depends of the elements and of the size of the mesh size used in the FEM model. In order to select an adequate mesh size a convergence mesh study is required, considering that a finer mesh leads to more accurate results, but at the same time increased the computational time, which is a major factor when performing FEM analysis of joints under cyclic loading.

In refined 3D FEM models the joint region is modelled making use of solid elements. In ABAQUS usually the C3DRH element, an 8-node linear brick element with reduced integration (Figure 2.39 (a)), is used. To make the FEM model simpler sometimes part of the beams and columns apart from the beam-to-column joint are modelled using 1D elements – in ABAQUS usually the B31 element is used, a 3D first order linear beam element with 2 nodes –Figure 2.39 (b) – with the section behaviour defined by 13 wall points, see Figure 2.39 (c).

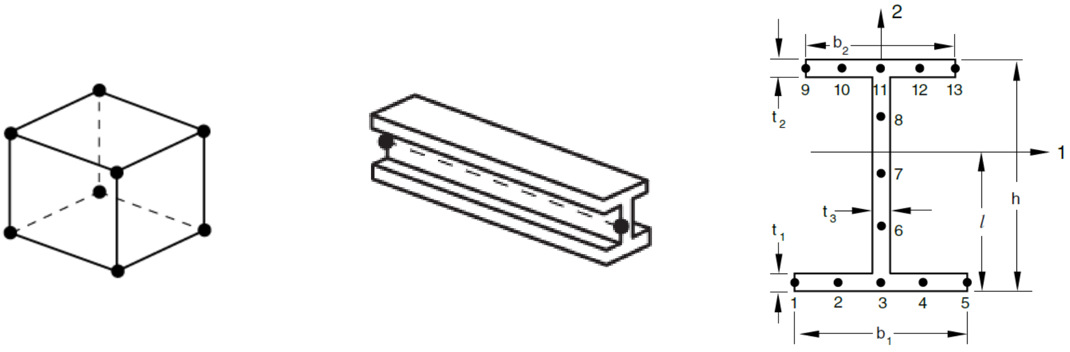

(a) (b) (c)

Figure 2.39 – FE elements available in ABAQUS: (a) brick linear element with 8 nodes, (b) beam element with 2 nodes and (c) beam in space with 13 nodes (ABAQUS, 2014b).

2.8.3.2. Materials

ABAQUS provides several material models, most of them based in plasticity and fracture theories. For cyclic loading, the material model usually considered for SBCJs is an associated plasticity model with a combination of isotropic and kinematic hardening which uses the von Mises yield criterion (ABAQUS, 2014a).

2.8.3.3. Constraints and contact interactions

The several parts of a joint beam, end-plate, column and bolts (head, shank and nut) are modelled along with the interactions between each other by continuity links (constraints or interactions).

Between the beam and the end-plate a *tie* constraint is usually imposed in ABAQUS, i.e. the two surfaces are tied together, each node on the slave surface (cross section of the beam) will have the same values for its degrees of freedom as the point on the master surface (surface of the end-plate) (ABAQUS, 2014a) .

Between the end-plate and the column flange and between the bolts and the end-plate or column flange surface-to-surface interactions are usually imposed in ABAQUS by general contact algorithm, which uses "hard contact" formulation in the tangential direction and the penalty method in the normal direction in order to resist the penetration (ABAQUS, 2014a). These interactions are illustrated in Figure 2.40.

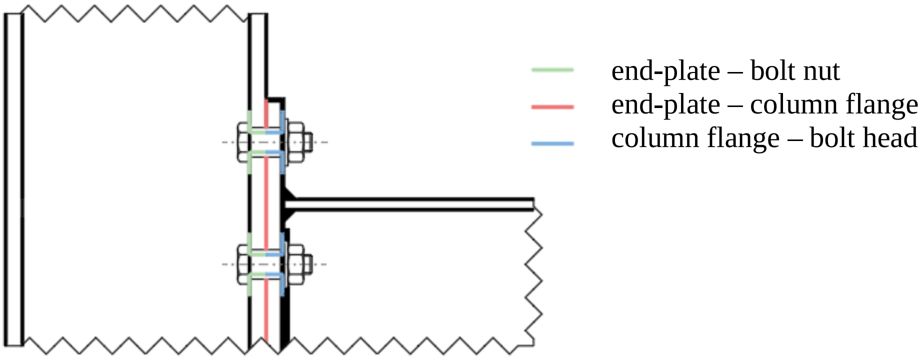

Figure 2.40 – Interactions usually considered in 3D refined FE models.

The interaction properties in a typical beam-to-column joint are presented in Table 2.6 and its contact properties are presented in Table 2.7.

Table 2.6 – Interactions properties.

contact region	master surface	slave surface	interaction properties
end-plate – bolt nut	end-plate	bolt head and shank	tangential and normal
end-plate – column flange	column	end-plate	tangential and normal
column flange – bolt head	column	bolt nut and shank	tangential and normal

Table 2.7 – Contact properties.

tangential behaviour		normal behaviour	
friction formulation:	penalty	pressure-overclosure:	“hard” contact
friction coeff.:	0.2	allow separation after contact	

2.8.4. Characterization of SBCJs and components from refined FEM models

A procedure for the characterization of the behaviour of beam-column joints and components from the results of refined FEM models will be explained in the following sections (Augusto, 2017).

Consider the beam-to-column joint FEM model represented in Figure 2.41 and the nodes DTi identified.

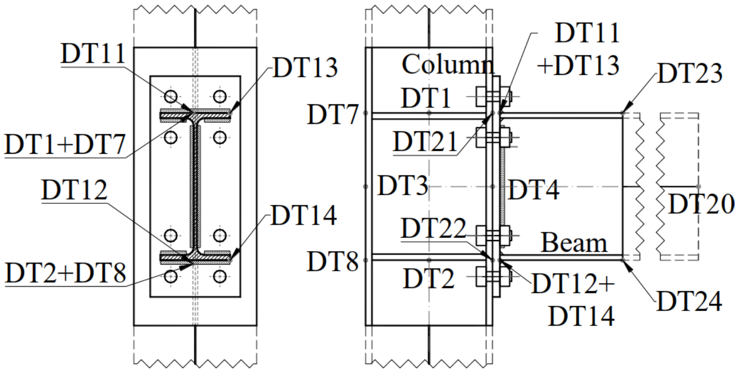

Figure 2.41 – Predefined nodes (Augusto, 2017).

2.8.4.1. Bending moment-rotation of the joint

To compute the $M - \phi$ behaviour a joint from the FEM model making use of the displacements and forces of the nodes identified in Figure 2.41 the following expressions are applied:

- bending moment

$$M_{\mathrm{Ed}} = \mathrm{DT20}_{\mathrm{RF2}} \cdot \mathrm{DT20}_{\mathrm{U2}} \tag{2.46}$$

- joint rotation

$$\phi_{\mathrm{total}} = \phi_{\mathrm{cw}} + \phi_{\mathrm{ep}} - \phi_{\mathrm{el,c}} - \phi_{\mathrm{el,b}} \tag{2.47}$$

- column web absolute rotation

$$\phi_{\mathrm{cw}} = \arctan\left(\frac{\mathrm{DT1}_{\mathrm{U3}} - \mathrm{DT2}_{\mathrm{U3}}}{\overline{\mathrm{DT1DT2}}}\right) - \phi_{\mathrm{el,c}} \tag{2.48}$$

- end-plate absolute rotation

$$\phi_{\mathrm{ep}} = \arctan\left(\frac{\mathrm{DT13}_{\mathrm{U3}} - \mathrm{DT14}_{\mathrm{U3}}}{\overline{\mathrm{DT13DT14}}}\right) - \phi_{\mathrm{cw}} \tag{2.49}$$

- elastic deformation of the column

$$\phi_{\mathrm{el,c}} = \frac{\mathrm{DT20}_{\mathrm{RF2}} \cdot d}{3EI_{\mathrm{y,c}} \cdot L}\left(L^2 - 3 \cdot L \cdot L_2 + 3 \cdot L_2^2\right) \tag{2.50}$$

- elastic deformation of the beam

$$\phi_{\mathrm{el,b}} = \frac{\mathrm{DT20_{RF2}}}{EI_{\mathrm{y,b}}}\left(d \cdot x - \frac{x^2}{2}\right) \tag{2.51}$$

where the term “absolute rotation” is used to refer to rotation measured in relation to a fixed referential and the term “rotation” is used to refer angular deformation. The adopted reference system (x, y, z) or (1, 2, 3) is presented in Figure 2.41.

In the former expressions, $RF2$ is the reaction force at nodes according to the axes yy, $U2$ and $U3$ is the spatial displacement at nodes according to the axes yy and zz, respectively, L is the length of the column between the supports, L_2 is the distance between the beam axis and the bottom support, d is the distance between the loading cell and the column flange, E is the Young’s modulus, $I_{y,\mathrm{b}}$ and $I_{y,\mathrm{c}}$ are the second moment of area of the section around the stronger axis of the beam and of the column, respectively.

2.8.4.2. Column web in compression and in tension

According to Augusto (Augusto, 2017), the internal forces in the column web in compression and tension may be computed through integration of the stress fields according to Eq. (2.52)

$$F = \left(\int^{h_i} \sigma_{33} \, dy\right) \cdot t_{wc} \tag{2.52}$$

where, σ_{33} (or σ_{zz}) is the normal horizontal stress in the column web along path P1 integrated along the length h_i (h_c for compression and h_t for tension), as illustrated in Figure 2.42.

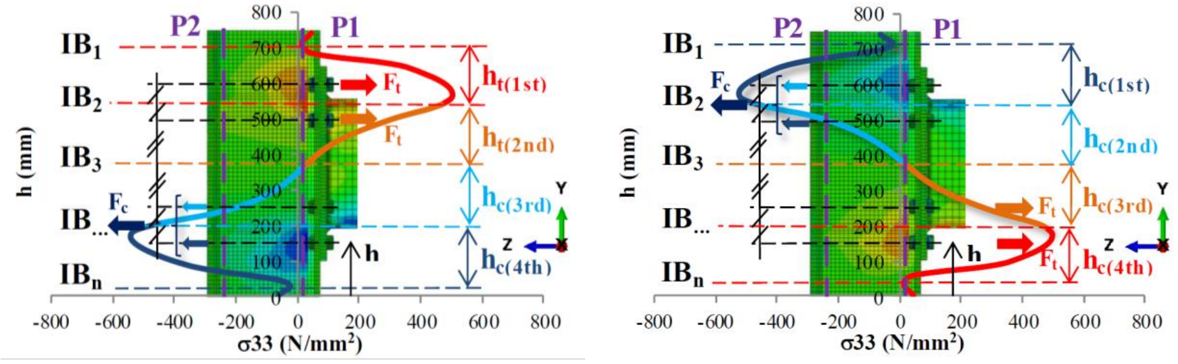

(a) (b)

Figure 2.42 – Stress integration for (a) negative and (b) positive moment (Augusto, 2017).

The deformation of the column web is obtained from the displacement fields. The displacements are extracted from paths P1 and P2, located in the column web beyond the root radius, as shown in Figure 2.43. The deformation is computed as the difference between the displacement in the nodes in the paths aligned flanges of the beam, according to Eq. (2.53)

$$d_{\mathrm{cw}} = \mathrm{P1}_{\mathrm{U3}} - \mathrm{P2}_{\mathrm{U3}} \tag{2.53}$$

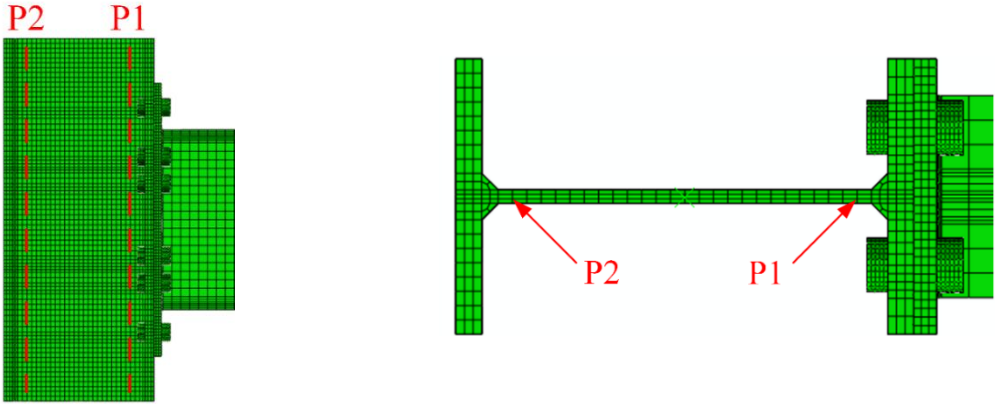

(a) (b)

Figure 2.43 – Location of the paths P1 and P2: (a) side elevation and (b) plan.

2.8.4.3. Column web panel in shear

The internal forces in the column web in shear (CWS) are obtained through integration of the stress fields according to Eq. (2.54) along path P3 in Figure 2.44(a)

$$V_{\mathrm{n}} = \left(\int^{\frac{t_{\mathrm{fc}}}{2}+r} \tau_{23}\right) \cdot t_i + \left(\int^{h_{\mathrm{wc}}} \tau_{23}\right) \cdot t_{\mathrm{wc}} + \left(\int^{\frac{t_{\mathrm{fc}}}{2}+r} \tau_{23}\right) \cdot t_i \qquad (2.54)$$

where, τ_{23} (or τ_{yz}) is the shear stress in the column web along path P3, t_{fc} and t_{wc} are the column flange and web thickness, h_{wc} is the high of the column web, r is the radius of root filled and t_i is the thickness according to Figure 2.44 (b).

The shear deformation of the column web is obtained through the displacements extracted from the nodes DT1 to DT4, illustrated in Figure 2.44, and computed according to Eq. (2.55).

$$\gamma = \arctan\left(\frac{\mathrm{DT1}_{\mathrm{U3}} - \mathrm{DT2}_{\mathrm{U3}}}{h_{\mathrm{b}}}\right) + \arctan\left(\frac{\mathrm{DT3}_{\mathrm{U2}} - \mathrm{DT4}_{\mathrm{U2}}}{h_{\mathrm{c}}}\right) \qquad (2.55)$$

where, $\mathrm{DT}i_{\mathrm{U3}}$ is the displacement along zz and h_{b} is the beam height.

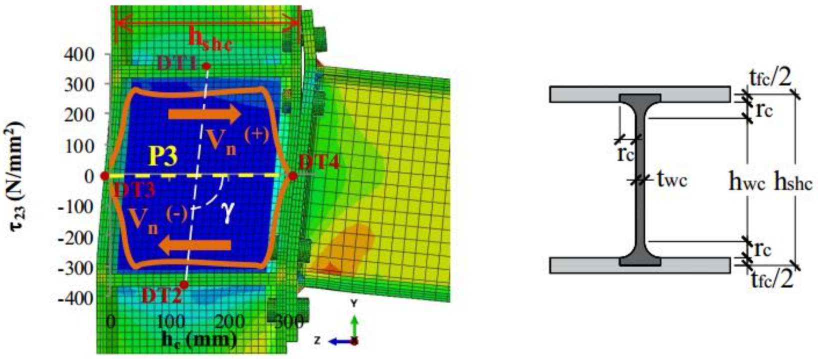

Figure 2.44 – Procedure to compute the shear force and shear deformation of the column web (Augusto, 2017).

In column web panels with transverse stiffeners, an additional shear component is considered by assuming a plastic mechanism of the moment resisting frame formed by the column flanges and the transverse stiffeners, whereby the plastic hinges occur in the column flanges (Augusto, 2017). The bending moment in the column flanges is computed according to Eq. (2.56)

$$M_{\text{fc}} = \int^{t_{\text{fc}}} z(\sigma_{22} d\text{A}), \qquad d\text{A} = b_{\text{c}} \cdot dz \tag{2.56}$$

where, t_{fc} is the thickness of the column flange, σ_{22} is the normal stress along yy along the column flange at a section with the maximum normal stress (see Figure 2.45), z is the lever arm and b_{c} is the width of the column flange.

The additional shear strength, V_{c}, is determined according to Eq. (2.57)

$$V_{\text{c}} = \frac{M_{\text{fc,P4}} + M_{\text{fc,P5}} + M_{\text{fc,P6}} + M_{\text{fc,P7}}}{h_{\text{b}} - t_{\text{s}}} \tag{2.57}$$

where, t_{s} is the thickness of the transverse stiffeners.

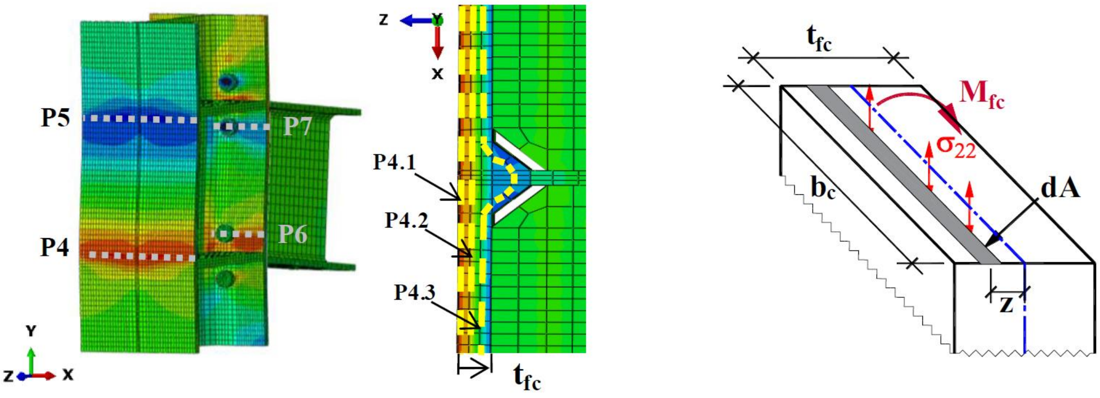

(a) (b) (c)

Figure 2.45 – Procedure to obtain the bending moment in the column flanges (Augusto, 2017).

2.8.4.4. Connection components

Augusto (2017) presents a procedure to determine the force-deformation curve of the three most significant basic components to the connection: (a) column flange in bending, (b) bolts in tension and (c) end-plate in bending.

The procedure to determine the forces of each component of the connection is the same presented in the previous section addressed to the components of the column web, namely the column web in compression or in tension (Section 2.8.4.2). Accordingly, Eq. (2.52) is used to compute the forces transmitted to the column web by the bolts, in the tension side, and by the column flange, in the compression side.

The procedure to determine the deformations associated to each component of the connection is based on the component's main deformation shapes observed in the FEM models. Accordingly, it was observed that the major contribution of both column flange in bending and end-plate in bending drives from the punch deformations around the bolt holes, see Figure 2.46(a). Additionally, the flip of the extended part of the end-plate and the elongation of the bolts are also considered relevant in this procedure. Figure 2.46(b) presents the pre-defined nodes where the displacements were extracted from the FEM models.

The displacements of the column flange in direction $U3$ (see Figure 2.47) are extracted from each bolt hole (in this case, two bolts per row, $\mathrm{CF}_{i,1}$ and $\mathrm{CF}_{i,2}$) and the average of the displacement measured are computed according to Eq. (2.58).

$$\mathrm{CF}_{i,\mathrm{U3}} = \left(\mathrm{CF}_{i,1,\mathrm{U3}} + \mathrm{CF}_{i,2,\mathrm{U3}}\right)/2 \tag{2.58}$$

The deformation of the column flange in the bolt zones, $d_{\mathrm{CF},i}$, is computed according to Eq. (2.59) for the external bolt row ($i = 1$) and for the internal bolt row ($i = 2$).

$$d_{\mathrm{CF},i} = \mathrm{CF}_{i,\mathrm{U3}} - \mathrm{WC}_{i,\mathrm{U3}} \tag{2.59}$$

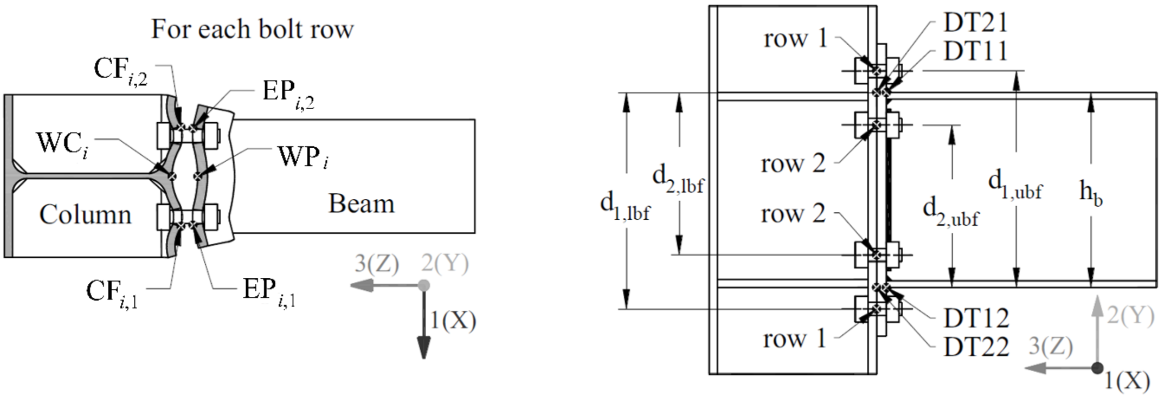

(a) (b)

Figure 2.46 – Predefined nodes where the displacements are extracted (Augusto, 2017).

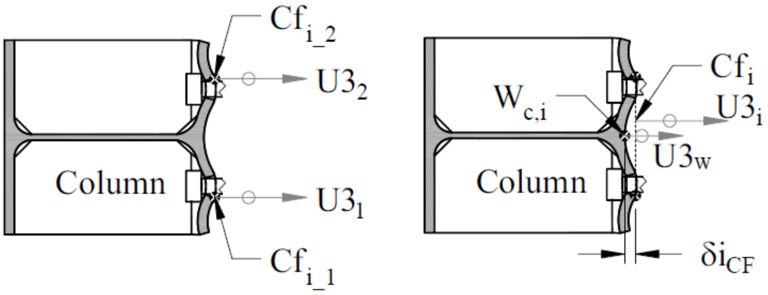

Figure 2.47 – Procedure to assess the contribution of the component column flange in bending (Augusto, 2017).

The relative displacement between the edges of the bolt holes of the end-plate, $\mathrm{EP}_{i,\mathrm{U3}}$, and at the beam web alignment, $\mathrm{WP}_{i,\mathrm{U3}}$, is determined for each bolt row, according to Eq. (2.60)

$$d_{\mathrm{EP},i} = \mathrm{EP}_{i,\mathrm{U3}} - \mathrm{WP}_{i,\mathrm{U3}} \tag{2.60}$$

For unstiffened extended end-plate connection, the flip of the extended part of the end-plate has a significant contribution to the connection rotation (Augusto, 2017) and it is determined through the following procedure. First, the contribution of each row in tension, d_{all}, is determined using Eq. (2.61).

$$d_{\mathrm{all},i} = d_{\mathrm{CF},i} + d_{\mathrm{B},i} + d_{\mathrm{EP},i} \tag{2.61}$$

Second, the gap between the end-plate and the column flange, at the beam flanges level (upper and lower beam flanges, $d_{\mathrm{flip_{EP}},\mathrm{ubf}}$ and $d_{\mathrm{flip_{EP}},\mathrm{lbf}}$, respectively), is determined using the displacement in nodes DT11, DT12, DT21 and DT22 (see Figure 2.46), according to Eqs. (2.62) and (2.63).

$$d_{\mathrm{flip_{EP}},\mathrm{ubf}} = (\mathrm{DT11}_{\mathrm{U3}} - \mathrm{DT21}_{\mathrm{U3}}) - d_{\mathrm{all,ubf}} \tag{2.62}$$

$$d_{\mathrm{flip_{EP}},\mathrm{lbf}} = (\mathrm{DT12}_{\mathrm{U3}} - \mathrm{DT22}_{\mathrm{U3}}) - d_{\mathrm{all,lbf}} \tag{2.63}$$

Finally, the flip deformation is added to the interpolated deformation of the bolt holes for the beam flange level, according to Eq. (2.64).

$$d_{\mathrm{EP}} = -\frac{\left(d_{\mathrm{EP},1} - d_{\mathrm{EP},2}\right)}{d_1 - d_2}(d_1 - h_b) - d_{\mathrm{EP},1} + d_{\mathrm{flip}} \tag{2.64}$$

where d_{flip} is $d_{\mathrm{flip,ubf}}$ or $d_{\mathrm{flip,lbf}}$ for the upper and lower beam flange zones, respectively.

2.8.4.5. Connection rotation

The rotation of the connection is computed using the deformation of the components in the outmost rows (d_{ubf} and d_{lbf} for upper and lower rows, respectively), see Eqs. (2.65) and (2.66).

$$d_{\mathrm{ubf}} = d_{\mathrm{CF,ubf}} + d_{\mathrm{B,ubf}} + d_{\mathrm{EP,ubf}} \tag{2.65}$$

$$d_{\mathrm{lbf}} = d_{\mathrm{CF,lbf}} + d_{\mathrm{B,lbf}} + d_{\mathrm{EP,lbf}} \tag{2.66}$$

The rotation itself is computed according to Eq. (2.67).

$$\phi = \arctan\left(\frac{d_{\mathrm{ubf}} - d_{\mathrm{lbf}}}{h_b}\right) \tag{2.67}$$

2.8.4.6. Bolts in tension

Augusto (Augusto, 2017) modelled bolts with solid finite elements considering the bolt shank, head and nut.

To compute the bolt deformation, the average of the displacements measured in bolts holes of the end-plate ($\mathrm{EP}_{i,1}$ and $\mathrm{EP}_{i,2}$), according to the direction U3, is determined first by Eq. (2.68).

$$\mathrm{EP}_{i,\mathrm{U3}} = \left(\mathrm{EP}_{i,1,\mathrm{U3}} + \mathrm{EP}_{i,2,\mathrm{U3}}\right)/2 \tag{2.68}$$

The deformation of the bolts is assumed as the difference between the average of the displacements measured at the column flange, $\mathrm{CF}_{i,\mathrm{U3}}$, and at the end-plate, $\mathrm{EP}_{i,\mathrm{U3}}$, according to Eq. (2.69).

$$d_{\mathrm{B},i} = \mathrm{CF}_{i,\mathrm{U3}} - \mathrm{EP}_{i,\mathrm{U3}} \tag{2.69}$$

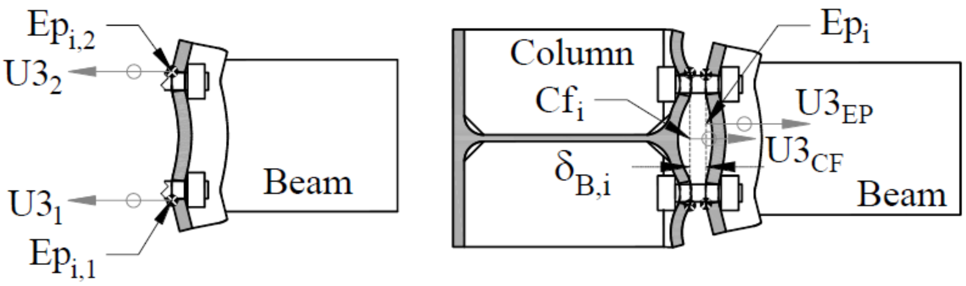

Figure 2.48 – Procedure to assess the component bolts in tension (Augusto, 2017).

Augusto (2017) recommends that the tension force in the bolts to be computed from the integration of stresses in the column web along a predefined length. However, in the presence of transverse stiffeners, according to Augusto (2017) the tension force in the bolts should be determined directly from the bolts through integration of the normal stresses, σ_{33}, along path P8 in the area of the bolt's shank, as illustrated in Figure 2.49 and according to Eq. (2.70)

$$F_{\mathrm{t,b}} = \int_{0}^{d_{\mathrm{b,i}}} \sigma_{33} b(y) dy \tag{2.70}$$

where b is the width of the shank of the bolt and y is a vertical coordinate with origin in node P8 and positive downward in Figure 2.49.

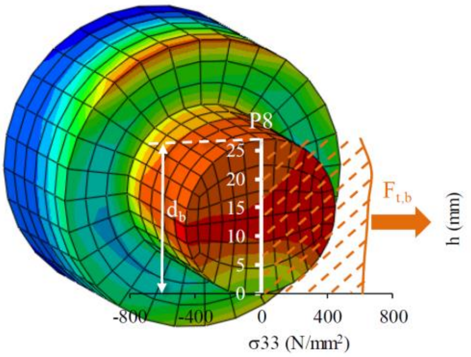

Figure 2.49 – Tension force of the bolts through stress integration (Augusto, 2017).

2.8.4.7. Critical assessment of the existing procedure

The procedure for the characterization of the joint components using FE developed by Augusto (2017) allows not only to characterize the joint/connection global behaviour but also to assess the isolated behaviour of their components. However, some issues concerning the characterization of the internal forces in the components require further clarification. In particular, the integration of the stresses along the column web, raises some concerns due to the possible lack of generalization in the definition of the integration boundaries, i.e. it is not clear where begins and where ends the integration length that should be used to compute the internal forces in the component column web in tension (CWT) for each row and for the column web in compression (CWC). Alternatively, the tension forces can also be computed directly in the bolts of each bolt row. However, when the tension force is directly extracted from the bolts the initial pre-stress of the bolts is considered and thus cannot be used to characterize forces in the other components.

Augusto methodology was applied to a joint, see Chapter 8 , where these issues were analysed more in detail.

2.9. Concluding remarks

In the literature, four different approaches can be identified to predict the cyclic behaviour of steel joints:

- adoption of sophisticated mathematical hysteretic models that can reproduce the relevant features that are observed in experimental tests on SBCJs (e.g. stiffness or strength degradation, hardening, pinching) that are subsequently statistically calibrated with an available set of test results, leading to a global hysteretic moment-rotation curve, see Section 2.4;

- implementation of a zone model based on the combination of the behaviours of the shear, compression and tension zones of the joint, see Section 2.5.3;
- implementation of a cyclic component model whereby all components are considered separately, each characterized using appropriate hysteretic component models (Oliveira, Costa, Shahbazian, *et al.*, 2021);
- advanced FEM simulations using solid elements that include geometrical and mechanical non-linearities, contact phenomena, damage, etc., allowing a full and accurate characterization of the cyclic behaviour steel joints, see Section 2.8.

The first approach is fully empirical, as most of the required parameters of the selected mathematical model have no physical basis, and has a narrow range. It thus lacks generality and is only useful within the range of calibration of the specific joint typologies and geometries. The second approach considers a mechanical basis for some of the zones, namely the column web panel in shear but maintains a narrow scope by bundling all relevant components in the compression and tension zones, not being able to identify the failure mode. The third approach is fully consistent with the component method for monotonic behaviour. It thus presents the additional advantage, for most components, of a small number of empirical parameters, leading to a wider range of validity, but it relies on an accurate characterization of the hysteretic behaviour of each component. The fourth approach requires the modelling of the different parts of the joint and their interactions. Depending on the purpose of the study, it can incorporate non-linearities at geometrical and material level as well as other parameters that can influence the behaviour of joint such as imperfections, residual stress, damage of the materials, thermal properties, cyclic hardening/softening, among others, allowing an accurate characterization of the joint in terms of stress/strain fields, resistance, deformability. However, it requires extensive knowledge of the finite element software by the user, care in the interpretation of the results. It can also be hard to relate the results of FEM models with design code requirements and is usually very time-consuming.

In the path to extend the component method to seismic loading, deep insight on the cyclic behaviour of a SBCJ components is required, as well as proper characterization of their hysteretic behaviour. The literature review was focused on one of the most dissipative components of a SBCJs, the T-stub.

- data collection on experimental testing provides the information required to characterize the hysteretic behaviour, to identify failure modes and governing physical phenomena, see Section 2.6;
- available analytical models are made by (i) adjusting models to the global behaviour of the T-stub but still rely on empirical parameters calibrated with experimental results or by (ii) refined models modelling the non-linear behaviour of each basic component, see Section 2.7.3.

PART II: CYCLIC COMPONENT BEHAVIOUR – CHARACTERIZATION & MODELLING

3 EXPERIMENTAL ASSESSMENT OF THE CYCLIC BEHAVIOR OF T-STUBS

3.1. Introduction

The study of the joint's behaviour discussed in the previous chapter allowed to identify the components that contribute mostly to the energy dissipation and influence the hysteric behaviour of the joint. One possible way to characterize the cyclic behaviour of these components is to perform experimental tests of the parts of the SBCJ that can be identified as components.

The equivalent T-stub is a simplified model with practical interest used in the component method to characterize the behaviour of the components column flange in bending and/or end-plate in bending. Accordingly, experimental cyclic tests on isolated T-stubs can be a source of information for the development and calibration of analytical models in the scope of the component method for these components. Bearing this in mind, an experimental campaign on isolated T-stub was conducted to characterize their cyclic behaviour for the plastic mechanisms associated to the failure modes identified in EC3-1-8 and to identify their governing physical phenomena.

This chapter describes the experimental campaign conducted at University of Coimbra and the experimental work by Piluso and Rizzano (2008) also devoted to the assessment of the cyclic behaviour of T-stubs.

3.2. Experiments at University of Coimbra

3.2.1. Experimental campaign

3.2.1.1. Overview

The T-stub specimens tested at University of Coimbra are built by coupling two T elements, see Figure 3.1, that have been cut from rolled HEA 200 and HEB 280 profiles from steel grade S355. These T-stubs are connected through the flanges by two high-strength partial threaded bolts M20x75 HR (class 10.9) according to EN 14399-3 (CEN, 2005a) with washers according to EN 14399-5 (CEN, 2005b). The experimental campaign involved the testing of 14 specimens, 7 derived from HEA 200 profile (A series) and 7 from HEB 280 (B series). With reference to each series of specimens, 2 monotonic (M) and 5 cyclic (C) testes have been carried out. Two distinct loading protocols were considered for the cyclic tests with variable amplitude (C1 and C2) , based on the loading protocol established for the experimental campaign of the European project EQUALJOINTS (Landolfo, 2017a). According to EN 1090-2 (BSI, 2008) preload may be use for slip resistance and for seismic connections. Therefore, two cases were considered: (i) with preloading force $F_{p,C} = 172$ kN in accordance with clause 8.5.1 of EN 1090-2 (BSI, 2008) and (ii) without preloading, i.e. hand tightening.

The range of variation of the geometrical and mechanical properties of the tested specimens was chosen to obtain FM1 and FM2 failure modes – see section 2.7.2. The FM3 is not interesting from the design point of view as it is a brittle failure mode and, therefore, must be avoided in designing steel joints.

In addition, 12 coupons tensile tests, 3 derived from the flange and 3 from the web of each profile, have been performed to establish the mechanical properties of the material. The tensile tests were performed according to ISO 6892-1 (ISO, 2009).

The experimental tests have been carried out at the University of Coimbra using a “walter+bay” Multipurpose Servohydraulic Universal Testing Machine Series LFV 600 kN and a “Servosis” 1000 kN Universal Testing Machine. Table 3.1 summarizes the experimental campaign on T-stubs.

The experimental campaign was also part of the Master thesis of Tambá (2020).

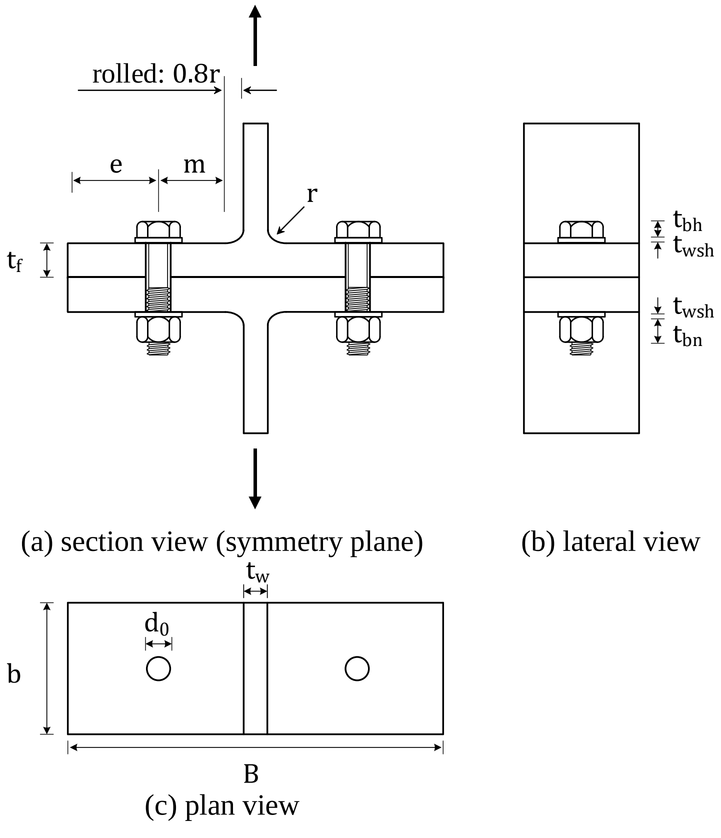

Figure 3.1 – Notation used to define the geometry of the T-stubs tested at University of Coimbra.

Table 3.1 – Experimental campaign on T-stubs.

A series			B series		
T-stub ID	loading protocol	bolt preloading	T-stub ID	loading protocol	bolt preloading
A1	C1	yes	B1	M	no
A2	C1	no	B2	C1	no
A3	C1	yes	B3	C2	yes
A4	C2	no	B4	M	yes
A5	M	yes	B5	C1	yes
A6	C2	yes	B6	C1	yes
A7	M	no	B7	C2	no

3.2.1.2. Geometrical properties of T-stubs

The meaning of the symbols used to define the geometry of the tested T-subs is provided in Figure 3.1. The actual geometry of the T-stubs was assessed before testing of the specimens and is listed in Table 3.2 as an average value of the two T elements that compose a T-stub together with the nominal geometry.

A bolt length of 75mm was selected for both A and B series, to ensure a shank length shorter than two times the flange thickness of the smallest T-stub, i.e. $l_s = 16.5 < 2t_{\mathrm{f}}$, see Figure 3.2. Table 3.3 summarizes the nominal geometrical properties of the bolts – for notation refer to Figures 3.1(b) and 3.2.

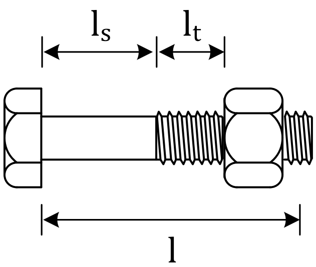

Figure 3.2 – Notation used to define the geometry of bolt.

Table 3.2 – Geometrical properties of tested specimens.

T-stub ID	B mm	t_f mm	t_w mm	b mm	e mm	r mm	m mm	e_1 mm	d mm
A (nominal)	200	10	6.5	100	35	18	47.35	50.59	61.75
A1	200.00	9.72	7.00	101.15	35.69	18	46.42	50.58	60.82
A2	200.00	10.04	7.00	100.79	35.60	18	46.51	50.40	60.91
A3	200.50	9.91	7.00	101.74	36.14	18	46.21	50.68	60.61
A4	201.00	10.10	7.01	101.39	36.23	18	46.37	50.90	60.77
A5	201.00	9.94	6.98	101.33	35.45	18	47.17	50.80	61.57
A6	201.00	10.00	6.99	101.35	35.23	18	47.38	50.64	61.78
A7	201.00	9.88	7.00	101.26	35.79	18	46.82	50.59	61.22
B (nominal)	280	18	10.5	125	60	24	55.55	50.80	74.75
B1	279.00	17.59	11.00	126.37	59.63	24	55.17	50.53	74.37
B2	279.00	17.88	10.98	124.97	59.02	24	55.80	50.43	75.00
B3	278.50	17.79	10.99	125.62	59.47	24	55.09	50.73	74.29
B4	279.00	18.07	10.98	126.11	60.10	24	54.71	50.83	73.91
B5	279.00	17.80	10.98	125.77	59.20	24	55.62	57.00	74.82
B6	278.50	17.92	10.99	126.45	59.76	24	54.80	50.59	74.00
B7	279.00	17.77	10.99	126.36	60.11	24	54.70	50.58	73.90

Table 3.3 – Dimensions of bolts, nuts and washers (nominal).

bolts					nuts	washers	
d_b mm	d_bh mm	t_bh mm	l mm	l_s mm	t_bn mm	d_wsh mm	t_wsh mm
20.0	32	12.50	75	16.5	18.0	37.0	4.0

3.2.1.3. Mechanical properties of structural steel

The mechanical properties of structural steel were obtained from steel coupons extracted from the web and flange of the T-stub elements through uniaxial tensile tests according to ISO 6892-1 (ISO, 2009), details are reported in Annex A.

The tensile coupon tests were performed using a testing rate based on strain rate control (method A) – clause 10.3 of the ISO 6892-1 (ISO, 2009) – and using the “Servosis” 1000 kN Universal Testing Machine. Strains were measured with electrical and mechanical strain gauges, see Figure 3.3.

(a) (b)

Figure 3.3 – Tensile coupon instrumentation and test set up.

The engineering and the true stress – strain curves of each coupon are presented in Figure 3.4 – the test results and procedure to compute the true stress – true strain curves are reported in detail in Annex A.

The four typical regions of the stress-strain curve of structural steel are patent: linear elastic region, yield plateau, strain hardening region and strain softening after reaching the maximum load. In most cases the coupons rupture did not occur within the length monitored by the mechanical strain gauge, which lead to loss of information between the maximum load and the rupture load of the test specimen, and thus it was not possible to obtain the complete curve.

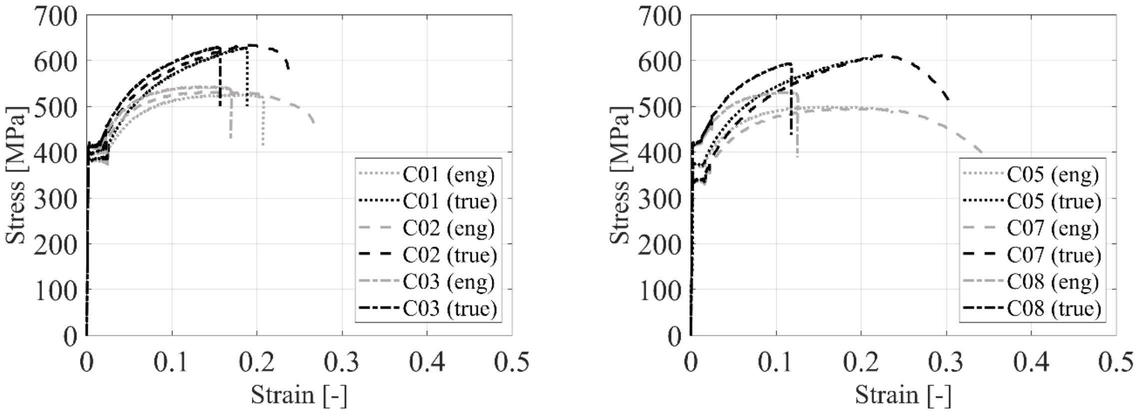

(a) A – web (b) B – web

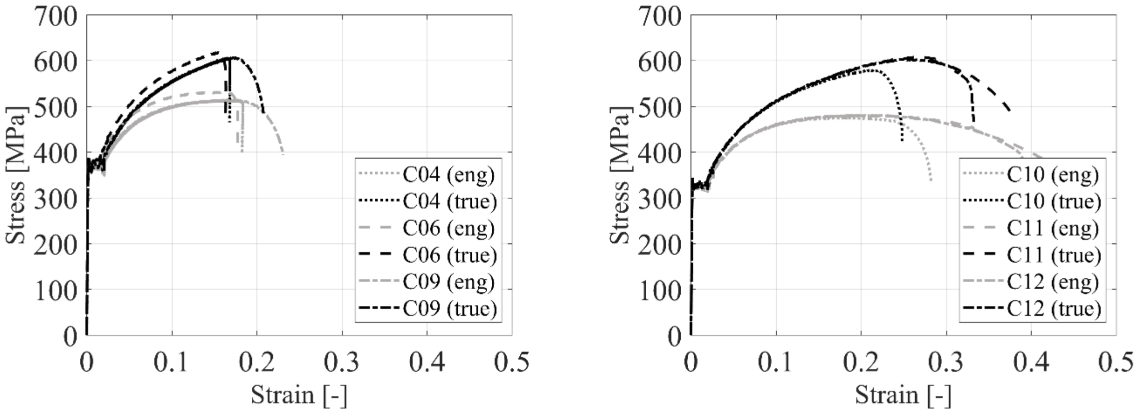

(c) A – flange (d) B – flange

Figure 3.4 – Engineering and true stress – strain curves.

The main characteristic of the true stress – true strain curves depicted are presented in Table 3.4, namely, the Young's modulus E, the yield and ultimate strain ε_y and ε_u, the yield and ultimate stress f_y and f_u. Additionally, is presented the load recorded at fracture F_f, and the minimum cross-sectional area measured after fracture S_f. Given the dispersion of the Young's modulus values gathered from tests, hereinafter is adopted the design value of 210 GPa.

Table 3.4 – True stress – true strain experimental values.

series	coupon ID	E	ε_y	f_y	ε_u	f_u	F_f	S_f
		MPa	-	MPa	-	MPa	kN	mm^2
A web	C01	210396	0.0020	384.8	0.1876	628.2	69.9	79.5
	C02	211747	0.0020	405.8	0.1854	634.4	76.7	108.5
	C03	195752	0.0025	417.7	0.1529	629.8	71.6	91.0
	μ	205965	0.0022	402.7	0.1409	614.4	72.8	93.0
A flange	C04	218732	0.0016	361.9	0.1532	594.0	98.8	115.6
	C06	262354	0.0016	381.9	0.1397	605.3	90.8	110.9
	C09	234471	0.0018	374.7	0.1610	595.7	97.6	114.7
	μ	238519	0.0017	372.8	0.1513	604.6	95.7	113.7
B web	C05	116074	0.0026	371.0	0.2097	604.6	126.4	115.2
	C07	195148	0.0020	357.7	0.2237	611.5	95.8	101.6
	C08	207855	0.0021	419.0	0.1166	593.7	102.7	119.0
	μ	173026	0.0022	382.6	0.1501	590.5	108.3	111.9
B flange	C10	209601	0.0017	329.5	0.1653	554.3	144.2	155.9
	C11	205681	0.0017	344.8	0.1826	568.7	142.9	220.9
	C12	211708	0.0017	335.0	0.1772	566.8	148.7	215.5
	μ	208997	0.0017	336.4	0.1750	571.1	145.2	197.5
	μ_{total}	206626						
	σ_{total}	32345						

3.2.1.4. Loading protocol for T-stubs

(i) Monotonic loading

The tests were carried out under displacement control with a speed of 0.025 mm/s up to collapse of the specimens.

(ii) Cyclic loading

The loading protocol adopted is based on the loading protocol established for the experimental campaign of the European project EQUALJOINTS (Landolfo, 2017a). In EQUALJOINTS project, a simplified protocol for testing of SBCJs is adopted, the "simplified" EQUALJOINTS protocol, in which the smaller cycles are grouped together, and the values of imposed rotation angle are rounded to level of mrad. The resulting simplified protocol is presented in Figure 3.5. The protocol can be continued after the maximum cycle of 0.040 rad by further loading at increments of 0.010 rad, with two cycles of loading at each step, as long as the state of the specimen and the experimental setup permit.

When transposing the previous protocol to the loading protocol for testing T-stubs, a conservative assumption is to assume the case in which the T-stub will be responsible for the entire deformation of the sub-frame, i.e.:

- the total rotation has origin in the connection, i.e., the beam and column deformations and CWS deformations are negligible;
- the connection deformation has origin only in the T-stub in tension;
- the T-stub deformation under compression is negligible;
- the centre of rotation is at a distance z from the axis of the T-stub, which is assumed to be equal to the distance between the axis of the beam flanges.

In the previous scenario, named C1 loading protocol, the relationship between the deformation, d, to apply to the T-stub and the rotation angle, θ, is given by

$$d = z \cdot \tan\theta \tag{3.1}$$

where it was assumed that $z = 435.4\ \text{mm}$, i.e., beam profile IPE450 adopted within EQUALJOINTS project.

From the C1 protocol another loading protocol for the stub was derived (protocol C2) dividing the deformations from loading protocol C1 by 3. The loading protocols adopted for testing T-stubs are presented in Table 3.5 and illustrated in Figure 3.6.

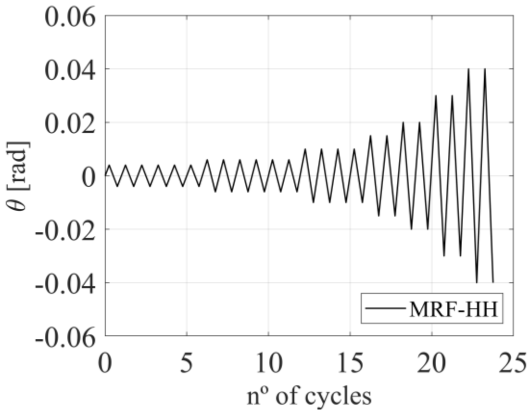

Figure 3.5 – Simplified loading protocol for MRF-HH.

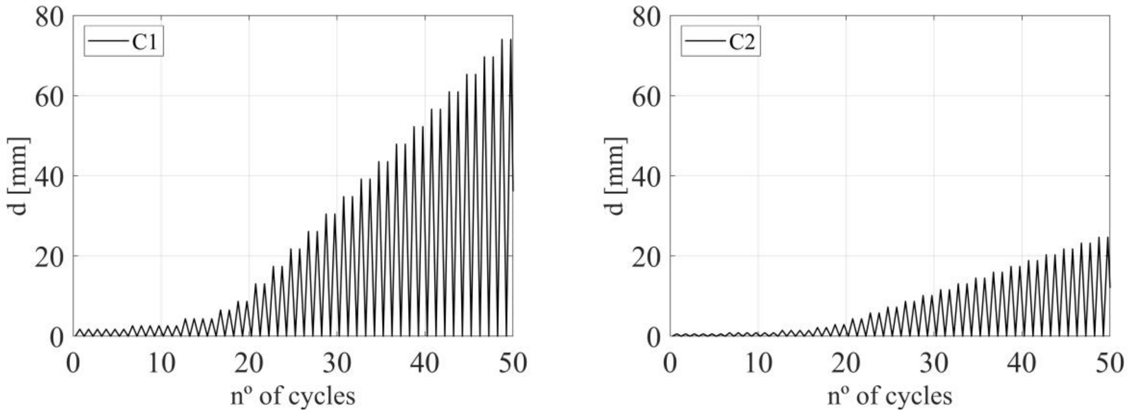

(a) C1 (b) C2

Figure 3.6 – Loading protocols for T-stubs.

Table 3.5 – Loading protocols.

nº of cycles	MRF-HH	C1	C2
	θ rad	d mm	d mm
6	0.004	1.74	0.58
6	0.006	2.61	0.87
4	0.010	4.35	1.45
2	0.015	6.53	2.18
2	0.020	8.71	2.90
2	0.030	13.06	4.35
2	0.040	17.42	5.81

3.2.1.5. Experimental set-up and instrumentation

The loading was displacement-controlled and the displacements were imposed to the webs of the T-stubs that were clamped to the testing machine, as shown in Figure 3.7(a). Instrumentation is shown in Figure 3.7. At opposite sides of the specimen, in the centreline of the webs, Linear Variable Displacement Transducers (LVDTs) were placed to measure the gap of the flanges of both T parts of each T-stub specimen. The load was recorded using the load cell of the Universal Testing Machine.

(a) (b) (c)

Figure 3.7 – Testing apparatus.

3.2.2. Experimental results overview

3.2.2.1. Monotonic behaviour

A and B series specimens present a FM1 plastic mechanism according to EC3-1-8 (CEN, 2005c) predictions. Test results are provided in terms of force-deformation ($F - d$) curves, where F is the applied force and d is the centreline gap between the T parts of the T-stub caused by F, see Figure 3.8(a-c).

In specimens A5 and A7, the collapse mechanism was complete yielding of the flange close to the bolts, plastic deformation of bolts and yielding of the flange near to the flange-to-web connection, corresponding to FM1, see Figure 3.8. Although rupture of the bolts can be observed in Figure 3.8, it does not govern the failure mode, since it occurs after complete yielding of the flange. In this case, the rupture of the bolts is caused by tension combined with bending due to the large deformations of the T-stub. The flexural deformation of the bolts could give rise, in some cases, to a premature failure of the bolts, affection the ultimate resistance of the T-stub, as observed in A7 specimen.

In specimens B1 and B4, mixed failure is achieved through failure of the bolts in tension and partial yielding of the flanges near to the flange-to-web connection, see Figure 3.8(d-f), corresponding to a FM2 – different from the predicted plastic mechanism by EC3-1-8 (CEN, 2005c).

The identification of the failure modes proposed by EC3-1-8 (CEN, 2005c) may be confirmed by analysing the T-stubs ductility. Figures 3.8(c) and 3.8(f) show that A series specimens present lower resistance but higher plastic deformation capacity compared to B series specimens which present higher resistance but lower plastic deformation capacity. It can be noticed that considerable hardening has been achieved, especially for specimens showing FM1 plastic mechanism.

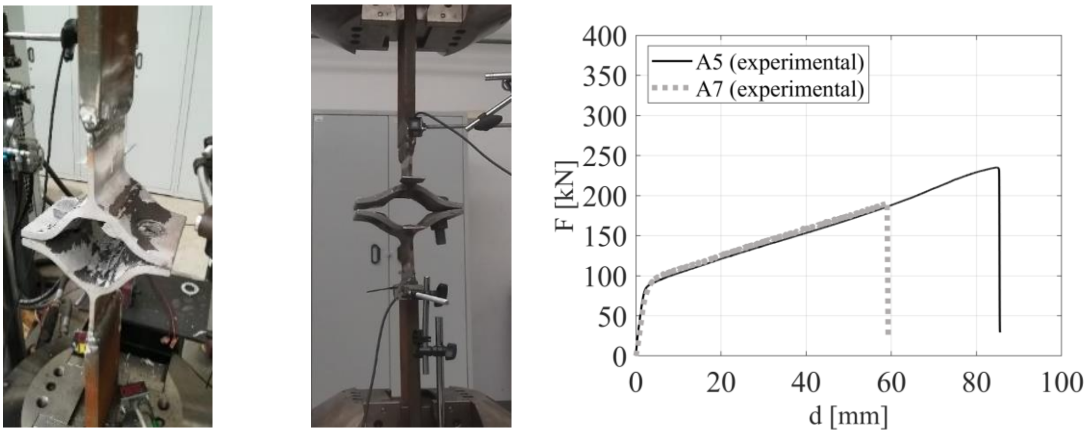

(a) A5 (b) A7 (c)

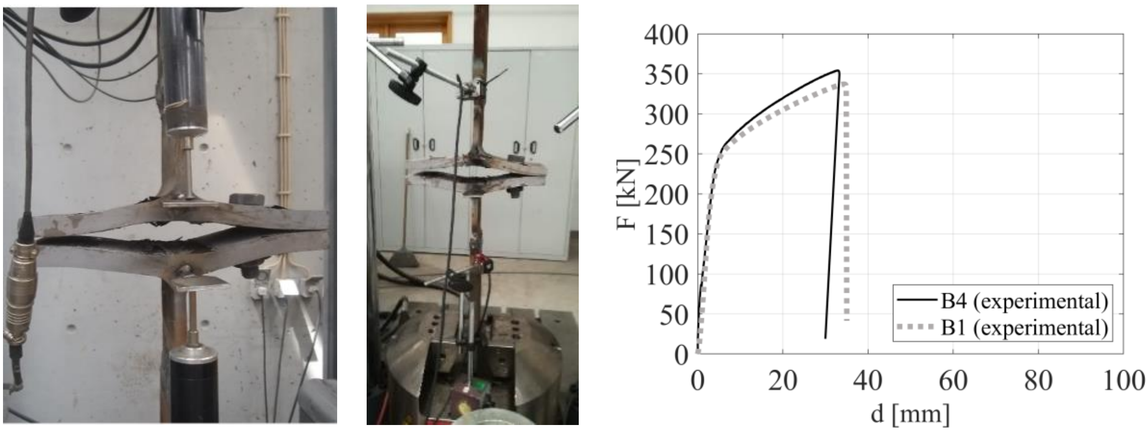

(d) B4 (e) B1 (f)

Figure 3.8 – Monotonic tests: specimens after failure and force-deformation curves.

3.2.2.2. Cyclic behaviour

Two preliminary tests were conducted in order to evaluate the test setup. The test conducted on A3 specimen showed that the testing machine "Servosis" is not fitted to apply compression forces required. The second preliminary test conducted on B6 specimen in universal test machine “walter+bay” showed that the welded plates to the T-stub web were to slender which caused buckling when compression loads were applied. Therefore, these two specimens are disregarded. The remaining specimens were tested in the universal test machine “walter+bay” and the welded plates to the web were cut to avoid buckling when in compression.

Cyclic tests on A series specimens show the same failure mode regardless of loading type protocol applied or the level of bolt preloading. The collapse of these specimens in cyclic conditions was determined by fracture of the T-stub flange – see Figure 3.9 – which follows the failure mode observed under monotonic loading – complete yielding of the T-stub flange – see Figure 3.8(a)-(b). The loading protocol had influence in the number of cycles: C2 loading protocol led to a higher number of cycles and to a lower plastic deformation capacity than the specimens tested under C1 loading protocol. The pinching phenomenon can be seen, being more pronounced in the ascending branches. In addition, the specimens without preloading show slip after the loading reversal (from tension to compression) point.

Likewise, cyclic tests on B series specimens show the same failure mode regardless of loading type protocol applied or the level of bolt preloading. The collapse of these specimens in cyclic conditions was determined by facture of the bolts in tension and partial yielding of the flanges – see Figure 3.9 – which follows the failure mode observed under monotonic loading – see Figure 3.8. As for A series, also in B series specimens show pinching, but being very pronounced for both ascending and descending branches. In addition, B series specimens with and without preloading show horizontal slip after the loading reversal (from tension to compression) – with the exception of B5, which may be an outlier. The same effect of the loading protocol on the behaviour of the specimens from A series was observed in B series.

(a) A1 (b) A6 (c) B5 (d) B3

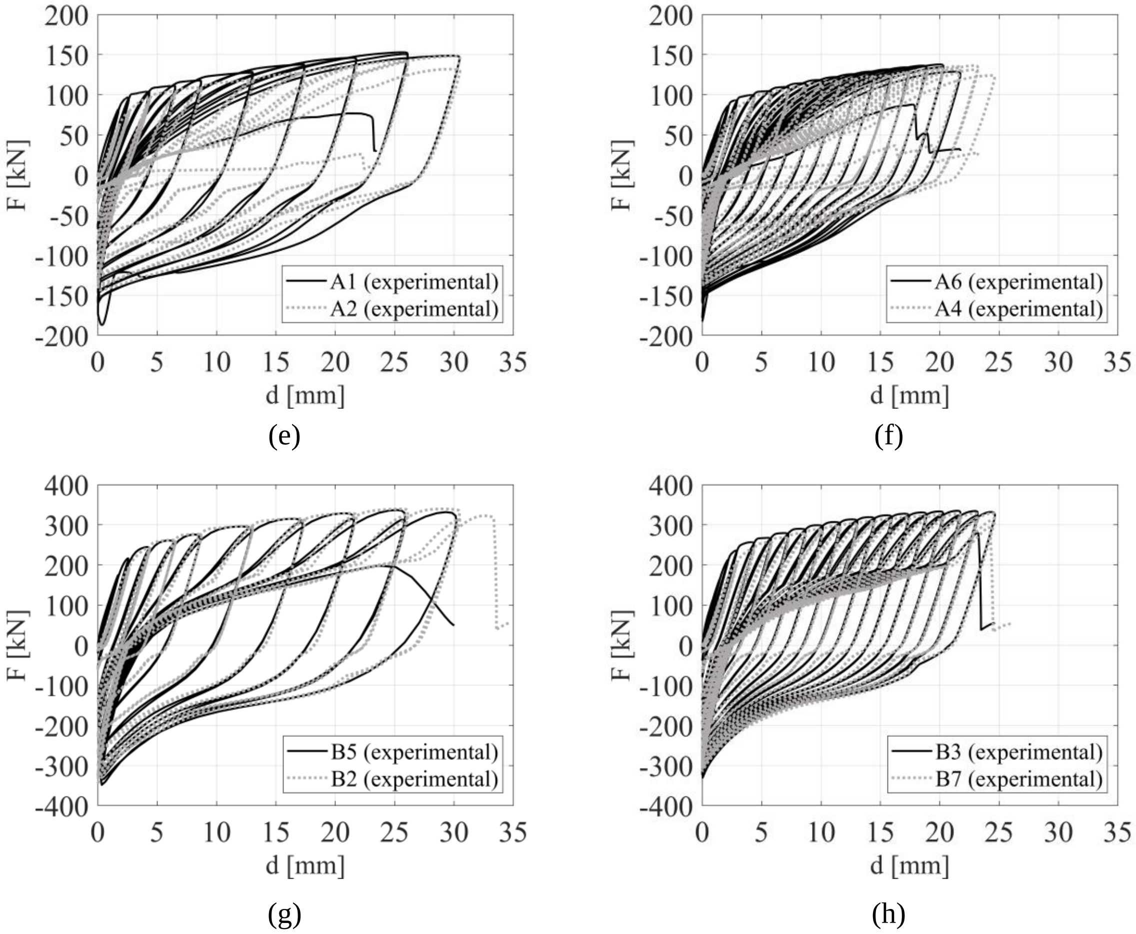

Figure 3.9 – Cyclic tests: (a)-(d) specimens after failure and (e)-(h) force-deformation curves.

3.2.2.3. Monotonic vs cyclic behaviour

The A series specimens tested under cyclic loading present a reduction greater than 50% of the plastic deformation capacity observed under monotonic loading, see Figure 3.10. It should be noted that the monotonic behaviour is in accordance to the upper bound of the cyclic behaviour but for A series specimens with preloading the monotonic post-limit behaviour is slightly below the upper bound of the cyclic behaviour.

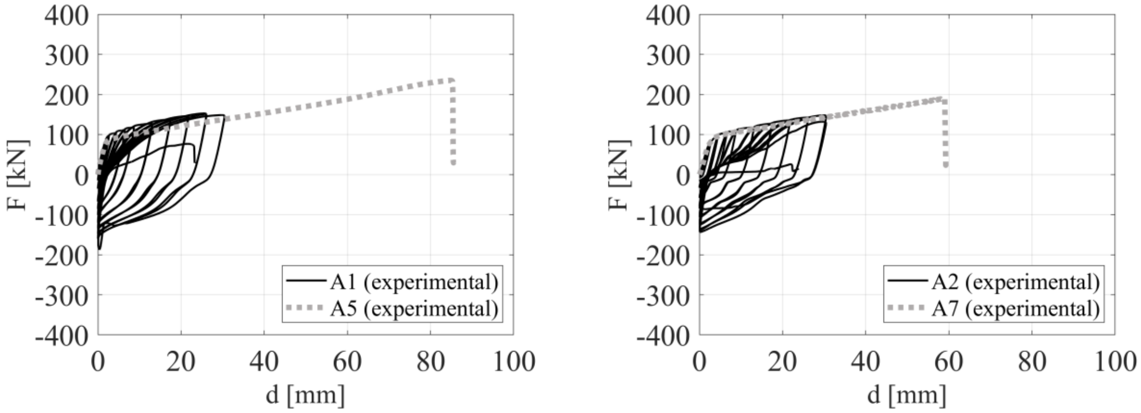

(a) w/ preloading

(b) w/o preloading

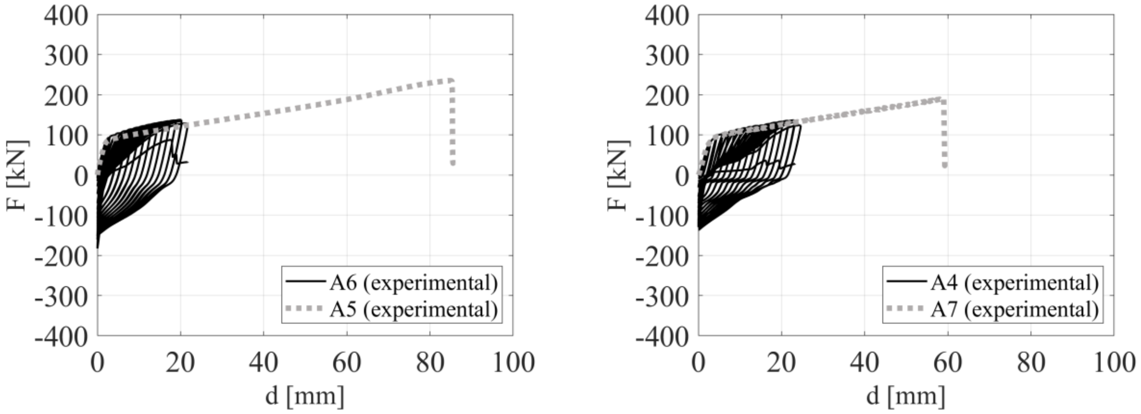

(c) w/ preloading

(d) w/o preloading

Figure 3.10 – Monotonic vs cyclic tests: force-deformation curves (A series).

The B series specimens tested under C1 loading protocol present roughly the same plastic deformation capacity as the ones tested under monotonic loading, see Figures 3.11(a) and 3.11(b). The specimens tested under C2 loading protocol present a 30% reduction of plastic deformation capacity when compared to specimens tested under monotonic loading, see Figures 3.11(c) and 3.11(d). Apart from that, it should be noted that the monotonic behaviour is in accordance to the upper bound of the cyclic behaviour.

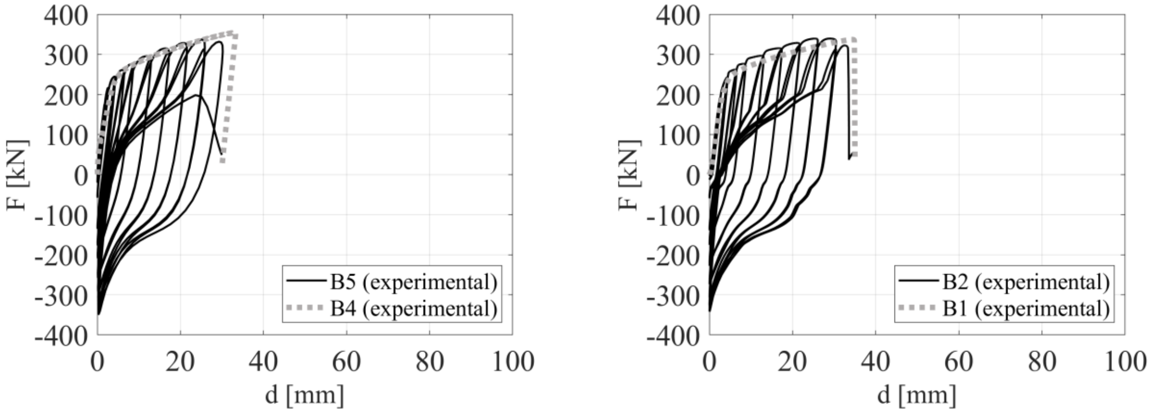

(a) w/ preloading

(b) w/o preloading

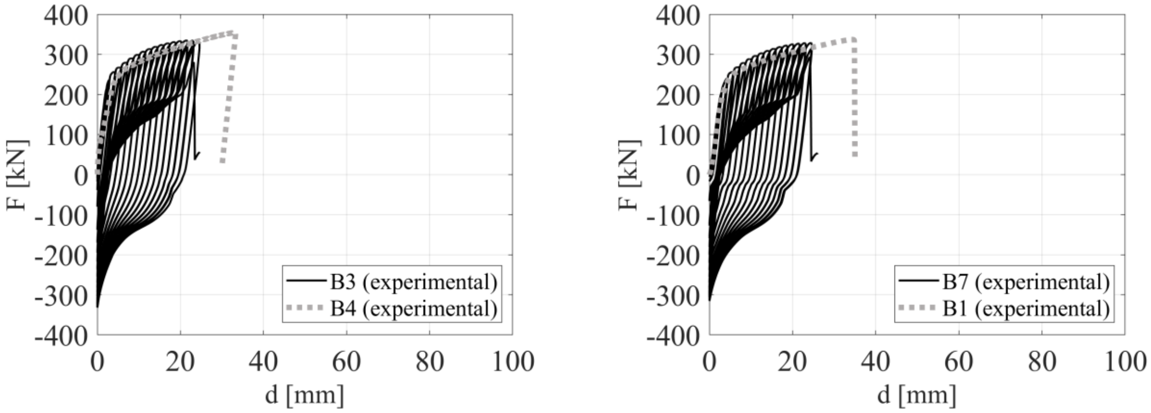

(c) w/ preloading

(d) w/o preloading

Figure 3.11 – Monotonic vs cyclic tests: force-deformation curves (B series).

3.3. Experiments by Piluso and Rizzano (2008)

3.3.1. Experimental campaign

The experimental campaign conducted by Piluso and Rizzano (2008) on T-stubs comprises two groups. The first group is constituted by elements obtained from rolled profiles (HEA 180 and HEB 180) of steel grade FE430 (equivalent to S275) by cutting along the web plane, while the second group is based on T elements composed by welding.

The T elements were connected through the flanges by means of two high strength bolts – M20 (8.8). Bolt tightening was executed by means of a calibrated wrench to assure a bolt pre-stressing force equal to 80% of the bolt yield axial force.

A total of twenty-eight specimens were tested, seven derived from HEA 180 profile (A series), seven from an HEB 180 profile (B series), seven composed by welding with flanges thickness equal to 12 mm (C series) and seven composed by welding with flange thickness equal to 18 mm (D series). With reference to each series of specimen, one monotonic test, five constant amplitude cyclic tests (CA) and one variable amplitude cyclic tests (VA) have been carried out. All the tests have been performed under displacement control.

Table 3.6 synthetizes the geometrical and mechanical properties of the selected specimens, while Figures 3.12 to 3.14 depicts their experimental results in terms of force-deformation ($F - d$) curves.

Table 3.6 – Geometrical and mechanical properties from Piluso and Rizzano (2008) experimental campaign.

A series		B series		C series	
T-tub ID	loading protocol	T-tub ID	loading protocol	T-tub ID	loading protocol
A1	M	B1	M	C1	M
A3	CA (20 mm)	B4	CA (12.5 mm)	C3	CA (20mm)
A4	CA (15 mm)	B5	VA	C4	CA (15 mm)
A6	CA (17.5 mm)	B6	CA (15 mm)	C6	CA (17.5 mm)
A7	VA	B7	CA (20 mm)	C7	VA

3.3.2. Experimental results overview

Piluso and Rizzano (2008) specimens, A, B and C series, were designed to fail according to plastic mechanism modes FM1, FM2 and FM1, respectively. Experimental tests under monotonic loading on T-stub of A and C series specimens was characterized by significant yielding of the flanges at the flange-to-web connection zone and at the bolt axis, i.e. these specimens exhibit the FM1 as expected. As for B series specimens, the collapse mechanism was characterized by minor yielding of the flanges and by significant plastic engagement of the bolts, corresponding to FM2 also as expected.

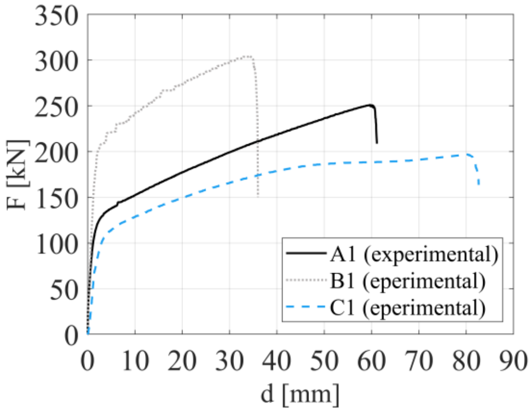

Figure 3.12 – Monotonic test results from Piluso and Rizzano (2008).

On the other hand, when subjected to cyclic loading, A and C series specimens developed cracking of the flanges in the central part of the flange at the flange-to-web connection zone which progressively propagated towards the flange edges up to complete fracture of one flange – this collapse mechanism under cyclic loading is different from the one shown in monotonic tests. Concerning B series specimens, due to relevant plastic deformation of the bolts, cyclic behaviour is characterized by slips before reloading, during these slips the axial force is equal to zero up to the recovery of the bolt plastic deformation before reloading.

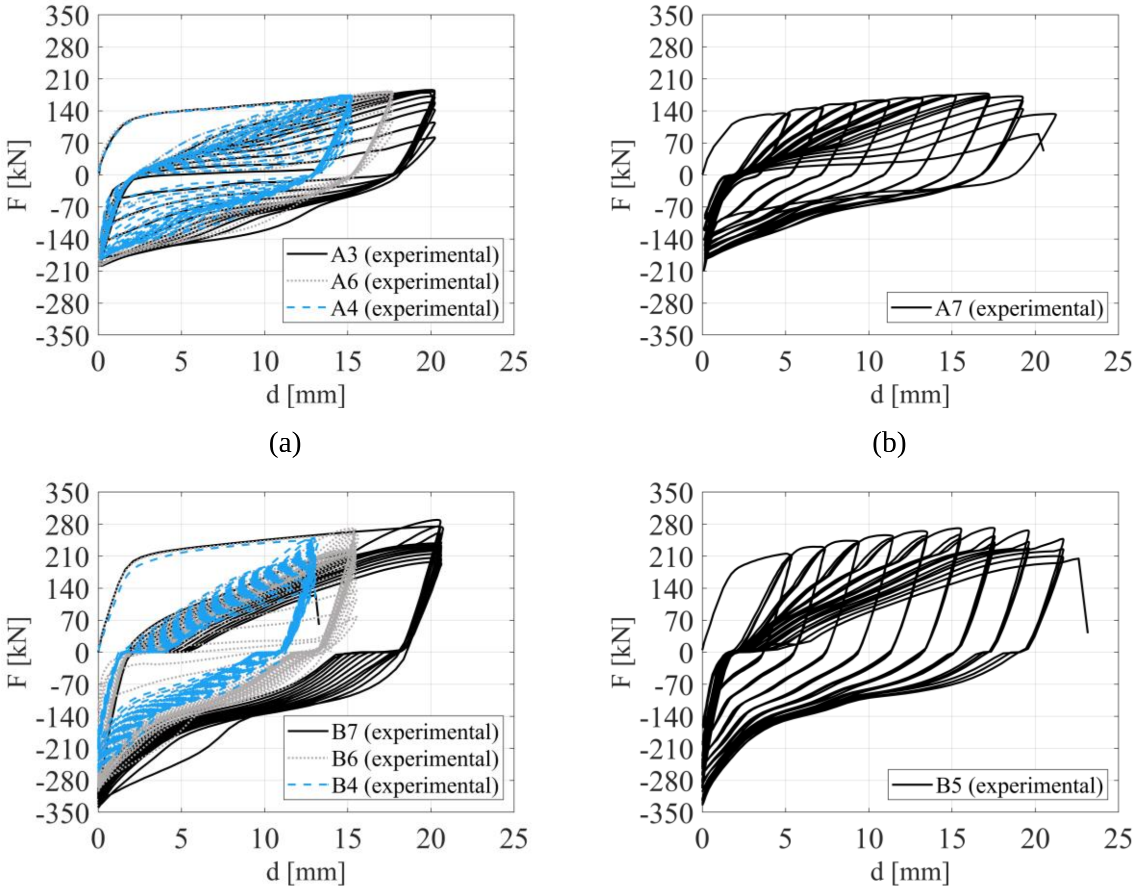

(a) (b)

(c) (d)

Figure 3.13 – Cyclic test results from Piluso and Rizzano (2008): rolled specimens.

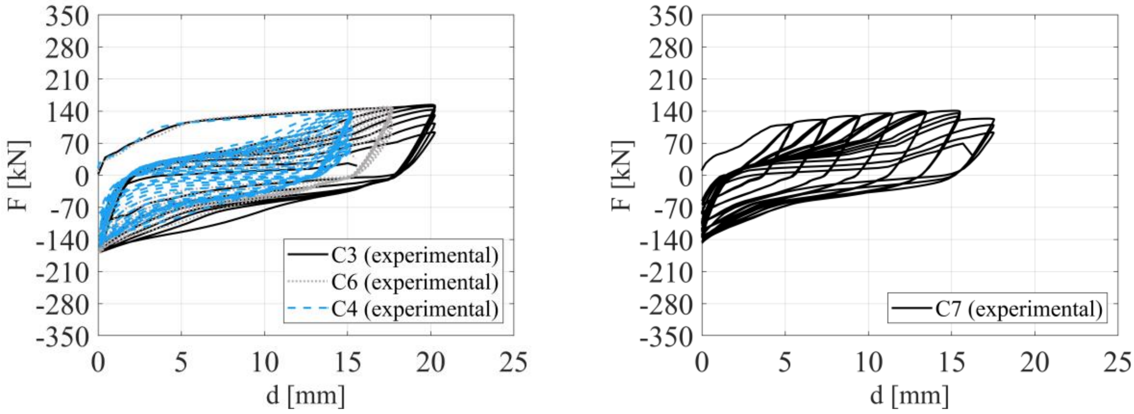

(a) (b)

Figure 3.14 – Cyclic test results from Piluso and Rizzano (2008): welded specimens.

3.4. Quantitative assessment

3.4.1. Introduction

A detailed quantitative assessment of the main mechanical properties of both reported experimental campaigns on T-stubs was undertaken. Obtained result are presented in terms of (i) peak force per cycle, (ii) initial stiffness per cycle, (iii) post-limit behaviour and (iv) hysteretic energy dissipation.

These two experimental campaigns – monotonic and variable amplitude cyclic tests at University of Coimbra (C1 and C2) and variable and constant amplitude cyclic tests by Piluso and Rizzano (CA and VA) – cover rolled and welded T-stub, two distinct failure modes (FM1 and FM2) and four loading protocols.

3.4.2. Monotonic behaviour

Definition of stiffness and strength for monotonic behaviour are given in Figure 3.15.

The reference strength F_0 is determined by the intersection of a linear regression over the post-limit response – starting from the maximum load point (d_u, F_u) and ending at the upper bound of the knee-range – with the vertical axis.

The post-limit stiffness K_{pl} is the slope obtained from this linear regression. The initial stiffness K_{ini} defined as the slope of a line regressed over the force-deformation curve from the origin to the point $0.5F_0$.

The intersection of these lines defines the yield point $\left(d_y, F_y\right)$. Table 3.7 summarizes the monotonic behaviour test results. The main conclusion from this table is that, as expected, the comparisons of specimens A5 and A7 and B1 and B4 testes at University of Coimbra revealed that specimens with bolt preloading have larger initial stiffness.

Table 3.7 – Monotonic test results.

author	T-stub ID	bolt pre-load.	K_{ini} kN/mm	δ_y mm	F_y kN	K_{pl} kN/mm	F_0 kN	δ_u mm	F_u kN	$\frac{K_{\mathrm{pl}}}{K_{\mathrm{ini}}}$
Oliveira *et al.* (2021)	A5	yes	55	1.6	87	1.8	84	84.7	235	3.2%
	A7	no	37	2.4	87	1.7	83	58.4	180	4.6%
Piluso and Rizzano (2008)	A1	yes	135	1.0	138	2.0	136	59.6	251	1.5%
Oliveira *et al.* (2021)	B1	no	70	3.5	249	2.7	239	34.4	337	3.8%
	B4	yes	89	2.8	250	3.2	241	33.0	354	3.7%
Piluso and Rizzano (2008)	B1	yes	145	1.5	218	2.9	214	34.2	304	2.0%
Piluso and Rizzano (2008)	C1	yes	50	2.4	119	1.6	116	80.3	197	3.2%

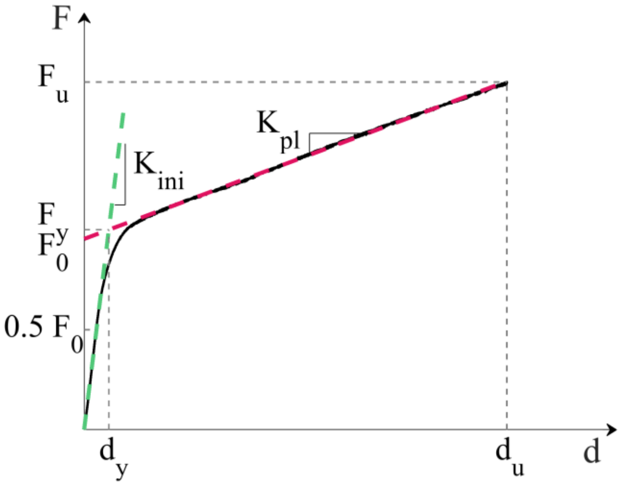

Figure 3.15 – Force-deformation characteristics from monotonic tests.

3.4.3. Cyclic behaviour

3.4.3.1. Peak force

Figures 3.16 to 3.18 illustrate the peak force per branch, both in positive and negative range, which allows to identify the following aspects throughout the loading history:

(i) *initial cycles*

In C1 and C2 tests, at the beginning of the load history, while there are no significant plastic deformations, the ascending branches (tension forces) present larger peak force than descending branches (compression forces), see Figure 3.16. In this phase, compression forces are rather small.

In VA tests, ascending branches also present larger peak force than descending branches, but as the applied deformation is larger than in C1 and C2 tests, plastic deformation lead to significant compression forces from the first cycle, see Figures 3.18(b), 3.18(d) and 3.17(b).

In CA tests, the same level of force in ascending and descending branches is observed from the first cycle due to the large amplitude deformations.

Preloaded T-stubs – A1, A6, B3 and B5 – present a peak force per cycle larger in the first and intermediate cycles than non-preloaded bolts, see Figure 3.16.

(ii) later cycles and collapse

In C1 and C2 tests, with the increase of the amplitude of the cycles the peak compressive forces reach values similar to the tension peak forces.

In variable amplitude tests – C1, C2 and VA loading protocols – T-stubs show hardening, as the deformation amplitude increases, up to the absolute peak force and then strength degradation up to failure. However, for the same amplitude cycles a small strength degradation is also observed in these testes.

On the other hand, in constant amplitude cyclic tests – CA loading protocol – T-stubs show consistent strength decrease for the same deformation amplitude, signalizing strength degradation.

After the bolt preload loss (non-linear regime), preloaded and non-preloaded T-stubs meet about the same peak force level, see Figure 3.16.

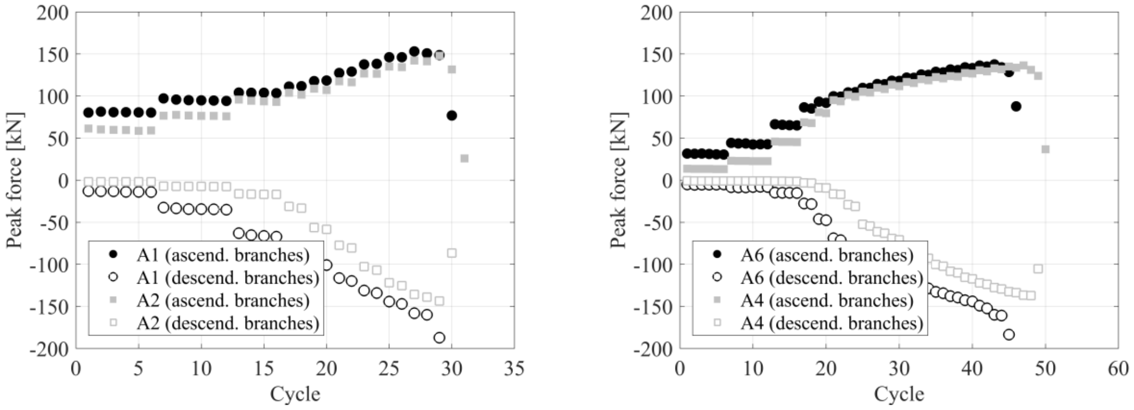

(a) load. protocol C1

(b) load. protocol C2

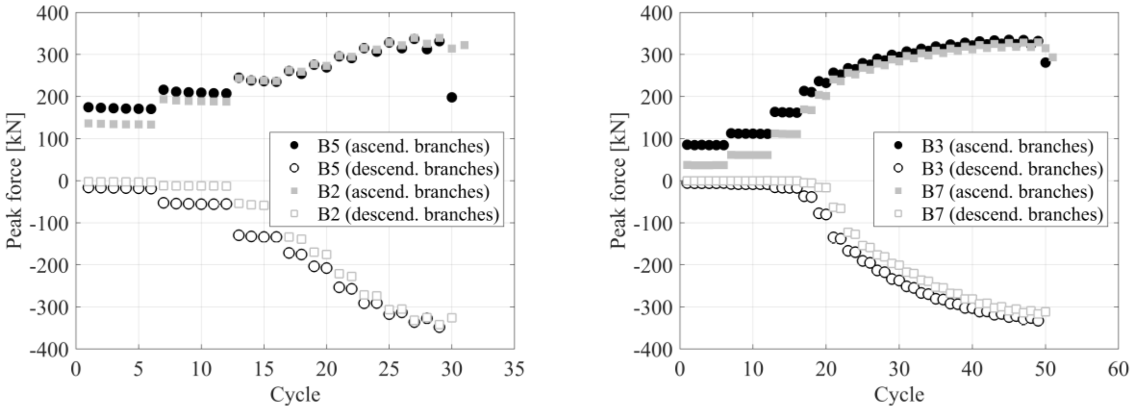

(c) load. protocol C1

(d) load. protocol C2

Figure 3.16 – Cyclic test results: peak force per cycle.

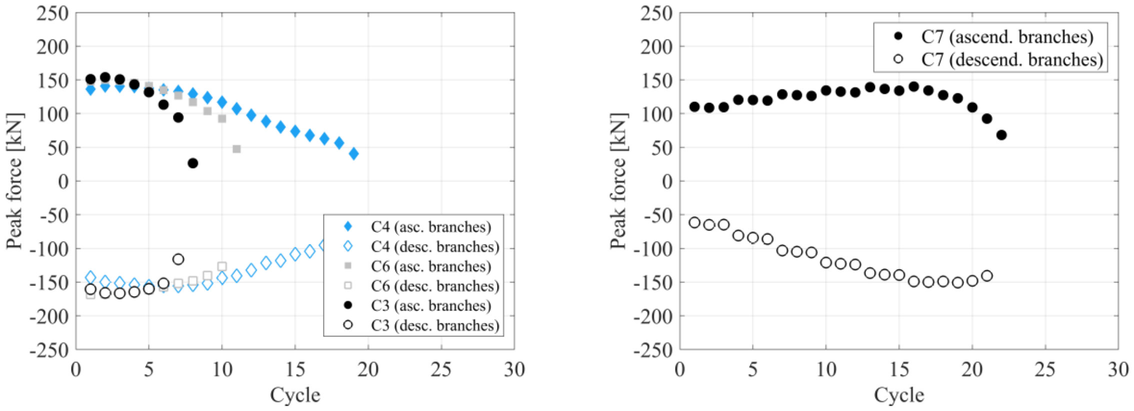

(a) load. protocol CA

(a) load. protocol VA

Figure 3.17 – Cyclic test results from Piluso and Rizzano (2008) welded specimens: peak force per cycle.

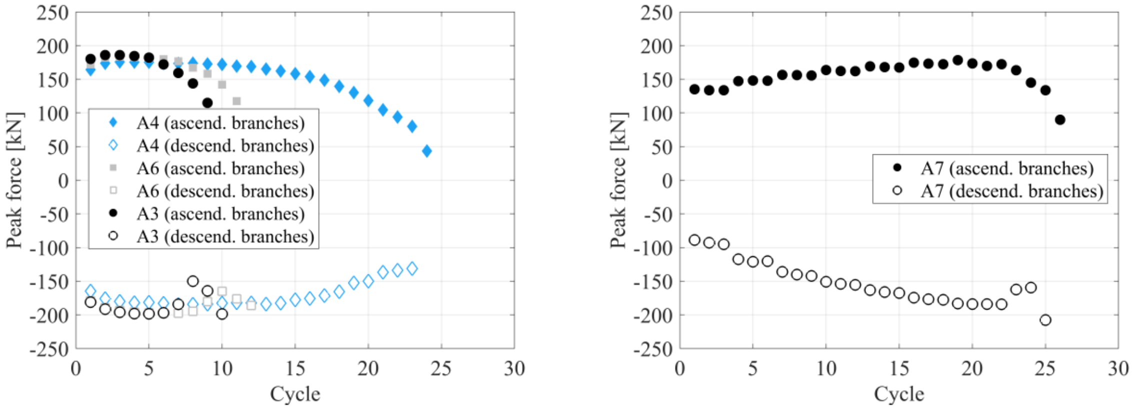

(a) load. protocol CA

(b) load. protocol VA

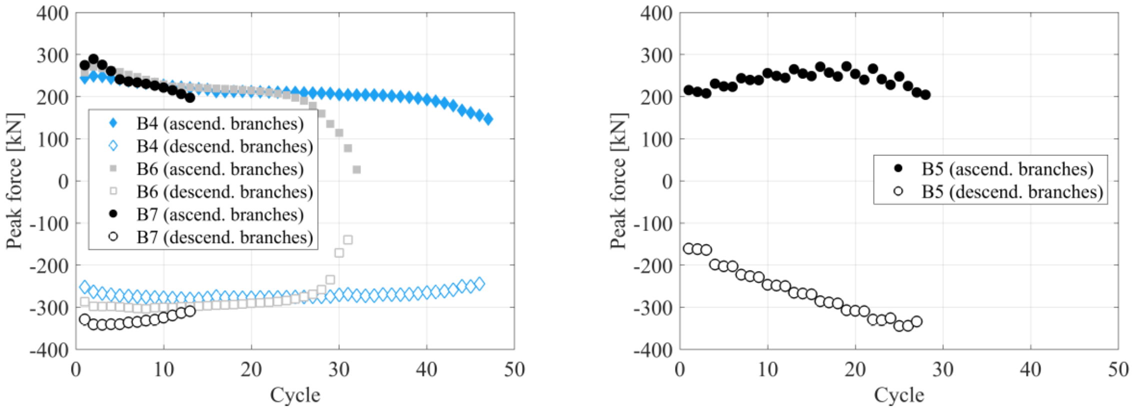

(c) load. protocol CA

(d) load. protocol VA

Figure 3.18 – Cyclic test results from Piluso and Rizzano (2008) rolled specimens: peak force per cycle.

3.4.3.2. Initial stiffness

The initial stiffness K_0 was determined for each ascending and descending branch as a slope of the regression line between the minimum or maximum strength, as relevant, and 25% of that strength, see Figure 3.19. This procedure was adopted to select the value of K_0 suitable for the MRA model, in which these branches are assumed to be initially linear with a slope equal to the initial stiffness K_0, see Figure 2.11. Figure 3.19 show the typical loop layout at an intermediate cycle of a T-stub (a) with and (b) without bolt preloading, both failing under FM1.

However, in first cycles, a non-linear behaviour is noticed at the beginning of the branch, see Figure 3.20. Accordingly, it is not possible to define an approximately linear behaviour in the beginning of these branches and thus they were disregarded.

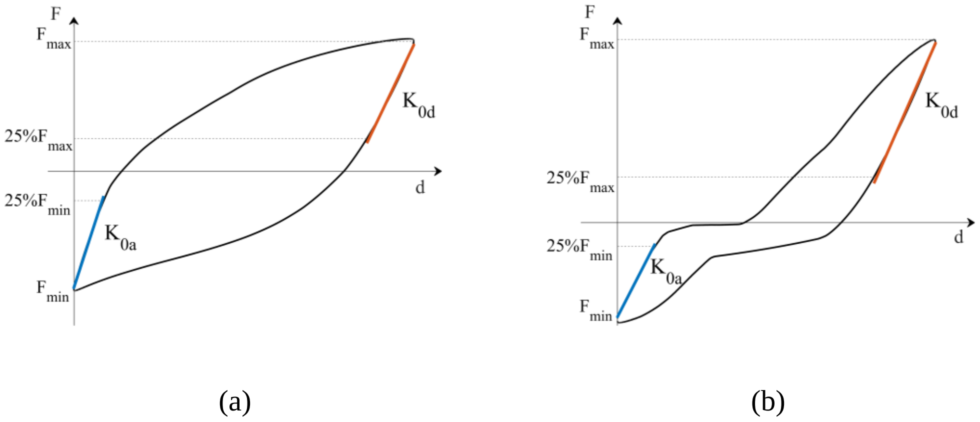

(a) (b)

Figure 3.19 – Extraction of the ascending and descending stiffness.

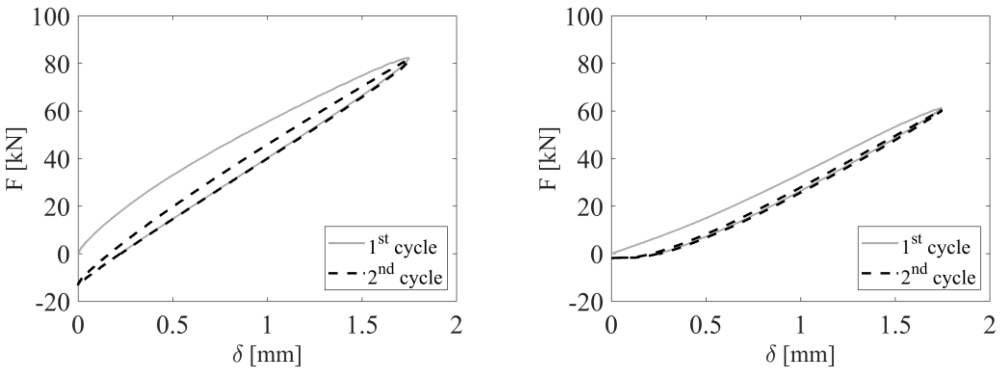

(a) A1 (preloaded) (b) A2 (non-preloaded)

Figure 3.20 – Evolution of the hysteretic response: 1st and 2nd cycle.

Figures 3.21 to 3.22 show the initial stiffness determined for each branch, which allows to identify the following features in the ascending and descending branches:

(i) ascending branches

- non-linear behaviour at the beginning of ascending branches mainly during the first half of the loading history in variable amplitude tests C1 and C2: these values are not representative for the computation of the initial stiffness, and therefore were disregarded;

- stiffness hardening: pronounced increase of stiffness in variable amplitude tests (C1, C2 and VA) and failing under FM1 – about 80% increase, and moderate in specimens failing according to FM2 – an average of 30% increase;
- K_{0a} is generally greater than K_{0d}, furnishing an asymmetric behaviour;
- preloaded specimens reach higher levels of K_{0a} – with the exception of B5, which may be an outlier, since it is the only case where a preloaded specimen has lower K_{0a} than a non-preloaded.

(ii) descending branches

- linear portion present since the first descending branch;
- K_{0d} is fairly stable during the load history in specimens tested under loading protocols C1 and VA, with a slight decrease along the loading history, see Figures 3.21(a), 3.21(c), 3.23(b), 3.23(c) and 3.22(b);
- preload and non-preloaded specimens tested under loading protocol C1 start with similar value of K_{0d}, see Figures 3.21(a) and 3.21(c); on the other hand, preloaded specimens tested under loading protocol C2 start with a larger K_{0d} than non-preloaded specimens, but both meet the same stiffness level after 20 cycles – see Figures 3.21(b) and 3.21(d) – as at the initial stage the applied displacements are really small and there are still no plastic deformations;

- around 20% decrease of stiffness in first cycles down to a stable value in specimens with bolt preloading – A6 and B3 – and tested under loading protocol C2 – see Figures 3.21(b) and 3.21(d);
- increase of stiffness in first cycles up to a stable value in specimens without bolt preloading and tested under loading protocol C2 – around 40% increase in specimens failing under FM1 and 20% in FM2 – see Figures 3.21(b) and 3.21(d), respectively;
- stiffness degradation in CA tests – see Figures 3.23(a), 3.23(c) and 3.22(a).

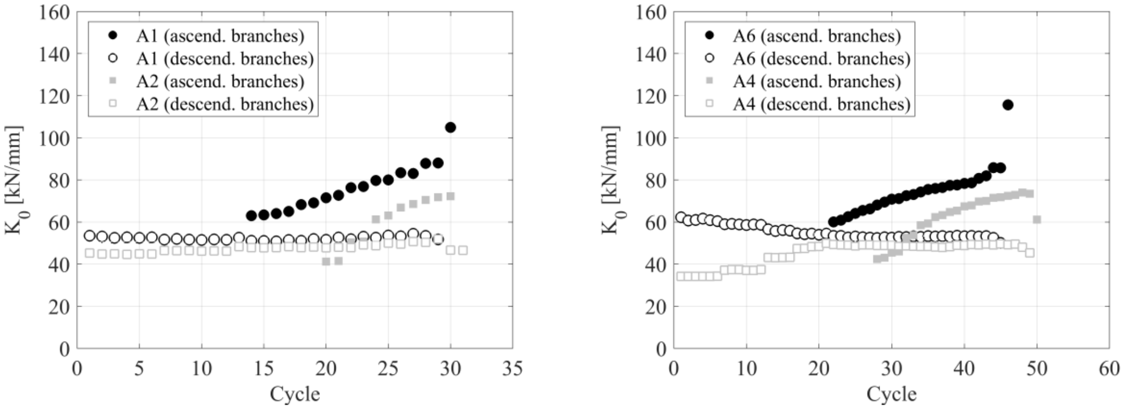

(a) load. protocol C1 (b) load. protocol C2

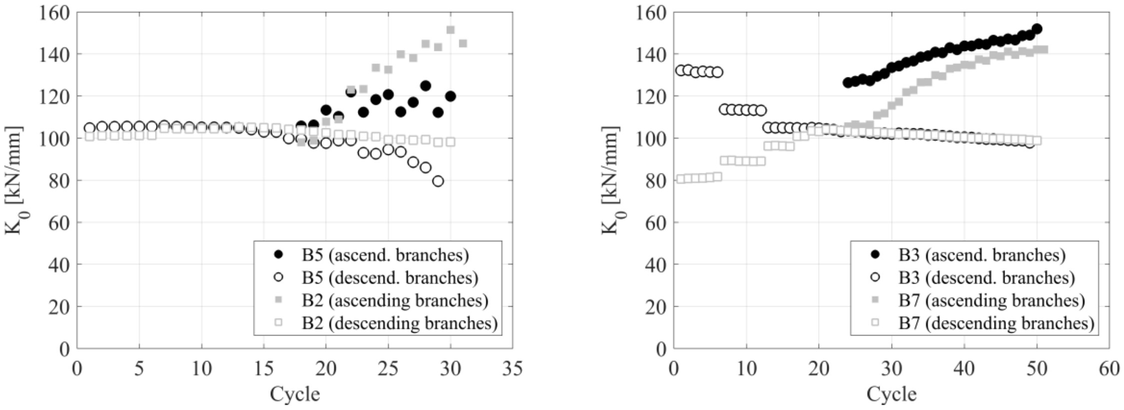

(c) load. protocol C1 (d) load. protocol C2

Figure 3.21 – Cyclic test results: initial stiffness per cycle.

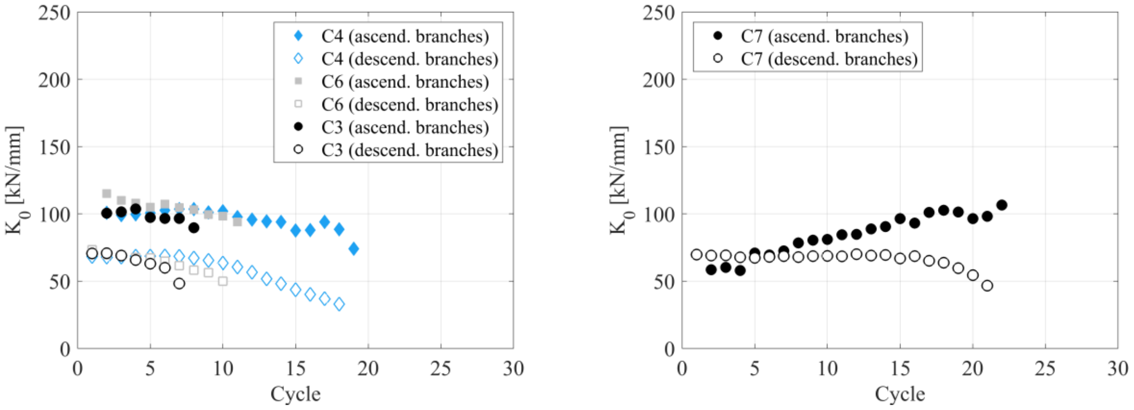

(a) load. protocol CA (b) load. protocol VA

Figure 3.22 – Cyclic test results from Piluso and Rizzano (2008) welded specimens: initial stiffness per cycle.

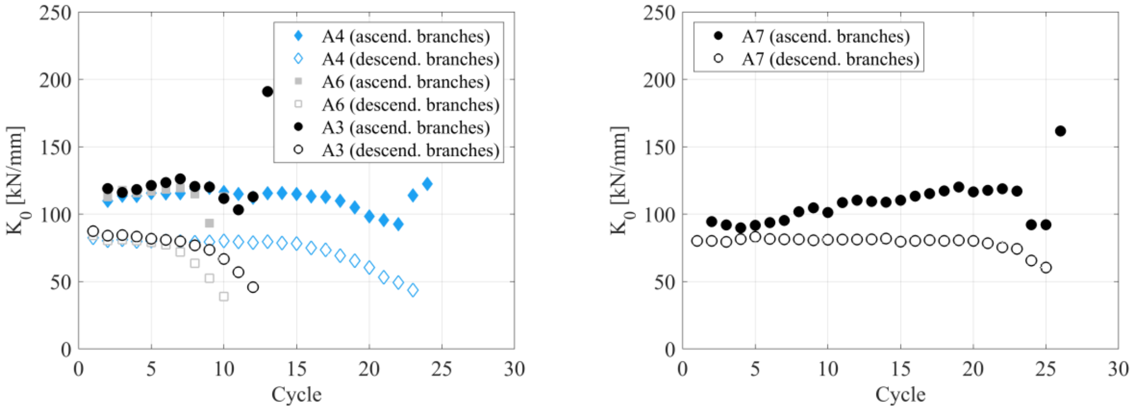

(a) load. protocol CA (b) load. protocol VA

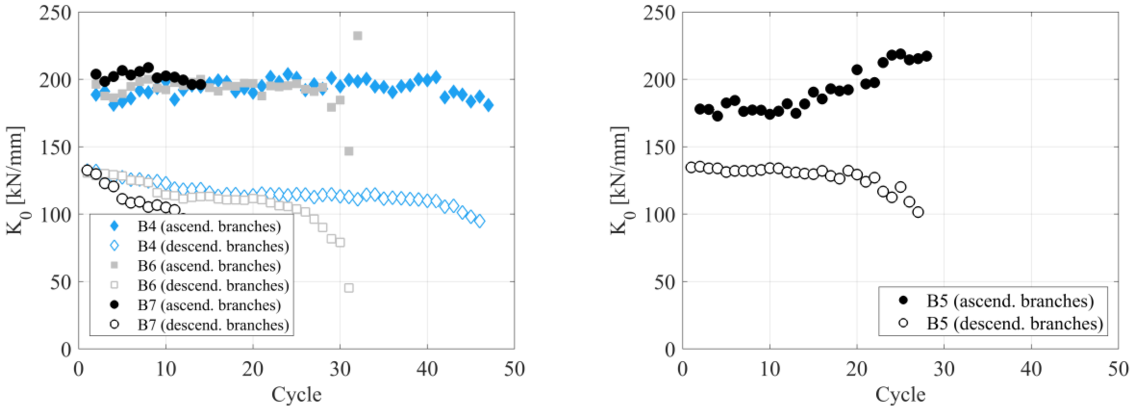

(c) load. protocol CA (d) load. protocol VA

Figure 3.23 – Cyclic test results from Piluso and Rizzano (2008) rolled specimens: initial stiffness per cycle.

Table 3.8 summarizes the selected initial stiffness to adopt in the MRA model, where K_{0a} was extracted from the first ascending branch in which was possible to identify a linear portion for Oliveira *et al.* (2021) specimens and from the second ascending branch for Piluso and Rizzano (2008) specimens, and K_{0d} from the first descending branch for all specimens.

Table 3.8 – Cyclic behaviour test results from rolled and welded specimens: initial stiffness.

author	T-stub ID	K_{0a} kN/mm	K_{0d} kN/mm	$\frac{K_{0d}}{K_{0a}}$	author	T-stub ID	K_{0a} kN/mm	K_{0d} kN/mm	$\frac{K_{0d}}{K_{0a}}$
Oliveira *et al.* (2021)	A1	67	54	0.80	Piluso and Rizzano (2008)	A3	113	84	0.75
	A2	41	45	1.10		A4	110	83	0.75
	A4	42	34	0.81		A6	119	87	0.73
	A6	60	62	1.04		A7	94	80	0.85
			μ	0.94				μ	0.77
			σ	0.13				σ	0.05
Oliveira *et al.* (2021)	B2	98	101	1.03	Piluso and Rizzano (2008)	B4	189	132	0.70
	B3	135	132	0.98		B5	178	135	0.76
	B5	115	105	0.91		B6	196	130	0.66
	B7	106	81	0.76		B7	204	132	0.65
			μ	0.92				μ	0.69
			σ	0.10				σ	0.04
Piluso and Rizzano (2008)	C3	101	71	0.70					
	C4	101	68	0.68					
	C6	115	73	0.64					
	C7	59	70	1.19					
			μ	0.80					
			σ	0.23					

3.4.3.3. Post-limit behaviour

Definition of stiffness and strength for cyclic behaviour are given in Figure 3.24. These characteristics were determined the same way as for monotonic behaviour but with regard to upper the envelope of the cyclic behaviour. Tables 3.9 and 3.10 summarizes the cyclic behaviour test results regarding the post-limit behaviour. An average value of 3.3% for K_{pl}/K_{0a} was found for FM1 and 2.2% for FM2 rolled specimens. In the case of FM1 welded specimens, and average of 2.6% was found.

Table 3.9 – Cyclic behaviour test results from A and C series: post-limit behaviour.

author	T-stub ID	bolt preload.	K_{pl} kN/mm	F_0 kN	δ_u mm	F_u kN	$\frac{K_{pl}}{K_{0a}}$
Oliveira *et al.* (2021)	A1	yes	2.1	103	25.7	153	3.1%
	A2	no	1.8	96	30.0	148	4.4%
	A4	no	1.9	94	22.9	136	4.5%
	A6	yes	2.4	93	20.0	137	4.1%
Piluso and Rizzano (2008)	A3	yes	2.9	124	19.9	179	2.6%
	A4	yes	2.6	126	15.1	164	2.3%
	A6	yes	2.7	126	17.4	171	2.2%
	A7	yes	3.2	128	17.0	177	3.3%
		μ	2.4			μ	3.3%
		σ	0.5			σ	0.9%
Piluso and Rizzano (2008)	C3	yes	2.2	109	19.8	151	2.2%
	C4	yes	2.2	104	15.0	136	2.2%
	C6	yes	2.1	112	17.1	147	1.9%
	C7	yes	2.6	105	15.2	141	4.4%
		μ	2.3			μ	2.6%
		σ	0.2			σ	1.0%

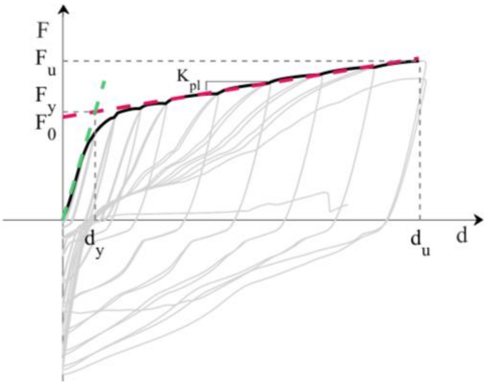

Figure 3.24 – Force-deformation characteristics from cyclic tests.

Table 3.10 – Cyclic behaviour test results from B series: post-limit behaviour.

author	T-stub ID	bolt preload.	K_{pl} kN/mm	F_0 kN	δ_u mm	F_u kN	$\frac{K_{pl}}{K_{0a}}$
Oliveira *et al.* (2021)	B2	no	2.9	263	28.9	339	3.0%
	B3	yes	2.9	274	21.5	334	2.2%
	B5	yes	2.8	262	25.1	337	2.5%
	B7	no	3.0	262	24.4	328	2.8%
Piluso and Rizzano (2008)	B4	yes	3.4	203	12.9	245	1.8%
	B5	yes	4.4	205	17.4	271	2.4%
	B6	yes	3.0	212	15.3	256	1.5%
	B7	yes	3.2	212	20.2	275	1.6%
		μ	3.2			μ	2.2%
		σ	0.5			σ	0.5%

3.4.3.4. Hysteretic energy dissipation

The hysteretic energy dissipation capacity is defined as the area under each hysteretic loop of the force-deformation curve. This area is estimated applying the trapezoidal rule to each deformation increment and summing the results. The energy dissipated in the first cycle, E_0, begins at the point of origin and ends when $F = 0$, the following cycles are numbered every time the descending brancges of the $F - \delta$ curve crosses the horizontal axis, see Figure 3.25.

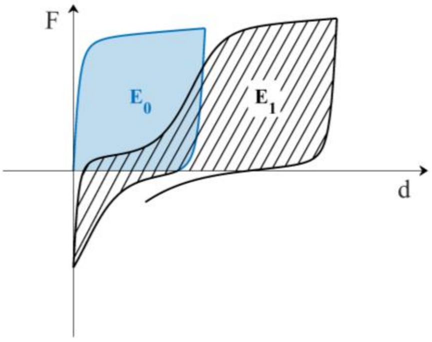

Figure 3.25 – Definition of energy per cycle.

Figures 3.26 to 3.28 depicts the hysteretic energy dissipation per cycle and the accumulated energy per cycle, emphasising the global T-stub capability to dissipate energy. The energy dissipation per cycle gradually increases with the cycle deformation amplitude – C1, C2 and VA loading protocols. On the contrary, it decreases for cycles at the same amplitude – CA loading protocol. The energy dissipation capacity of the T-stub is influenced by the following features:

(i) loading protocol

- loading protocol C1 vs C2 – specimens A6, A4, B3 and B7 (C2 test protocol) as expected present smaller energy dissipation capacity per cycle, but reach a larger total energy dissipation capacity, as the number of cycles to failure is also larger, see Figure 3.26; on the other hand, specimens A1, A2, B2 and B5 (C1 test protocol) show a more rapid accumulation of energy dissipation, due to the presence of plastic deformation since first cycles, see Figure 3.26;
- loading protocol CA vs VA – specimens in CA tests as expected present degradation of energy dissipation capacity per cycle, but in some cases reach a larger total energy dissipation capacity, as the number of cycles to failure is also

larger, see Figures 3.27 and 3.28; on the other hand, specimens A7, B5 and C7 (VA test protocol) show a more slow accumulation or energy dissipation capacity, due to smaller amplitude cycles;

(ii) bolt preloading – preloaded T-stubs present larger energy dissipation capacity that non-preloaded, see Figure 3.26;

(iii) failure mode – T-stub failing according to FM2 present larger energy dissipation capacity, see Figures 3.26 and 3.27.

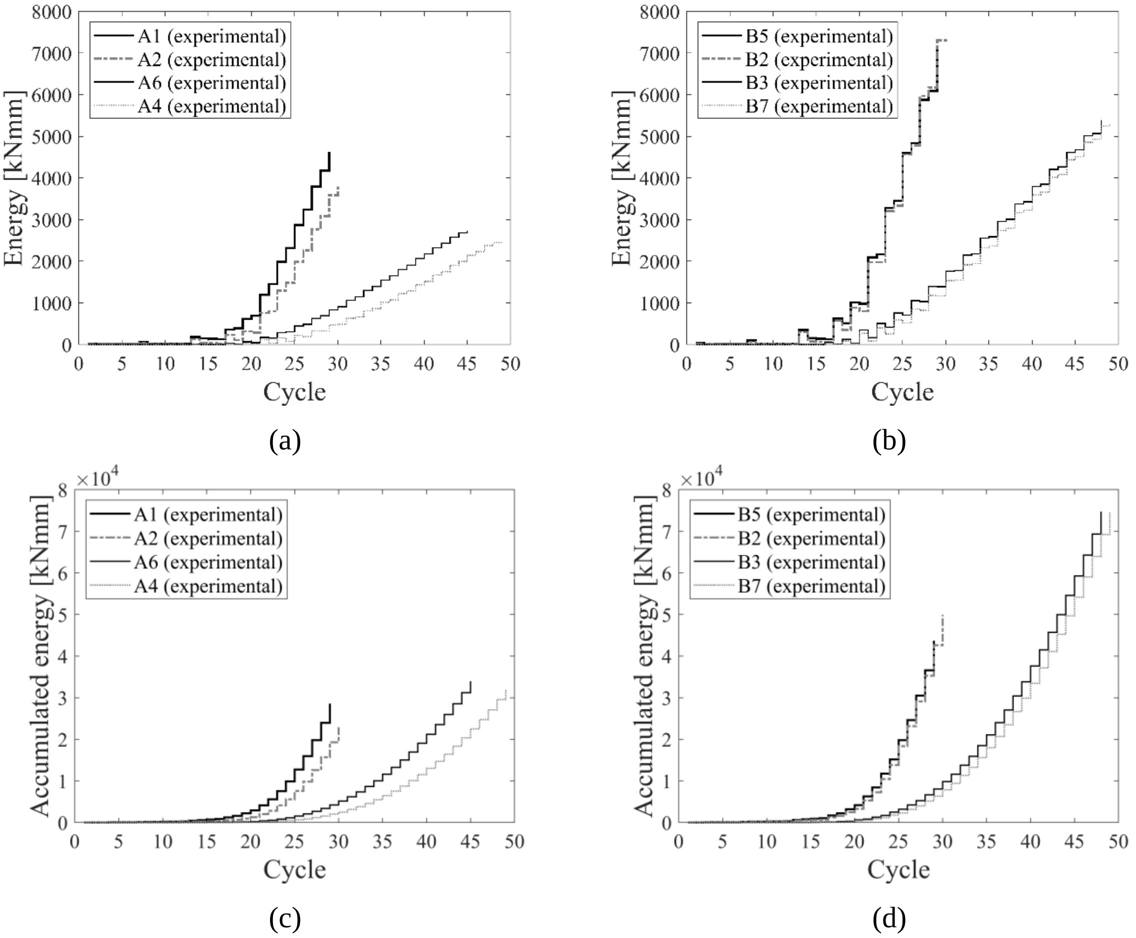

(a) (b)

(c) (d)

Figure 3.26 – Cyclic test results: (a)-(b) energy per cycle and (c)-(d) accumulated energy per cycle.

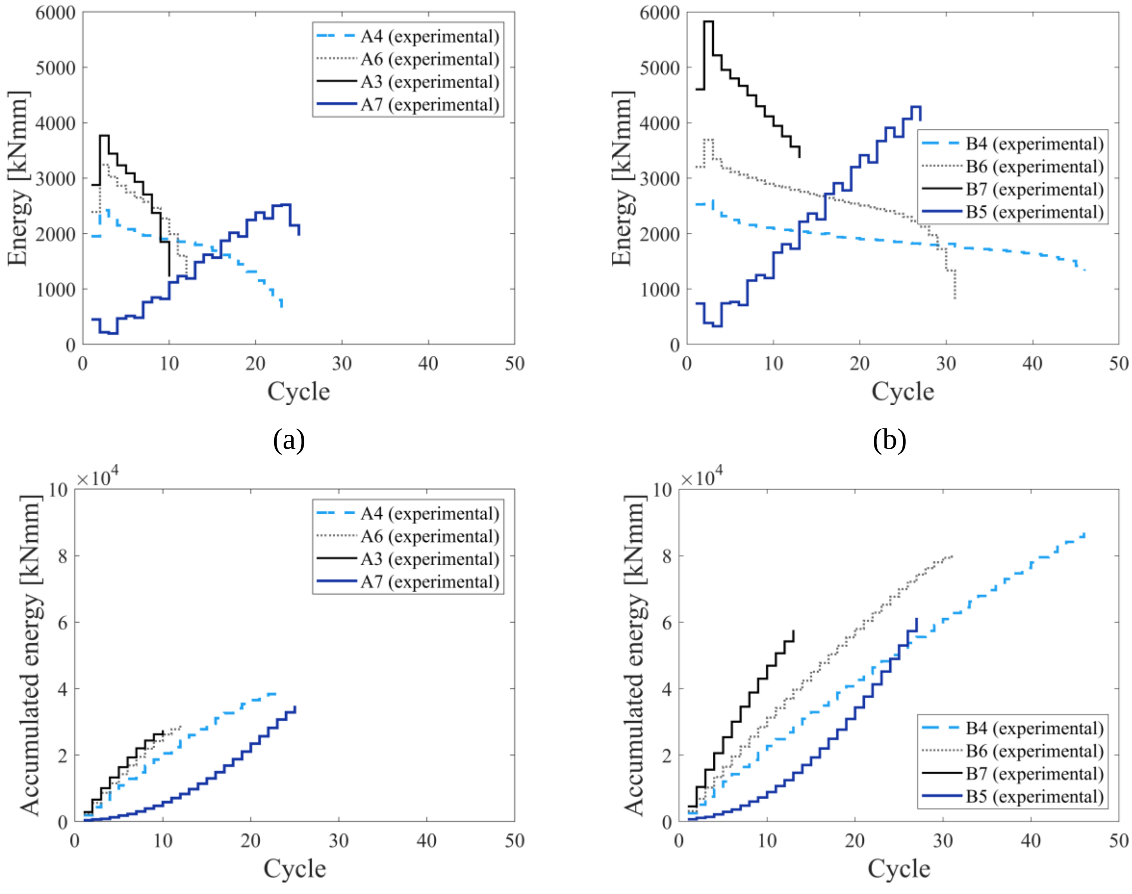

(a) (b)

(c) (d)

Figure 3.27 – Cyclic test results from Piluso and Rizzano (2008) rolled specimens: (a)-(b) energy per cycle and (c)-(d) accumulated energy per cycle.

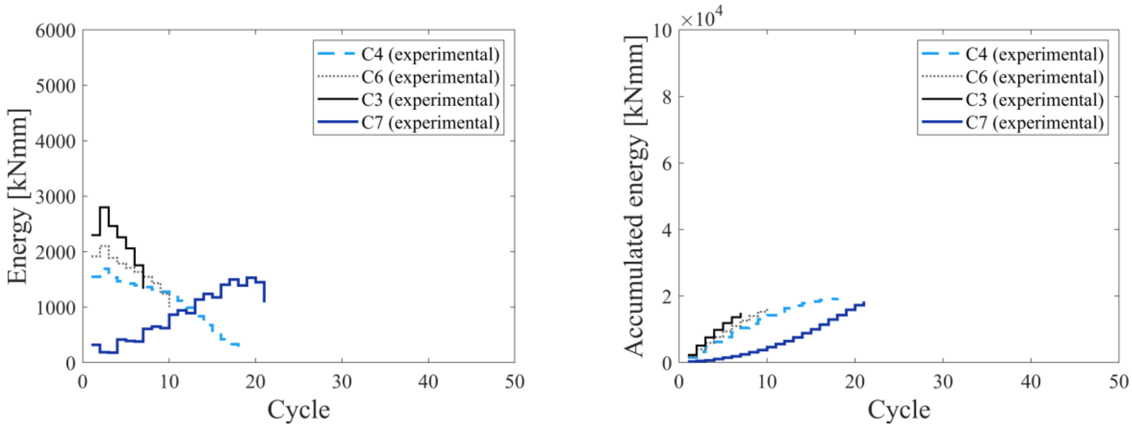

(a) (b)

Figure 3.28 – Cyclic test results from Piluso and Rizzano (2008) welded specimens: (a) energy per cycle and (b) accumulated energy per cycle.

3.4.4. Comparison with design methods

Tables 3.11 and 3.12 summarize the predicted and observed plastic mechanism modes and failure modes, according to EC3-1-8 and Piluso *et al.* (2001a) proposal, respectively, see Section 2.7.2.1. The B series from Oliveira *et al.* (2021) experimental campaign is the only case where the observed experimental behaviour differs from plastic mechanism mode predicted by EC3-1-8. On the other hand, all specimens exhibit the predicted failure mode according to Piluso *et al.* (2001a) proposal.

The force-deformation behaviour of the tested specimens is compared with EC3-1-8 predictions for elastic stiffness and plastic resistance in Tables 3.13 to 3.15. The elastic stiffness $K_{\mathrm{ini,exp}}$ was computed by means of a regression line of the initial loading branch of the monotonic behaviour and the linear portion of the second ascending branch of the cyclic behaviour. By comparing the results, there is an average ratio between the EC3 predictions and the experiments of 1.9 and 3.2 for A and B series, respectively, and 1.4 for C series. Eurocode prediction considerably overestimates the initial stiffness. In addition, the reference strength F_0 – an input parameter of the MRA model – is compared with $F_{T,Rd}$ determined by method 1 (M1) and 2 (M2) according to EC3 (M2 considers the influence of the bolt action). Both predictions proposed by the Eurocode present accurate results. The remaining characteristics of the force-deformation response, namely the post-limit stiffness and the deformation capacity, cannot be compared with any code provisions since it does not cover the post-limit behaviour.

Table 3.11 – Predicted and observed plastic mechanism modes and failure modes: A and B series.

		plastic mechanism formation mode			failure mode (analytical)			failure mode (experimental)
author	T-stub ID	β_{Rd}	$\beta_{Rd,\mathrm{lim}}$	mode	β_u	$\beta_{u,\mathrm{lim}}$	mode	mode
Oliveira *et al.* (2021)	A1	0.174	0.606	1	0.244	0.467	1	1
	A2	0.185	0.605	1	0.259	0.466	1	1
	A4	0.188	0.610	1	0.264	0.471	1	1
	A5	0.179	0.600	1	0.251	0.463	1	1
	A6	0.181	0.598	1	0.253	0.461	1	1
	A7	0.178	0.605	1	0.250	0.467	1	1
Piluso and Rizzano (2008)	A1	0.380	0.669	1	0.496	0.505	1	1
	A3	0.387	0.671	1	0.505	0.506	1	*
	A4	0.388	0.668	1	0.504	0.504	1	*
	A6	0.377	0.668	1	0.497	0.505	1	*
	A7	0.385	0.669	1	0.503	0.505	1	*
Oliveira *et al.* (2021)	B1	0.541	0.684	1	0.746	0.573	2	2
	B2	0.546	0.679	1	0.754	0.570	2	2
	B3	0.551	0.683	1	0.760	0.573	2	2
	B4	0.574	0.687	1	0.793	0.576	2	2
	B5	0.546	0.680	1	0.754	0.571	2	2
	B7	0.556	0.687	1	0.768	0.576	2	2
Piluso and Rizzano (2008)	B1	0.687	0.669	2	1.120	0.502	2	2
	B4	0.682	0.670	2	1.114	0.502	2	*
	B5	0.700	0.669	2	1.143	0.502	2	*
	B6	0.677	0.671	2	1.105	0.503	2	*
	B7	0.689	0.670	2	1.129	0.502	2	*

*described in section 3.4

Table 3.12 – Predicted and observed plastic mechanism modes and failure modes: C series.

		plastic mechanism formation mode			failure mode (analytical)			failure mode (experimental)
author	T-stub ID	β_{Rd}	$\beta_{Rd,\mathrm{lim}}$	mode	β_u	$\beta_{u,\mathrm{lim}}$	mode	mode
Piluso and Rizzano (2008)	C1	0.270	0.666	1	0.449	0.544	1	1
	C3	0.258	0.658	1	0.429	0.540	1	*
	C4	0.260	0.657	1	0.432	0.539	1	*
	C6	0.261	0.656	1	0.433	0.539	1	*
	C7	0.258	0.655	1	0.428	0.538	1	*

Table 3.13 – EC3 predictions of initial stiffness and plastic resistance: A series.

		experimental		EC3-1-8			ratios		
author	T-stub ID	$K_{0,\mathrm{exp}}$	$F_{0,\mathrm{exp}}$	$K_{\mathrm{eq,EC3}}$	$F_{T,Rd}$ (M1)	$F_{T,Rd}$ (M2)	$\frac{K_{\mathrm{eq,EC3}}}{K_{0,\mathrm{exp}}}$	$\frac{F_{T,Rd}}{F_{0,\mathrm{exp}}}$	$\frac{F_{T,Rd}}{F_{0,\mathrm{exp}}}$
		kN/mm	kN	kN/mm	kN	kN	-	(M1)	(M2)
Oliveira *et al.* (2021)	A1	67	103	84	77	93	1.25	0.74	0.90
	A2	41	96	91	81	99	2.22	0.85	1.04
	A4	42	94	94	83	101	2.22	0.88	1.07
	A5	55	84	86	79	96	1.56	0.94	1.14
	A6	60	93	86	80	97	1.43	0.86	1.04
	A7	37	83	86	79	95	2.35	0.95	1.15
Piluso and Rizzano (2008)	A1	135	136	232	134	167	1.72	0.98	1.23
	A3	113	124	240	137	170	2.13	1.10	1.37
	A4	110	126	237	137	170	2.15	1.09	1.35
	A6	119	126	227	133	165	1.91	1.05	1.31
	A7	94	128	235	136	169	2.49	1.06	1.32
						μ	1.9	1.0	1.2
						σ	0.4	0.1	0.1

Table 3.14 – EC3 predictions of initial stiffness and plastic resistance: B series.

author	T-stub ID	experimental		EC3-1-8			ratios		
		$K_{0,\text{exp}}$	$F_{0,\text{exp}}$	$K_{\text{eq,EC3}}$	$F_{T,Rd}$ (M1)	$F_{T,Rd}$ (M2)	$\frac{K_{\text{eq,EC3}}}{K_{0,\text{exp}}}$	$\frac{F_{T,Rd}}{F_{0,\text{exp}}}$	$\frac{F_{T,Rd}}{F_{0,\text{exp}}}$
		kN/mm	kN	kN/mm	kN	kN	-	(M1)	(M2)
Oliveira *et al.* (2021)	B1	70	239	304	238	273	4.31	1.00	1.14
	B2	98	263	304	241	276	3.10	0.92	1.05
	B3	135	274	311	243	278	2.31	0.88	1.01
	B4	89	241	328	253	290	3.70	1.05	1.21
	B5	115	262	305	241	276	2.64	0.92	1.06
	B7	106	262	317	245	281	3.00	0.94	1.07
Piluso and Rizzano (2008)	B1	145	214	560	238	238	3.86	1.11	1.11
	B4	189	203	556	237	237	2.95	1.17	1.17
	B5	178	205	568	239	239	3.19	1.16	1.16
	B6	196	212	557	237	237	2.84	1.12	1.12
	B7	204	212	563	238	238	2.76	1.12	1.12
						μ	3.2	1.0	1.1
						σ	0.6	0.1	0.1

Table 3.15 – EC3 predictions of initial stiffness and plastic resistance: C series.

author	T-stub ID	experimental		EC3-1-8			ratios		
		$K_{\text{ini,exp}}$	$F_{0,\text{exp}}$	$K_{\text{eq,EC3}}$	$F_{T,Rd}$ (M1)	$F_{T,Rd}$ (M2)	$\frac{K_{\text{eq,EC3}}}{K_{\text{ini,exp}}}$	$\frac{F_{T,Rd}}{F_{0,\text{exp}}}$	$\frac{F_{T,Rd}}{F_{0,\text{exp}}}$
		kN/mm	kN	kN/mm	kN	kN	-	(M1)	(M2)
Piluso and Rizzano (2008)	C1	50	116	117	95	111	2.3	0.83	0.96
	C3	101	109	105	91	106	1.0	0.84	0.97
	C4	101	104	105	92	107	1.0	0.88	1.03
	C6	115	112	105	92	107	0.9	0.82	0.96
	C7	59	105	103	91	106	1.8	0.87	1.01
						μ	1.4	0.85	0.99
						σ	0.5	0.02	0.03

3.5. Main phenomena to account for by the hysteretic model

An “ideal” hysteretic behaviour is characterized by stable loops with large energy dissipation. Accordingly, it has no pinching nor degradation and is characterized by identical ascending and descending branches. An “ideal” hysteretic behaviour for constant amplitude (CA) cyclic loading, is represented in Figures 3.29(a) and 3.29(b), and for amplitude (VA) cyclic loading in Figures 3.29(c) to 3.29(f).

However, as shown in previous sections, the cyclic behaviour of a bolted T-stub strongly deviates from an ideal hysteretic behaviour. Hence, it is necessary to identify the phenomenon responsible for these deviations and adopt a hysteretic model that can replicate them. The analysis of the experimental results, illustrated with some results in Figure 3.29, allows to identify these phenomena, as follows:

- stiffness degradation: reduction of stiffness as the number of the cycle increases
    - initial stiffness degradation (reduction of the slope of the linear behaviour at the beginning of each branch) is observed mainly in CA tests, see Figures 3.29(a) and 3.29(b);
    - progressive reloading stiffness degradation (every time the force-deformation curve crosses the horizontal axis).
- stiffness hardening: progressive increase of stiffness as the number of cycles increase – observed in the unloading branch (compression) in CA and VA tests, more pronounced in preloaded specimens.

- strength degradation in all cycles for CA tests (and in the last cycles for variable amplitude tests signalizing the collapse), see Figures 3.29(c) to 3.29(f);
- slip before reloading (a branch with zero stiffness and axial force equal to zero): is observed in specimens with bolt preloading failing under FM2, see Figures 3.29(b) and 3.29(d);
- slip after load reversal from tension to compression (reduction of stiffness after reloading in the descending branch, i.e. compression): is observed in specimens without bolt preloading, see Figures 3.29(e) and 3.29(f).
- pinching: hysteretic loops passing closer to the horizontal axis when the direction of the load is reversed, moving further away from the hysteretic behaviour of an ideal dissipative system; the curvature of the branch changes from single curvature to double curvature:
    - pinching is observed immediately after the first load cycle;
    - pinching phenomena increases with the increase of the number of cycles.
- the shape of the curve is influenced by the loading protocol, the presence or not of the bolt preloading and the failure mode observed.

Table 3.16 summarizes the phenomenon that characterize a cyclic behaviour of coupled T-stubs according to (i) the observed failure mode – FM1 or FM2, (ii) the presence or not of bolt preloading and (iii) the loading protocol applied – constant amplitude (CA) or variable amplitude (VA).

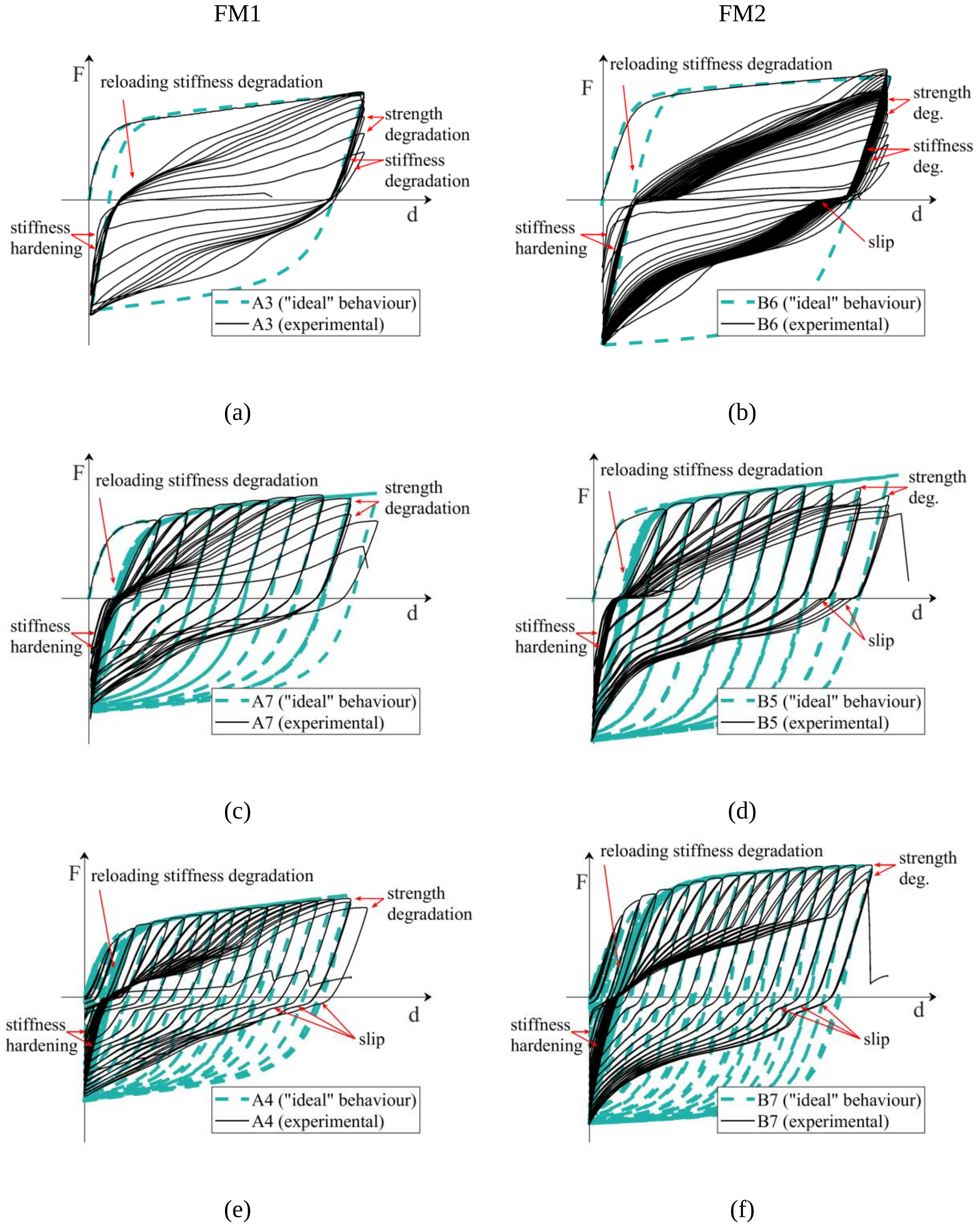

Figure 3.29 – Qualitative assessment of cyclic tests: (a)-(b) preloaded tested under CA, (c)-(d) preloaded tested under VA and (e)-(f) non-preloaded tested under VA (adapted from Oliveira *et al.* (2021) and Piluso and Rizzano (2008)).

Table 3.16 – Qualitative assessment of T-stubs cyclic behaviour.

failure mode	FM1			FM2		
bolt preloading	w/		w/o	w/		w/o
amplitude	CA	VA	VA	CA	VA	VA
stiffness deg. (tension)	✓	×*	×*	✓	×*	×*
stiffness hard. (compression)	✓	✓	✓	✓	✓	✓
strength deg.	✓	×*	×*	✓	×*	×*
reloading stiffness deg.	✓	✓	✓	✓	✓	✓
slip	×	×	✓	✓	✓	✓

*in the last cycles identifying collapse

3.6. Concluding remarks

Chapter 3 was dedicated to the experimental assessment of the monotonic and cyclic behaviour of T-stubs.

An experimental campaign was conducted on 14 T-stubs at University of Coimbra. Additionally, tensile tests on coupons were performed in order to characterize the mechanical behaviour of steel. The experiments presented above can be regarded as a reliable database for the characterization of bolted T-stubs.

Available experiments by Piluso and Rizzano (2008) on the same topic were collected and presented to complement the experimental campaign at University of Coimbra.

The two experimental campaigns cover rolled and welded T-stub compositions, two distinct failure modes (FM1 and FM2) and four loading protocols – monotonic and variable amplitude cyclic tests at University of Coimbra (C1 and C2) and variable and constant amplitude cyclic tests by Piluso and Rizzano (CA and VA).

A quantitative and a qualitative analysis of the T-stub behaviour was performed to provide a better understanding of their cyclic behaviour and to identify governing physical phenomena. The following issues were addressed making use of the experimental campaign results:

- the assessment of the criteria for identification of the failure modes: the experimental tests have confirmed the location of the yield lines developed in the T-stub with reference to the ultimate conditions according the prediction proposed by Piluso *et al.* (2001a, 2001b);
- the evolution of the mechanical properties under cyclic conditions, in particular the peak force, the initial stiffness, the post-limit behaviour and the hysteretic energy dissipation;
- the governing physical phenomena under cyclic conditions were identified, namely strength degradation, initial stiffness degradation, initial stiffness hardening in unloading branches (compression), slip and pinching;
- the influence of bolt preloading, loading protocol and the observed failure modes over the mechanical properties under cyclic conditions was identified.

The information gathered from these experimental campaigns provide solid information about the cyclic behaviour of T-stubs required to develop mechanical models to characterize this component in the cyclic component model framework.

4 CYCLIC MODELLING OF T-STUBS: GLOBAL MODELS

4.1. Introduction

The characterization of the cyclic behaviour of the T-stub, one of the components required to feed the CCM, by means of experimental tests was tackled in the previous chapter. To predict the cyclic behaviour of a SBCJ through the modelling of the cyclic response of each basic component, models for the cyclic behaviour of the components are required. Two approaches available in technical literature regarding the modelling of the cyclic behaviour of T-stubs are addressed in this chapter: (i) a semi-analytical model with empirical parameters calibrated on the basis of experimental tests and (ii) a mathematical model based on curve fitting of experimental curves. Both approaches provide a complete definition of the force-deformation response of the T-stub. Accordingly, first, existing semi-analytical models from the literature to predict the behaviour of T-stubs are discussed and applied. Then, the MRA model, a multi-parameter mathematical model able to reproduce the range of hysteretic behaviours (stiffness and strength degradation, pinching effect and hardening), whose capability of reproducing the hysteretic behaviour of steel joints was already validated in the literature, is also applied to T-stubs.

The main purpose of the work developed in the current chapter is: (i) to provide evidence that the MRA model can provide a superior procedure to capture and model the complex cyclic behaviour of T-stubs and (ii) to define a suitable range of parameters needed to feed the MRA model for T-stubs so that these parameters can be used to compute manually and compared with the ones computed in the next chapter for the decoupled T-stub model.

4.2. Available analytical models

4.2.1. Initial stiffness

Faella *et al.* (1998b) presented a formulation to evaluate the initial stiffness of non-preloaded and preloaded T-stubs which was adopted in the model for T-stubs monotonic behaviour by Piluso *et al.* (2001a, 2001b), hereinafter referred as PFR model, and in the model for T-stubs cyclic behaviour by Piluso and Rizzano (2008), hereinafter referred as PR model, see Section 2.7.2.2. Table 4.1 summarizes the predicted initial stiffness of non-preloaded T-stubs computed according to Faella *et al.* (1998a, 2000), see Section 2.7.2.2. Results computed considering the conventional location of the restraining line, m, are compared with the ones computed adopting the proposal for m', see Eq. (2.32). In addition, the predicted values are compared with the experimental ones. Adopting the ζ coefficient – see Eq. (2.33) – in predicting the stiffness of tested specimens, improves the accuracy in terms of average value and of coefficient of variation. However, it worsens the overestimation for FM1 specimens (A series). Table 4.2 summarizes the predicted initial stiffness of preloaded T-stubs. Results computed neglecting the bolt preloading – see Eqs. (2.24) and (2.25) – are compared with the ones accounting the bolt preloading – Eqs. (2.29) and (2.30). The conventional location of the restraining line was computed according to m' – see Eq. (2.32). PFR model predictions accounting bolt preloading considerably overestimates the initial stiffness with an average ratio of 2.1. Neglecting the bolt preloading, the model underestimates the initial stiffness for FM1 and overestimates for FM2 providing an average ratio of 1.2. Therefore, these predictions will be considered in the application of the PFR and PR models.

Table 4.1 – Prediction of initial stiffness of non-preloaded T-stubs: comparison between experimental results and PFR model (2001a, 2001b).

T-stub ID	$K_{0,\mathrm{exp}}$ kN/mm	prediction with $\zeta = 0.8$ $K_{0,\mathrm{PFR\ model}}$ kN/mm	prediction with $\zeta = 0.8$ $\frac{K_{0,\mathrm{PFR\ model}}}{K_{0,\mathrm{exp}}}$	prediction with ζ as Eq. (2.32) $K_{0,\mathrm{PFR\ model}}$ kN/mm	prediction with ζ as Eq. (2.32) $\frac{K_{0,\mathrm{PFR\ model}}}{K_{0,\mathrm{exp}}}$
A2	41	52	1.26	57	1.40
A4	42	53	1.26	59	1.39
A7	37	49	1.33	55	1.51
B1	70	186	2.65	149	2.12
B2	98	187	1.91	149	1.52
B7	106	196	1.85	154	1.46
		μ	1.7	μ	1.6
		σ	0.5	σ	0.3

Table 4.2 – Prediction of initial stiffness of preloaded T-stubs: comparison between experimental results and PFR model (2001a, 2001b).

T-stub ID	$K_{0,\mathrm{exp}}$ kN/mm	neglecting bolt preloading $K_{0,\mathrm{PFR\ model}}$ kN/mm	neglecting bolt preloading $\frac{K_{0,\mathrm{PFR\ model}}}{K_{0,\mathrm{exp}}}$	accounting bolt preloading $K_{0,\mathrm{PFR\ model}}$ kN/mm	accounting bolt preloading $\frac{K_{0,\mathrm{PFR\ model}}}{K_{0,\mathrm{exp}}}$
A1	67	55	0.82	133	1.98
A5	55	55	1.01	132	2.41
A6	60	55	0.92	131	2.19
B3	135	152	1.13	224	1.66
B4	89	159	1.80	231	2.61
B5	115	154	1.34	221	1.91
		μ	1.2	μ	2.1
		σ	0.3	σ	0.3

4.2.2. Monotonic behaviour

Force-deformation curves of the tested specimens were simulated by means of the analytical model presented by Piluso *et al.* (2001a, 2001b) (PFR model), described in section 2.7.2.2, considering the material constitutive behaviour and the geometrical properties of tested specimens.

a) Material constitutive behaviour

Regarding the material properties, tensile tests have been carried out to evaluate the true stress – true strain curve of the T-stub flanges, as described in section 3.2.

The experimental curve has been represented by means of a quadrilinear model, see Figure 2.33(a). The characteristic values of the multilinear modelling of true stress – true strain curve for each coupon of HEA 200 flange and HEB 280 flange, as well as the main values A and B, respectively, are summarized in Table 4.3.

As an example, Figure 4.1 shows the engineering stress – engineering strain curve, true stress – true strain curve and the corresponding quadrilinear approximations for two coupons, one of HEA 200 flange and another of HEB 280 flange. As already mentioned, the differences in the ultimate strain from the experimental true-stress – true strain relation and the model are expected because the fracture of the coupons was outside the instrumented region of the coupons.

Figure 4.2 shows the quadrilinear modelling of the true stress – true strain curve (mean values) for HEA 200 flange and HEB 280 flange.

Table 4.3 – Characteristic values of the multilinear modelling of true stress – true strain curve.

coupon ID	ε_y -	ε_h -	ε_u -	ε_f -	f_y MPa	f_u MPa	f_f MPa	E GPa
C04	0.0017	0.019	0.153	0.777	362	600	855	210
C06	0.0018	0.015	0.140	0.691	382	612	819	210
C09	0.0018	0.021	0.161	0.77	375	603	850	210
A	0.0018	0.018	0.151	0.746	373	605	842	210
C10	0.0016	0.017	0.165	1.027	330	561	925	210
C11	0.0016	0.021	0.183	0.661	345	577	647	210
C12	0.0016	0.020	0.177	0.724	335	575	690	210
B	0.0016	0.019	0.175	0.804	336	571	754	210

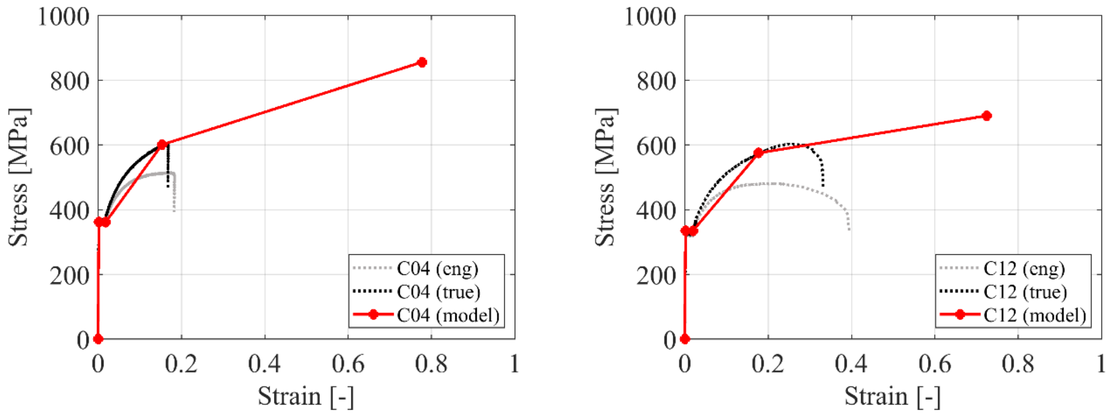

(a)

(b)

Figure 4.1 – Modelling of the true stress – true strain curve for coupon (a) C04 and (b) C12.

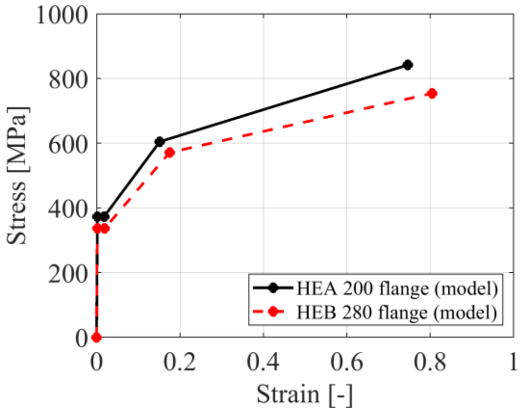

Figure 4.2 – Modelling of the true stress – true strain curve (mean values) for HEA 200 flange and HEB 280 flange.

b) Force-deformation curve

The predicted failure mode corresponds to the ones identified for the experimental results, i.e. FM1 for A series specimens and FM2 for B series specimens – see Figure 3.8. For all specimens tested under monotonic loading, the multilinear model and the experimental curve of the force-deformation curve are compared in Figure 4.3. The comparison shows a good agreement in terms of stiffness, resistance and deformation capacity. However, the prediction of the ultimate deformation and resistance of B series specimens is about 40% greater than the observed experimentally.

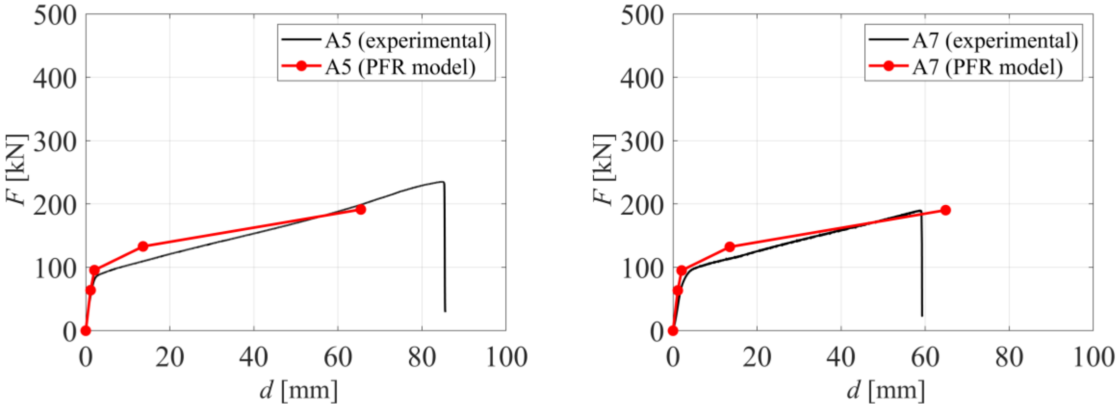

(a) w/ preloading (b) w/o preloading

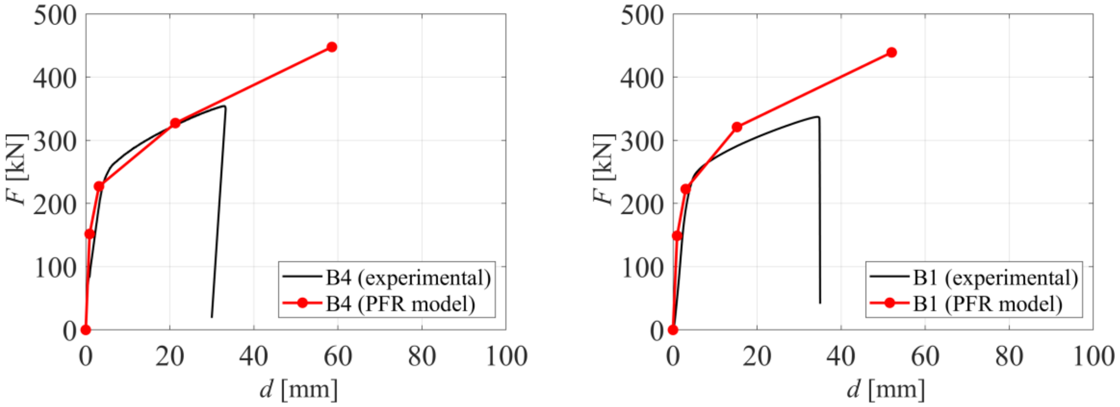

(c) w/ preloading (d) w/o preloading

Figure 4.3 – Comparison between experimental results and PFR model.

4.2.3. Cyclic behaviour

Once the monotonic behaviour has been predicted, the cyclic behaviour was derived according to the analytical model proposed by Piluso and Rizzano (2008) (PR model) described in Section 2.7.3. In PR model, the procedure is applicable for constant and variable deformation amplitude (CA and VA, respectively). However, the description of the procedure by Piluso and Rizzano (2008) addresses only CA loading protocols. As the experimental campaign conducted at University of Coimbra – see Section 3.2 – was addressed for VA loading protocols, the following assumptions were adopted (see Figure 4.4) in the application of the PR model for VA loading protocols:

- first cycles with low deformation amplitude the dissipated energy is very small – see Section 0, therefore it is assumed that there is no stiffness nor strength degradation and cyclic behaviour is assumed linear;
- d_{max} is variable and equal to the deformation amplitude corresponding to the loading protocol in each cycle;
- the unloading branch (tension) has a slope of K_0;
- $\tan \alpha = \frac{F_{\mathrm{max}}}{d_{\mathrm{A}} - \frac{F_{\mathrm{max}}}{K_0}}$ since the deformations d_{A} and d_{max} are variable.

Regarding FM1 specimens, the cyclic model and the experimental force-deformation curve are compared in Figure 4.5. The comparison shows in general good agreement. However, for specimens without preloading the model fails to reproduce accurately the pinching effect, see Figures 4.5(b) and 4.5(d). In addition, the monotonic multilinear model is compared to the upper bound of the cyclic force-deformation curve showing good agreement in terms of initial stiffness and resistance but fails to determine the deformation capacity as observed previously.

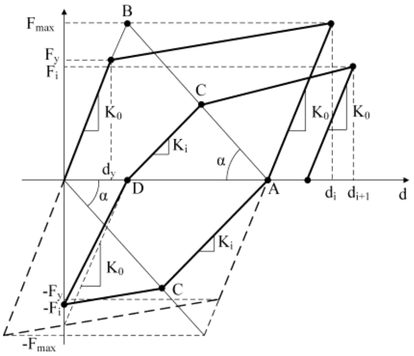

Figure 4.4 – Cyclic model for FM1 for VA.

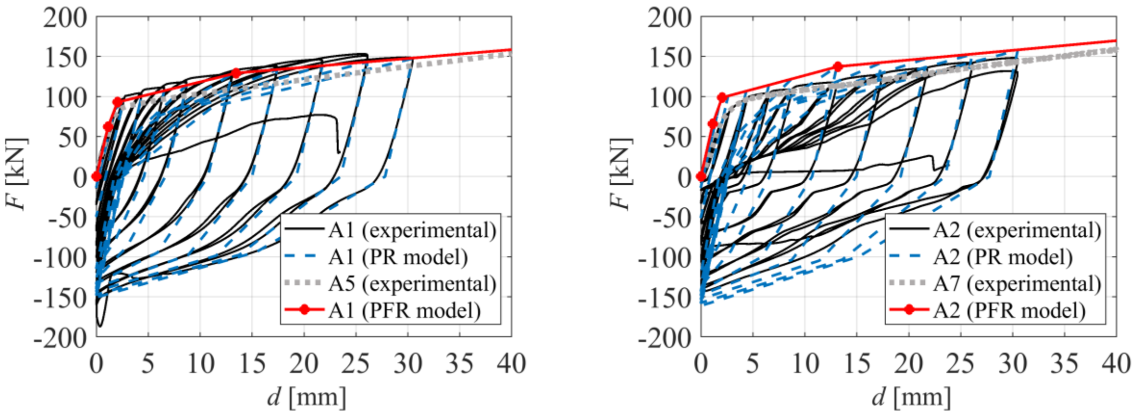

(a) load. protocol C1 – w/ preloading (b) load. protocol C1 – w/o preloading

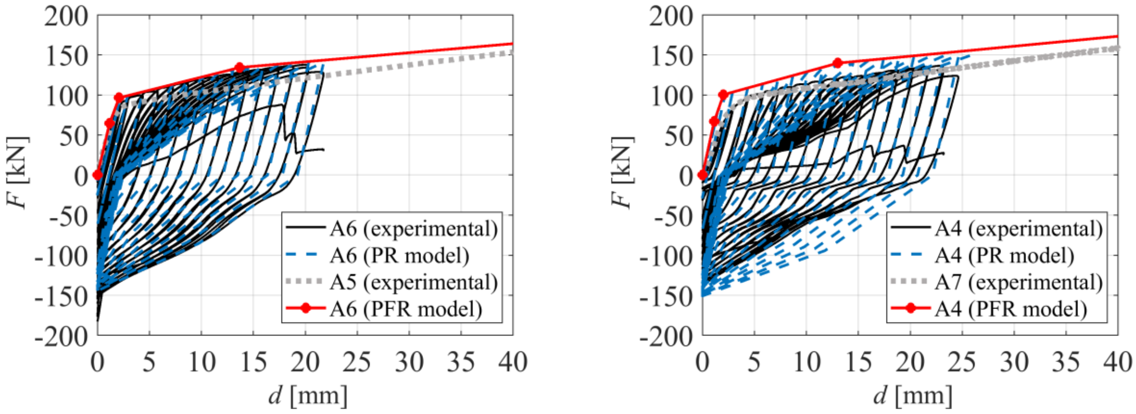

(c) load. protocol C2 – w/ preloading (d) load. protocol C2 – w/o preloading

Figure 4.5 – Comparison between experimental results and PR model for FM1 specimens.

For FM2 specimens, the cyclic model and the experimental force-deformation curve are compared in Figure 4.6. The comparison shows that the model fails to reproduce the pinching effect for specimens with and without preloading. For specimens tested with loading protocol C1, the slip presents high values when compared with the experimental curve. On the other hand, for specimen tested under loading protocol C2 presents the slip in the opposite direction. In addition, the initial stiffness K_0 computed according to the monotonic multilinear model is not sufficiently accurate, as can be observed in every unloading branch up to the horizontal axis.

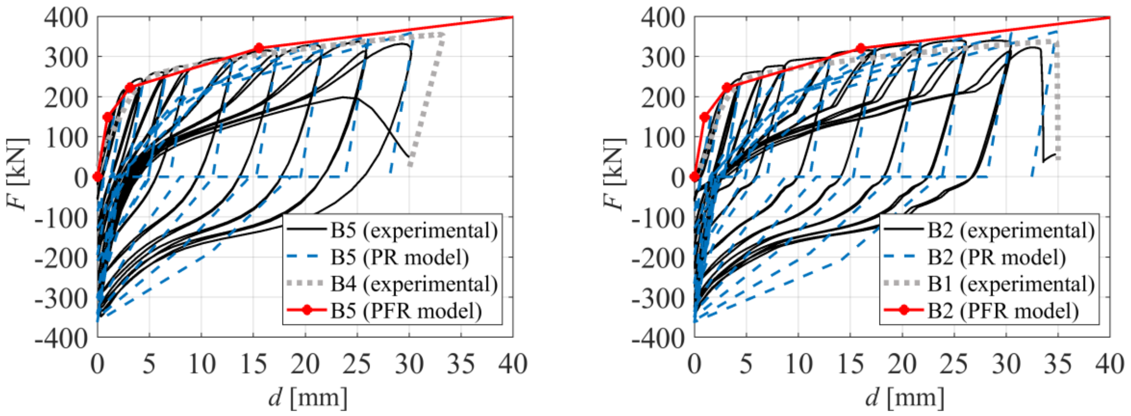

(a) load. protocol C1 – w/ preloading (b) load. protocol C1 – w/o preloading

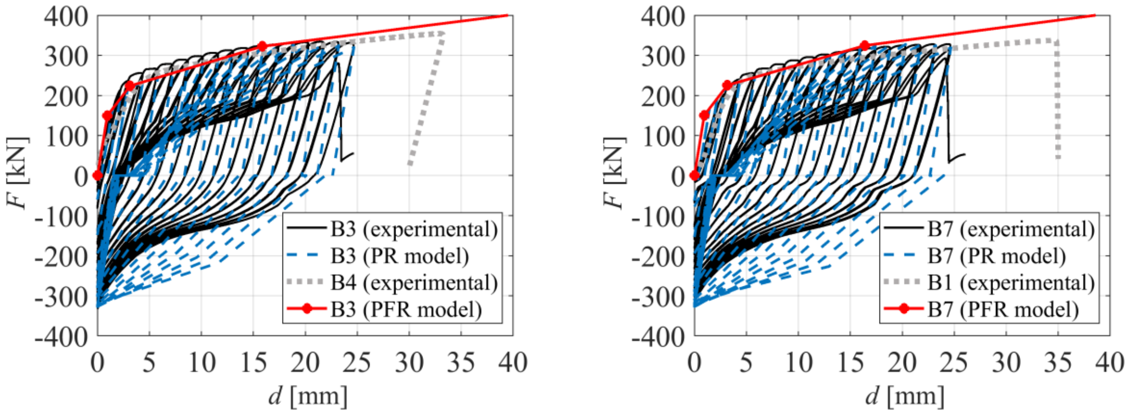

(c) load. protocol C2 – w/ preloading (d) load. protocol C2 – w/o preloading

Figure 4.6 – Comparison between experimental results and PR model for FM2 specimens.

The cyclic model is also assessed in terms of hysteretic energy dissipation. In Figure 4.7, the results are compared against experimental results. The comparison shows that the model strongly overestimates the energy dissipation for high amplitude cycles in FM2 and for preloaded bolts in FM1 (T-stubs A2 and A4), as a consequence of the misfit of the pinching level, which is higher than the experimental results.

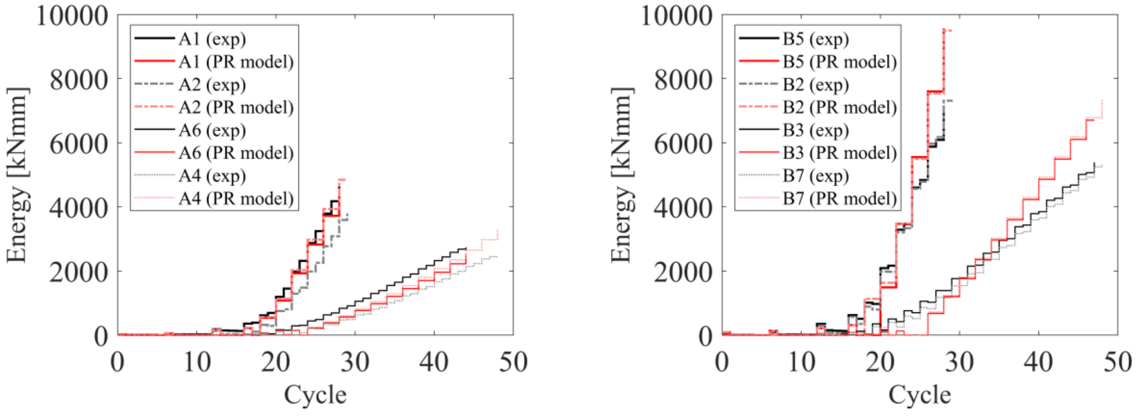

(a) (b)

Figure 4.7 – Hysteretic dissipation energy per cycle: comparison between PR model and experimental results.

4.3. Computation of MRA parameters

4.3.1. Introduction

The calibration, i.e. the definition of the set of parameters to be inserted in the MRA model to fit the response of experimental tests as close as possible, was performed using MultiCal software (Chisari *et al.*, 2017). MultiCal is a tool for the automatic calibration of hysteretic structural models. It finds the parameter set of a given model fitting best multiple experimental curves in the framework of multi-objective optimization managed by Genetic Algorithms. This software uses external software packages, such as, the MRA model implemented in

SeismoStruct (2016) by Nogueiro *et al.* (2007). The operation of MultiCal and the calibrations procedure goes as follows:

- launch MultiCal with a Command Prompt;
- experimental curves are provided in .csv files – the deformation history will be used as input for the numerical model, and corresponding to that, a numerical force history will be computed;
- selection of a hysteretic model (MRA model in the current case);
- MultiCal is equipped with a pre-processor facility to create template optimization files without running the calibration analysis; this feature enables the user to quickly prepare template input files for the solver; a set of three .txt files are generated which allows the user to define:
    - the population size and the number of generations of the Genetic Algorithm – number of experiments, offspring population size and number of generations;
    - the parameters related to the hysteretic model selected – to enable the calibration of a given parameter a range of values must be defined, to disable a constant value must be set;
    - the output variables to extract and objectives to minimise: stress history, energy history and envelope curve;

- The multi-objective discrepancy minimization is carried out by means of Genetic Algorithms, and in particular Non-dominated Sorting Genetic Algorithm II (Deb *et al.*, 2002).

In order to minimize the MRA model misfit to the experimental tests, three criteria were use: (i) energy, (ii) force and (iii) envelope. A set of MRA model parameters (30 parameters – 15 for each branch – being 18 empirical parameters without physical meaning) were calibrated considering the following effects: (i) the pinching effect (ii) stiffness degradation and (iii) strength degradation. The parameters were calibrated for each series of specimens, i.e. for each set with the same geometric and mechanical properties independently of the type of loading protocol or the presence or not of bolt preloading.

4.3.2. Calibration assumptions

For the calibration of the MRA parameters, the following assumptions were considered:

- two of the MRA pinching parameters were made fixed: $t_2 = 0.3$ and $C = 1.0$;
- the initial stiffness K_0, the post-limit stiffness K_{pl} and the resistance F_0 was taken from experimental results as average values of each T-stub series, see Table 4.4; the experimental initial stiffness was considered instead of the value provided by EC3 due to the large discrepancies, see Annex C;
- the lower bound curve is assumed to share some of the same characteristics as the upper one (see Figure 2.10): $K_{0,1}/K_0$, $K_{pl,1}/K_p$ and N_1/N are equal to 1, and $F_{0,1}/F_0$ was calibrated;

- the calibration was enabled by defining a range of values: $t_1 = [0, 30]$, $N = [0.1, 5.0]$ and $F_{0,1}/F_0 = [0,\ 0.50]$; more than one analysis was required to find a good solution where the range of values was shortened by trial and error until the reliable solution was found;
- genetic algorithms parameters: number of experiments = 50, offspring population size = 50 and number of generations = 100 – leading to a total of 5050 solutions (the total analysis time for each T-stub series took about 10 hours);
- the cyclic behaviour of the T-stub was related with its failure mode;

Table 4.4 – Experimental results: average values.

author	series	$\overline{K}_{0a}$ kN/mm	$\overline{K}_{0d}$ kN/mm	$\overline{K}_p$ kN/mm	$\overline{F}_0$ kN
Oliveira *et al.* (2021)	A	53	49	2.1	96
Piluso and Rizzano (2008)	A	109	84	2.8	126
Oliveira *et al.* (2021)	B	113	105	2.9	265
Piluso and Rizzano (2008)	B	192	132	3.5	208
	C	94	70	2.3	107

4.3.3. Calibration of the MRA parameters

Table 4.5 summarizes the MRA parameters calibrated for FM1 and FM2. It can be observed that the specimens that failed according to FM2 present a smaller shaper parameter, since its curve shape is rounder in the knee-range of the global curve, with $N = 1.8$, and for FM1 was obtained $N = [2.4, 3.6]$. Regarding the pinching parameter t_1, its influence on the curve is noticed in the concavity of the branches – for higher values of t_1, more pronounced is the concave shape. Ascending branches present a lower level of pinching than the descending branches, giving the calibration results of $t_{1a} = [4.0, 9.0]$ and $t_{1d} = [5.0, 25.0]$. Taking a closer look to the descending branches, a clear distinction between the pinching level of specimens failing according to FM1 and FM2, is observed, being higher for FM2. Relating these parameters to the respective FM, in particular with the increase of $\overline{\beta_u}/\overline{\beta_{u,lim}}$, the following tends stands out: (i) N decreases; (ii) t_{1a} remains stable within the short range $t_{1a} = [4.0, 9.0]$; and (iii) t_{1d} increases. Nonetheless, a wider sample is required to verify these trends. Apart from the calibration of these empirical parameters, the following ratios were also analysed: $F_{0,\mathrm{l}a}/F_{0a}$ and $F_{0,\mathrm{l}d}/F_{0d}$. The descending branches present higher ratios. However, no trend related to the FM is drawn as for the empirical parameters.

Table 4.5 – MRA parameters calibrated: shape, pinching and ratios.

author	series	$\frac{\overline{\beta_u}}{\overline{\beta_{u,lim}}}$	$N_a = N_d$	t_{1a}	t_{1d}	$\frac{F_{0,\mathrm{l}a}}{F_{0a}}$	$\frac{F_{0,\mathrm{ld}}}{F_{0d}}$
Oliveira *et al.* (2021)	A	0.55	3.6	4.0	5.0	0.05	0.09
Piluso and Rizzano (2008)	C	0.80	2.5	9.0	15.0	0.03	0.30
	A	0.99	2.4	6.0	11.0	0.03	0.34
Oliveira *et al.* (2021)	B	1.33	1.8	5.0	23..0	0.04	0.43
Piluso and Rizzano (2008)	B	2.24	1.8	5.0	25.0	0.03	0.35

Strength and stiffness degradation were mainly observed in constant amplitude cyclic tests, as discussed in Sections 3.4.3.1 and 3.4.3.2, respectively. Table 4.6 summarizes the empirical parameters related to stiffness and strength degradation calibrated for those specimens. These empirical parameters were calibrated individually for each specimen. Calibration results show that the specimens submitted to higher amplitude present higher stiffness and strength degradation coefficients. On the other hand, specimens failing according to FM2 present lower level of stiffness and strength degradation than FM1.

Table 4.6 – MRA parameters calibrated for CA tests: stiffness and strength degradation.

T-stub ID	i_K	i_F	T-stub ID	i_K	i_F	T-stub ID	i_K	i_F
A3	0.012%	0.025%	C3	0.010%	0.035%	B4	0.001%	0.002%
A4	0.008%	0.010%	C4	0.008%	0.025%	B6	0.005%	0.006%
A6	0.010%	0.015%	C6	0.008%	0.030%	B7	0.005%	0.005%

4.3.4. Comparison with experimental results

Figures 4.8 to 4.13 illustrate the force-deformation curves computed using MRA model with parameters calibrated from MultiCal against experimental results. These show a high degree of accuracy of the MRA model in reproducing the cyclic behaviour of a T-stub – the set of parameters calibrated show in general a good fit to the experimental results in terms of force – $r^2 = [0.85, 0.97]$. The pinching effect was successfully reproduced for ascending and descending branches. However, the model does not seem capable of reproducing the slip at reloading and the stiffness and strength degradation observed in constant amplitude cyclic tests. The comparison shows that the case with degradation fails to reproduce the firsts cycles due to the pronounced pinched observed experimentally after the first loading branch. The main reason for this mismatch is the fact that the MRA model considers the pinching parameters – t_1, t_2 and C – as constants, whereas experimental results shows that the ascending and descending branches of constant amplitude tests changes its concavity over the loading history requiring thus the variation of these parameters with the loading history. Moreover, the pinching parameters computed provide a concave upward/downward for ascending/descending branches throughout all the loading history. However, taking as example the ascending branches, their concavity goes through three phases: (i) at the beginning – a concave downward; (ii) half through – nearly linear; and (iii) final stage – a concave upward. This phenomenon is more pronounced in constant amplitude tests due to the large amount of dissipated hysteretic energy since the first loading cycle.

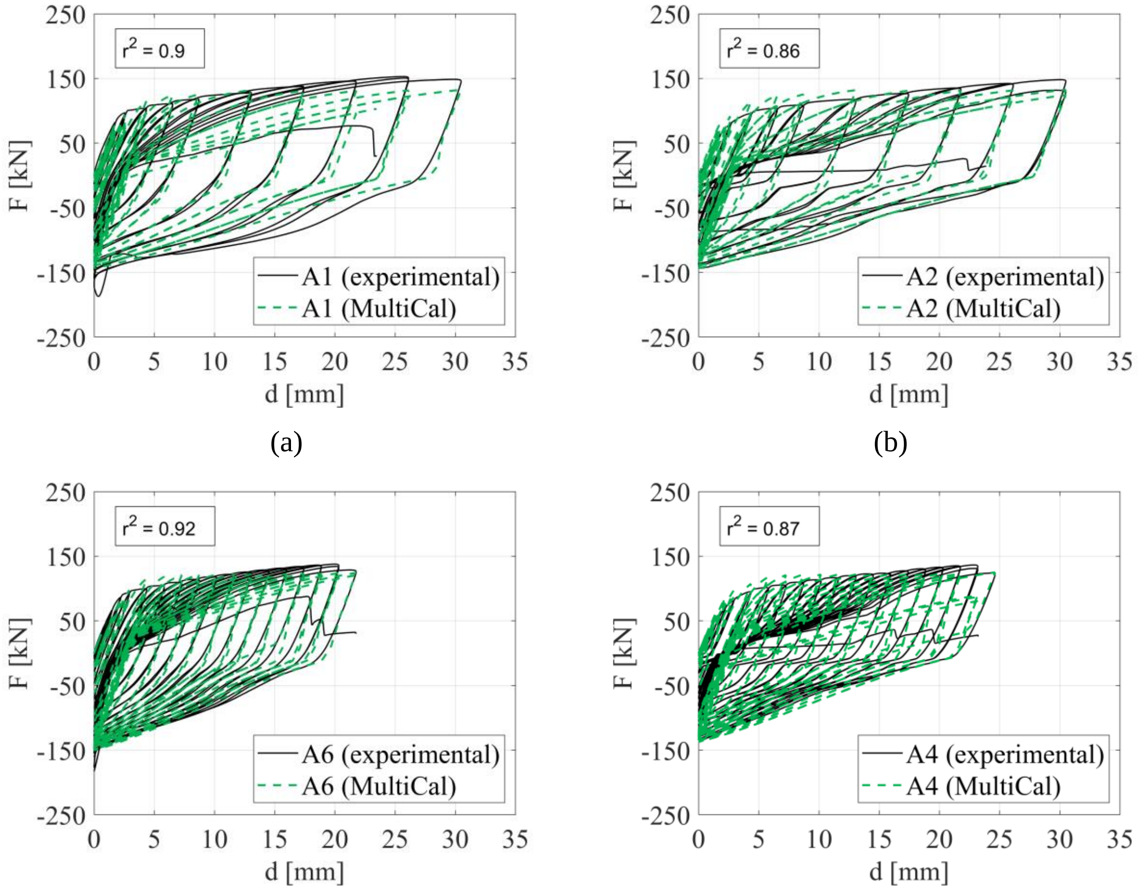

(a) (b)

(c) (d)

Figure 4.8 – Comparison between MRA model (MultiCal) and experimental results from Oliveira *et al.* (2021) rolled specimens failing under FM1.

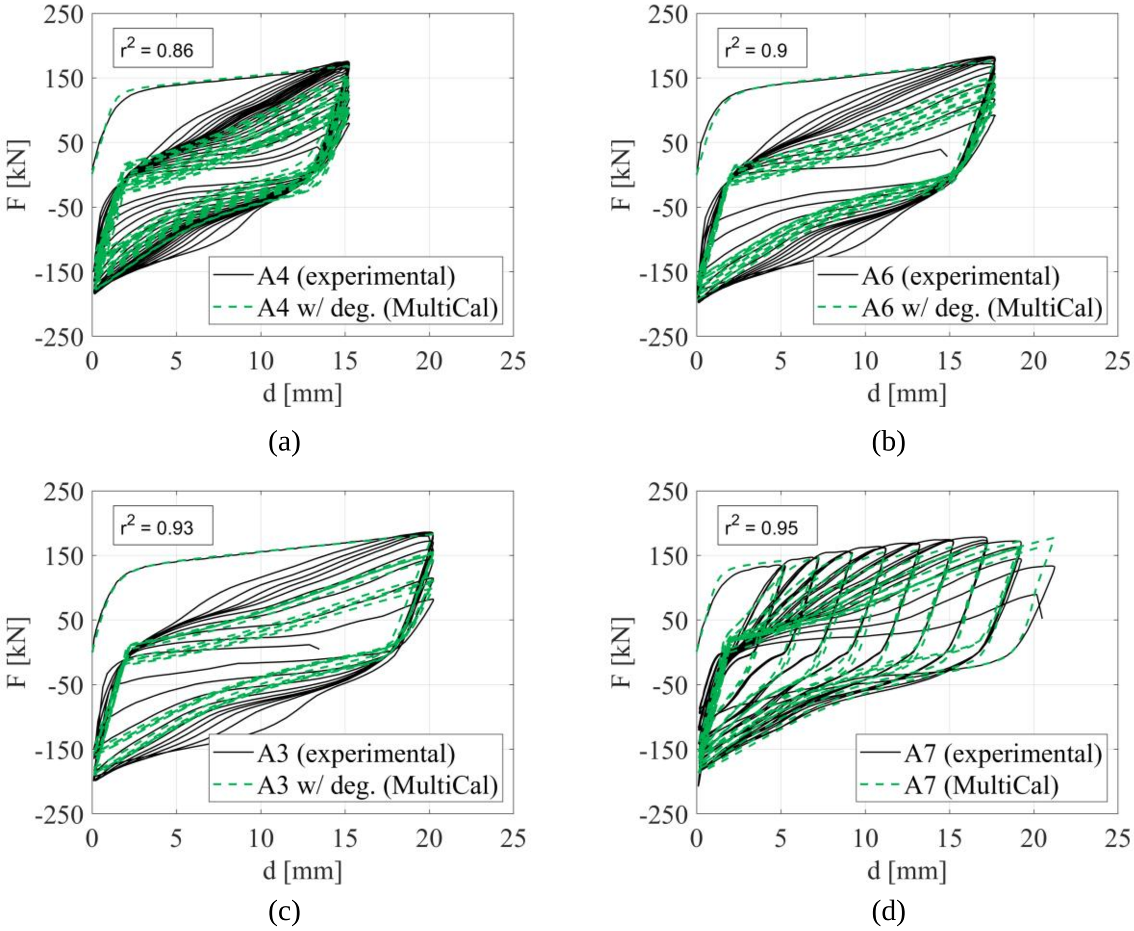

(a) (b)

(c) (d)

Figure 4.9 – Comparison between MRA model (MultiCal) and experimental results from Piluso and Rizzano (2008) rolled specimens failing under FM1.

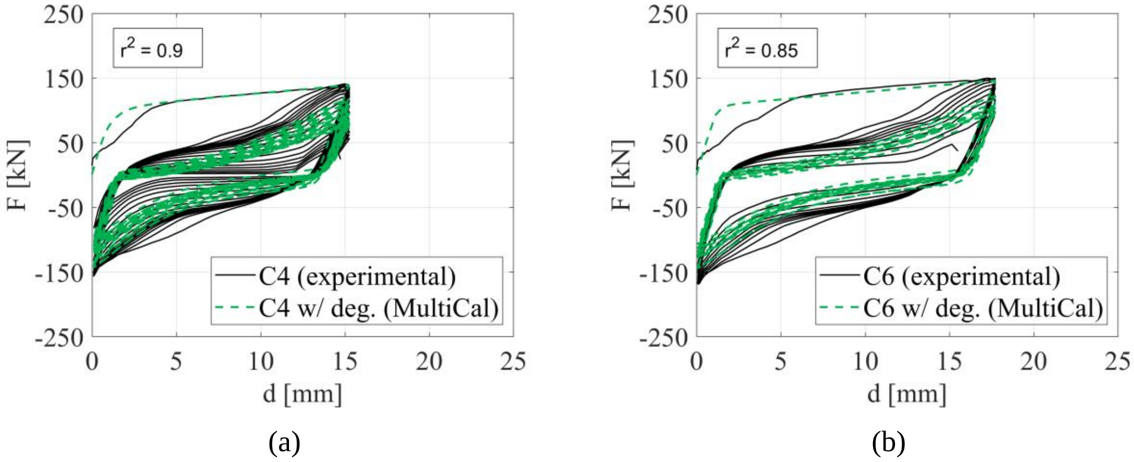

(a) (b)

Figure 4.10 – Comparison between MRA model (MultiCal) and experimental results from Piluso and Rizzano (2008) welded specimens failing under FM1: (a) C4 and (b) C6.

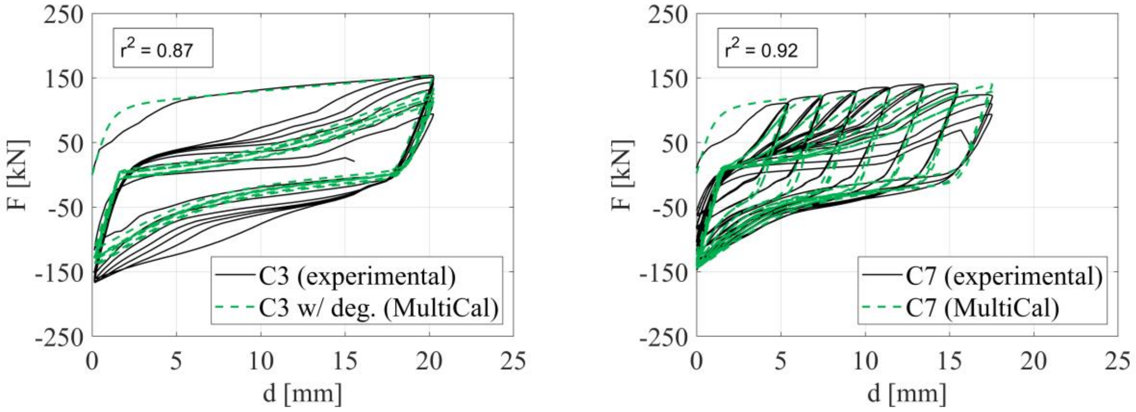

(a) (b)

Figure 4.11 – Comparison between MRA model (MultiCal) and experimental results from Piluso and Rizzano (2008) welded specimens failing under FM1: (a) C3 and (b) C7.

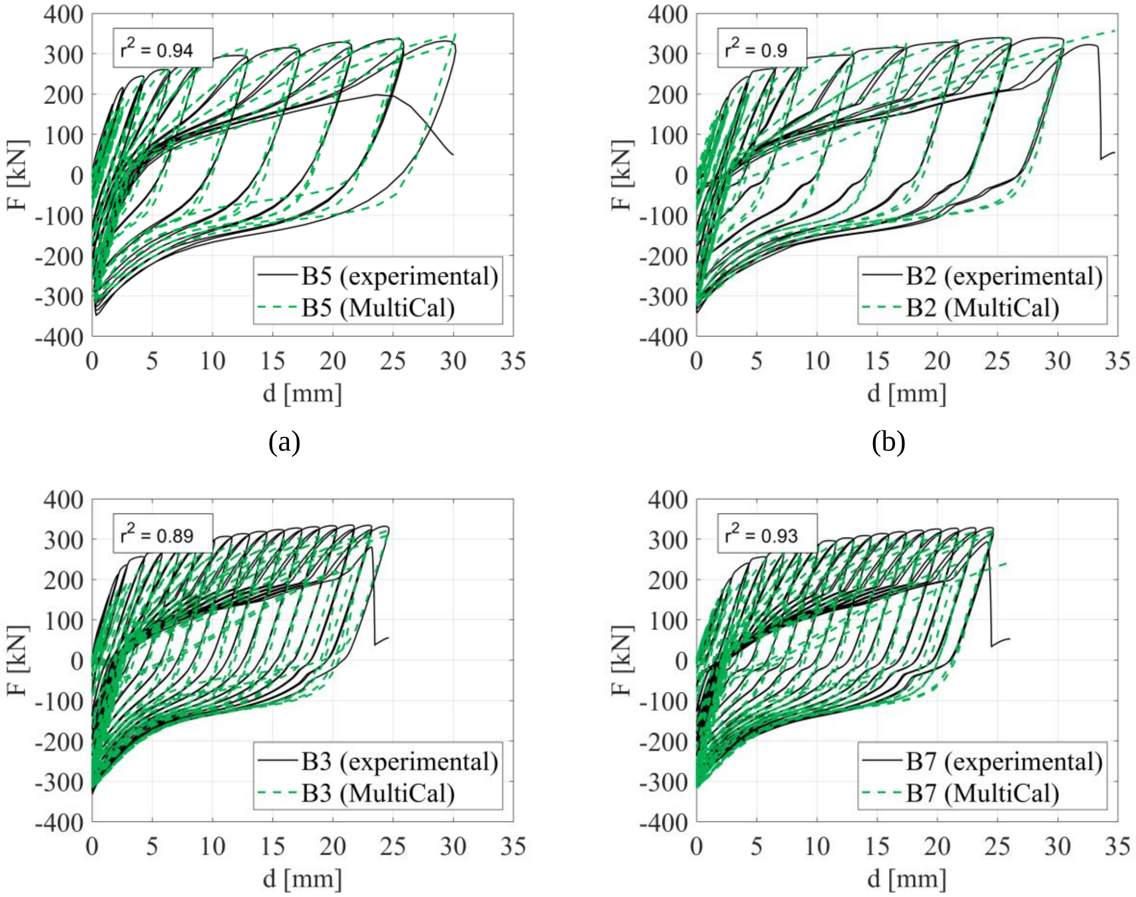

(a) (b)

(c) (d)

Figure 4.12 – Comparison between MRA model (MultiCal) and experimental results from Oliveira *et al.* (2021) rolled specimens failing under FM2.

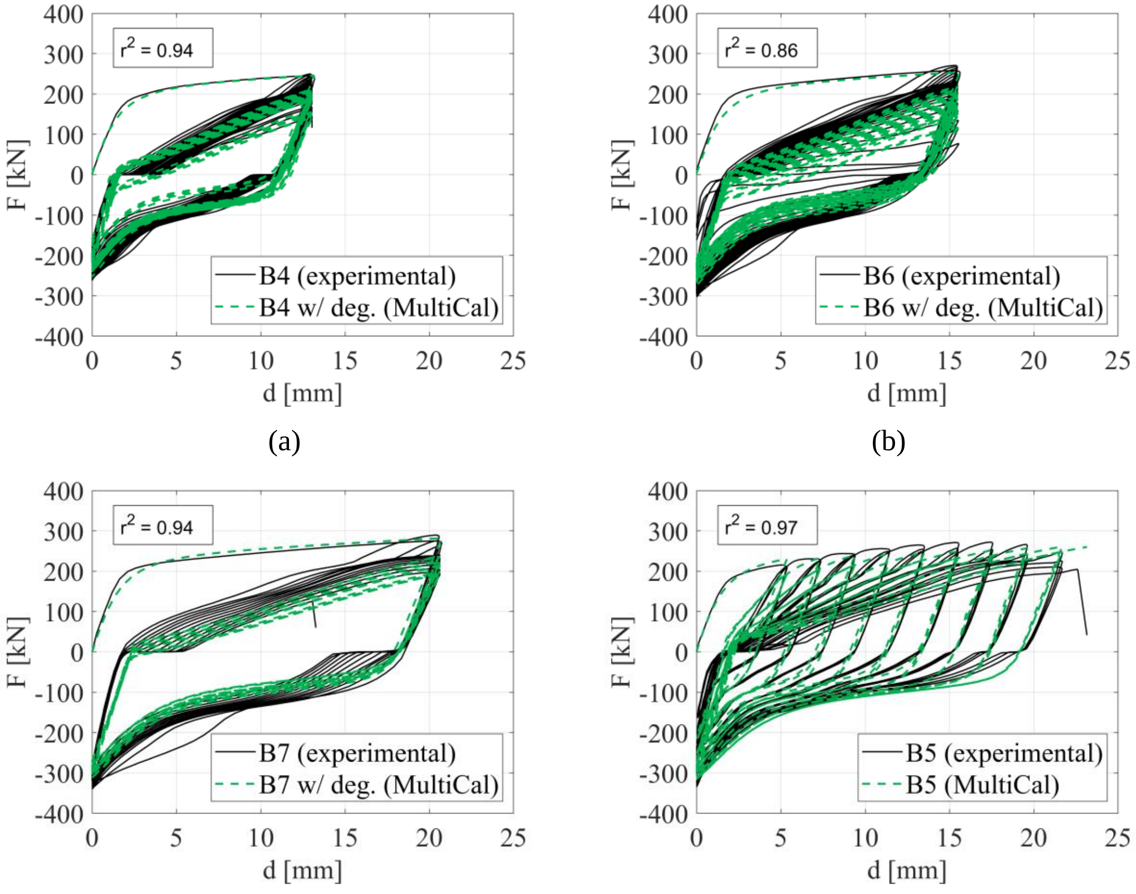

(a) (b)

(c) (d)

Figure 4.13 – Comparison between MRA model (MultiCal) and experimental results from Piluso and Rizzano (2008) rolled specimens failing under FM2.

4.3.5. Sensitivity analysis

The MRA parameters were calibrated for twenty T-stubs (five sets of four T-stubs) with distinct geometry and mechanical properties, bolt pre-loading levels, failure modes, and loading protocols. Within the same failure mode, a set of MRA parameters were obtained for each T-stub series. A clear range of values was observed for each failure mode, where higher values of pinching are achieved for FM2. However, these are empirical parameters and no correlation was found with the geometric properties of the specimens. Therefore, to assess the sensitivity of the T-stubs behaviour to the MRA parameters, a sensitivity analysis (SA) was carried out to test the performance of the mean values of each range. The SA was carried out only for variable amplitude tests, since the MRA model did not reproduce properly the pinching behaviour in the calibration phase for constant amplitude tests. Table 4.7 summarizes the MRA parameters considered in the analysis.

Table 4.7 – Sensitivity analysis parameters.

FM	SA	$N_a = N_d$	t_{1a}	t_{1d}	$F_{0,1a}/F_{0a}$	$F_{0,1d}/F_{0d}$
1	min	2.4	4	5	0.03	0.09
	mean	2.8	6.3	10.3	0.04	0.24
	max	3.6	9	15	0.05	0.34
2	min	1.8	5	23	0.03	0.35
	mean	1.8	5	24	0.03	0.39
	max	1.8	5	25	0.04	0.43

The response curves obtained using the mean values (SA mean), presented in Figure 4.14 for FM1, show a good agreement between the model and the experimental results in terms of force – $r^2 = [0.78, 0.93]$. The model has distanced themselves from the experimental results mainly in higher amplitude cycles, in particular, the pinching level of the descending branches of Oliveira *et al.* (2021) specimens (A1, A2 and A6) – where the mean value $t_{1d} = 10.3$ represents a higher level of pinching than experimental evidence. On the other hand, FM1 mean values adjust well to specimens A7 and C7 from Piluso and Rizzano (2008) tests. FM2 mean values adjust well to all specimens as expected, as the range of MRA parameters for FM2 is narrow, less impact of the use of mean values is expected – see Figure 4.15.

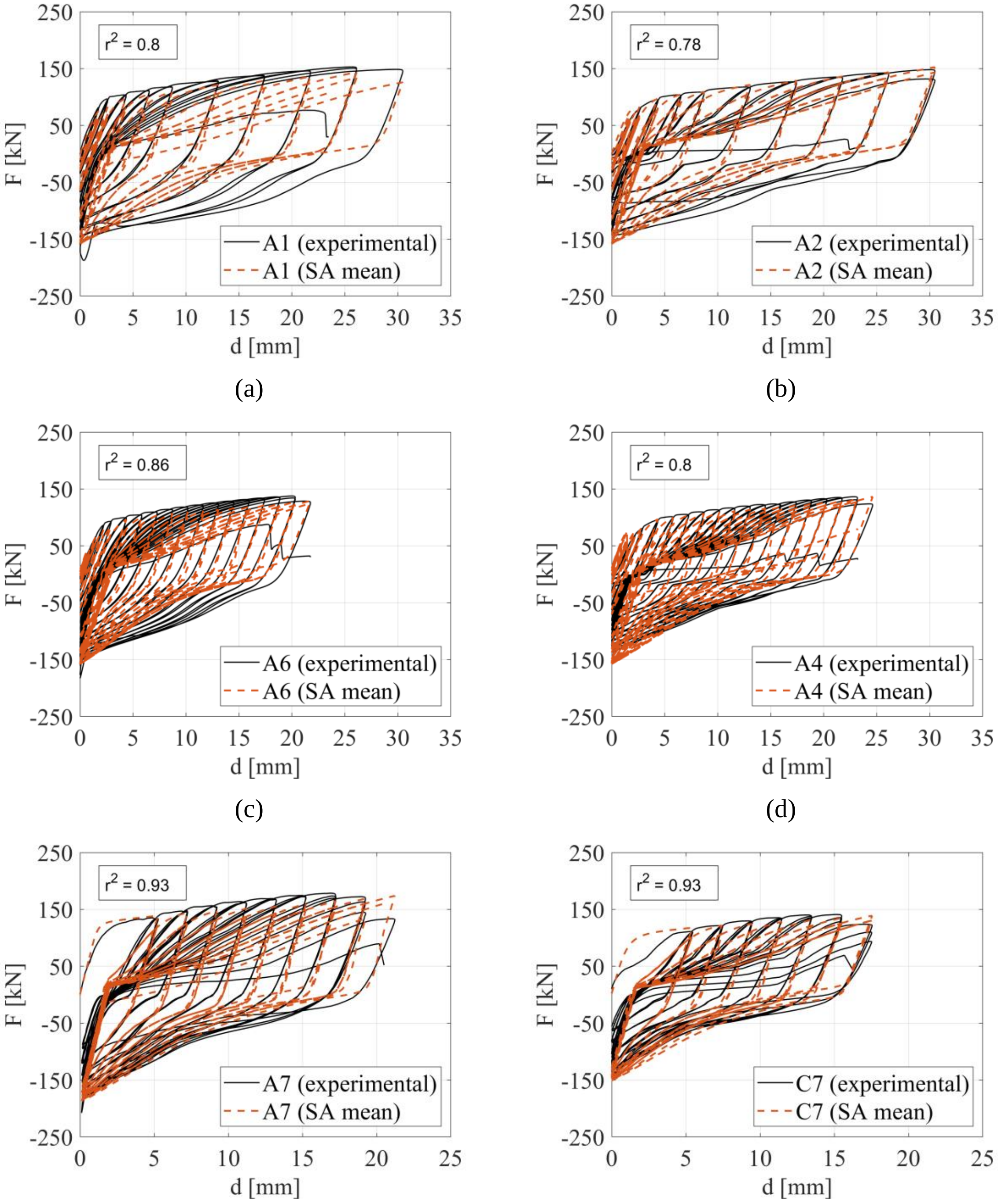

(a) (b)

(c) (d)

(e) (f)

Figure 4.14 – Sensitivity analysis (mean): rolled and welded specimens failing under FM1.

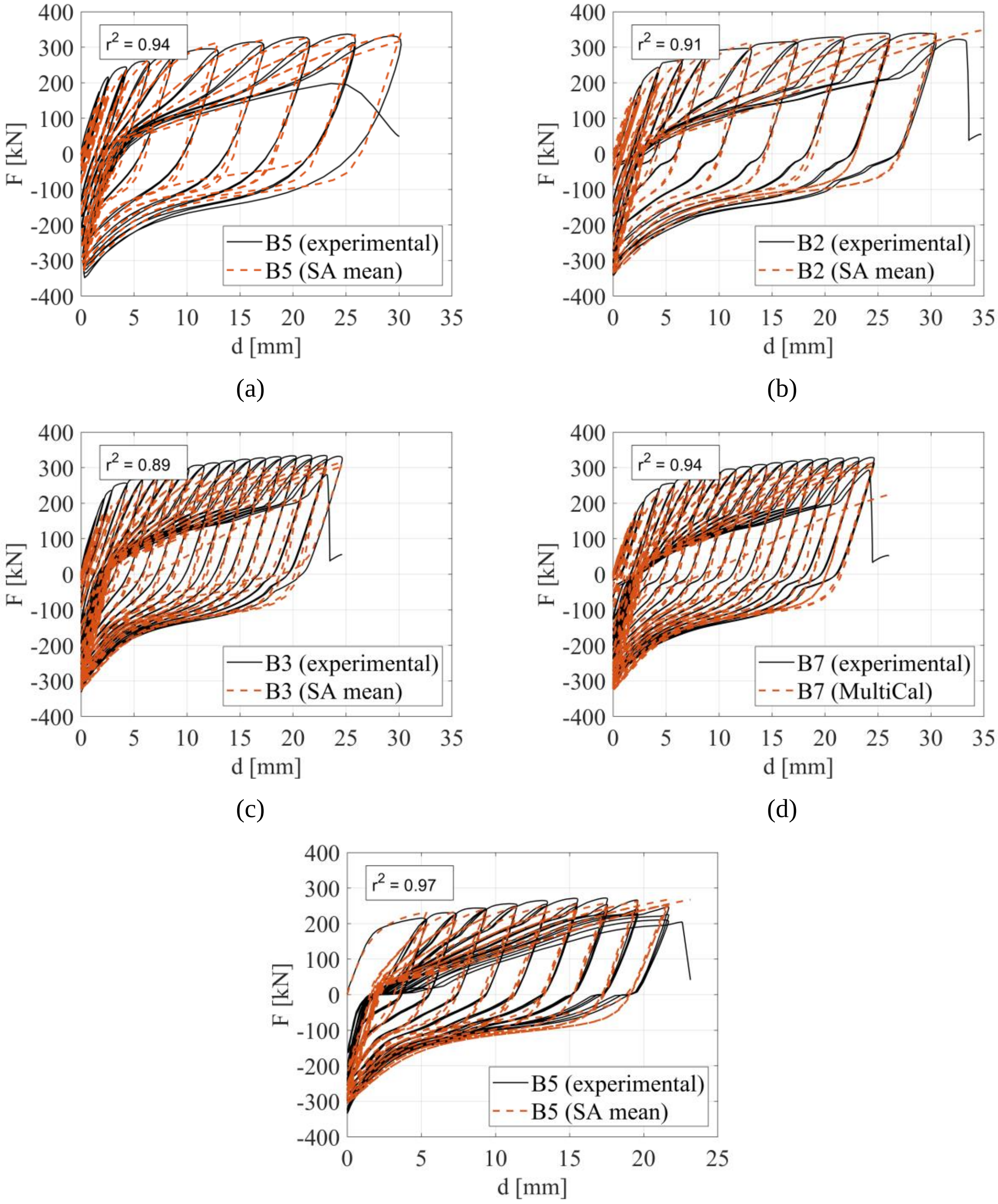

(a) (b)

(c) (d)

(e)

Figure 4.15 – Sensitivity analysis (mean): rolled specimens failing under FM2.

4.3.6. Discussion

The correspondence between the MRA model using the of the calibrated parameters and the use of its mean values (SA mean) to the experimental results was evaluated in terms of the three objectives parameters (i) force, (ii) dissipated energy and (iii) envelope (lower and upper) through the coefficient of determination r^2, whose main results are summarized in Table 4.8. These results show that:

(i) a suitable range of MRA parameters for T-stubs can be defined using as criterion the failure mode of the T-stub;

(ii) the MRA model does not seem capable of reproducing the slip at reloading;

(iii) the MRA models fails to reproduce part of the cyclic behaviour in specimens tested under CA cyclic loading, as the model considers the pinching level constant throughout the loading history, and the experimental evidence seems to show that these parameters should be dependent of dissipated energy;

(iv) adopting the mean values of the calibrated MRA parameters, provides a good agreement between the MRA model and experimental behaviour under variable amplitude.

4.4. Comparison between models

The performance of the two modelling procedures addressed in this chapter are assessed in terms of accumulated dissipated energy – see Figures 4.16 to 4.18. The PR model, the MRA (calibration) and MRA (SA mean) are compared against experimental results.

Table 4.8 – Correspondence of the calibrated MRA parameters and the use of its mean values to the experimental results – rolled specimens under FM1.

author	T-stub ID	LP	calibration F	calibration E_h	calibration lower env.	calibration upper env.	SA (mean) F	SA (mean) E_h	SA (mean) lower env.	SA (mean) upper env.
Oliveira *et al.* (2021)	A1	C1	0.90	0.88	0.83	0.58	0.80	0.61	0.43	0.39
	A2	C1	0.86	0.97	0.96	0.73	0.78	0.99	0.78	0.93
	A4	C2	0.87	0.94	0.97	0.87	0.80	0.99	0.96	0.75
	A6	C2	0.92	0.98	0.96	0.87	0.86	0.76	0.78	0.61
Piluso and Rizzano (2008)	A3	CA	0.93	0.60	0.70	0.99	-	-	-	-
	A4	CA	0.86	0.34	0.85	0.98	-	-	-	-
	A6	CA	0.90	0.32	0.80	0.97	-	-	-	-
	A7	VA	0.95	0.99	0.99	0.61	0.93	0.99	0.97	0.44
		μ	0.90	0.75	0.88	0.83	0.83	0.87	0.78	0.62
Oliveira *et al.* (2021)	B2	C1	0.90	0.99	0.86	0.88	0.91	0.99	0.98	0.89
	B3	C2	0.89	1.00	0.90	0.72	0.89	1.00	0.91	0.63
	B5	C1	0.94	1.00	0.88	0.94	0.94	1.00	0.89	0.92
	B7	C2	0.93	0.98	0.85	0.86	0.94	0.98	0.93	0.85
Piluso and Rizzano (2008)	B4	CA	0.94	0.98	0.84	0.99	-	-	-	-
	B5	VA	0.97	1.00	0.94	0.75	0.97	0.96	0.83	0.95
	B6	CA	0.86	0.23	0.76	0.95	-	-	-	-
	B7	CA	0.94	0.66	0.74	0.97	-	-	-	-
		μ	0.92	0.86	0.85	0.88	0.93	0.99	0.91	0.85
Piluso and Rizzano (2008)	C3	CA	0.87	0.21	0.37	0.82	-	-	-	-
	C4	CA	0.90	0.64	0.81	0.81	-	-	-	-
	C6	CA	0.85	0.30	0.72	0.55	-	-	-	-
	C7	VA	0.92	0.99	0.98	0.51	0.93	0.95	0.97	0.43
		μ	0.89	0.54	0.72	0.67	0.93	0.95	0.97	0.43

The PR model results deviates from experimental ones. It overestimates the accumulated hysteretic energy, as also observed in the force-deformation response in Figures 4.5 and 4.6, due to the misfit of the pinching level, which led to the overestimates the energy dissipation for high amplitude cycles, see Figure 4.7, with the exception of preloaded specimens under FM1 (A1 and A6).

The MRA (calibration) results, as expected, are in agreement with experimental evidence, with the exception of non-preloaded specimens under FM1 (A2 and A4) due to the model not being able to reproduce the slip at reloading, see Figure 4.14.

The MRA (SA mean) results are in agreement with experimental ones, with the exception of the preloaded specimens under FM1 (A1 and A6) in which the model underestimates the accumulated hysteretic energy, as already observed in the force-deformation response in Figure 4.14.

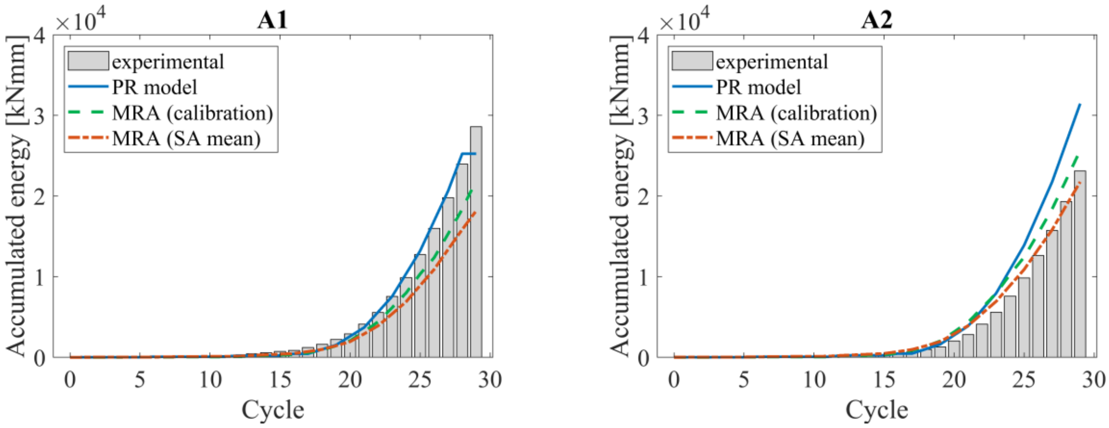

(a) (b)

Figure 4.16 – Accumulated dissipated energy: comparison between models for Oliveira *et al.* (2021) specimens under FM1.

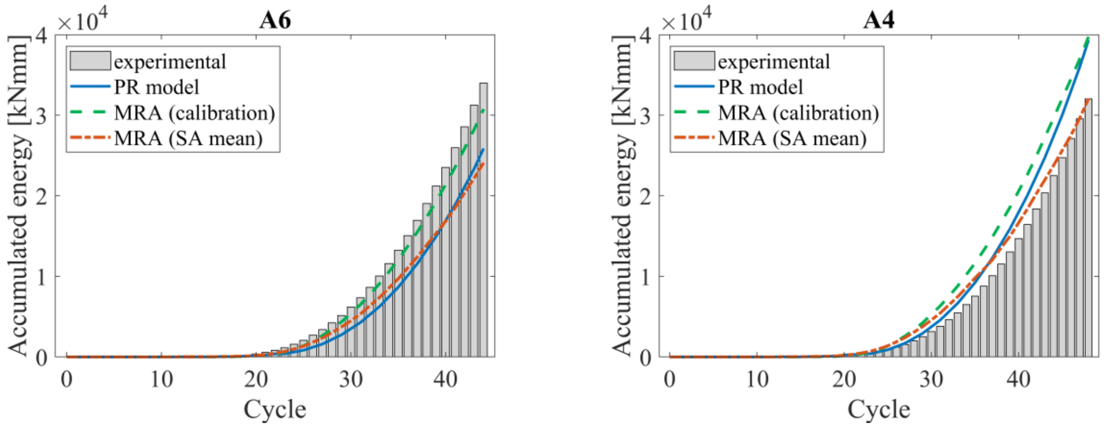

(a) (b)

Figure 4.17 – Accumulated dissipated energy: comparison between models for Oliveira *et al.* (2021) specimens under FM1.

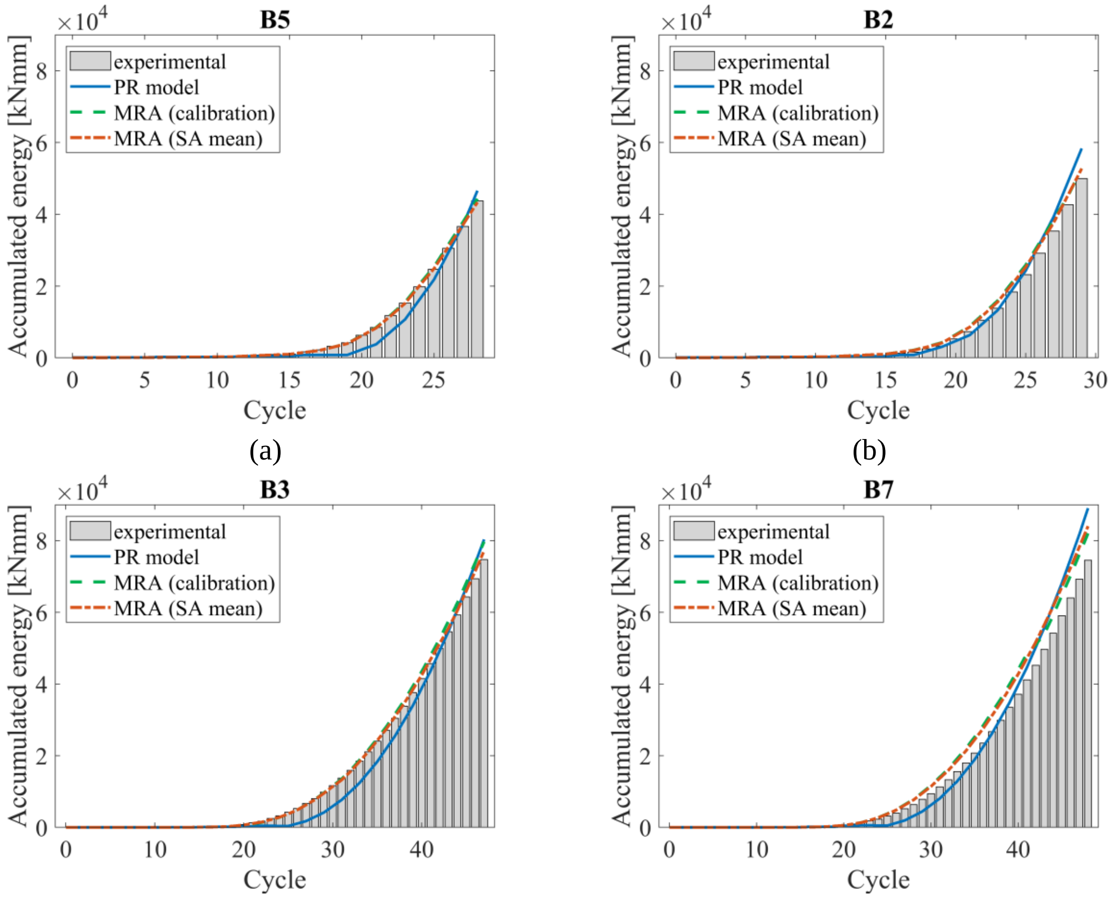

(a) (b)

(c) (d)

Figure 4.18 – Accumulated dissipated energy: comparison between models for Oliveira *et al.* (2021) specimens under FM2.

4.5. Concluding remarks

A preliminary characterization of the cyclic behaviour of the T-stub was conducted. Two modelling procedures: (i) a semi-analytical model and (ii) a multi-parameter mathematical model, were assessed and compared against experimental results.

Analytical models to predict the monotonic and the cyclic behaviour of T-stubs found in the literature (Piluso, Faella and Rizzano, 2001a, 2001b; Piluso and Rizzano, 2008) were applied and compared with the experimental results. Some conclusions are drawn from this comparison:

- both models for predicting the monotonic and cyclic behaviour start from the knowledge of their geometrical and mechanical properties, but the cyclic model relies on empirical parameters;
- the monotonic model shows a good agreement in terms of stiffness, resistance and deformation capacity for FM1 specimens. However, the model overestimates the prediction of the ultimate deformation and resistance of FM2 specimens;
- the cyclic model does not predict the premature failure of the T-stub, observed through experimental evidence, when compared with the theoretical model for predicting the monotonic behaviour.

A multi-objective calibration software (Chisari *et al.*, 2017) was used to calibrate the MRA model parameters (Richard and Abbott, 1975; Della Corte, De Matteis and Landolfo, 2000; Nogueiro *et al.*, 2007) and reproduce the force-deformation response. Results compared with experimental results. The following conclusion were drawn from this comparison:

- it is possible to set MRA model parameters to fit the response of experimental tests;
- distinct ranges of MRA model parameters are required for two types of failure modes;
- adopting the mean values of the established ranges, provide good agreement between the MRA model results and the experimental behaviour;
- the MRA model is a powerful mathematical model that can be used to reproduce the cyclic complex behaviour of SBCJs and its components since it considers several phenomena, in particular the pinching effect.

5 CYCLIC MODELLING OF T-STUBS: DECOUPLED COMPONENT MODEL

5.1. Introduction

Among the various components of a SBCJ, the T-stub is probably the most complex and presents specific challenges particularly related to the prediction of its cyclic behaviour. On the other hand, the T-stub is a highly dissipative component and thus the seismic behaviour of SBCJ relies heavily on it.

Nowadays, modelling the cyclic behaviour of the T-stub is usually made by adjusting models to the global behaviour of the T-stub without requiring their decoupling in tension and compression sub-components, as discussed in Chapter 4. However, in the scope of the application of the component method to the modelling of the cyclic behaviour of SBCJs, this decoupling is necessary.

This chapter presents a framework and the implementation of a decoupled component model for the T-stub aimed for cyclic loading. This decoupled model splits the single hysteretic spring (0D element) representation of the end-plate/column flange in bending into two separate hysteretic springs, one accounting for tensile forces and the other accounting with compressive forces. Equivalence rules are derived for the definition of the properties of the decoupled model, its consequences in terms of modelling are considered and the parameters required by the modified versions of the MRA model are calibrated. The model is validated by comparison with experimental test results.

5.2. Rationale for decoupling the T-stub

As explained in detail in (Oliveira, Costa, Shahbazian, *et al.*, 2021), it is advantageous to decouple the tension and compression behaviours into separate sub-components, leading to the simplification of the cyclic characterization of each component, while simultaneously facilitating the identification of the underlying physical phenomena. As typically, under cyclic loading, the T-stub supports tensile and compressive forces – see Figure 3.29 – it is required to split the corresponding spring that represents its behaviour into two-separate tension-only and compression-only springs. This is required because it is not possible to accurately reproduce the cyclic behaviour of a joint that comprises a tensile zone with equivalent T-stubs with a coupled T-stub spring because some components are, by nature, physically and by definition, tension-only or compression-only.

Consider a typical component model for the simple case of a bolted end-plate SBCJ subject to hogging moment with two rows of bolts. For hogging moments, the tensile zone (top row) is only able to carry load in tension, while the compression zone is only able to carry load in compression. This component model does not work for the same joint subjected to cyclic loading because when the bending moment reverses (sagging moment) it is not possible to transfer compressive force through the top springs, neither tensile force through the bottom springs. To overcome this problem, two solutions are possible: (i) to duplicate the rows of springs – additional compressive row at the top and additional tensile row at the bottom – extending the force-deformation component law of each spring into the negative (positive) displacement sector with almost zero stiffness (not zero because of numerical convergence), see Figure 5.1(a), as proposed by Simões da Silva *et al.* (2004), so that whenever the force changes sign, force is no longer transferred through the row in tension but instead through the row in compression; or (ii) to extend the rows of springs with the compressive components in the top row and the tensile components in the bottom row – extending the force-deformation component law of each tension-only (compression-only) spring into the negative (positive) force sector with very high stiffness (not infinite because of numerical convergence), see Figure 5.1(b).

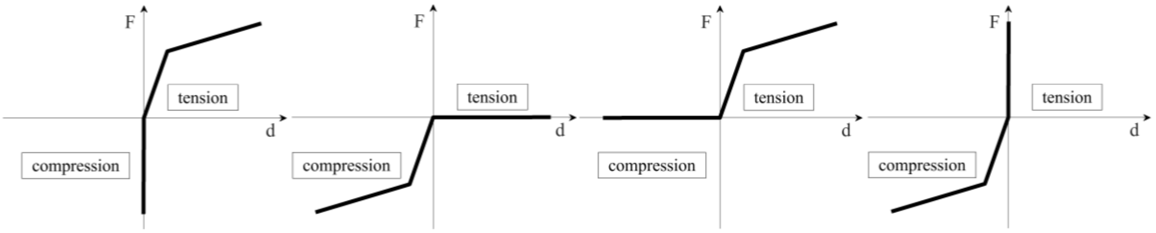

(a) (b)

Figure 5.1 – Extended force-deformation laws for tension-only and compression-only components.

Focusing on a single spring row for illustration, Figure 5.2 shows the two alternatives for each tension/compression zone of the model, yielding the same result. In this paper, the authors opted for alternative 1 (but the conclusions would be equally valid if alternative 2 had been chosen, with the necessary adaptations) because it is a more flexible option that ultimately will allow to relate tension-only and compression-only components that have the same deformation using an appropriate arrangement of rigid elements.

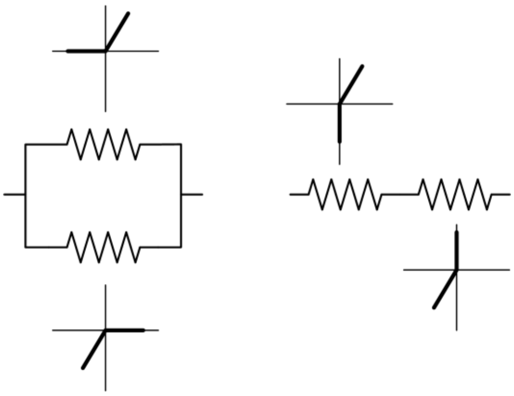

(a) Alternative 1 (b) Alternative 2

Figure 5.2 – Alternative implementation of component row to tackle load reversal.

Figure 5.3 illustrates the top zone of the joint, only considering, for simplicity, the T-stub corresponding to the end-plate in bending, the column web panel in tension and the column web panel in compression, implemented in parallel, according to alternative 1. Figure 5.3(a) shows the model using the coupled T-stub (C), while Figure 5.3(b) implements the decoupled T-stub (D) model.

To illustrate the difference between the two models, consider the simple displacement control load history shown in Figure 5.4, applied to the degree of freedom 1 – see Figure 5.3 – for the coupled and decoupled implementations.

Figure 5.5 illustrates the constitutive relations assigned to each component. In row 1, tensile components, T-stub and CWT for M1 and T-stub-T and CWT for M2 are active for positive deformations. In row 2, compression component CWC for M1 and T-stub-C and CWC for M1 are activated for negative deformations. Figures 5.6 and 5.7 show the response of each component for M1 and M2, respectively.

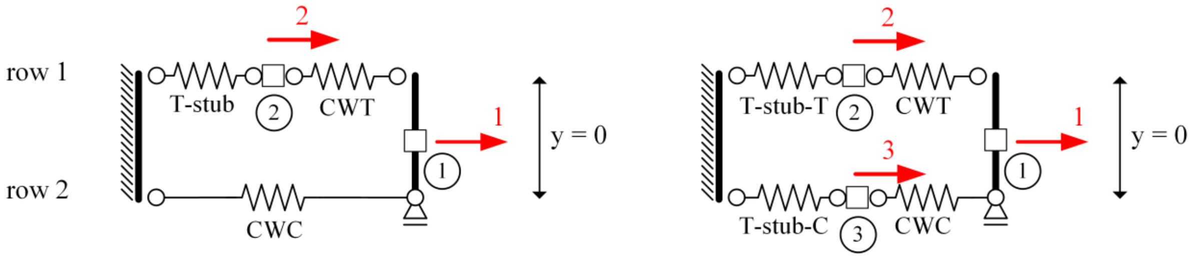

(a) (b)

Figure 5.3 – (a) coupled (M1) and (b) decoupled (M2) implementations for top row of a joint.

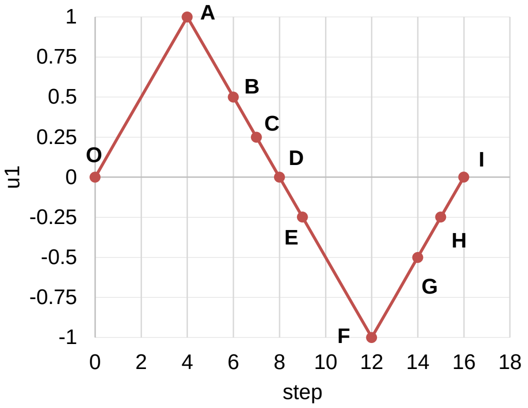

Figure 5.4 – Load history.

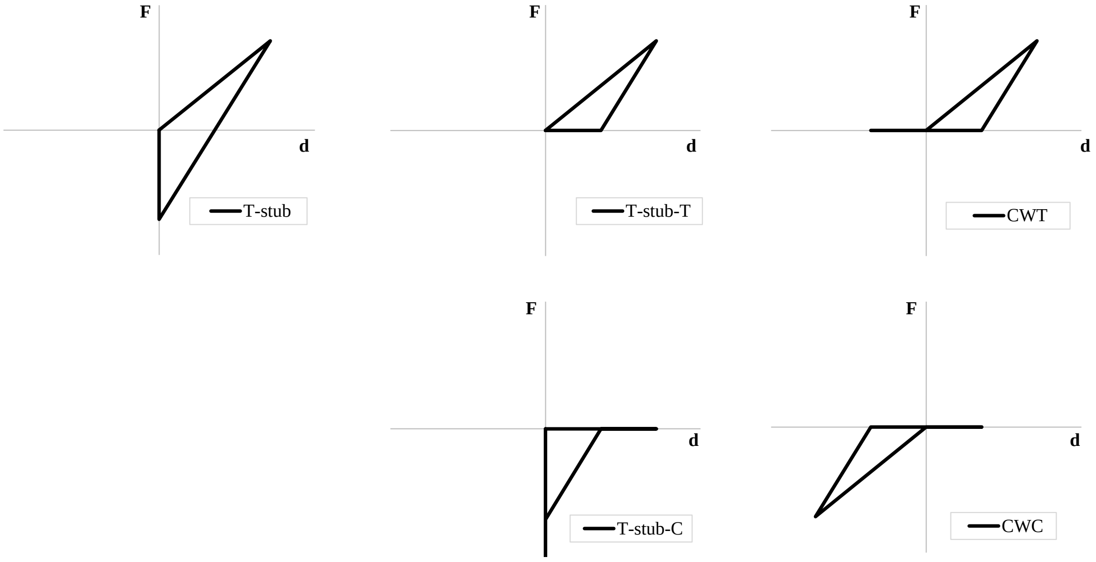

(a) (b) (c)

Figure 5.5 – Constitutive relations for each component (spring): (a) coupled implementation; (b) decoupled implementation, and (c) both implementations.

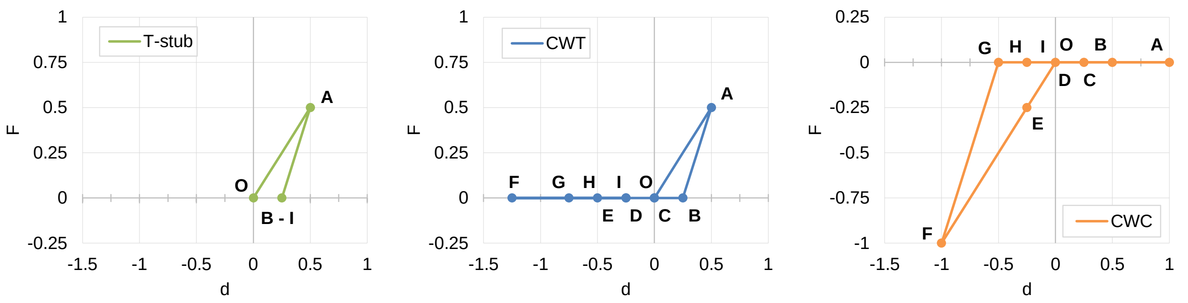

(a) (b) (c)

Figure 5.6 – Force-deformation response of each spring: coupled implementation (M1).

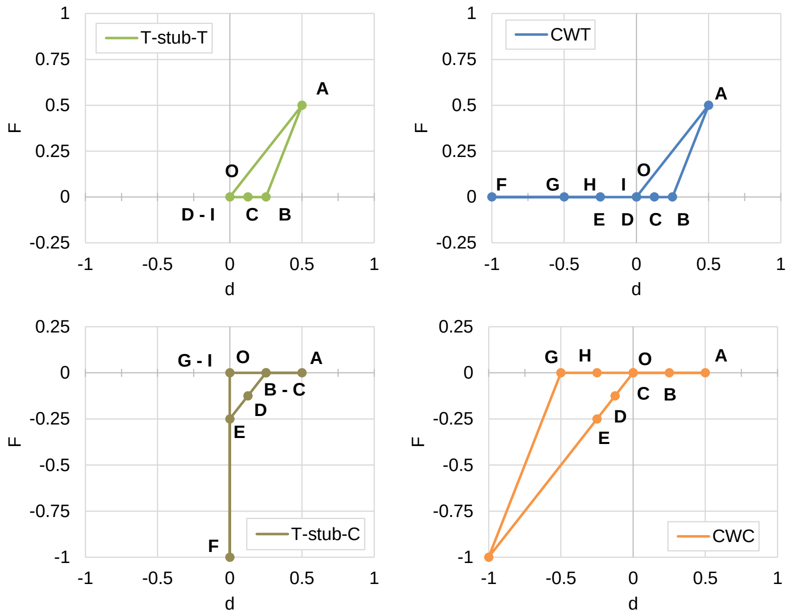

Figure 5.7 – Force-deformation response of each spring: decoupled implementation (M2).

Figure 5.8 compares the total force-deformation response for M1 and M2, showing that the coupled implementation is unable to mobilize the T-stub in compression, thus justifying the relevance and need for the decoupling process.

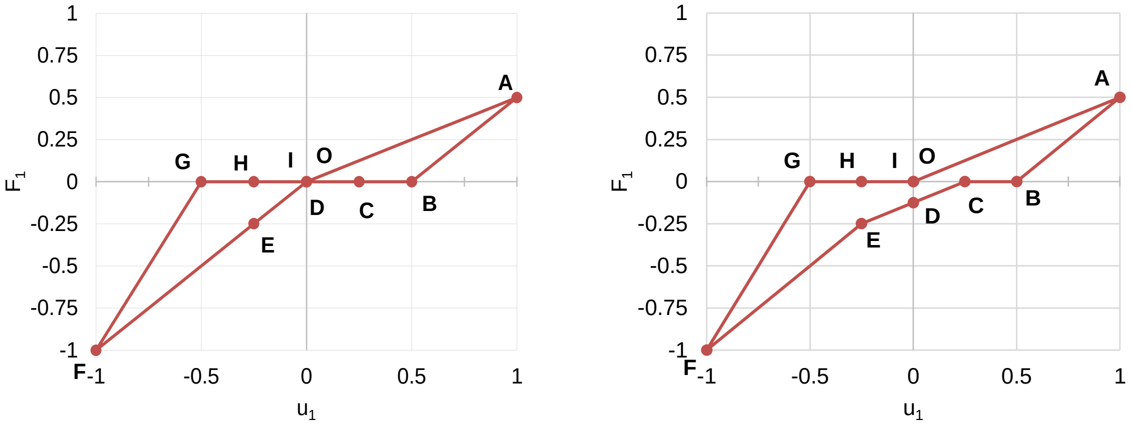

(a) M1 (b) M2

Figure 5.8 – Force-deformation response of the assembly of components: (a) coupled and (b) decoupled implementations.

5.3. Tension-only and compression-only components

Figure 5.9(a) depicts a typical cyclic force-deformation hysteretic response of a spring that develops tension and compressive forces and whose behaviour can be described using the MRA model presented in Section 2.4.1. Modelling the tension and compression behaviours using decoupled components requires the adaptation of the MRA model (Oliveira, Costa, Shahbazian, *et al.*, 2021). Using Eqs. (2.6) to (2.14) as the mathematical expressions that define each non-linear branch, the behaviour of each decoupled component is described in Figure 5.9(b) for tension-only and in Figure 5.9(c) for compression-only behaviours – a tension (compression)-only component is a component that supports only tension (compression) forces.

To get a continuous constitutive law, a linear behaviour is assigned to tension-only and compression-only behaviours when the force in these components is close to zero (stress free region of the constitutive laws) – henceforth referred as boundary line – with $F = \beta K_0 \cdot d$, where β corresponds to a very small percentage of the component's initial stiffness avoiding convergence issues in the non-linear solver of the mechanical model for the SBCJ. Figure 5.9 also illustrates that a deformation limit d_{lim} can also be defined to establish the limit for the reloading branch when the component becomes active thus not requiring the simultaneous activation/deactivation of the tension only and compression-only components.

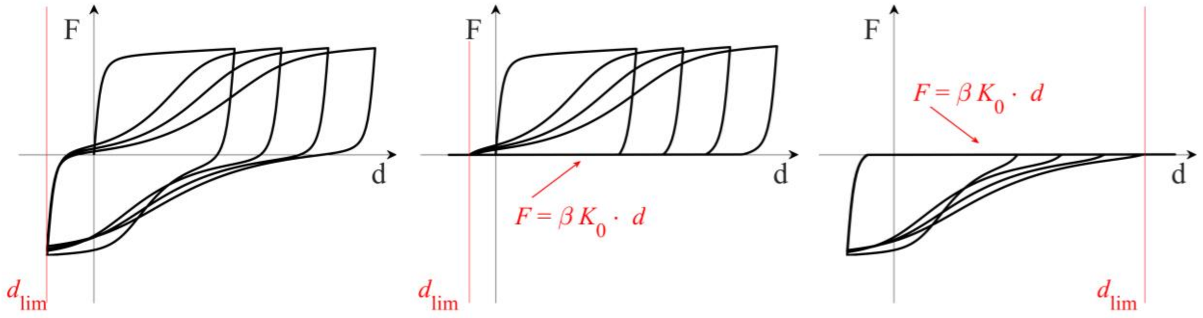

(a) (b) (c)

Figure 5.9 – Constitutive relations for dissipative components: (a) tension-compression; (b) tension-only; (c) compression-only.

5.4. Methodology for decoupling the T-stub

In this section an assessment on the consequences and requirements of the decoupling of a tension-compression behaviour into a tension-only and a compression-only component will be analysed and discussed.

5.4.1. Decoupled tension-compression component model

Consider the single coupled tension-compression spring (CTCM) of Figure 5.10(a) and the equivalent decoupled model with two springs (DTCM) of Figure 5.10(b), whereby component

(1,1) will be tension-only and component (2,1) will be compression-only. All the components constitutive relation will be defined using the MRA model.

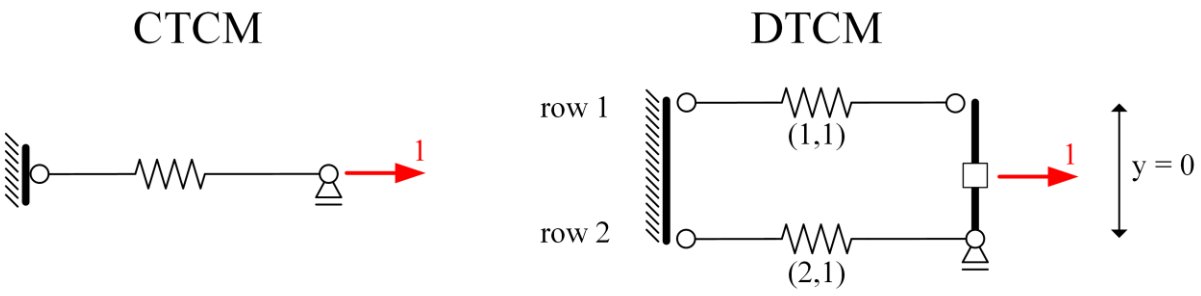

(a) (b)

Figure 5.10 – (a) coupled component cyclic model (CTCM) and (b) decoupled component model (DTCM) with tension-only and compression-only components.

The components of the DTCM are assumed to have the same geometric position and a displacement control load history is applied to the degree of freedom 1 in Figure 5.10. The displacement is assumed vary according to Figure 5.11, that represents the typical load history of a bolted T-stub: variable (VA) and constant amplitude (CA).

As already mentioned, the MRA model comprises 30 parameters – 15 for each branch – 18 of those without physical meaning but the same MRA model parameters are assigned to the ascending and descending branches in the current analysis. A parametric study is done to define strategies to account for each parameter in the decoupling procedure. Hence, five analyses were performed dealing with the following parameters: (i) residual stiffness parameter β, (ii) shape parameter N, (iii) strength degradation i_F, (iv) pinching parameters t_1, t_2 and C and (v) hardening H_h. The compatibility between coupled and decoupled models is assessed through the coefficient of determination, r^2, using the method of least squares – $r^2 = 1$ indicates that the DTCM perfectly fits the CTCM behaviour.

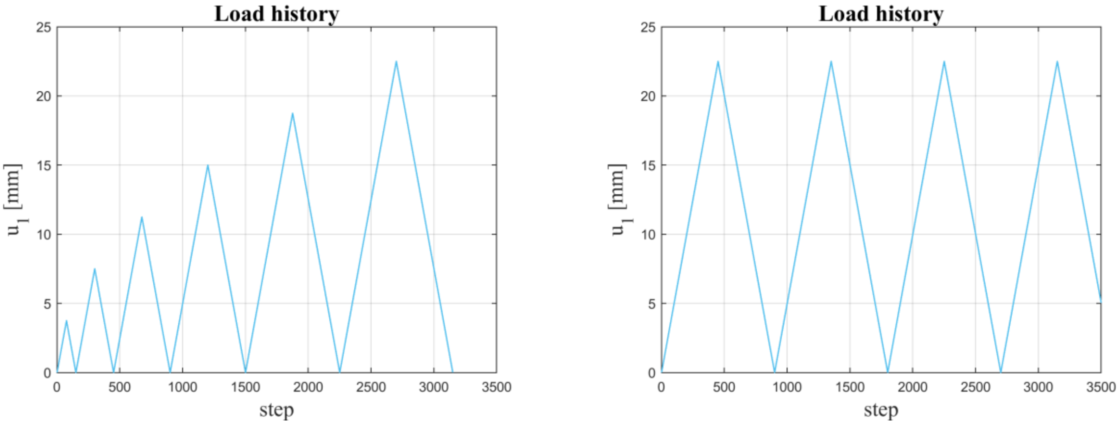

(a) (b)

Figure 5.11 – Load history: (a) VA and (b) CA.

5.4.2. Residual stiffness parameter

The residual stiffness parameter β defines the percentage of the initial stiffness used to model the stress-free region of the tension-only or compression-only components, see Section 5.3. The parameter β is required because in a non-linear analysis a residual stiffness needs to be assigned to the nominally horizontal branches (stress-free branches) of the force-deformation constitutive relations of the components.

To establish an appropriate upper bound value for β, four values were tested: 2%, 1%, 0.1%, and 0.01%. Figure 5.12 shows the force-deformation curves of the CTCM vs DTCM for the selected values of β. The comparison shows that $\beta = 2\%$ does not provide accurate results. Exact match ($r^2 = 1$) is achieved for $\beta = 0.01\%$ but good results are also achieved for $\beta = 0.1\%$ ($r^2 = 0.997$). Figures 5.1(b) and 5.1(d) show the force-deformation curves of each component (DTCM) for $\beta = 2\%$ and $\beta = 0.01\%$, respectively. $\beta = 0.01\%$ will henceforward be used.

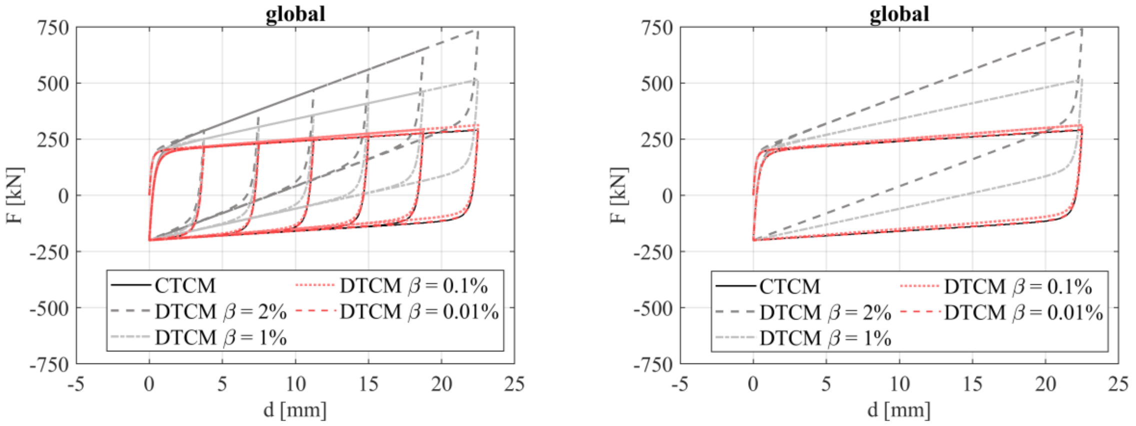

(a) (b)

Figure 5.12 – Assessment of β in the behaviour of the CTCM and DTCM (global): (a) VA and (b) CA.

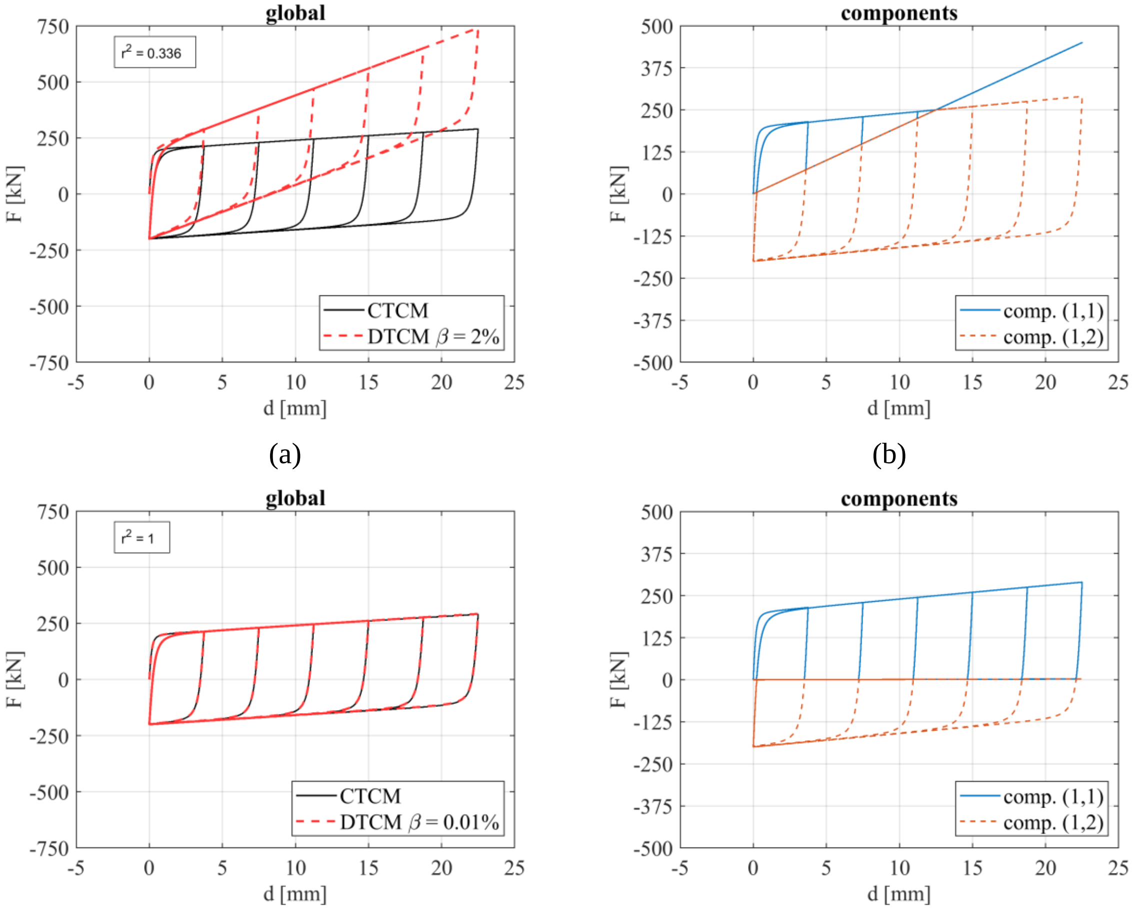

(a) (b)

(c) (d)

Figure 5.13 – Assessment of β in the behaviour of the DTCM (global and components): VA.

5.4.3. Shape parameter

Figures 5.14(a) and 5.14(b) shows the force-deformation curves of the CTCM for four values of N (0.5, 1.0, 2.0, and 4.0) showing that N has a great influence on the curve shape. It shows that the parameter N has an impact not only in the corner (round or straight) of each branch, but also in the global behaviour (narrow or wide) – for lower values of N the curves are rounder, and the global cycles are narrower. For illustration proposes, Figures 5.14(c) and 5.14(d) shows the force-deformation curves of the CTCM vs DTCM considering $N = 2.0$ showing that N has no impact on the accuracy of the DTCM.

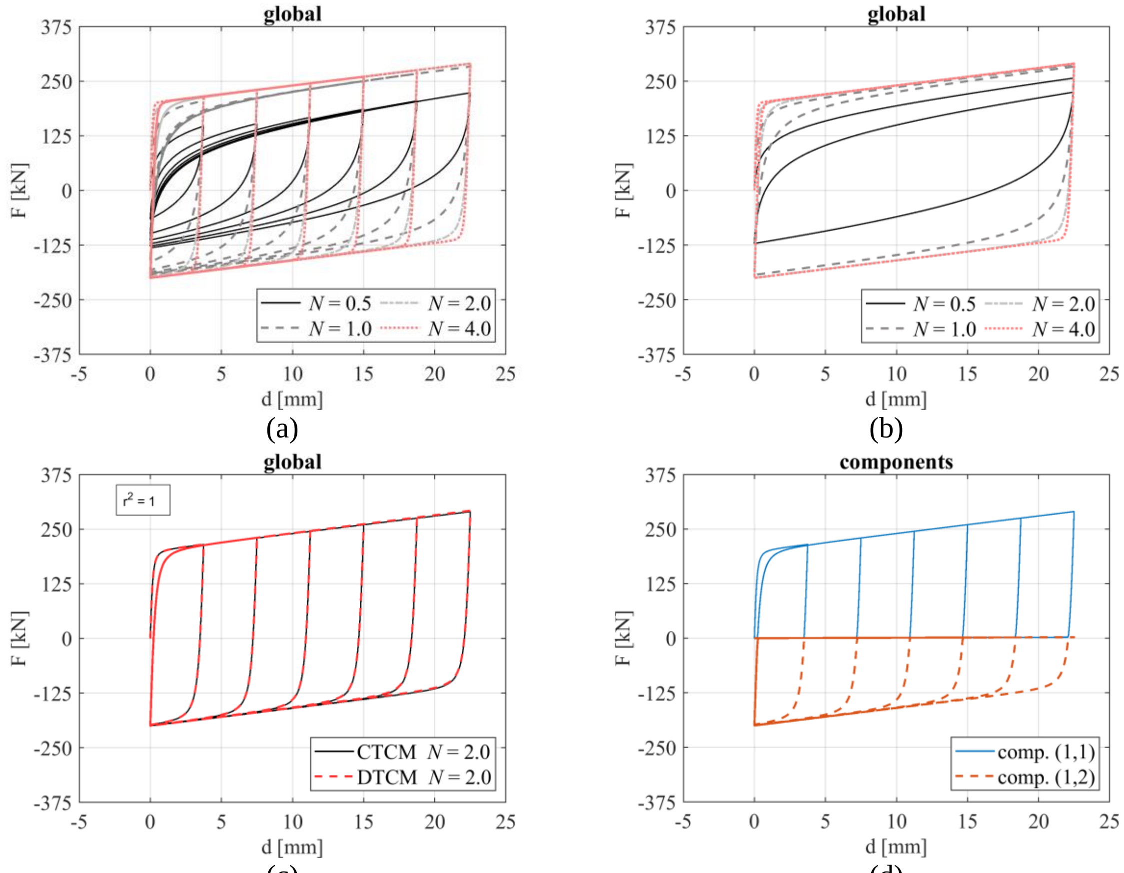

(a) (b)

(c) (d)

Figure 5.14 – Assessment of N in the behaviour of the CTCM (global): (a) VA and (b) CA, and of the DTCM (c) global and (d) components for VA with $N = 2.0$.

5.4.4. Strength and stiffness parameters

Degradation of strength corresponds to a progressive reduction of the load bearing capacity for the same deformation level as the number the cycles increases, i.e. with the accumulation of plastic deformation of the components. For the current study, stiffness degradation corresponds to the reduction of the slope of the linear part of the unloading branches. To assess the strength and stiffness degradation, three levels of i_F (0.2, 0.6, and 1.2), and three of i_K (0.010, 0.015 and 0.030) were considered in the MRA model.

Figures 5.15 and 5.16 show the force-deformation curves of the CTCM with and without strength degradation. The higher the value of i_F, the higher the level of degradation. Figure 5.17(a) shows the results of the CTCM and the DTCM models with $i_F = 0.6$ showing a poor match. On the other hand, Figure 5.18(a) shows the results of the CTCM with $i_F = 0.6$ vs DTCM with $i_F = 1.2$ assigned to both components showing a reasonable, but not perfect, match ($r^2 = 0.992$). The reason behind this improvement is that, because the components in the DTCM are tension-only and compression-only, the energy dissipated by each component E_h (area enclosed by each branch) is only half of the one in the CTCM model. Accordingly, as illustrated in Figure 5.18(a), since the formula that takes in consideration the strength degradation has a direct relation between i_F and E_h, see Eq. (11), a simple procedure to account for the full energy dissipation in the DTCM is to assign a degradation level for the components in the DTCM twice the one assigned to the CTCM. Similar conclusions are drawn for stiffness degradation due to the similarity of the expressions that account for these effects in the MRA model.

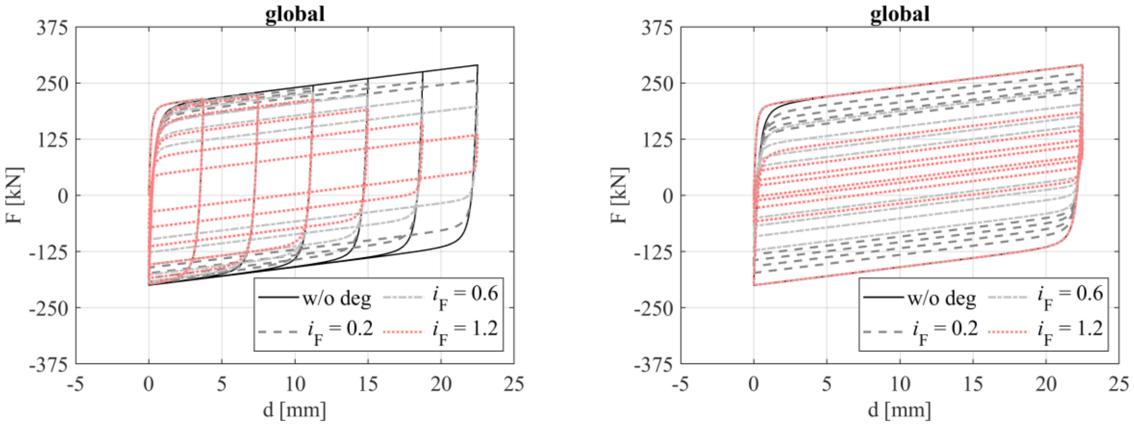

(a) (b)

Figure 5.15 – Assessment of i_F in the behaviour of the CTCM (global): (a) VA and (b) CA.

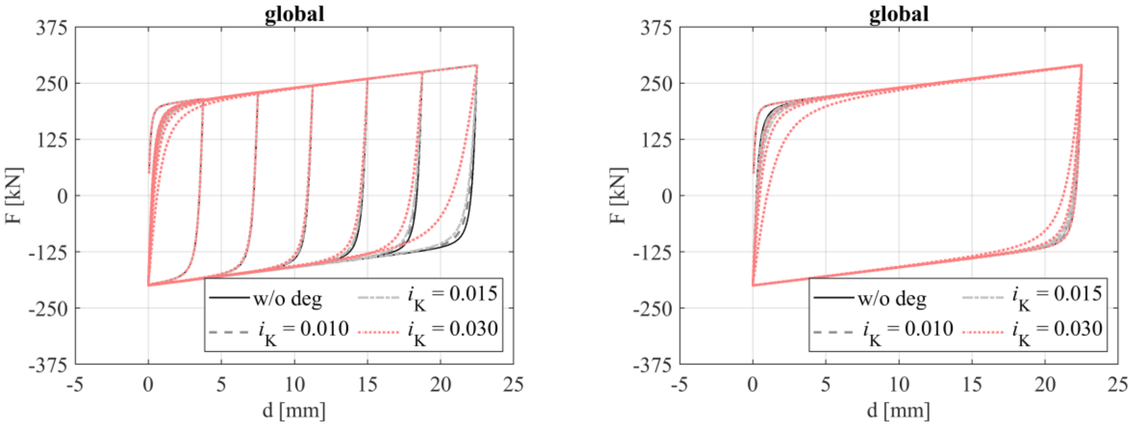

(a) (b)

Figure 5.16 – Assessment of i_K in the behaviour of the CTCM (global): (a) VA and (b) CA.

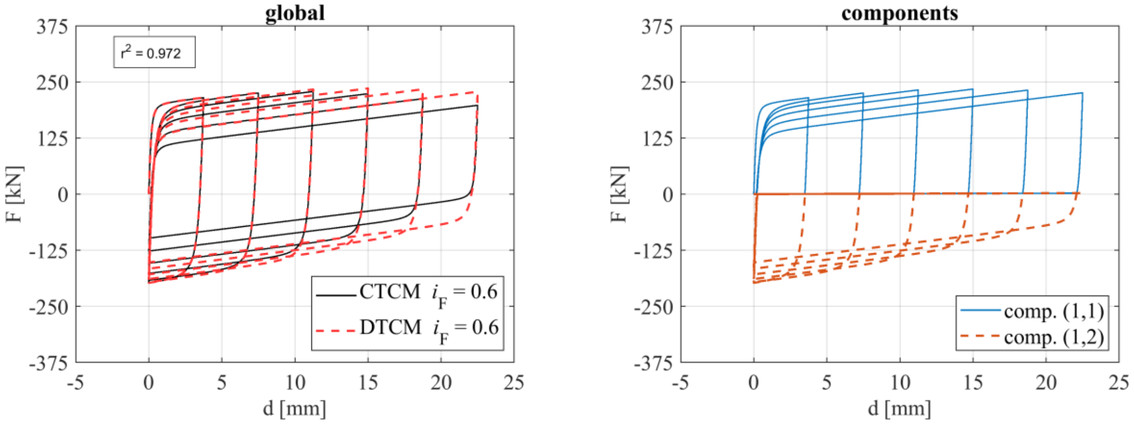

(a) (b)

Figure 5.17 – Assessment of i_F in the behaviour of the DTCM (global and components): VA.

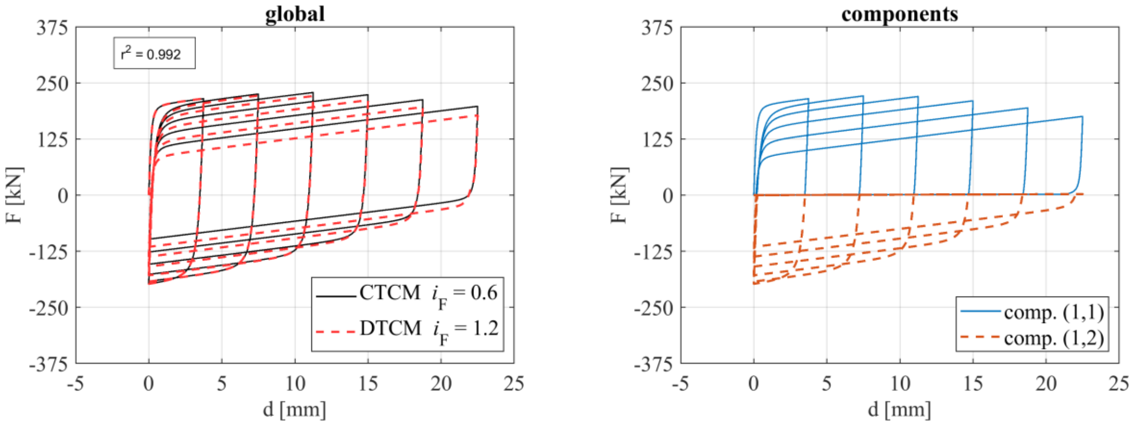

(a) (b)

Figure 5.18 – Assessment of i_F in the behaviour of the DTCM (global and components): VA.

To clarify the reason for not having $r^2 = 1$ in the latter case, an illustration of the dissipated energy calculations is presented in Figure 5.19 that shows how the energy dissipated to be considered in each branch of the MRA models is computed. Taking a closer look at the component in tension-only in Figure 5.19(a), it is only possible to compute the area E_0 after computing branch number 0 and 1. Therefore, these two branches were computed considering zero dissipated energy. On the other hand, for the component in compression-only, it is only possible to compute the area E_0 after computing branches number 0, 1 and 2. Therefore, these three branches are computed also considering zero dissipated energy. This gap has repercussions in the following branches and in the alignment of branches between the tension-only component and the compression-only component. For example, to compute branch number 4, the dissipated energy $E_0 + E_1$ is used for the tension-only component and E_0 for the compression-only component, see Figure 5.19(b). This will lead to the misalignment of branches observed in the last cycle of Figure 5.18(d), as the discrepancy in the amount of dissipated energy used in the calculations for each component is larger.

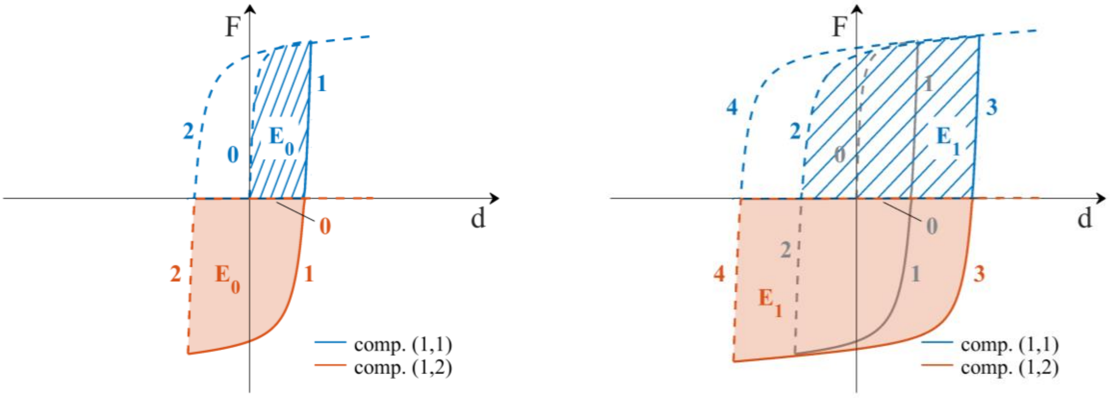

(a) (b)

Figure 5.19 – Computation of dissipated energy, E_h.

5.4.5. Pinching parameters

To account for the pinching phenomenon in the MRA model, two limit curves are introduced, representing a lower and an upper bound to each branch – both limit curves have an MRA type law, see Figure 2.10. The lower bound curve has the same characteristic as the upper bound curve, apart from the strength, $F_{0,\mathrm{l}}$, whose value is assumed ten times smaller than $F_{0,\mathrm{u}}$ in this example. As stated before, the transition law, defined by the parameter t, is obtained through three empirical parameters, namely, t_1, t_2 and C, see Eqs. (2.10) and (2.11).

As already stated, these three parameters are constants, but the parameter t is variable as it depends on deformation and is computed for each point of the force-deformation curve. To assess the influence of the parameters t_1, t_2 and C on the modelling of the pinching phenomena, a small parametric analysis was performed.

Figures 5.20 to 5.22 show the force-deformation curves of the CTCM without and with pinching by carrying each pinching parameter: (i) t_1: 0, 5, 10, and 20 assuming $t_2 = 0.3$ and $C = 1.0$; (ii) t_2: 0, 0.2, 0.5, and 1.0 assuming $t_1 = 10$ and $C = 1.0$ and (iii) C: 0, 0.5, 1.0, and 1.5 assuming $t_1 = 10$ and $t_2 = 0.3$. These figures show that increasing any of the pinching parameters, an upward concavity is formed for the ascending branches and a downward concavity for the descending branches. Figure 5.20 shows that the smaller the value of t_1, the lower the effect on the curve shape and the larger the value of t_1, the narrow the curve shape is. For $t_1 = 0$ no concave curve is formed, and independently of the value of t_1, the plastic strength always decreases for a certain deformation level when pinching is considered within this range of parameters. In Figure 5.21, for $t_2 = 0$, t becomes equal to 1 – see Eq. (2.10) – and the pinching effect becomes null. The empirical parameter t_2 also has an impact in the curve like t_1. The higher the level of t_2, the larger the loss of strength capacity for the same deformation level. In Figure 5.22, for $C = 0$, t becomes equal to 1 – see Eqs. (2.10) and (2.11) – and the pinching effect disappears. The parameter C seems to control de position of the inflection point of the curve. The higher the parameter C the higher the horizontal coordinate of the inflection point and thus the larger the loss of strength capacity for the same deformation level.

For illustration proposes, Figure 5.23 presents the force-deformation curves of the CTCM and the DTCM for $t_1 = 10.0$, $t_2 = 0.3$ and $C = 1.0$ showing that an exact match ($r^2 = 1$) between the models has been achieved for all the combinations of t_1, t_2, C, without requiring any adjustment arising from the decoupling process.

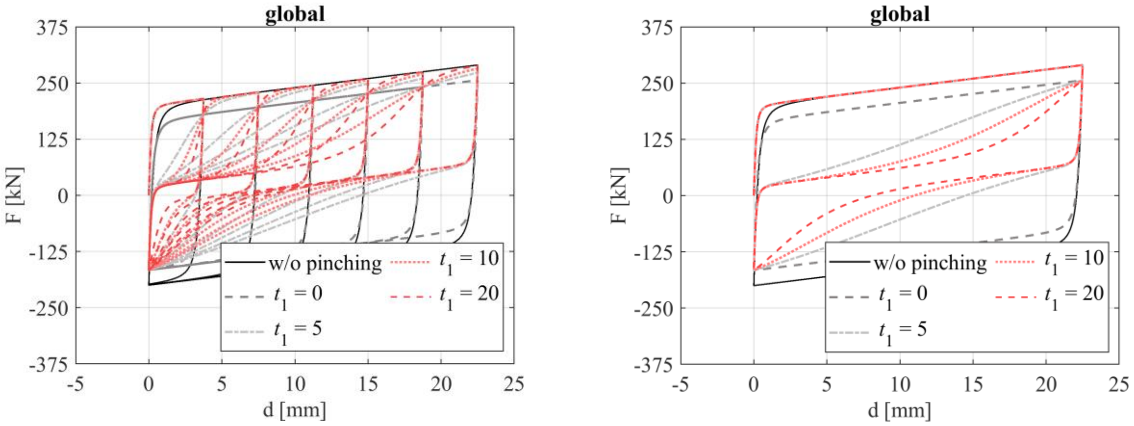

(a) (b)

Figure 5.20 – Assessment of t_1 in the behaviour of the CTCM (global): (a) VA and (b) CA.

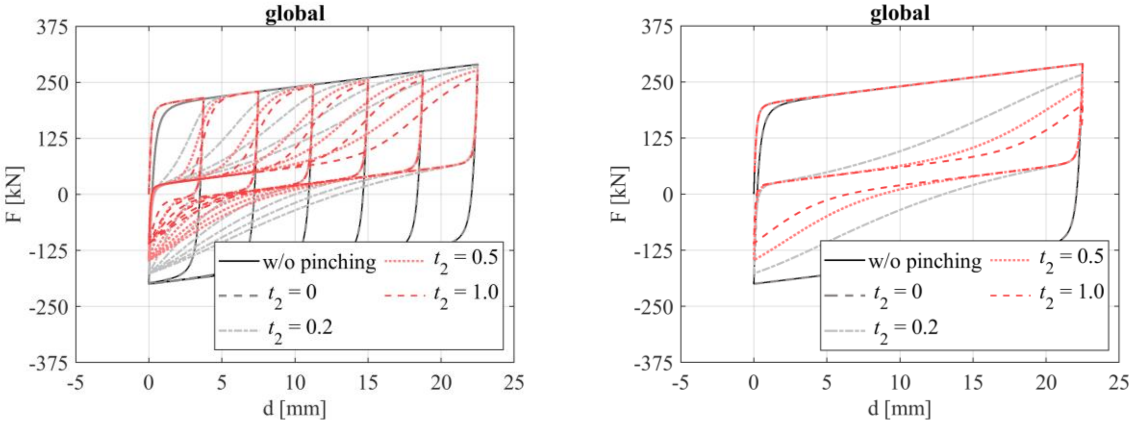

(a) (b)

Figure 5.21 – Assessment of t_2 in the behaviour of the CTCM (global): (a) VA and (b) CA.

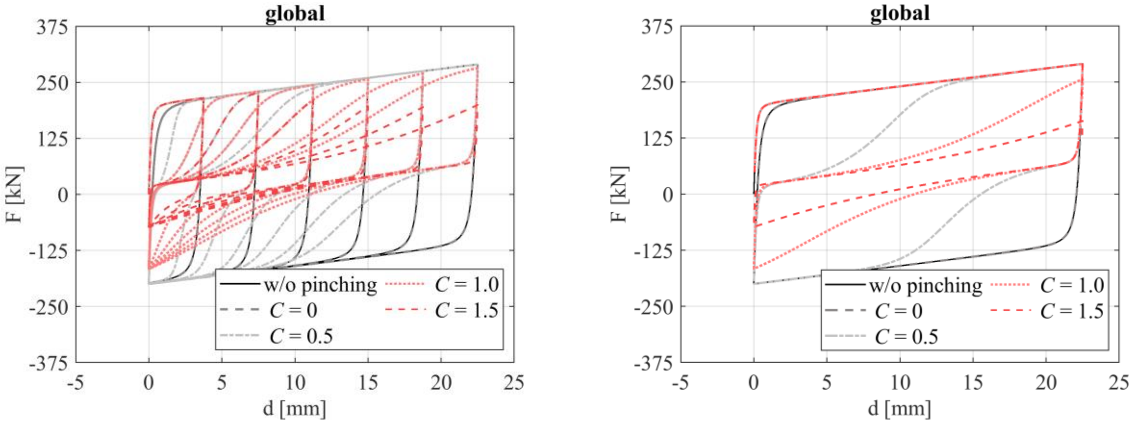

(a) (b)

Figure 5.22 – Assessment of C in the behaviour of the CTCM (global): (a) VA and (b) CA.

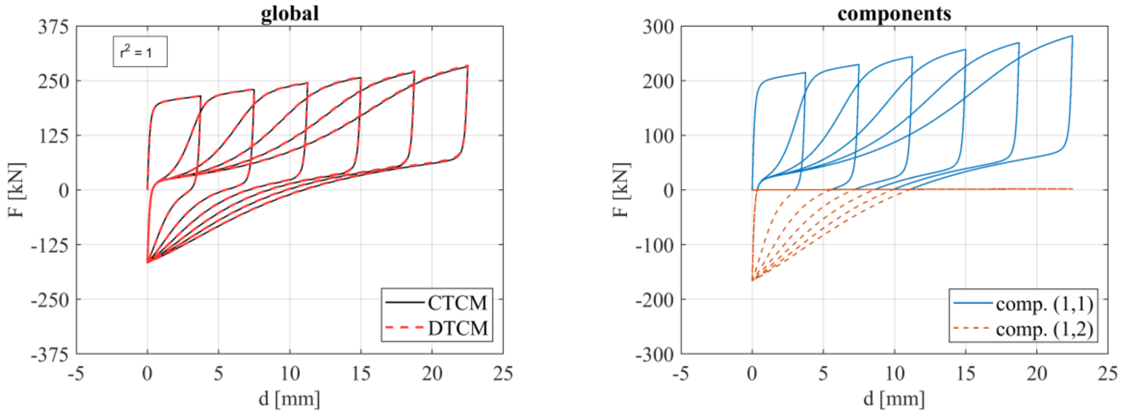

(a) (b)

Figure 5.23 – Assessment of t_1, t_2 and C in the behaviour of the DTCM (global and components):VA.

5.4.6. Hardening

Hardening due to cyclic plastic deformation is considered to be isotropic. To assess the hardening effect, three levels of H_h were considered: 0.01, 0.02 and 0.03. Figure 5.24 shows the force-deformation curves of the CTCM with and without hardening. The higher the level of H_h, the larger the increase of strength capacity for the same deformation level. Figure 5.25 shows the force-deformation curves of the CTCM and the DTCM with $H_h = 0.03$ showing that H_h has no impact on the accuracy of the DCTCM.

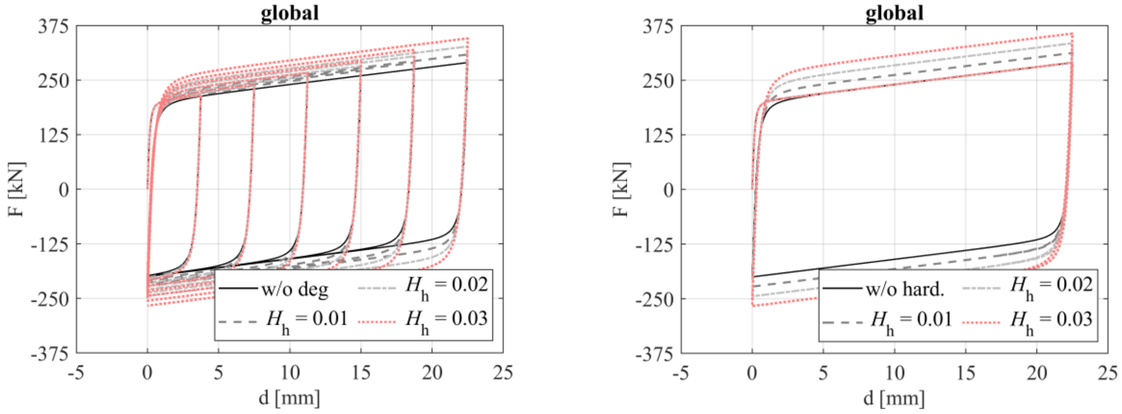

(a) (b)

Figure 5.24 – Assessment of H_h in the behaviour of the CTCM (global): (a) VA and (b) CA.

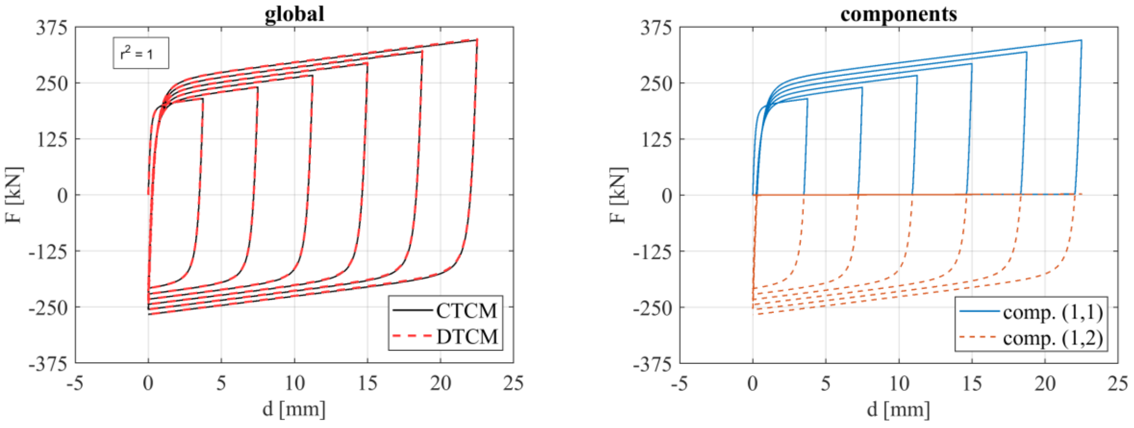

(a) (b)

Figure 5.25 – Assessment of H_h in the behaviour of the DTCM (global and components): VA.

5.4.7. Summary

To achieve a good equivalence between the coupled and decoupled models, the following is required:

(i) a low value is required for the residual stiffness parameter β; a compromise between rigor and numerical efficiency is 0,1%;

(ii) the shape parameter N does not require any adaptation due to the decoupling of components and the same parameters can be used in the components of both models;

(iii) it is necessary to assign a degradation level to the components of the DTCM twice the one assigned to the component in the CTCM;

(iv) the pinching parameters t_1, t_2 and C and hardening coefficient H_h do not require any adaptation due to the decoupling of components and the same parameters can be used in the components of both models.

The correspondence between the CTCM and DTCM was evaluated through the coefficient of determination r^2, whose main results with respect to the VA load history are summarized in Table 5.1.

Table 5.1 – Correspondence between models (VA).

residual stiffness parameter		shape parameter		strength degradation coefficient			pinching parameters						hardening coefficient	
β	r^2	N	r^2	$i_{F,\text{CTCM}}$	$i_{F,\text{DTCM}}$	r^2	t_1	r^2	t_2	r^2	C	r^2	H_h	r^2
2%	0.336	0.5	1	0.2	0.2	0.997	0	1	0	1	0	1	0.01	1
1%	0.784	1.0	1	0.2	0.4	0.999	5	1	0.2	1	0.5	1	0.02	1
0.1%	0.997	2.0	1	0.6	0.6	0.972	10	1	0.5	1	1.0	1	0.03	1
0.01%	1	4.0	1	0.6	1.2	0.992	20	1	1.0	1	1.5	1	0.04	1

5.5. T-stub decoupled cyclic component model (TS-CCM)

5.5.1. Description of the model

It was shown that, with minor adjustments, it is possible to model the cyclic behaviour of a generic tension-compression component decoupling it into tension-only and compression-only sub-components. Based on these findings, a cyclic component model of a bolted T-stub was developed using tension-only and compression-only sub-components with constitutive relations based on the MRA model.

Figure 5.26(a) represents the usual component model for a T-stub in tension. It comprises two springs in series, representing the bolts in tension (1) and the column flange/endplate in bending (2). Bolts are usually design to remain in elastic regime and thus the behaviour of the spring (1) is assumed linear.

Figure 5.26(b) represents the equivalent decoupled T-stub cyclic component model (TS-CCM). It consists of an arrangement of springs in parallel, whereby the top row comprises the component bolts in tension (1,1) and the component column flange/end-plate in bending – tension (1,2) and the bottom row includes the component column flange/end-plate in bending – compression (2,1). Springs (1,2) and (2,1) represent the same component but split its behaviour in tension-only and compression-only, respectively. It is noted that, in this model, row 1 is assumed to be in the same geometric position of row 2 and thus, the model has only two kinematic degrees of freedom.

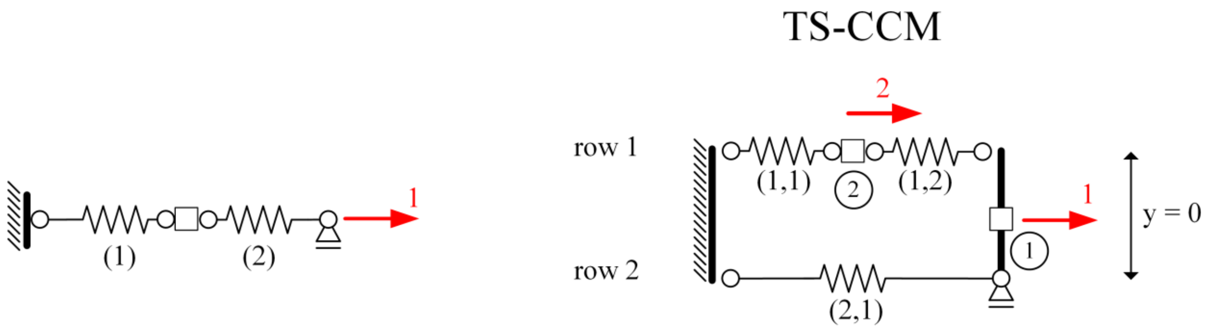

(a) (b)

Figure 5.26 – T-stub cyclic component models: (a) coupled and (b) decoupled (TS-CCM).

In practice, not all T-stubs connect steel members with the same stiffness – e.g. small beams may be connected to very large and stiff columns – so that the flanges of the two T-elements may be different. Hence, the two following situations may arise: (i) a bolted T-stub with only one flange in bending – $K_{\mathrm{f,u}}$, see Figure 5.27(a); (ii) a bolted T-stub with two flanges in bending – $K_{\mathrm{f,u}}$ and $K_{\mathrm{f,l}}$, see Figure 5.27(b). To cater for both situations in a simple way in the decoupled TS-CCM, the flange or flanges in bending are represented by equivalent springs (1,2) and (2,1) – $K_{\mathrm{f,spring}}$, see Figure 5.27(c).

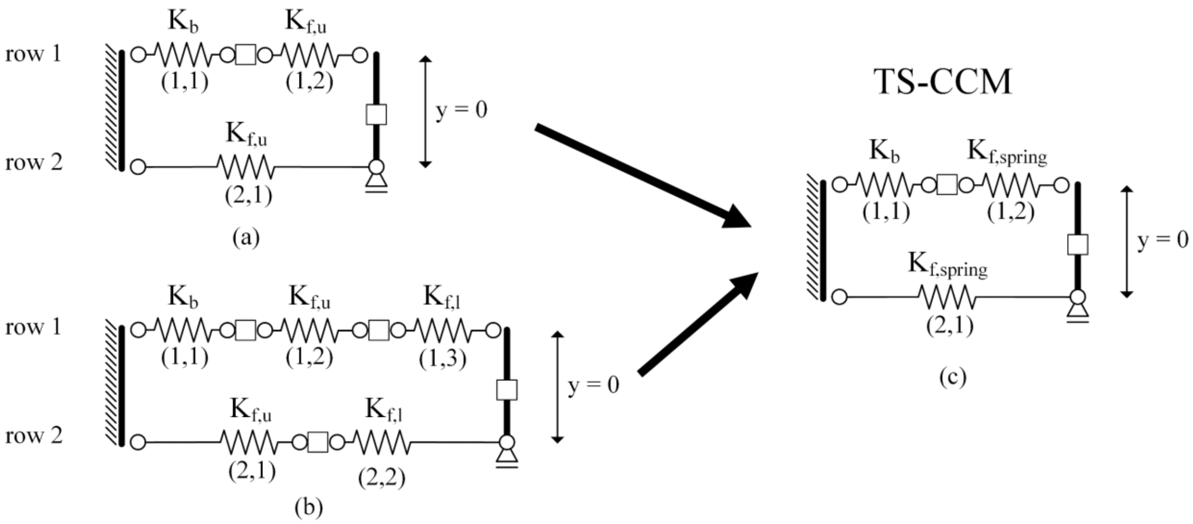

Figure 5.27 – TS-CCM: equivalent stiffness model.

The equivalent stiffness of the tension zone (row 1) of a double T-stub is given by:

$$K_{\mathrm{eq}} = \frac{1}{\frac{1}{K_b} + \frac{1}{K_{\mathrm{f,u}}} + \frac{1}{K_{\mathrm{f,l}}}} \tag{5.1}$$

and in the case of using an equivalent spring

$$K_{\mathrm{eq}} = \frac{1}{\frac{1}{K_b} + \frac{1}{K_{\mathrm{f,spring}}}} \tag{5.2}$$

where K_b is the stiffness of the bolts in tension.

This simplification is discussed to emphasize the need to appropriately consider the bolt stiffness in a coupled T-stub. In a joint, when complex non-linear behaviours are of concern in the context of cyclic loading, the combination into a single equivalent spring is not trivial and it is preferred to consider two independent T-stubs.

5.5.2. Incremental iterative procedure

The computation of the force-deformation behaviour $F_1 - u_1$ of the TS-CCM for a generic load history assuming a displacement control procedure, where u_1 is the control degree of freedom, requires the implementation of an incremental-iterative procedure where the displacements in coordinates 1 and 2 – see Figure 5.26(b) – at the end of each increment i are:

$$\begin{cases} u_1^i = u_1^{i-1} + \delta u_1^i \\ u_2^i = u_2^{i-1} + \delta u_2^i \end{cases} \tag{5.3}$$

where u_1^{i-1} and u_2^{i-1} are the displacements u_1 and u_2 at the end of the increment $i-1$ and δu_1^i and δu_2^i are the variation of u_1 and u_2 in the increment i.

In the same way, the external forces in coordinates 1 and 2 at the end of each increment i are

$$\begin{cases} F_1^i = F_1^{i-1} + \delta F_1^i \\ F_2^i = F_2^{i-1} + \delta F_2^i \end{cases} \tag{5.4}$$

where F_1^{i-1} and F_2^{i-1} are the nodal forces F_1 and F_2 at the end of the increment $i-1$ and δF_1^i and δF_2^i are the variation of F_1 and F_2 in the increment i.

The internal forces in coordinates 1 and 2 are related to the deformation of the components through the compatibility relations

$$\begin{cases} d_{1,1} = u_2 \\ d_{1,2} = u_1 - u_2 \\ d_{2,1} = u_1 \end{cases} \tag{5.5}$$

where $d_{m,n}$ is the deformation of the component n located in row m.

The internal forces in coordinates 1 and 2 can be computed using the equilibrium relations

$$\begin{cases} IntF_1[u_1, u_2] = -f_{1,2} \pm f_{2,1} \\ IntF_2[u_1, u_2] = -f_{1,1} + f_{1,2} \end{cases} \tag{5.6}$$

where $f_{m,n}$ is the internal force in component n located in row m.

Assuming that, at the end of the increment $i-1$, F_1^{i-1} and u_2^{i-1} (matching the imposed values u_1^{i-1} and F_2^{i-1}) are known, the goal is to compute δF_1^i and δu_2^i required to balance a new set of imposed F_2^i and u_1^i through an iterative procedure. The Modified Newton-Raphson method was used to compute the axial force F_1 vs axial displacement u_1 relation making $F_2 = 0$.

The unbalanced forces in each iteration j of increment i are

$$\begin{cases} Q_1 = IntF_1\left[u_1^i, u_2^{i,j}\right] - F_1^{i,j} \\ Q_2 = IntF_2\left[u_1^i, u_2^{i,j}\right] - F_2^i \end{cases} \tag{5.7}$$

where

$$F_1^{i,j} = F_1^i + \delta F_1^{i,j} \tag{5.8}$$

and

$$u_2^{i,j} = u_2^i + \delta u_2^{i,j} \tag{5.9}$$

Because the only unknown in Eq. (5.7) are $\delta F_1^{i,j}$ and $\delta u_2^{i,j}$ in the increment i, the system of internal forces to be solved in each increment is

$$\begin{cases} Q_1\left[\delta F_1^{i,j}, \delta u_2^{i,j}\right] = 0 \\ Q_2\left[\delta u_2^{i,j}\right] = 0 \end{cases} \tag{5.10}$$

In each iteration j of increment i, a better guess of the unknowns $\left(\delta F_1^{i,j+1}, \delta u_2^{i,j+1}\right)$ can be computed expanding the system in Eq. (5.10) into a Taylor's series around the point $\left(\delta F_1^{i,j}, \delta u_2^{i,j}\right)$, leading to:

$$\begin{cases} Q_1\left[F_1^{i,j}, u_2^{i,j}\right] + \left(\delta F_1^{j+1} - \delta F_1^{j}\right) \dfrac{\partial Q_1}{\partial \delta F_1}\left[F_1^{i,j}, u_2^{i,j}\right] + \left(\delta u_2^{j+1} - \delta u_2^{j}\right) \dfrac{\partial Q_1}{\partial \delta u_2}\left[F_1^{i,j}, u_2^{i,j}\right] = 0 \\ Q_2\left[u_2^{i,j}\right] + \left(\delta u_2^{j+1} - \delta u_2^{j}\right) \dfrac{\partial Q_2}{\partial \delta u_2}\left[u_2^{i,j}\right] = 0 \end{cases} \tag{5.11}$$

or, in matrix format

$$\boldsymbol{b}^j + \boldsymbol{A}^j \boldsymbol{\delta}^{j+1} = 0 \rightarrow \boldsymbol{\delta}^{j+1} = -\left(\boldsymbol{A}^j\right)^{-1} \boldsymbol{b}^j \tag{5.12}$$

where

$$\boldsymbol{b}^j = \begin{bmatrix} IntF_1\left[u_1^i, u_2^{i,j}\right] - F_1^{i,j} \\ IntF_2\left[u_1^i, u_2^{i,j}\right] - F_2^i \end{bmatrix} \tag{5.13}$$

$$\boldsymbol{A}^j = \begin{bmatrix} \dfrac{\partial Q_1}{\partial \delta F_1}\left[F_1^{i,j}, u_2^{i,j}\right] & \dfrac{\partial Q_1}{\partial \delta u_2}\left[F_1^{i,j}, u_2^{i,j}\right] \\ 0 & \dfrac{\partial Q_2}{\partial \delta u_2}\left[u_2^{i,j}\right] \end{bmatrix} \tag{5.14}$$

$$\boldsymbol{\delta}^j = \begin{bmatrix} \delta F_1^{j+1} - \delta F_1^j \\ \delta u_2^{j+1} - \delta u_2^j \end{bmatrix} \tag{5.15}$$

Using centred finite differences to compute the Jacobean matrix $\boldsymbol{A}$ we will have

$$\boldsymbol{A}^j = \begin{bmatrix} -1 & \dfrac{IntF_1\left[u_1^i, u_2^{i,j} + \dfrac{du}{2}\right] - IntF_1\left[u_1^i, u_2^{i,j} - \dfrac{du}{2}\right]}{du} \\ 0 & \dfrac{IntF_2\left[u_1^i, u_2^{i,j} + \dfrac{du}{2}\right] - IntF_2\left[u_1^i, u_2^{i,j} - \dfrac{du}{2}\right]}{du} \end{bmatrix} \tag{5.16}$$

where $du = 10^{-10}$ was used.

The solution of the problem in each increment can be achieved with the iterative computation of Eq. (5.12).

5.6. Validation

5.6.1. Introduction

The validation of the decoupling procedure for cyclic modelling of T-stubs is carried out in this section. This requires first that a sample of experimental test results is selected, then that the parameters of the MRA model are computed and finally that the results of the coupled and decoupled models are compared.

A set of experimental tests on T-stub by Oliveira *et al.* (2021) and Piluso and Rizzano (2008) was selected, see Table 5.2. The T-stubs in these experimental campaigns cover rolled and welded T-stub compositions and two distinct failure modes.

The selected specimens were tested under variable amplitude cyclic loading. Constant amplitude tests were disregarded from this analysis since, as already shown in Section 4.3, the MRA is not able to properly reproduce the pinching effect because the pinching level varies for high levels of accumulated energy dissipation and the MRA model assumes it as a constant.

Geometrical and mechanical properties as well as the observed and predicted failure modes of the selected T-stubs are summarized in Chapter 3 .

The compatibility between the model and the experimental results is assessed through the coefficient of determination r^2, using the method of least squares.

Table 5.2 – Selected specimens.

author	T-stub ID	composition	test set up	beam profile	steel grade	bolt size and class	bolt preloading
Oliveira *et al.* (2021)	A1	rolled	coupled	HEA200	S355	M20 (10.9)	80%
	B5			HEB280			
Piluso and Rizzano (2008)	A7	rolled	coupled	HEA180	Fe430*	M20 (8.8)	80%
	B5			HEB180			
	C7	welded		-			

*equivalent to S275

5.6.2. Computation of the MRA parameters

5.6.2.1. Assumptions

For the calibration of the MRA parameters, the following assumptions were considered:

(i) the component bolts in tension (1,1) is tension-only and was classified as non-dissipative, and thus, a linear behaviour was assigned;

(ii) the components tension-only (1,2) and compression-only (2,1) were classified as dissipative; the models represented in Figure 5.9 were assigned to these components with $\beta = 0.01\%$;

(iii) the same MRA parameters were assigned for branches experiencing deformation in the same direction, e.g. ascending branches of both tension-only and compression-only components – $K_{0a,(1,2)} = K_{0a,(2,1)}$;

(iv) the initial stiffness of the bolt in tension component (1,1) was taken according to the EC3-1-8 (CEN, 2005c), i.e. $K_b = K_{b,\mathrm{EC3}}$;

(v) the initial stiffness of the flange in bending component (1,2) and (2,1) was computed according to Eq. (5.17) taking $K_{\mathrm{eq}} = K_{0,\mathrm{exp}}$ and $K_b = K_{b,\mathrm{EC3}}$

$$K_{\mathrm{f,spring}} = \frac{1}{\frac{1}{K_{0,\mathrm{exp}}} - \frac{1}{K_{b,\mathrm{EC3}}}} \tag{5.17}$$

(vi) the post-limit stiffness and the resistance of the flange in bending components (1,2) and (2,1) was taken from the experimental results, i.e. $K_{pl} = K_{pl,\mathrm{exp}}$ and $F_0 = F_{0,\mathrm{exp}}$;

(vii) the MRA pinching parameters were fixed: $t_2 = 0.3$ and $C = 1$.

5.6.2.2. MRA parameters without physical meaning

In order to validate the capability of the decoupled T-stub model to simulate the cyclic behaviour of T-stubs and validate the use of this model for this end, a calibration of the MRA parameters without physical meaning was carried out by trial and error for the small sample of specimens presented in Table 5.2 assigning values to the MRA parameters that, inserted in the model, fit the experimental as close as possible to the numerical cyclic responses.

Table 5.3 summarizes the MRA parameters used for FM1 and FM2, where subscripts a and d are used with reference to the ascending and descending branch, respectively. Despite the MRA model featuring degradation, the selected specimens for this analysis do not present significant strength nor stiffness degradation, unless at the final stage close to the collapse. Accordingly, as discussed in Section 3 , this parameter was not considered, and the study focused on the MRA shape and pinching parameters only.

Table 5.3 – MRA parameters calibrated: shape, pinching and ratios.

author	T-stub ID	$\frac{\beta_u}{\beta_{u,lim}}$	FM	N_a	N_d	t_{1a}	t_{1d}	$\frac{K_{pld}}{K_{pla}}$	$\frac{F_{0,1a}}{F_{0a}}$	$\frac{F_{0,1d}}{F_{0d}}$	$\frac{F_{0d}}{F_{0a}}$
Oliveira *et al.* (2021)	A1	0.52	1	3.6	2.5	5	5	1	0.16	0.42	1.75
Piluso and Rizzano (2008)	C7	0.80	1	3.4	2.5	10	15	1	0.15	0.40	1.62
	A7	1.00	1	2.5	2.5	6	15	1	0.10	0.50	1.60
Oliveira *et al.* (2021)	B5	1.32	2	2.2	1.8	12	21	1	0.48	0.48	1.53
Piluso and Rizzano (2008)	B5	2.28	2	2.2	1.8	6	30	1	0.20	0.40	1.94

5.6.3. Comparison with experimental results

Figures 5.28 to 5.30 (left side) compare the results of the application of the coupled T-stub model for the five selected experimental test results, showing a good match between the models and the experimental tests.

From the qualitative and quantitative points of view, Figures 5.28 to 5.30 show a high degree of accuracy of the model in reproducing the cyclic behaviour of a T-stub. These figures show that the TS-CCM can reproduce the pinching effect and its characteristics identified in Section 3.5, namely: (i) branches with a concave shape and the (ii) progressive reloading stiffness degradation. However, the model does not seem capable of reproducing the slip at reloading. The set of parameters calibrated show in general a very good fit to the experimental results in terms of force – $r^2 = [0.939;\ 0.960]$.

It can be observed that the specimens present a curve shape rounder in the knee-range, especially in the descending branches, and thus, a lower shape parameter is assigned to them, i.e. $N_d \leq N_a$.

Regarding the empirical parameter t_1, as already shown in Section 5.4.5, its influence on the curve shape is noticed in the concavity of the branches – for higher values of t_1, more pronounced is the concave shape. Therefore, higher values of $t_{1d} = [21; 30]$ are used for high levels of pinching, observed mainly in the descending branches of the specimens that failed according to FM2. Less pronounced pinching – branches shape close to a straight line up with slight concave shape – is seen mostly in the ascending branches of specimens failing according to FM1 and FM2, where $t_{1a} = [5; 10]$ and $t_{1a} = [6; 12]$, respectively, and in the descending branches of the ones failing according to FM1 where $t_1 = [5; 15]$.

Furthermore, with regard to the ultimate failure mode, it was observed that when the ratio $\beta_u/\beta_{u,\text{lim}}$– failure mode computed according to Piluso *et al.* (2001a, 2001b) – directly correlates with the level of pinching of the descending branches. However, a larger sample is necessary to confirm this trend. Apart from that, Table 5.3 summarizes the ratios between descending and ascending branches parameters with physical meaning – i.e. initial stiffness, post-limit stiffness and strength.

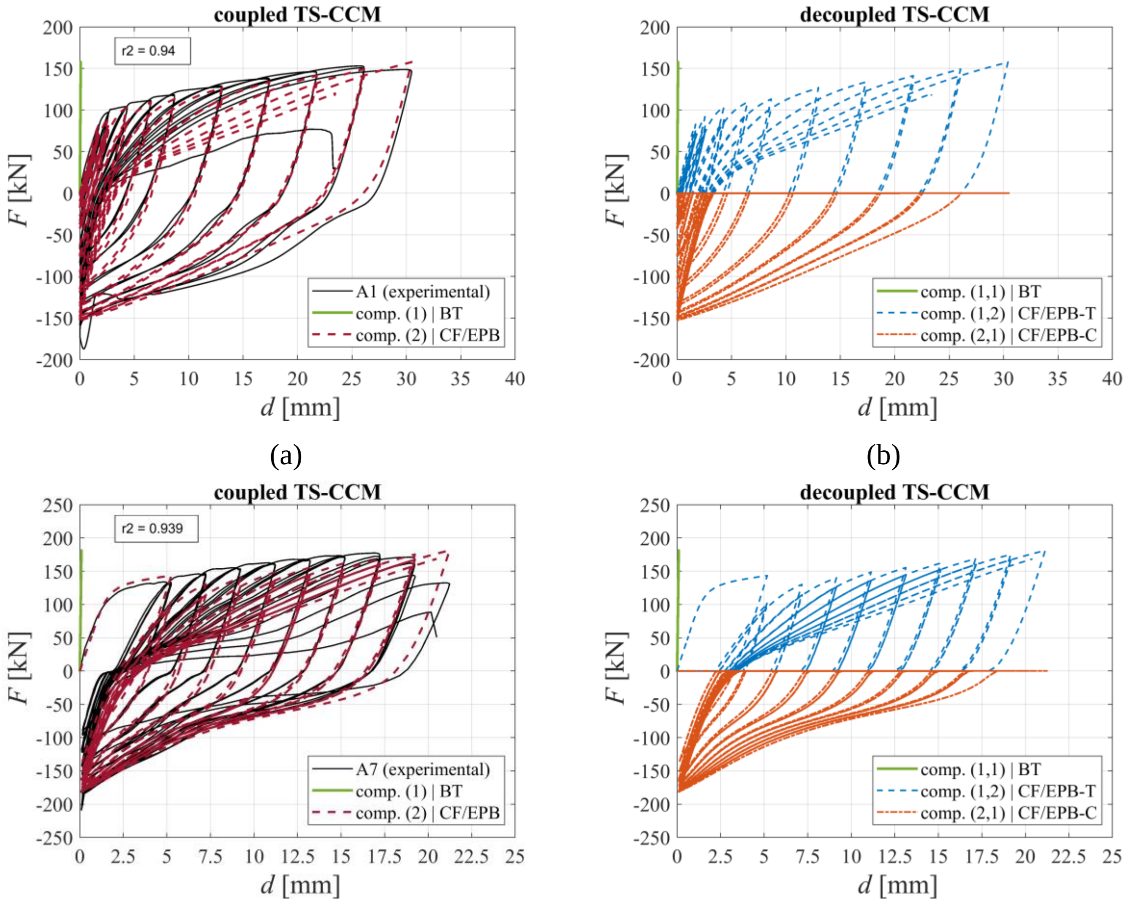

(a) (b)

(c) (d)

Figure 5.28 – TS-CCM and experimental data: (a)-(b) Oliveira *et al.* (2021) and (c)-(d) Piluso and Rizzano (2008) rolled specimens failing under FM1.

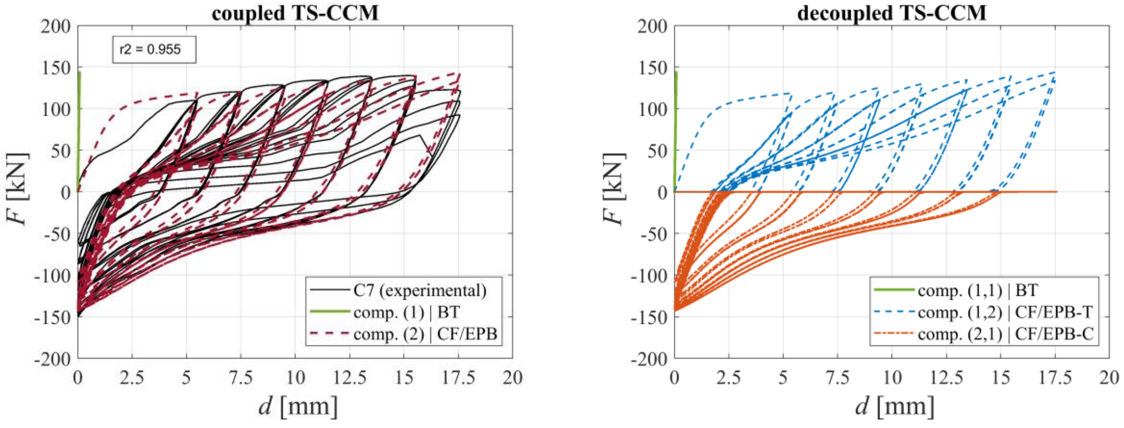

(a) (b)

Figure 5.29 – TS-CCM and experimental data: Piluso and Rizzano (2008) welded specimen failing under FM1.

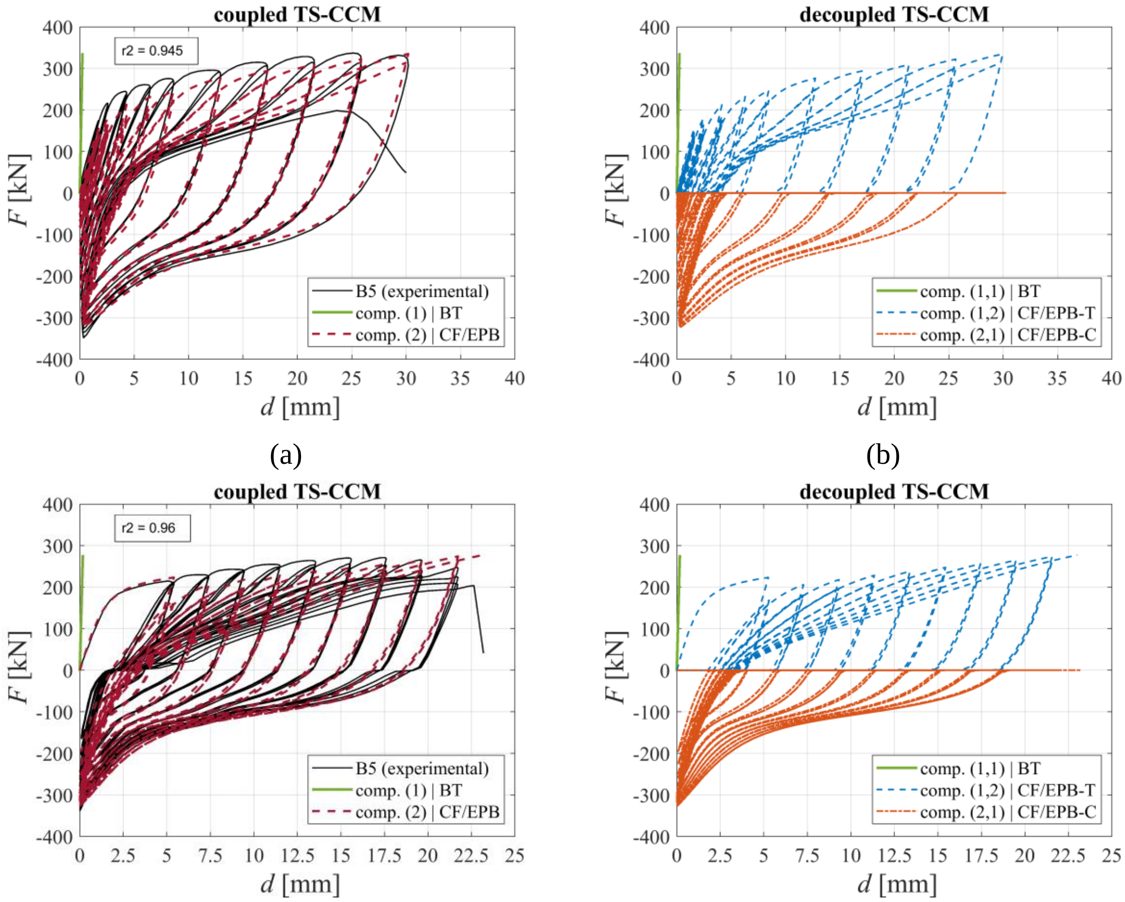

(a) (b)

(c) (d)

Figure 5.30 – TS-CCM and experimental data: (a)-(b) Oliveira *et al.* (2021) and (c)-(d) Piluso and Rizzano (2008) rolled specimens failing under FM2.

5.6.4. Comparison between coupled and decoupled models

Figures 5.28 to 5.30 compare the results of the application of the coupled T-stub model and the decoupled model to the five selected experimental test results using the parameters presented in Table 5.3, showing an exact match between the two cases, therefore proving the correct implementation of the decoupling.

5.7. Sensitivity analysis

5.7.1. MRA parameters range

MRA parameters were calibrated for five distinct bolted T-stubs with different geometries and failure modes. Within the same failure mode, distinct MRA parameters were obtained. A clear range of values was observed for each failure mode, with higher values of pinching being noted for FM2. However, these are empirical parameters with no correlation to the geometric and material properties of the specimens. Therefore, to assess the sensitivity of the T-stub behaviour to the MRA parameters and ratios, a sensitivity analysis (SA) was carried out to test the performance of the mean values of each range. In this context, three analyses were conducted by applying the minimum, mean and maximum values of the range for each parameter to each T-stub. Apart from the comparison in terms of force, the hysteretic energy dissipation, E_h, was used as a criterion of analysis of sensitivity. Table 5.4 summarizes the MRA parameters considered in each analysis.

Table 5.4 – Sensitivity analysis: shape and pinching parameters, and ratios.

FM	SA	N_a	N_d	t_{1a}	t_{1d}	$\frac{K_{pld}}{K_{pla}}$	$\frac{F_{0,1a}}{F_{0a}}$	$\frac{F_{0,1d}}{F_{0d}}$	$\frac{F_{0d}}{F_{0a}}$
	min	2.5	2.5	5.0	5.0	1	0.10	0.40	1.60
1	mean	3.2	2.5	7.0	11.7	1	0.14	0.44	1.66
	max	3.6	2.5	10.0	15.0	1	0.16	0.50	1.75
	min	2.2	1.8	6.0	21.0	1	0.20	0.40	1.53
2	mean	2.2	1.8	9.0	25.5	1	0.34	0.44	1.73
	max	2.2	1.8	12.0	30.0	1	0.48	0.48	1.94

The response curves obtained using the mean values (SA mean), presented in Figures 5.31 to 5.33, show a good agreement between the model and the experimental results. Regarding specimens failing under FM1, the worst agreement with the experimental results is noted in the higher amplitude cycles. Taking a closer look at the ascending branches in Figures 5.31 and Figure 5.32, the mean value – $t_{1a} = 7.0$ – presents a reasonable level of pinching to match the experimental response. In the descending branches, the mean value – $t_{1d} = 11.7$ – represents a higher level of pinching than the observed experimentally for specimen A1 and a lower level of pinching for specimen C7. Good agreement with the experimental results is observed for specimens failing under FM2. The mean values – $t_{1a} = 9.0$ and $t_{1d} = 25.5$ – are acceptable for the level of pinching in the ascending branch compared to the experimental observation and had no significant effect in the descending branches when comparing to the minimum and maximum values.

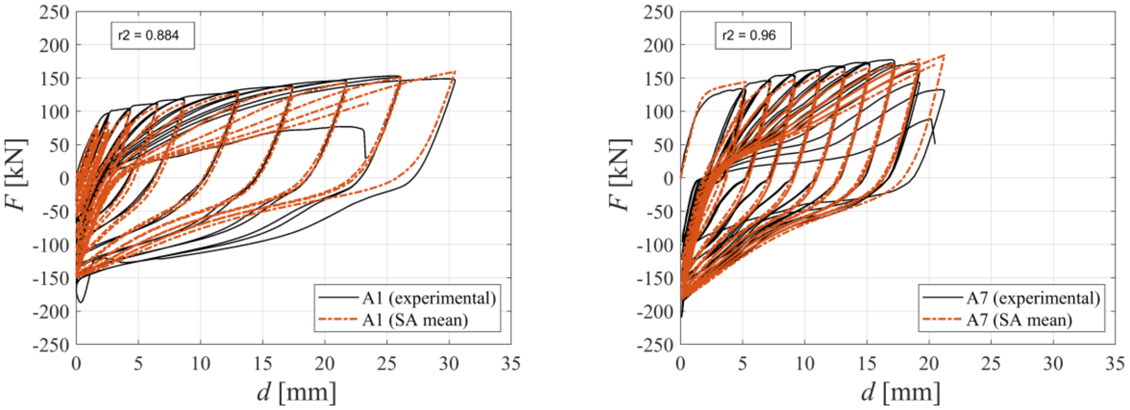

(a) (b)

Figure 5.31 – Sensitivity Analysis (mean): (a) Oliveira *et al.* (2021) and (b) Piluso and Rizzano (2008) rolled specimens failing under FM1.

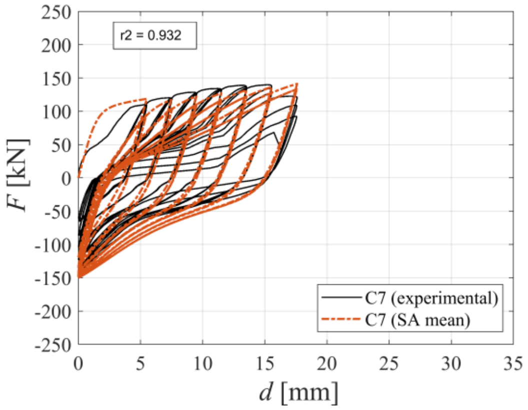

Figure 5.32 – Sensitivity Analysis (mean): Piluso and Rizzano (2008) welded specimen.

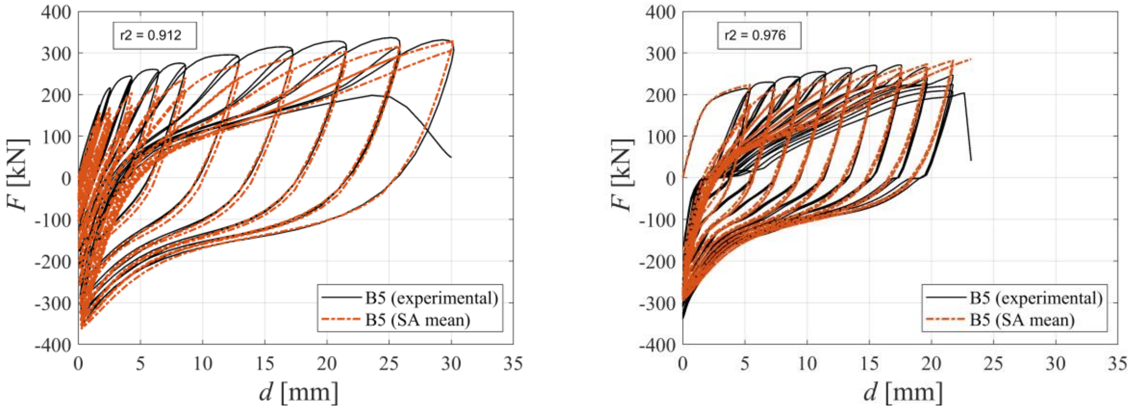

(a) (b)

Figure 5.33 – Sensitivity Analysis (mean): (a) Oliveira *et al.* (2021) and (b) Piluso and Rizzano (2008) rolled specimens failing under FM2.

The sensitivity of the model to the range of MRA parameters considered can also be assessed through energy dissipation. Figures 5.34 to 5.36 present the hysteretic energy dissipation, E_h, per cycle comparing the three SA sets of parameters (min, mean and max) to the experimental results. Adopting the mean values, good agreement between the model and the experimental results is observed in most cycles. The main differences are: (i) in the last cycles, where experimental data revealed strength degradation, which was not simulated in this analysis – see Figures 5.34(b) and 5.35; and (ii) in the particular case of specimen A1 – see Figure 5.34(a) –

in which the parameters did not provide a good adjustment to the experimental data in the ascending and descending branches and thus the dissipated energy of the model is always lower than the experimental data. Despite the discrepancy in the pinching level when using the mean values, the results in terms of hysteretic energy dissipation are in accordance with the experimental data.

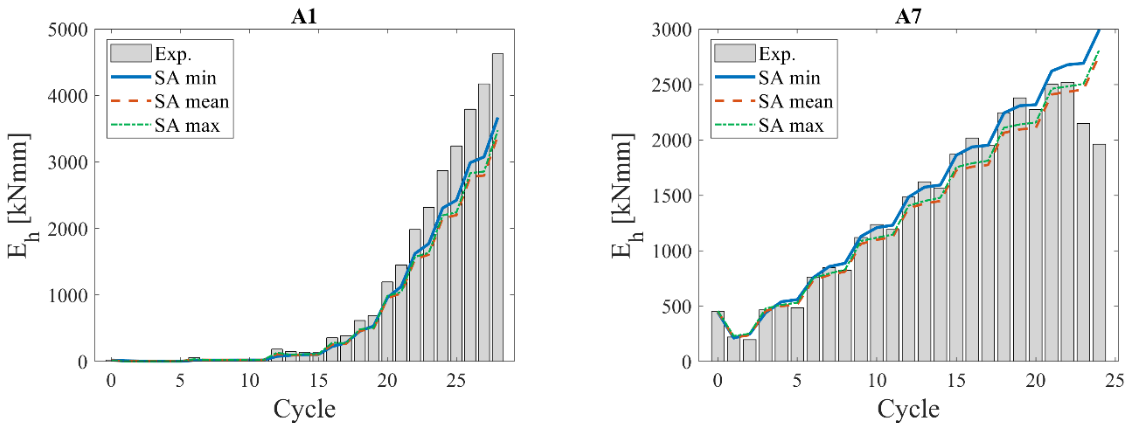

(a) (b)

Figure 5.34 – Hysteretic energy dissipation per cycle (SA): (a) Oliveira *et al.* (2021) and (b) Piluso and Rizzano (2008) rolled specimens failing under FM1.

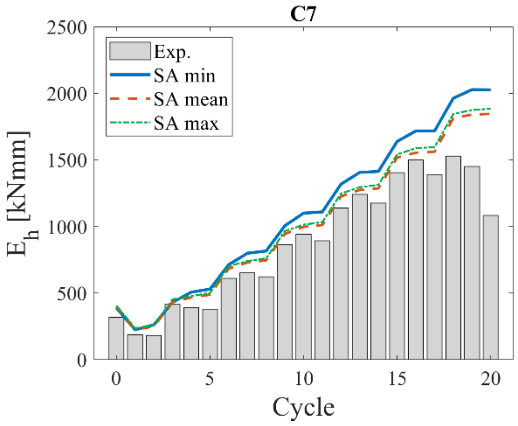

Figure 5.35 – Hysteretic energy dissipation per cycle (SA): Piluso and Rizzano (2008) welded specimen failing under FM1.

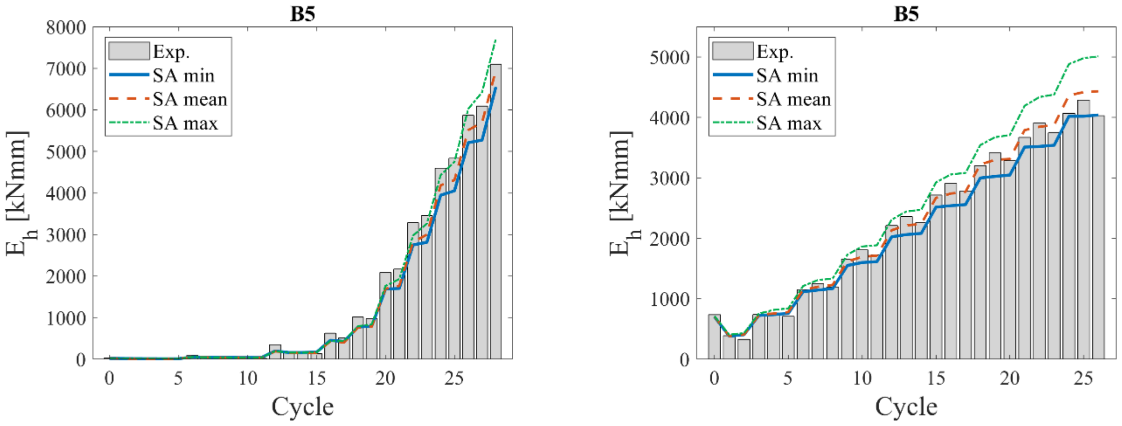

(a) (b)

Figure 5.36 – Hysteretic energy dissipation per cycle (SA): (a) Oliveira *et al.* (2021) and (b) Piluso and Rizzano (2008) rolled specimens failing under FM2.

Table 5.5 summarizes the coefficient of determination r^2 of the fit between the model and experimental results in terms of force and hysteretic energy dissipation. The average ratio of the SA mean is 0.933 for comparison in terms of force and 0.899 in terms of energy, being the one closer to 1 from all SA.

Table 5.5 – Sensitivity analysis: coefficient of determination.

author	T-stub ID	FM	SA min.		SA mean		SA max.	
			F	E_h	F	E_h	F	E_h
Oliveira *et al.* (2021)	A1	1	0.740	0.873	0.884	0.761	0.918	0.793
Piluso and Rizzano (2008)	C7	1	0.893	0.729	0.932	0.835	0.931	0.811
	A7	1	0.933	0.918	0.960	0.923	0.958	0.926
Oliveira *et al.* (2021)	B5	2	0.924	0.965	0.912	0.986	0.887	0.993
Piluso and Rizzano (2008)	B5	2	0.978	0.973	0.976	0.991	0.955	0.938
		μ	0.894	0.892	**0.933**	**0.899**	0.930	0.892

5.7.2. Comparison with refined 3D FEM models

To enlarge the database used to assess the computed MRA parameters that have no physical meaning, a parametric study with refined 3D finite element method (FEM) models was undertaken. The refined 3D FEM models were developed by Santos in (Oliveira *et al.*, 2023) using the ABAQUS software (ABAQUS, 2022) and validated against experimental data. The main geometric parameters that were varied in the study are: (i) bolt size, (ii) flange thickness t_{f}, and (iii) edge distance e. The range of parameters was selected considering the relevant FM and to widen the range of the ratio $\beta_u/\beta_{u,lim}$. Table 5.6 summarizes the main characteristics of the T-stubs.

Table 5.6 – Details of the parametric study with refined 3D FEM models.

T-stub ID	beam profile	bolt size and class	t_{f} mm	e mm	$\frac{\beta_u}{\beta_{u,lim}}$
A-exp	HEA200	M20 (10.9)	9.72	35.69	0.52
A-M16	HEA200	M16 (10.9)	10	35	0.81
A-M22	HEA200	M22 (10.9)	10	35	0.46
A-t8	HEA200	M20 (10.9)	8	35	0.35
A-t12	HEA240	M20 (10.9)	12	35	0.82
A-e30	HEAA^{+}200	M20 (10.9)	10	30	0.56
A-e40	HEA200	M20 (10.9)	10	40	0.55
B-exp	HEA280	M20 (10.9)	17.80	59.20	1.32
B-M16	HEA280	M16 (10.9)	18	60	2.02
B-M22	HEA280	M22 (10.9)	18	60	1.12
B-t15.5	HEA320	M20 (10.9)	15.5	60	1.02
B-t20.5	HEB320	M20 (10.9)	20.5	60	1.81
B-e55	HEA280	M20 (10.9)	18	55	1.30
B-e65	HEA280	M20 (10.9)	18	65	1.41

5.7.2.1. Description of the refined 3D FEM models

The 3D FEM models are generated with solid element type C3D8RH with “Hex” element shape, allowing for non-linear geometrical and material behaviour, assuming at least four elements through the thickness of each plate element. The model is composed of two different parts: (i) the T-stub (see Figure 5.37) and (ii) the components of the bolt as a single part (washer + nut + head). The boundary conditions considered are similar to those considered in the experimental tests, i.e. the tip of the web of the lower T-stub is fixed, while the cyclic loading protocol is applied to the upper one. The analysis comprised two steps:

- Step 1 – preload the bolts with a force equivalent to the preload force defined in EC3-1-8 (CEN, 2005c), using the “Bolt Load” function in ABAQUS;
- Step 2 – application of the cyclic loading protocol.

Normal and tangential contact properties were introduced through the *Surface-to-Surface* contact option, considering the default “hard-contact” property allowing for separation for the first property, and a penalty formulation with a friction coefficient equal to 0.2 for the second.

The material properties were introduced using the Hardening combined method with the half-Cycle available in the software. In this way, it is possible to include the material nonlinearity of the materials and the kinematic hardening component due to cyclic loading. For the T-stub plates, the average results of the true stress – true plastic strain curves from coupon tests were used (D’Aniello *et al.*, 2017), while for the bolts, the formulation of D’Aniello *et al.* (2017) to characterize the tensile behaviour of bolt 10.9 HR was used.

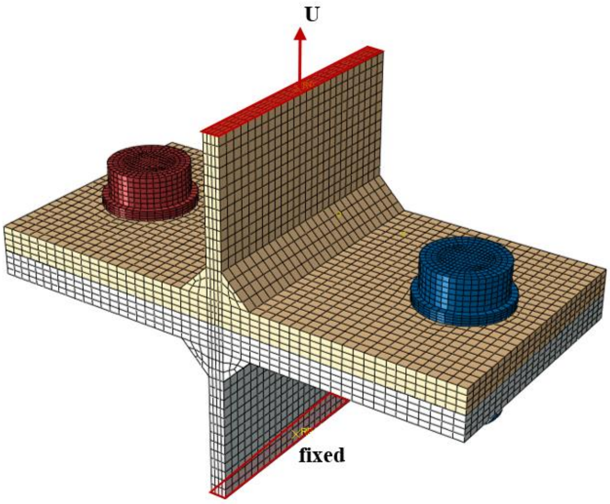

Figure 5.37 – 3D FEM model.

5.7.2.2. Validation of the refined 3D FEM models

Figure 5.38 depicts the results of the FE calculations for specimens A1 and B5 against experimental results by Oliveira *et al.* (2021). The numerical results are compliant with the experimental response, showing that the FE model is accurate.

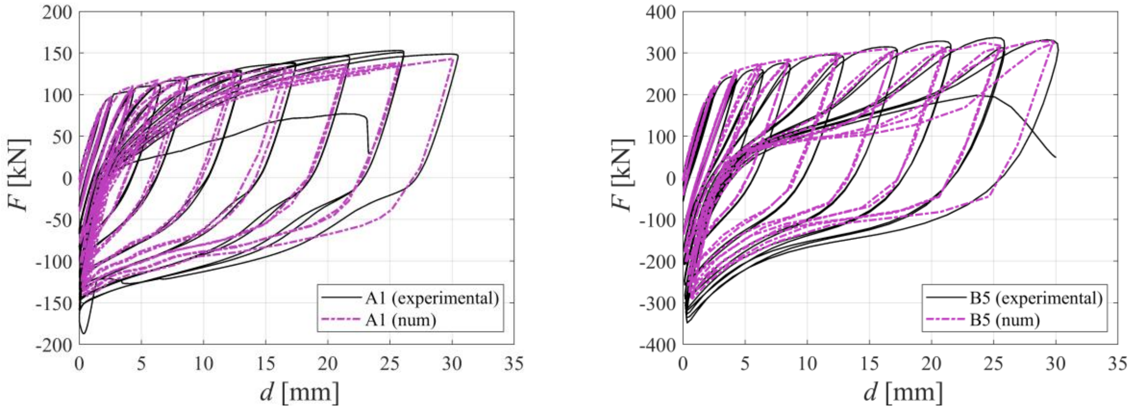

(a) (b)

Figure 5.38 – Validation of the numerical results against experimental results by Oliveira *et al.* (2021).

5.7.2.3. Results of the refined 3D FEM analysis

Table 13 summarizes the resistance and stiffness obtained from the numerical results. The extraction process of these properties from FEM results follows the procedure used in Section 3.4 for experimental tests.

Table 5.7 – Numerical results.

T-stub ID	$F_{0,\text{num}}$ kN	$K_{0a,\text{num}}$ kN/mm	$K_{0d,\text{num}}$ kN/mm	$K_{pl,\text{num}}$ kN/mm	$K_{b,\text{EC3}}$ kN/mm
A	116	70	54	0.8	1929
A-M16	100	58	45	0.9	1306
A-M22	119	73	59	0.7	2091
A-t8	79	44	37	0.5	2097
A-t12	155	105	77	1.1	1742
A-e30	106	56	46	0.5	1903
A-e40	127	93	70	1.2	1903
B	269	131	101	2.2	1399
B-M16	235	193	93	3.0	935
B-M22	292	221	121	2.0	1677
B-t15.5	219	152	95	1.6	1517
B-t20.5	338	284	133	2.0	1281
B-e55	263	192	104	1.7	1389
B-e65	310	252	132	2.0	1389

Figure 5.39 shows the force-deformation curves of the T-stub for varying bolt size (a)-(b), flange thickness (c)-(d) and edge distance (e)-(f). Regardless of the parametric variation, each T-stub series exhibit the expected failure mode, i.e. FM1 for the A series and FM2 for the B series. The initial stiffness and strength all increase with the increase of the above parameters. The pinching level shows slight variations within the same FM.

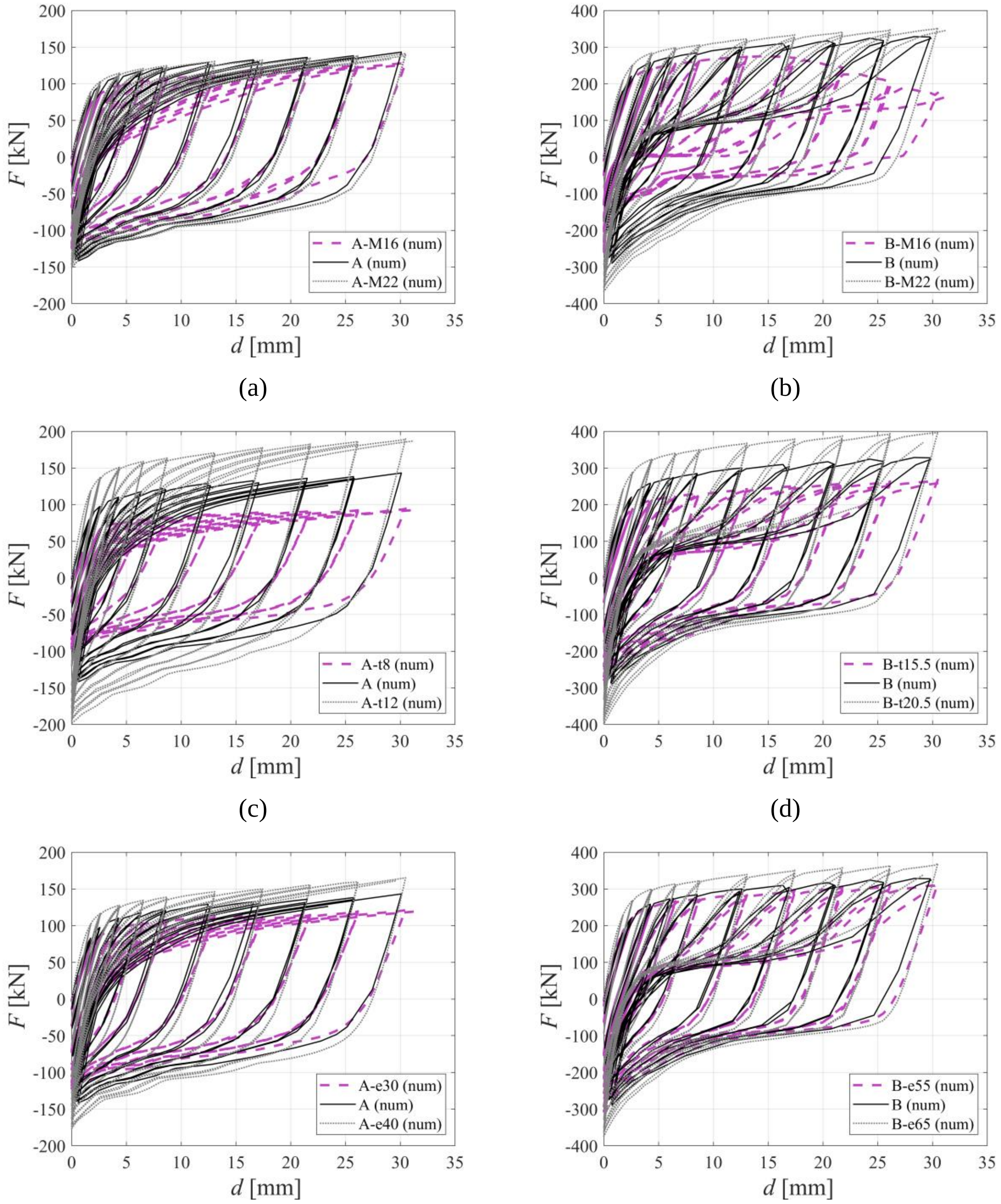

(a) (b)

(c) (d)

(e) (f)

Figure 5.39 – FE parametric study: (a)-(b) bolt size, (c)-(d) flange thickness and (e)-(f) edge distance.

5.7.2.4. Assessment of the MRA parameters against refined 3D FEM models

The validation of the proposed MRA parameters was performed by applying the mean values of the MRA parameters (see Table 5.4) to the parametric study sample. The cyclic curves obtained using the mean values, presented in Figures 5.40 and 5.41, show a good agreement between the TS-CCM and the numerical results. However, for both FM groups, the TS-CCM shows worse results for the load level at the end of the descending branches, meaning that the mean value of the ratio F_{0d}/F_{0a} (see Table 5.4) does not lead to a good match to the results of the refined 3D FEM models. The pinching level agrees for each FM group. To account the clear strength degradation shown by the refined 3D FEM model B-M16, a strength degradation value of $i_F = 0.001$ was considered. Table 5.8 summarizes the goodness of fit between the TS-CCM and the numerical results from refined 3D FEM models. The set of mean parameters calibrated for the MRA shows in general a very good fit to the numerical results of the refined 3D FEM models: the average ratio is 0.938 in terms of force and 0.938 in terms of energy, which compare with 0.933 and 0.899, respectively for the calibration set.

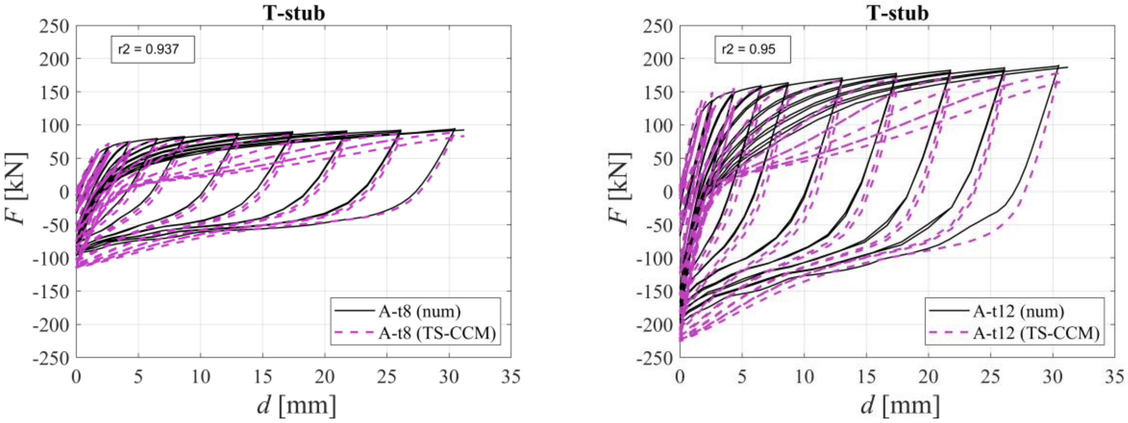

(a) A-t8 (b) A-t12

Figure 5.40 – Numerical vs TS-CCM results: A series.

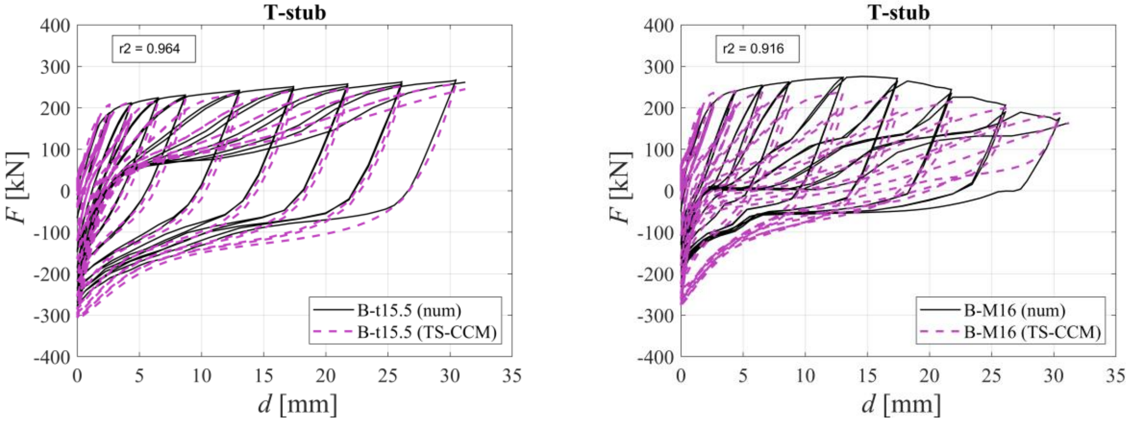

(a) B-t15.5 (b) B-M16

Figure 5.41 – Numerical vs TS-CCM results: B series.

Table 5.8 – Goodness of fit between the TS-CCM and numerical results.

T-stub ID	F	E_h
A1-num	0.939	0.917
A1-M16	0.930	0.958
A1-M22	0.938	0.931
A1-t8	0.937	0.931
A1-t12	0.950	0.970
A1-e30	0.937	0.953
A1-e40	0.910	0.912
B5-num	0.959	0.974
B5-M16	0.916	0.914
B5-M22	0.959	0.975
B5-t15.5	0.964	0.991
B5-t20.5	0.943	0.922
B5-e55	0.898	0.857
B5-e65	0.952	0.931
μ	0.938	0.938
σ	0.019	0.034

5.8. Concluding remarks

Due to the need to account tension-only and compression-only components in the scope of the development of a cyclic component method, a generic decoupled cyclic component model (DTCM) was developed and validated to ensure that it provides results that are equivalent to the coupled model (CTCM). The following conclusions could be established:

- the residual stiffness parameter β required by the tension-only and compression-only MRA models needs to be quite low; a good match is achieved for $\beta = 0.1\%$;
- the shape parameter has a great influence on the curve shape; however, the comparison between the CTCM and DTCM shows accurate results which can be achieved using the same parameter in both models;
- when comparing both models with the same degradation level, a mismatch is observed, which is related to the way the dissipated energy is computed and updated in the incremental and iterative procedure; apart from that, general agreement between CTCM and DTCM has been achieved if a double degradation level is assigned to the components of the DTCM when compared to the component in the CTCM;
- exact match between models has been achieved for all combinations of the pinching/hardening parameters tested using the same pinching/hardening parameters in both models;
- the modelling of the complex cyclic tension-compression behaviour through the component model with decoupled tension-only and compression-only components is feasible.

Based on the last conclusion, a cyclic decoupled component model was developed for the modelling of the cyclic behaviour of T-stubs (TS-CCM) and the parameters for the constitutive relations of the components using the MRA model were computed and validated. It was shown that:

- a suitable range of MRA parameters for the decoupled components was defined using as a criterion the failure mode of the T-stub;
- adopting the mean values of the ranges established (Table 5.4), provides a good agreement between the TS-CCM and the experimental behaviour.

The decoupled cyclic component model of a T-stub (TS-CCM) efficiently and accurately reproduces the load reversal and the transition from tension to compression and vice-versa. Hence, it solves the main difficulty of the numerical implementation of a global cyclic model for a steel joint (Oliveira, Costa, Shahbazian, *et al.*, 2021), opening the way for the reliable prediction of the hysteretic cyclic response of steel joints; this is nowadays possible since the basic properties of the components of a steel joint (stiffness, resistance and ductility) are already available in codes of practice (e.g. EC3-1-8 (CEN, 2005c)).

PART III: CYCLIC COMPONENT MODEL – DEVELOPMENT & IMPLEMENTATION

6 CYCLIC COMPONENT MODEL CONCEPT

6.1. Introduction

The design procedures for dissipative SBCJs lack reliable models for predicting their behaviour under cyclic conditions. On the other hand, the component method (CM) allows accurate prediction for quasi-static monotonic behaviour of SBCJs. The CM has been coded in Eurocode 3 and has been extensively applied in the last decades for design proposes.

This chapter proposes an extension of the CM for the prediction of the cyclic behaviour of SBCJs, hereinafter named Cyclic Component Model (CCM).

6.2. Background

EC3-1-8 (CEN, 2005c) provides a simple procedure for the evaluation of the initial stiffness and the plastic resistance of SBCJs, named component method (CM). The CM also allows the calculation of the full non-linear moment–rotation response of a joint based on adequate characterisation of the non-linear behaviour of each component (Gervásio, Simões da Silva and Borges, 2004).

Figure 6.1 illustrates the relevant components in a typical external end-plate SBCJ and the mechanical model resulting from component assembly for static monotonic loading for hogging (Figure 6.1(a)) and for sagging (Figure 6.1(b)) bending moments.

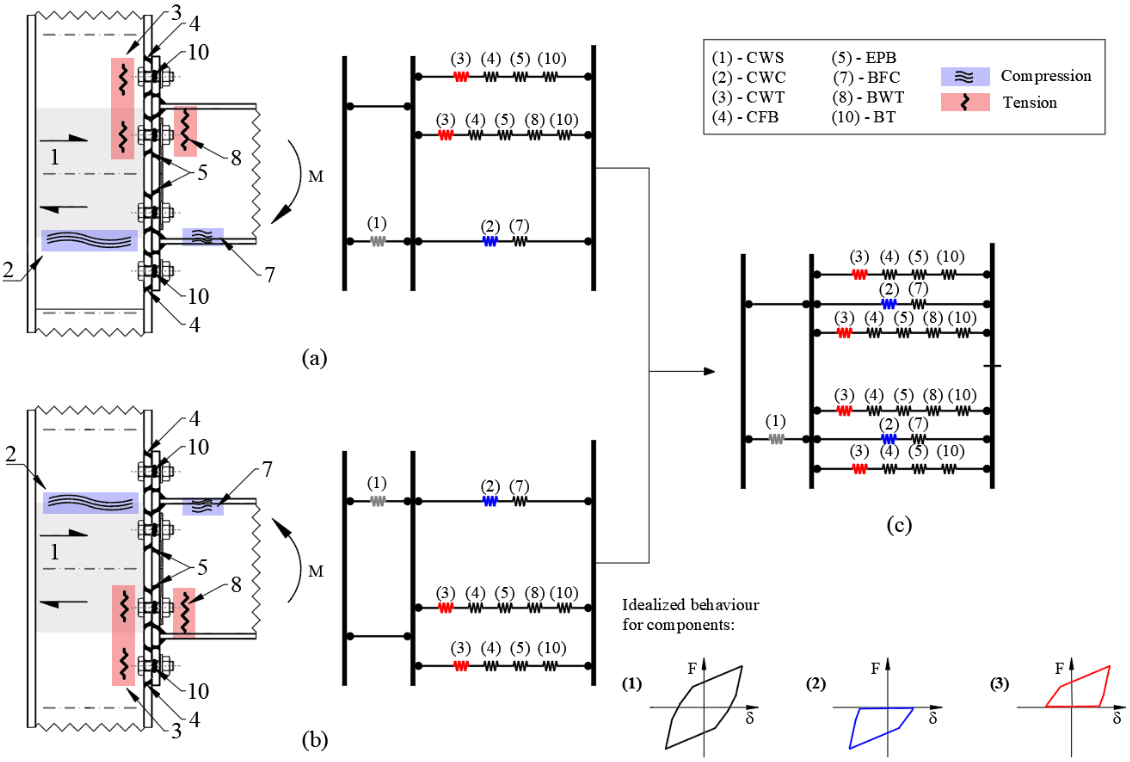

Figure 6.1 – Component models for double-extended end-plate SBCJ for (a) hogging, (b) sagging bending moments, and (c) proposed CCM.

Based on the nature of the CM, each component represents a physical part of a joint and is associated with a specific resultant stress and displacement. Hence, the CM, as illustrated in Figure 6.1(a), cannot deal with sagging bending because different active/relevant components are present, and similarly, the CM, as shown in Figure 6.1(b), cannot deal with hogging bending.

In the context of the behaviour of steel joints subjected to both bending moment and an axial force, de Lima *et al.* and Simões da Silva *et al.* (2004; 2004) proposed the CM for $M - N$ interactions, which can overcome the above problem by defining components that only become active in tension or compression, as illustrated in Figures 6.2 and 6.3. This strategy was successfully implemented for static monotonic loading and is available for use in the freeware, ‘NASCon’ (de Lima *et al.*, 2005).

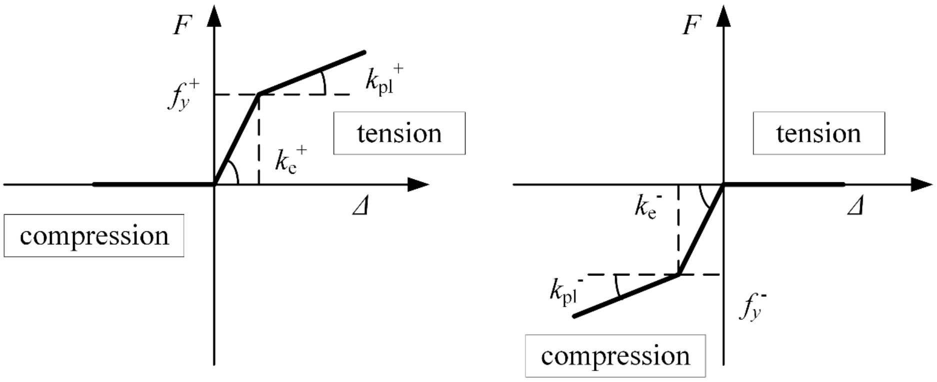

(a) (b)

Figure 6.2 – Typical component behaviour to account $M - N$ interactions according to Lima *et al.* (2004) and Simões da Silva *et al.* (2004): (a) tension-only and (b) compression-only components.

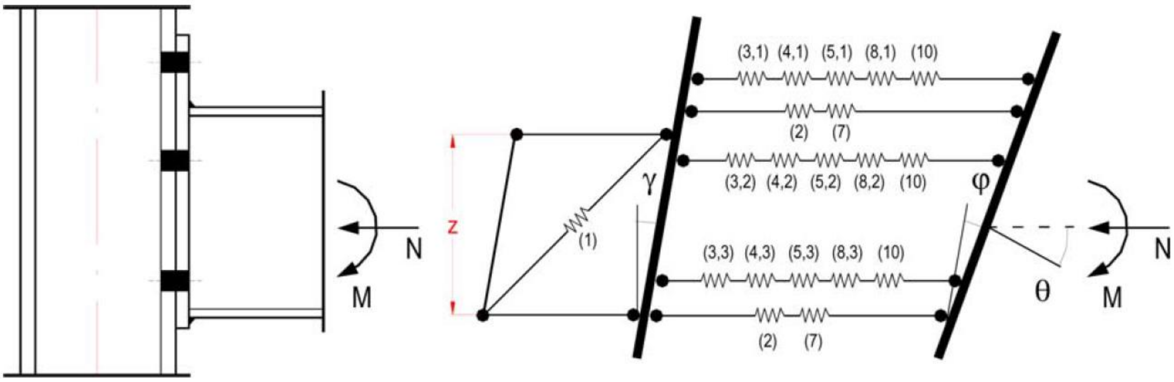

Figure 6.3 – Component assembly for $M - N$ interactions according to Lima *et al.* (2004) and Simões da Silva *et al.* (2004).

Several authors have recently studied and proposed the application of mechanical models not only for monotonic conditions (Shi and Chen, 2017; Zhu, Rasmussen and Yan, 2019; Gil-Martín and Hernández-Montes, 2020) but also for cyclic conditions based on the extension of the CM (Iannone *et al.*, 2011; Latour, Piluso and Rizzano, 2011; D’Aniello, Cassiano and Landolfo, 2016; D’Aniello *et al.*, 2017; Tartaglia *et al.*, 2018; Latour and Rizzano, 2019). Among the several authors who have addressed the development of models to simulate the cyclic behaviour of steel joints, Latour *et al.* (2011) showed that the CM approach can accurately reproduce the cyclic moment–rotation response of steel joints. However, the model developed by Latour *et al.* (2011) does not provide a general implementation consistent with the well-proven CM for static monotonic responses. In addition, it cannot address directly joint configurations with multiple bolt rows because it combines all the components in only one row of components in tension and one row of elements in compression.

Furthermore, the component approach reduces the empirical nature of the models of the type presented in Section 2.4, i.e. for the overall behaviour of joints, by providing a mechanical basis for the process.

6.3. Framework and assumptions

The main idea of the Cyclic Component Model (CCM) relies in the work by Lima *et al.* (2004) and Simões da Silva *et al.* (2004) and considers a model that is able to handle sagging and hogging bending moments assembling in a single model the components required by the models used for both cases. However, some components will be active only in tension and others and others in compression through the development and assigning of appropriate constitutive relations to these components based in the constitutive models for components already available for quasi-static conditions but that account also for the cyclic behaviour. Figure 6.1(c) graphically illustrates the assembly of the CCM.

According to Simões da Silva *et al.* (2009), although several components are considered relevant in a SBCJ even for cyclic behaviour, only a few components show relevant energy dissipation, hereafter called as ‘critical components’ or ‘dissipative components’. This is important because, despite the significant simplifications potentially provided by the CM when compared to 3D non-linear FE models, the problem of modelling the cyclic behaviour of SBCJ using the CM still encloses a high level of complexity.

Following the latte finding, the development of the CCM resulted from the following assumptions:

(i) the beam–to–column joint behaviour is computed imposing the compatibility of deformations and equilibrium of internal force in the mechanical model was ell as the respect of the constitutive relations assigned to components;

(ii) hysteretic behaviour is only considered for a small number of components, which are the dissipative components;

(iii) the non-dissipative components are assumed to behave linear and elastic;

(iv) the constitutive relations of the components are defined with respect to the appropriate effective widths that reflect the geometry of the joint, and in particular, the spacing of the bolt rows according to EC3-1-8 (CEN, 2005c);

(v) the hysteretic behaviour of the dissipative components is modelled using the Richard–Abbott model (Nogueiro *et al.*, 2007);

(vi) with exception of Column Web panel in Shear (CWS), the components are tension-only or compression-only, i.e. they support tension or compression forces, respectively, see Figure 6.2;

(vii) in the mechanical model, components that represent the same physical part of the joint but with different internal forces (tension or compression) are placed in parallel (de Lima *et al.*, 2004; Simões da Silva *et al.*, 2004);

(viii) a catalogue of the tension-only and compression-only hysteretic force–deformation behaviours is developed to allow for the best adjustment to the real cyclic behaviour of each component (Swanson and Leon, 2000; Kim and Engelhardt, 2002; Piluso and Rizzano, 2008; Iannone *et al.*, 2011).

The identification of dissipative components is based on the prior evaluation of the behaviour of the SBCJ for hogging and sagging bending moments under quasi-static monotonic loading conditions based on the following procedure:

- Step 1: the moment–rotation constitutive relations under monotonic conditions for hogging and sagging bending, respectively, are determined using appropriate component models (e.g. see Figure 6.1 for a double extended SBCJ) based on EC3-1-8 (CEN, 2005c) and the constitutive relations for the components that account for the post-elastic phase (Simões da Silva, Santiago and Vila Real, 2002);
- Step 2: the ‘yielding’ sequence of the various components until failure is determined for hogging and sagging bending moments;
- Step 3: the dissipative components are identified as those that present plastic deformations; accordingly, the components that remain in the elastic range are considered as non-dissipative.

The classification of the components is performed before the cyclic analysis and does not change during the load history.

6.4. Characterization of cyclic behaviour of components

6.4.1. Overview

In accordance with the assumptions and the detailed procedure for the cyclic model presented in the previous section, two groups of components need to be characterised: (i) non-dissipative and (ii) dissipative components. In addition, the force-deformation constitutive relations of the components should be implemented, where appropriate, with tension-compression, tension-only or compression-only behaviours.

6.4.2. Non-dissipative components

Figure 6.2 represents the elastic and holonomic cyclic constitutive relations assigned to non-dissipative components for tension-only and compression-only behaviour, see Figures 6.2(a) and 6.2(b), respectively.

6.4.3. Dissipative components

For the illustration of the diversity of the constitutive relations that can be derived from the original MRA model (and used in the scope of the CCM) – see Section 5.3 for detailed description, Figures 5.9 and 6.4 present some variants. These are tension–compression (Figures

5.9(a) and 6.4(a)), tension-only (Figures 5.9(b) and 6.4(b)) and compression-only (Figures 5.9(c) and 6.4(c)) behaviours.

Figure 5.9 illustrates the cases with pinching, typical of the T-stub components, i.e. column flange and end-plate in bending components. Whereas Figure 6.4 illustrates the cases without pinching and without degradation, usually seen in the column web components, namely (a) tension-compression for the CWS, (b) tension-only for the CWT and (c) compression-only for the CWC.

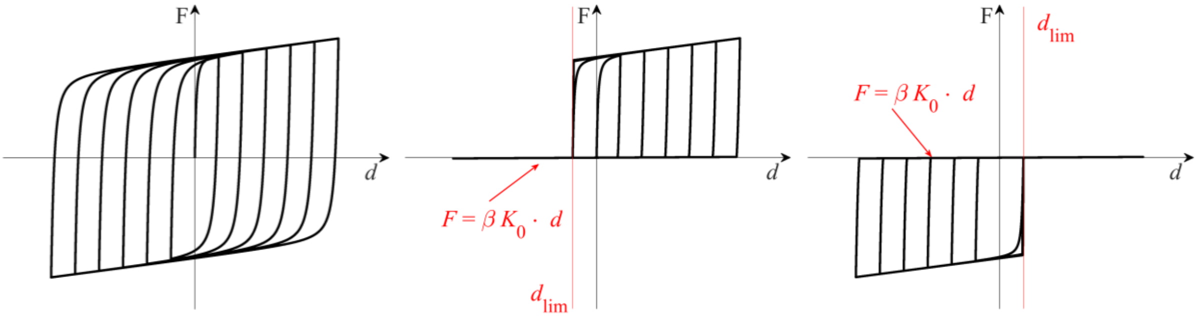

(a) tension-compression (b) tension-only (c) compression-only

Figure 6.4 – Constitutive relations for dissipative components.

6.5. Concluding remarks

This chapter describes concept behind the development of the CCM for predicting the cyclic behaviour of SBCJs. The CCM is a component-based method that uses the principles of the CM coded in EC3-1-8 (CEN, 2005c) providing a familiar and general framework for prediction of the cyclic behaviour of SBCJs. The CCM also allows the assessment of the influence of key geometrical and mechanical properties of the SBCJs in their cyclic response.

7 COMPUTATIONAL IMPLEMENTATION

7.1. Introduction

The CCM proposed in the previous chapter requires a tool to solve the non-linear governing equations system of the mechanical model considering the compatibility of deformations imposed by the rigid elements and the boundary conditions, the static equilibrium, and the constitutive relations of the components. Therefore, a computer program, named UCyclic, was developed in MATLAB (2019) to assist the computation of the SBCJs response, the input of the model and the analysis of results. The program is organized in three interconnected modules:

(i) CurveFitting module was developed to identify the parameters of the MRA model from the force-deformation response of components extracted from experimental tests or refined 3D FEM models;

(ii) CompModel Calculator module is a FEM based program developed to compute the quasi-static cyclic non-linear behaviour of SBCJs through an incremental-iterative procedure with displacement control;

(iii) ResultsAnalyser module assists the user in the analysis of the behaviour of the joint, the connection and individual components.

This chapter describes the computational implementation of the current stage of the CCM.

7.2. CurveFitting

7.2.1. Introduction

The CurveFitting module is a pre-processor used to identify the parameters of the MRA model from the force-deformation response of dissipative extracted form experimental tests or refined 3D FEM models under either monotonic or cyclic loading. The parameters required for each component can be computed for symmetrical or asymmetrical behaviour. However, it is also possible to impose some parameters, such as the initial stiffness or/and the strength (e.g. computed according to EC3-1-8 (CEN, 2005c)), and compute the best-fit solution for the remaining parameters.

7.2.2. Curve fitting process

Figure 7.1 shows the flowchart of the curve fitting process implemented in CurveFitting module.

The program identifies a fit to the force-deformation data using the MRA model (see Section 2.4.1.4) and it allows six curve fitting types (CFT):

- CFT1: not imposing any parameter;
- CFT2: imposing the same K_0 for the ascending and the descending branches;
- CFT3: imposing different values of K_0 for the ascending (K_{0a}) and the descending (K_{0d}) branches;
- CFT4: imposing the same K_0 and F_0 for the ascending and the descending branches;

- CFT5: imposing different values of K_0 and F_0 for the ascending ($K_{0\mathrm{a}}$, $F_{0\mathrm{a}}$) and for the descending ($K_{0\mathrm{d}}$, $F_{0\mathrm{d}}$) branches;
- CFT6: imposing the main four MRA parameters (K_0, K_{pl}, F_0 and N) to assess visually the implementation of the mechanical behaviour (see section 6.4) with the obtained MRA parameters.

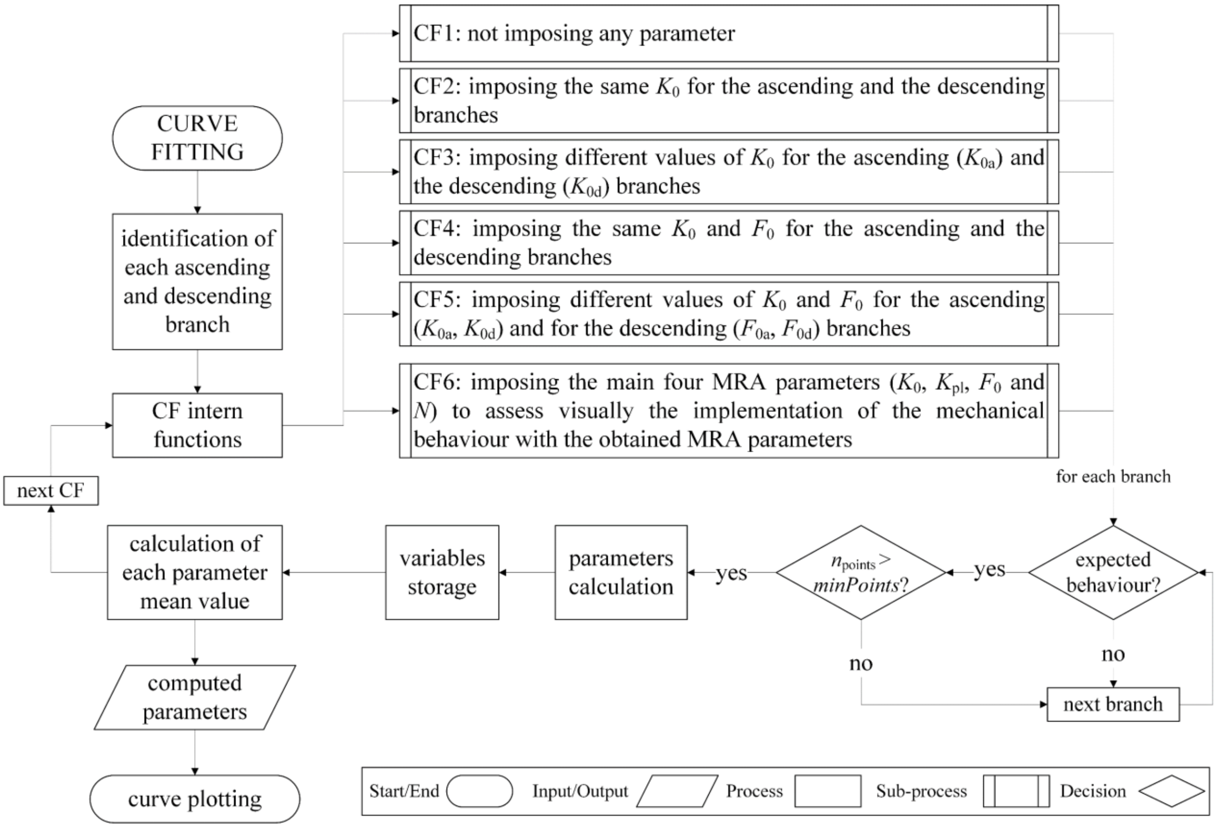

Figure 7.1 – CurveFitting flowchart.

To perform the curve fitting, a function already available in MATLAB is used (least-squares fitting) that allows several types of least-squares fitting. Nonlinear least-squares was chosen to fit data using the MRA equation. This procedure uses an iterative approach which starts with an initial guess for each coefficient and then employs the Trust-region algorithm to adjust the coefficients (MATLAB, 2015).

CurveFitting module records the fit for each ascending and descending branch in figures and exports all the computations to an output .xlsx file.

7.3. CompModel Calculator

7.3.1. Introduction

The CompModel Calculator is a FEM-based software developed to compute the quasi-static monotonic and cyclic non-linear behaviour of CM based mechanical model – illustrated in Figure 6.1 – using and incremental-iterative procedure with displacement control according to Meek (1991) that also accounts future need for implementing alternative non-linear methods (load control, arc-length).

CompModel Calculator may be used to predict the quasi-static monotonic and cyclic behaviour of SBCJs with arbitrary dimensions that lie within the limits of application of EC3-1-8 (CEN, 2005c). The user can independently define components and their behaviour based on the typology of the joint.

7.3.2. Mechanical model

The algorithm was developed by assuming an external SBCJ. Figure 7.2 shows the free-body diagram for a generic joint test and defines the notation for the forces applied around the joint.

Usually, the column top has a roller support and the bottom has pinned support. The joint is subjected to bending caused by the vertical load (P) applied at the beam's end.

Figure 7.2 also shows the support reactions (R and H), the shear and bending forces at the joint core periphery – column and beam shear forces (V_c and V_b) and bending moments (M_c and M_b) – and the internal forces diagrams (bending moment and shear).

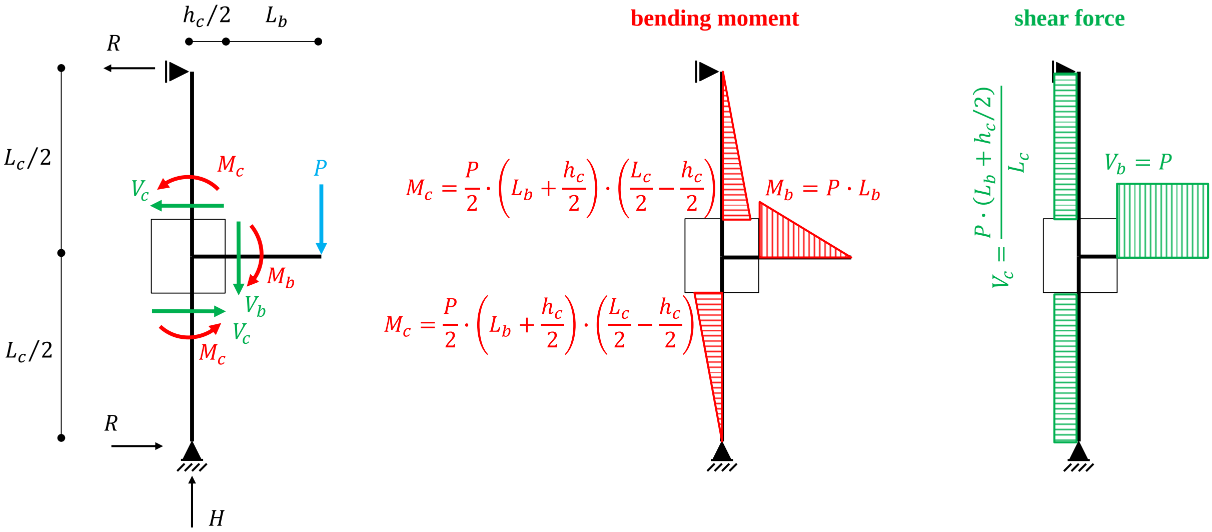

Figure 7.2 – General external joint test: shear forces and bending moments acting on a joint periphery, reaction forces and internal forces diagrams.

The mechanical model of the joint concerns a general joint typology, with an arbitrary number of components (springs) per row and an arbitrary number of rows, see Figure 7.3.

At the current stage of development, as kinematic restrictions the mechanical model considers only the conservation of plane sections at the connection-beam interfaces and the connection-column web panel in shear (CWS) interfaces. These kinematic restrictions are considered in the mechanical model through two 1D rigid elements placed along the column axis direction (y axis). The 1D rigid element at the connection-CWS interface (left rigid element in Figure 7.3, generalized node 2) is pinned at the bottom end (centre of the beam flange, $y = 0$) and the CWS component is placed at the CWS-upper column interface ($y = y_{\mathrm{CWS}}$) connected to the 1D rigid element at the connection-CWS interface (right rigid element in Figure 7.3, generalized node 2). The CWS component is also connected to node 1 in Figure 7.3 that is prevented from having displacements. The 1D rigid element at the connection-beam interface (generalized node 3 in Figure 7.3) is prevented from having vertical displacement and the space between the two rigid elements (main assembly) is where the connection components will be assembled.

The components are numbered sequentially, within the main assembly, starting from the first (top) row (higher y): the model is assumed to have r rows and each row is assumed to have S_m components plus the CWS (not accounted in one of the rows), leading to $\sum_{m=1}^{r} S_m + 1$ components – the number assigned to each component is displayed next to the related spring in Figure 7.3. The model thus includes n_d nodes (nodes: 1, 4, …, n_d) – assigned between two components, a row with a single component does not require an additional node – and two generalised nodes (nodes 2 and 3).

The displacements of the nodes are the primary unknown variable of the problem, a node between two components (0D element) has one degree of freedom (DOF) in the x direction, node 1 has no DOFs, generalized node 2 has one DOF and generalized node 3 has three DOFs. Each component is oriented according to x axis and the local coordinate system considered is represented in Figure 7.4. All the nodes are restrained against vertical displacement leading to $n_f = n_d$ degrees of freedom (DOFs) – the numbering of the DOFs is displayed next to the related arrows in Figure 7.3.

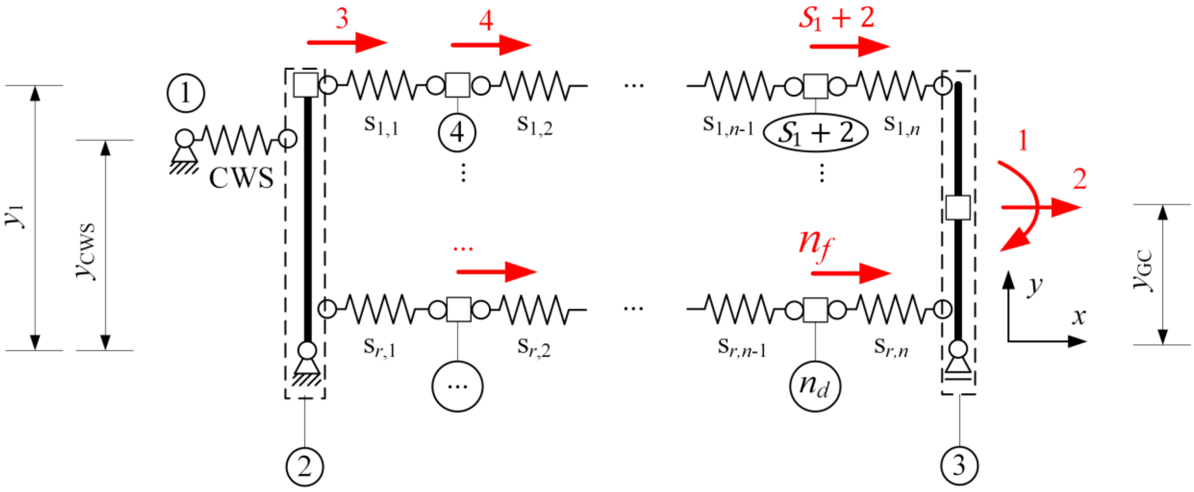

Figure 7.3 – Generic joint geometry, global mode numbering, components numbering and global DOFs.

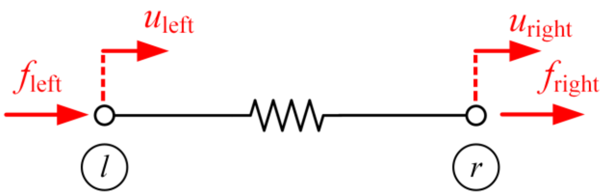

Figure 7.4 – Simple spring: local coordinate system.

7.3.3. Algorithm

7.3.3.1. Tangent stiffness of each component

Tangent stiffness, $k_n^{i,j}$, is one of the most critical parts of the iterative procedure. Accordingly, several procedures for computing the tangent stiffness of each component were implemented. These are used in succession, i.e. in case one fails to lead to convergence the next used is used.

The basic tangent stiffness values of each component in each iteration j of an increment i were computed according to the following steps:

1) compute the deformation for each component n, $d_n^{i,j}$;

2) compute the internal forces in each component n for deformations $d_n^{i,j}$ and $d_n^{i,j} \pm \Delta/2$ using the constitutive relations of the components (Δ is a very small increment of deformation of the component, see Figure 7.7);
3) compute the forward and backward finite differences according to the following expressions:

$$k_{1n}^{i,j} = \frac{f_n^{i,j} \cdot d_n^{i,j} - f_n^{i,j} \cdot \left(d_n^{i,j} - \frac{\Delta}{2}\right)}{\frac{\Delta}{2}}, k_{2n}^{i,j} = \frac{f_n^{i,j} \cdot \left(d_n^{i,j} + \frac{\Delta}{2}\right) - f_n^{i,j} \cdot d_n^{i,j}}{\frac{\Delta}{2}} \tag{7.1}$$

$$k_n^{i,j} = \frac{f_n^{i,j} \cdot \left(d_n^{i,j} + \frac{\Delta}{2}\right) - f_n^{i,j} \cdot \left(d_n^{i,j} - \frac{\Delta}{2}\right)}{\Delta} \tag{7.2}$$

The tangent stiffness values for each component in the assembling of the global stiffness matrix were assumed in the following order:

1) maximum value – the tangent stiffness is given by the maximum value between $k_{1n}^{i,j}$ and $k_{2n}^{i,j}$;
2) central finite difference – the tangent stiffness is given by $k_n^{i,j}$;
3) forward finite difference – the tangent stiffness is given by $k_{2n}^{i,j}$;
4) backward finite difference – the tangent stiffness is given by $k_{1n}^{i,j}$;
5) forward and backward finite difference – this method depends on the direction of the rotation, as well as on the position of the component in relation to the neutral axis:

a) if the last joint rotation increment is positive:
   i) and the component is above the neutral axis, the tangent stiffness is given by $k_{2n}^{i,j}$;
   ii) and the component is below the neutral axis, the tangent stiffness is given by $k_{1n}^{i,j}$;
b) if the last joint rotation increment is negative:
   i) and the component is above the neutral axis, the tangent stiffness is given by $k_{1n}^{i,j}$;
   ii) and the component is below the neutral axis, the tangent stiffness is given by $k_{2n}^{i,j}$;

In addition, for case 1) (maximum value) and 5) (forward and backward finite difference) to account for cases with values of the displacements very small (close to the origin) in tangent stiffness computation, the following additional measures were considered:

a) if the deformation $d_n^{i,j}$ is too small and positive, i.e. $0 \leq d_n^{i,j} \leq \Delta/2$, the tangent stiffness is given by $k_{2n}^{i,j}$;
b) if the deformation $d_n^{i,j}$ is too small and negative, i.e. $-\Delta/2 \leq d_n^{i,j} \leq 0$, the tangent stiffness is given by $k_{1n}^{i,j}$.

Accordingly, case 1) (maximum value) was initially assumed and if the iterative procedure fails then case 2) (central finite difference) would be assumed instead and so on until convergence is reached.

7.3.3.2. Assembling of global stiffness matrix

For the mechanical model proposed, a global stiffness matrix is assembled from the tangent stiffness for all components. The global stiffness matrix is symmetrical, therefore, only the lower or upper half needs to be determined.

Eq. (7.3) represents the generic global stiffness matrix, where each row and each column of the matrix is associated to a DOF.

$$\boldsymbol{K}_g = \begin{bmatrix} K_{1,1} & & & & & & \\ K_{2,1} & K_{2,1} & & & & & \\ K_{3,1} & K_{3,2} & K_{3,3} & & & & \\ \vdots & \vdots & \vdots & \ddots & & & \\ K_{i,1} & K_{2,1} & K_{i,3} & \dots & K_{i,j} & & \\ \vdots & \vdots & \vdots & \vdots & \vdots & \ddots & \\ K_{n_f,1} & K_{n_f,2} & K_{n_f,3} & \dots & K_{n_f,j} & \dots & K_{n_f,n_f} \end{bmatrix} \tag{7.3}$$

The stiffness term $K_{i,j}$ from the global stiffness matrix $\boldsymbol{K}_g$, where both i and j varies from 1 till the total number of DOFs (n_f), represents the force that is required in DOF j to prevent any displacement when a unitary displacement is imposed in DOF i. According to the model assembly in Figure 7.3, the non-null elements of the lower half of the global stiffness matrix were computed using the following procedure:

(i) *first row*

The first row of the assembled stiffness matrix is related to DOF 1, i.e. the rotation in node 3 (see Figure 7.3). The element in row 1 of the global stiffness matrix is given by:

$$K_{1,1} = \sum_{m=1}^{r} (y_m - y_{\mathrm{GC}})^2 \cdot k_{m,\mathrm{rightmost}} \tag{7.4}$$

where $k_{m,\mathrm{rightmost}}$ is the tangent stiffness for the last (the rightmost) spring in each row, y_m is the y coordinate of components of row m and y_{GC} is the y coordinate of beam geometric centre.

(ii) second row

The second row of the assembled stiffness matrix is related to DOF 2, i.e. the displacement along x of the centroid of the beam in the generalized node 3 (see Figure 7.3). The elements in the two first columns in row 2 of the global stiffness matrix are given by:

$$K_{2,1} = \sum_{m=1}^{r} (y_m - y_{\mathrm{GC}}) \cdot k_{m,\mathrm{rightmost}} \tag{7.5}$$

$$K_{2,2} = \sum_{m=1}^{r} k_{m,\mathrm{rightmost}} \tag{7.6}$$

(iii) third row

The third row is related to DOF 3, i.e. the displacement along x of the left 1D rigid elemnt assigned on the topmost row (node 2, see Figure 7.3). The elements in the first three columns in row 3 of the global stiffness matrix are given by:

$$K_{3,1} = K_{3,2} = 0 \tag{7.7}$$

$$K_{3,3} = k_{\mathrm{CWS}} \left(\frac{y_{\mathrm{CWS}}}{y_1}\right)^2 + \sum_{m=1}^{r} \left(\frac{y_m}{y_1}\right)^2 \cdot k_{m,\mathrm{leftmost}} \tag{7.8}$$

where $k_{m,\mathrm{leftmost}}$ is the tangent stiffness for the first (the leftmost) spring in each row and y_{CWS} is the y coordinate of the CWS spring.

(iv) remaining rows

The remaining elements of the global stiffness matrix are given by:

- CASE 1: neither the last nor the first DOF of the row

If the node which the DOF is assigned is neither the leftmost nor the rightmost of a row of the model assembly, then:

$$K_{\mathrm{DOF,DOF-1}} = -k_{\mathrm{left}} \tag{7.9}$$

$$K_{\mathrm{DOF,DOF}} = k_{\mathrm{left}} + k_{\mathrm{right}} \tag{7.10}$$

where k_{left} and k_{right} are the tangent stiffness of the components which are immediately in the left and in the right, respectively, side of the node where the DOF is assigned.

- CASE 2: last DOF of the row (rightmost)

If the node which the DOF is assigned to is the last one (the rightmost) of a row of the model assembly (besides node 3, see Figure 7.3), then:

$$K_{\mathrm{DOF,1}} = -(y_m - y_{\mathrm{GC}}) \cdot k_{\mathrm{right}} \tag{7.11}$$

$$K_{\mathrm{DOF},2} = -k_{\mathrm{right}} \tag{7.12}$$

$$K_{\mathrm{DOF},\mathrm{DOF}-1} = -k_{\mathrm{left}} \tag{7.13}$$

$$K_{\mathrm{DOF},\mathrm{DOF}} = k_{\mathrm{left}} + k_{\mathrm{right}} \tag{7.14}$$

- CASE 3: first DOF of the row (leftmost)

If the node which the DOF is assigned to is the first one (the leftmost) of a row of the model assembly (besides node 2, see Figure 7.3), then:

$$K_{\mathrm{DOF},\mathrm{DOF}} = k_{\mathrm{left}} + k_{\mathrm{right}} \tag{7.15}$$

$$K_{\mathrm{DOF},3} = -\left(\frac{y_m}{y_1}\right) \cdot k_{\mathrm{left}} \tag{7.16}$$

- CASE 4: only DOF of the row

If the node which the DOF is assigned to is the only one of the row (besides nodes 2 and 3, see Figure 7.3) then:

$$K_{\mathrm{DOF},1} = -(y_m - y_{\mathrm{GC}}) \cdot k_{\mathrm{right}} \tag{7.17}$$

$$K_{\mathrm{DOF},2} = -k_{\mathrm{right}} \tag{7.18}$$

$$K_{\mathrm{DOF},3} = -\left(\frac{y_m}{y_1}\right) \cdot k_{\mathrm{left}} \tag{7.19}$$

$$K_{\mathrm{DOF},\mathrm{DOF}} = k_{\mathrm{left}} + k_{\mathrm{right}} \tag{7.20}$$

The rest of the elements of the global stiffness matrix $\boldsymbol{K}_g$ are equal to zero (null).

7.3.3.3. Internal forces vector

To compute the internal forces vector for increment i and iteration j ($\boldsymbol{IntF}^{i,j}$), the following procedure was considered:

$$IntF_1^{i,j} = \sum_{m=1}^{r} -f_{m,\text{rightmost}}^{i,j} \cdot (y_n - y_{CG}) \tag{7.21}$$

$$Int_2^{i,j} = \sum_{m=1}^{r} -f_{m,\text{rightmost}}^{i,j} \tag{7.22}$$

$$IntF_3^{i,j} = -f_{\text{CWS}}^{i,j} \cdot \frac{y_{\text{CWS}}}{y_1} + \sum_{m=1}^{r} f_{m,\text{leftmost}}^{i,j} \cdot \frac{y_m}{y_1} \tag{7.23}$$

$$IntF_{\text{DOF}}^{i,j} = -f_{m,\text{left}}^{i,j} + f_{m,\text{right}}^{i,j} \tag{7.24}$$

where $f_{\text{CWS}}^{i,j}$ is the internal force in component column web panel in shear (CWS), $f_{m,\text{rightmost}}^{i,j}$ and $f_{m,\text{leftmost}}^{i,j}$ are the internal forces of rightmost and leftmost components in row m, respectively, $f_{m,\text{right}}^{i,j}$ and $f_{m,\text{left}}^{i,j}$ are the internal forces of components in the left and right side on the node where the DOF is assigned to, respectively.

7.3.3.4. Hysteretic energy dissipation

The MRA model considers the accumulated dissipated energy (E_h) to assess the strength and stiffness degradations, see Eqs. (2.12) and (2.13), respectively.

The hysteretic energy dissipated in a cycle corresponds to the area enclosed by the $F - d$ curve. In CompModel Calculator the hysteretic energy dissipated by each component is computed at the end of each increment using the trapezoidal rule. Figure 7.5(a) illustrates the procedure for an increment i (A_i).

The parameter E_h in the MRA model cannot be updated continuously because that would leave to convergence problems. On the other hand, to avoid a “jump” in the $F - d$ curve of each component when $F = 0$ due to the update of the energy dissipated E_h in the previous half cycle, E_h is updated in the MRA model only in the transition points between the ascending and the descending branches (and vice versa). As an example, Figure 7.5(b) shows the dissipated energy in the first half cycle, E_0, which begins at the point of origin and ends when $F = 0$ (dot No. 1) – the dissipated energy E_0 is taken into count only in the end of the descending branch (dot A). Similarly, the same is done for the following half cycles.

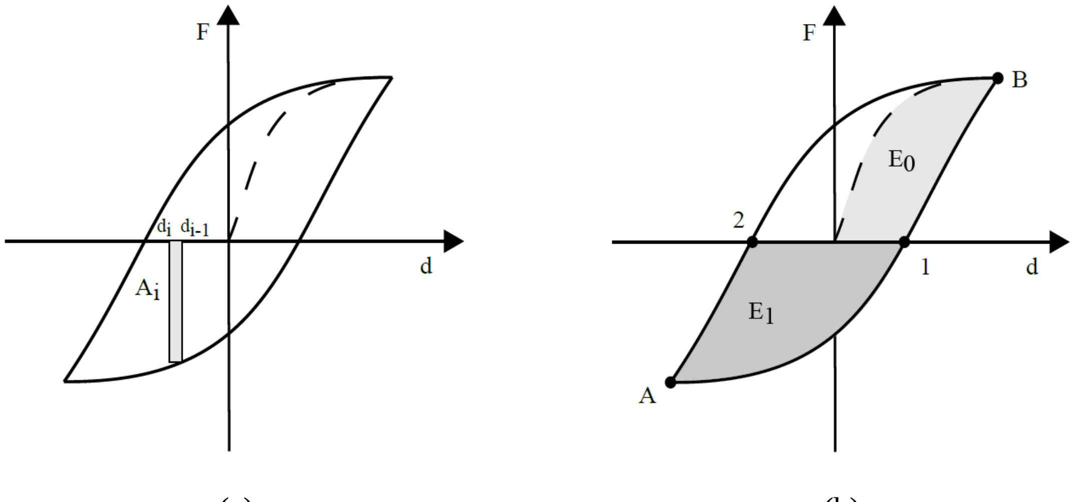

(a) (b)

Figure 7.5 – Computation of hysteretic energy dissipated: (a) area below the hysteretic curve for increment i and (b) half cycles and E_h update.

7.3.3.5. Iterative incremental procedure

In the scope of FEM, for linear behaviour, the equilibrium conditions of the model can be stated as

$$\boldsymbol{F} = \boldsymbol{K}_g \cdot \boldsymbol{U} \tag{7.25}$$

where $\boldsymbol{F}$ is the vector of external nodal forces and $\boldsymbol{U}$ is the vector of nodal displacements.

Due to the non-linear behaviour of the components, the equilibrium of the mechanical model cannot be expressed in terms of Eq. (7.25). However, Eq. (7.25) can be used to solve iteratively the system of non-linear equations considering small increments of load/displacement. Accordingly, in CompModel Calculator the system of nonlinear equations is solved iteratively using a path-follow incremental procedure with displacement control in the DOF 1 (node 3), corresponding to the rotation of the joint. To do so, Eq. (7.25) is used in the following incremental format:

$$\delta\boldsymbol{F}^{\mathrm{T}} = \boldsymbol{K}_g \cdot \delta\boldsymbol{U} \tag{7.26}$$

$$\delta\boldsymbol{F}^{\mathrm{T}} = [\delta M \quad \delta F \quad 0 \quad \dots \quad 0]_{1\times n_f} \tag{7.27}$$

$$\delta\boldsymbol{U}^{\mathrm{T}} = \left[\delta\phi \quad \delta U_2 \quad \delta U_3 \quad \dots \quad \delta U_{n_f}\right] \tag{7.28}$$

The details of the calculation and the incremental iterative procedure applied (Meek, 1991; Borges, 2003) meek are described in the following paragraphs for a generic increment/step:

- **First iteration ($j = 1$)**

(i) compute the global stiffness matrix

Based on tangent stiffness and the position of the springs, the global stiffness matrix is determined as described in Section 7.3.3.2.

(ii) compute the reference external load vector

The reference external load vector in the first iteration, which relates the magnitudes of the forces/bending moments applied to the joint is

$$\boldsymbol{R}^{\mathrm{T}} = [R_{1,1} \quad R_{1,2} \quad R_{1,3} \quad \cdots \quad 0] \tag{7.29}$$

where, $R_{1,1} = M/M$, $R_{1,2} = N/M$, $R_{1,3} = V/M$, being M the bending moment in the connection, N the axial force in the connection and V the horizontal shear force in the top interface of the joint (from the upper column).

If the usual layout in experimental tests is considered (Figure 7.2), then $R_{1,1} = 1$, $R_{1,2} = 0$ and $R_{1,3}$, which represents the relieve in the CWS due to R (Figure 7.2), is given by

$$R_{1,3} = \left(\frac{1}{L_{\mathrm{c}}} + \frac{1}{L_{\mathrm{c}} \cdot L_{\mathrm{b}}} \cdot \frac{h_{\mathrm{c}}}{2}\right) \cdot \frac{y_{\mathrm{CWS}}}{y_1} \tag{7.30}$$

(iii) compute the variation of nodal displacements caused by reference external load vector

$$\delta \boldsymbol{U}'^{i,1} = \left(\boldsymbol{K}_{\mathrm{g}}^{i,1}\right)^{-1} \cdot \boldsymbol{R} \tag{7.31}$$

where δU_1 is the imposed increment of the joint rotation, i.e. $\delta U_1 = \delta\phi$;

(iv) compute the external load vector multiplier

$$\lambda^{i,1} = \delta U_1 / \delta U_1'^{i,1} \tag{7.32}$$

(v) compute the total variation of the nodal displacement vector in the iteration

$$\delta \boldsymbol{U}^{i,1} = \lambda^{i,1} \cdot \delta \boldsymbol{U}'^{i,1} \tag{7.33}$$

(vi) update the nodal displacement vector

$$\boldsymbol{U}^{i,1} = \boldsymbol{U}^{i-1,1} + \delta \boldsymbol{U}^{i,1} \tag{7.34}$$

(vii) update the external nodal forces vector

$$\boldsymbol{F}^{i,1} = \boldsymbol{F}^{i-1,1} + \lambda^{i,1} \cdot \boldsymbol{R} \tag{7.35}$$

(viii) compute the nodal displacements

$$v_{\mathrm{leftmost}} = U_3^{i,1} \cdot \frac{y_n}{y_1} \tag{7.36}$$

$$v_{\mathrm{rightmost}} = U_2^{i,1} + U_1^{i,1} \cdot (y_i - y_{\mathrm{GC}}) \tag{7.37}$$

$$v_{\mathrm{middle}} = U_{\mathrm{DOF}}^{i,1} \tag{7.38}$$

$$v_{\mathrm{CWS}} = U_3^{i,1} \cdot \frac{y_{\mathrm{CWS}}}{y_1} \tag{7.39}$$

where v_{leftmost} and $v_{\text{rightmost}}$ are the nodal displacements in implicit nodes, i.e. auxiliary nodes (with no DOF assigned to them) at the beginning and the end of each row (leftmost and rightmost nodes), v_{middle} are the nodal displacements in actual nodes (with a DOF assign to), which are located between two components and v_{CWS} is the nodal displacement of the right end of the CWS component.

(ix) compute the components deformation

$$d_{\text{CWS}} = v_{\text{CWS}} \tag{7.40}$$

$$d_n = v_{\text{right}} - v_{\text{left}} \tag{7.41}$$

where d_{CWS} and d_n are the deformation in the CWS and in component n, respectively, and v_{left} and v_{right} are the nodal displacements on the left and the right nodes of that component.

(x) compute the components force

Computed according to the mechanical behaviour (constitutive relations) assigned to them, see Section 6.4.

(xi) compute the unbalanced forces vector

$$\boldsymbol{Q}^{i,1} = \boldsymbol{F}^{i,1} + \boldsymbol{IntF}^{i,1} \tag{7.42}$$

The internal forces vector is computed as described in Section 7.3.3.3.

(xii) variables storage

All the variables presented in this section needed for the next iteration are stored.

- **Iterative procedure ($\boldsymbol{j} \geq \mathbf{2}$)**

(xiii) update of variables

Variables as d_{start}, F_{start} and E_h are updated based on the last iteration.

(xiv) compute global stiffness matrix

(xv) compute the reference external load vector

(xvi) compute the variation of the vector of nodal displacements due to the external load vector

$$\delta \boldsymbol{U}'^{i,j} = \left(\boldsymbol{K}_{\text{g}}^{i,j}\right)^{-1} \cdot \boldsymbol{R} \tag{7.43}$$

(xvii) compute the variation of nodal displacement due to unbalance load vector

$$\delta \boldsymbol{U}''^{i,j} = \left(\boldsymbol{K}_{\text{g}}^{i,j}\right)^{-1} \cdot Q^{i,j-1} \tag{7.44}$$

(xviii) compute the external load vector multiplier

$$\lambda^{i,j} = -\,\delta U_1''^{i,j} / \delta U_1'^{i,j} \tag{7.45}$$

(xix) compute the total variation of displacement vector

$$\delta \boldsymbol{U}^{i,j} = \lambda^{i,j} \cdot \delta \boldsymbol{U}'^{i,j} + \delta \boldsymbol{U}''^{i,j} \tag{7.46}$$

(xx) update the nodal displacement vector

$$\boldsymbol{U}^{i,j} = \boldsymbol{U}^{i,j-1} + \delta \boldsymbol{U}^{i,j} \tag{7.47}$$

(xxi) update the external nodal forces vector

$$\boldsymbol{F}^{i,j} = \boldsymbol{F}^{i,j-1} + \lambda^{i,j} \cdot \boldsymbol{R} \tag{7.48}$$

(xxii) compute the nodal displacements

(xxiii) compute the components deformation

(xxiv) compute the components force

(xxv) compute the unbalanced forces vector

$$\boldsymbol{Q}^{i,j} = \boldsymbol{F}^{i,j} + \boldsymbol{IntF}^{i,j} \tag{7.49}$$

(xxvi) Convergence check

$$\frac{\sqrt{\sum_{k=1}^{n_f}\left(\boldsymbol{Q}_k^{i,j}\right)^2}}{\sqrt{\sum_{k=1}^{n_f}\left(\boldsymbol{F}_k^{i,j}\right)^2}} \leq tolF, \frac{\sqrt{\sum_{k=1}^{n_f}\left(\delta\boldsymbol{U}_k^{i,j}\right)^2}}{\sqrt{\sum_{k=1}^{n_f}\left(\boldsymbol{U}_k^{i,j}\right)^2}} \leq tolD \tag{7.50}$$

The convergence was reached if the norm of unbalanced forces and the variation of the norm of nodal displacements in the iteration are small enough (e.g. $tolF = tolD = 0.0001$).

(xxvii) compute the hysteretic energy dissipation

As described in Section 7.3.3.4, the hysteretic energy dissipation is calculated as the area below the curve for each increment i at the end of each iteration j (but will only be updated when a new branch is started).

Figure 7.6 shows the flowchart of the iterative procedure.

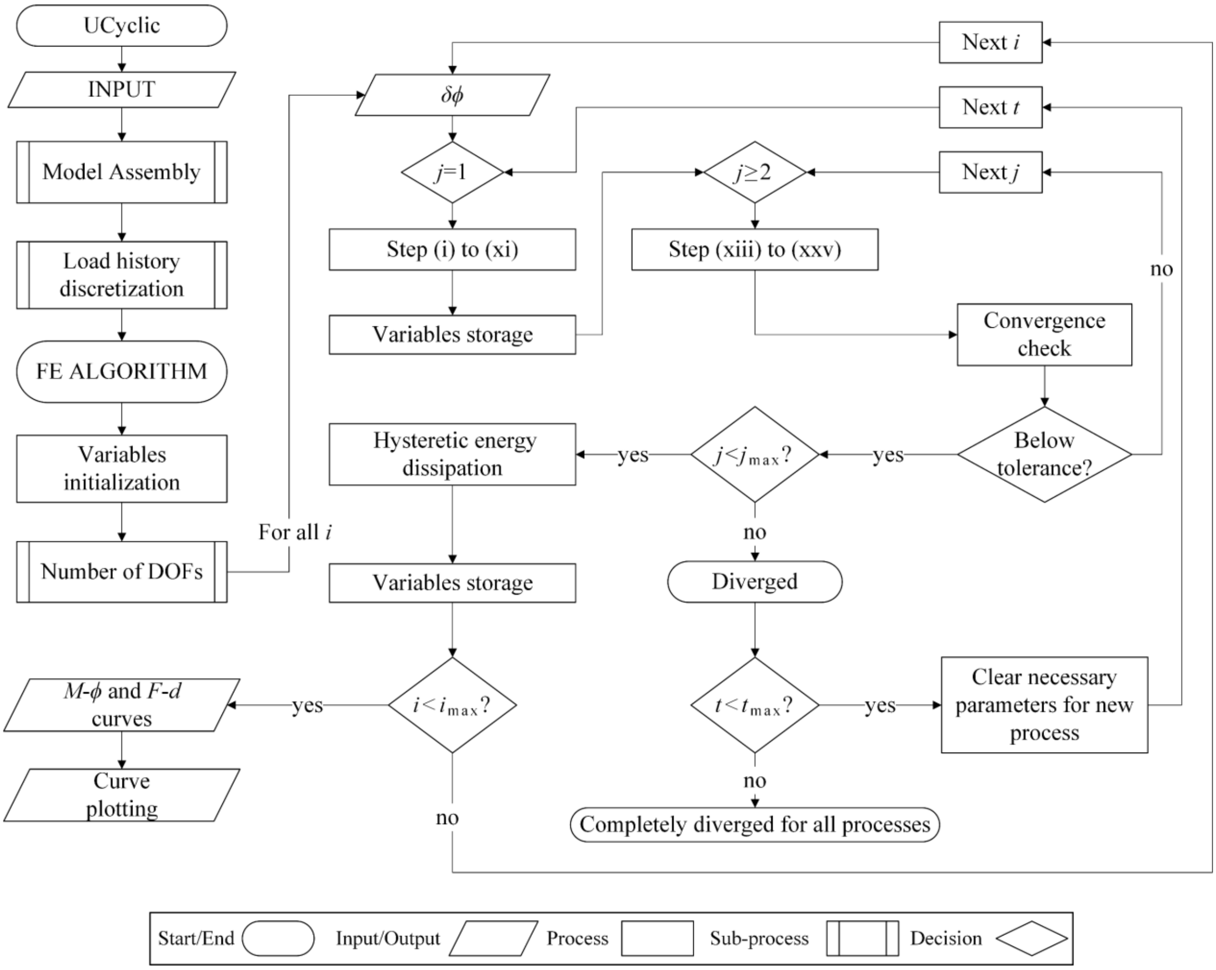

Figure 7.6 – Iterative procedure (CompModel Calculator flowchart).

7.3.3.6. Implementation of the MRA model

At the beginning of each iteration j the following quantities are assumed to be known for each component (see Figure 7.7(a)):

- internal force (f_{start}) and deformation (d_{start}) of the component in the beginning of the branch (in Figure 7.7 is represented for an ascending branch) – these values are null at the beginning of the analysis;

- internal force (f^{i-1}) and deformation (d^{i-1}) of the component in the end of the last step;
- variation of the deformation in the component from the end of the last step ($\delta d = d^{i} - d^{i-1}$).

The procedure to compute the internal force in the component according to the MRA model is:

1. Compare d^{i-1} and d_{start}:

    1.1. If $d^{i-1} \geq d_{\text{start}}$ → starting of the analysis or coming from an ascending branch;

        1.1.1. If $\delta d \geq 0$ → CASE 1: the component will continue in the ascending branch;

        - no changes in $(f_{\text{start}}, d_{\text{start}})$ in the beginning of the branch;

        1.1.2. If $\delta d < 0$ → CASE 2: the component will change to a descending branch;

        - changes in $(f_{\text{start}}, d_{\text{start}})$ in the beginning of the branch: $f_{\text{start}} = f^{i-1}$ and $d_{\text{start}} = d^{i-1}$;

    1.2. If $d^{i-1} < d_{\text{start}}$ → coming in a descending branch;

        1.2.1. If $\delta d > 0$ → CASE 3: the component will change to an ascending branch;

        - changes in $(f_{\text{start}}, d_{\text{start}})$ in the beginning of the branch: $f_{\text{start}} = f^{i-1}$ and $d_{\text{start}} = d^{i-1}$;

        1.2.2. If $\delta d \leq 0$→ CASE 4: the component will continue in the descending branch;

- no changes in $(f_{\text{start}}, d_{\text{start}})$in the beginning of the branch.

The former analysis must be done whenever the force in the component needs to be computed, however the changing of the state parameters f_{start} and d_{start} should only be done definitely at the end of each increment i (step) after the convergence is achieved, i.e. the changes in CASE 2 and 3 are only valid in the current iteration for the specific computation.

Note also that, according to the procedure presented, the computation of the tangent stiffness (section 7.3.3.1) of each component will be done using a point in the ascending branch and other in the descending branch according to Figure 7.7(b).

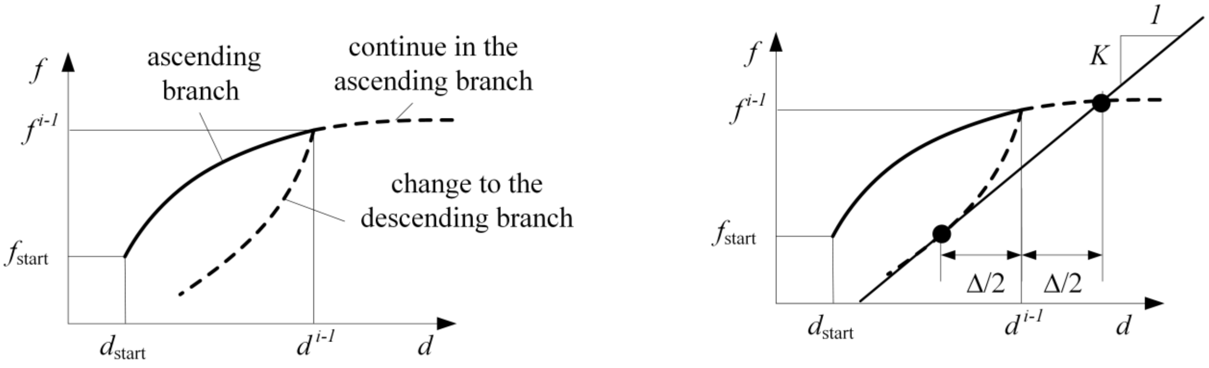

Figure 7.7 – Implementation of MRA model.

7.3.3.7. Global response

The global response of the model refers to the joint behaviour and the behaviour of the two main parts that compose the joint, the CWS and the connection. The bending moment – rotation $(M - \phi)$ behaviour of the joint is given by the response of the DOF 1 located in node 3, see Figure 7.3. The equations used to obtain the $M - \phi$ curve of the CWS and connection can be found in Table 7.1.

Table 7.1 – Equations for the extraction of the $M - \phi$ curves from the CCM.

joint	$M_{joint} = F_1$	(7.51)
	$\phi_{joint} = u_1$	(7.52)
CWS	$M_{\text{CWS}} = F_{\text{CWS}} \cdot y_{\text{CWS}} - F_3 \cdot y_1$	(7.53)
	$\phi_{\text{CWS}} = d_{\text{CWS}}/y_{\text{CWS}}$	(7.54)
connection	$M_{connection} = F_1$	(7.55)
	$\phi_{connection} = \phi_{joint} - \phi_{\text{CWS}}$	(7.56)

7.3.4. Refined cyclic component model

Some components, due to iteration with other components and due to the hysteresis associated to cyclic loading, show different behaviour in cyclic conditions when compared with their behaviour in monotonic conditions and thus may require a more refined modelling approach, e.g. the CFB and the EPB develops high compressive forces for elongation deformations due to the plastic deformations in the previous cycles, see Figures 2.7 and 2.8. Taking as reference the mechanical model for quasi-static monotonic conditions, these differences may require the introduction of additional kinematic restrictions in the mechanical model for cyclic conditions, e.g. an explicit relation between the deformation of the load introduction components (CWT and CWC), see Figure 7.8.

Although not implemented in the scope of this thesis, a refined cyclic component model was developed that accounts for the possibility for additional kinematic restrictions in the mechanical model through additional 1D rigid elements, see Figure 7.9. Detailed description of the model, namely construction of the global stiffness matrix and internal forces vector, and an illustrative example of application can be found in Annex D.

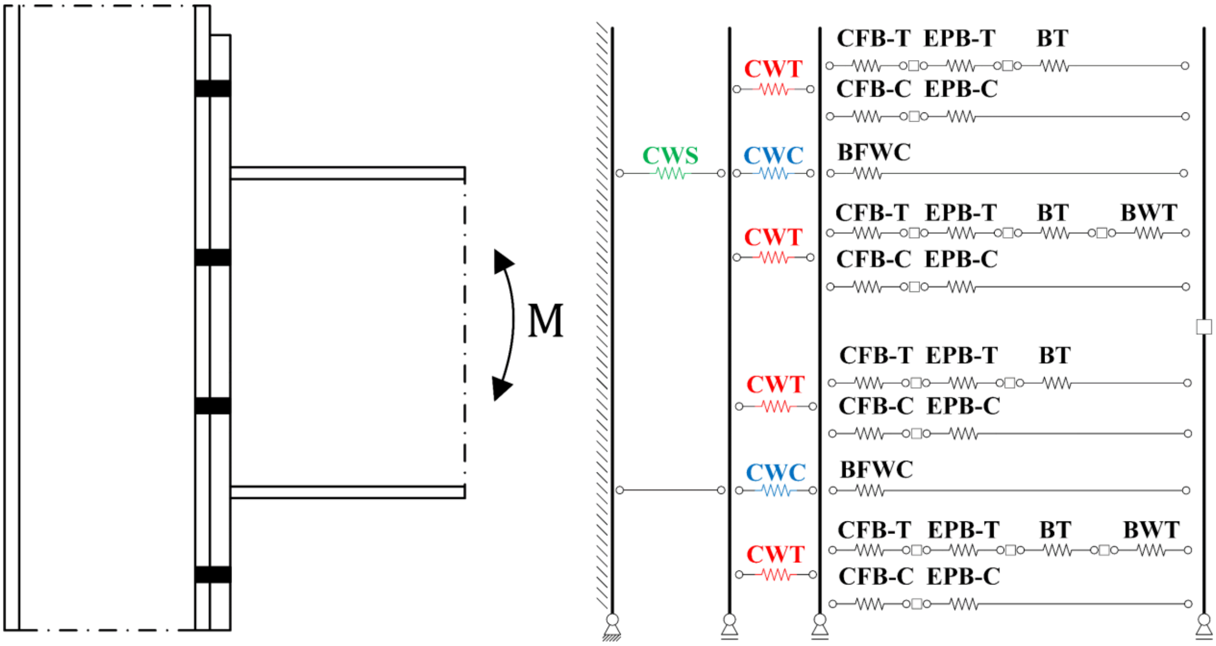

Figure 7.8 – Refined layout for components in CCM.

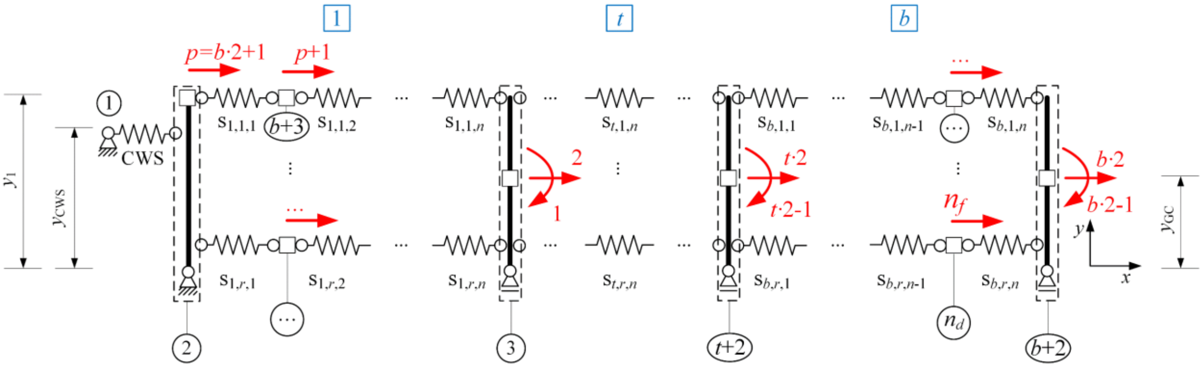

Figure 7.9 – Refined mechanical model.

7.4. Results Analyser

The Results Analyser is a module created to assist the visual assessment of the output results, showing the force-deformation behaviour of several components at the same time, see Figure 7.10. The red dot identifies the same step in all graphs, highlighting which components are active or inactive in a particular step.

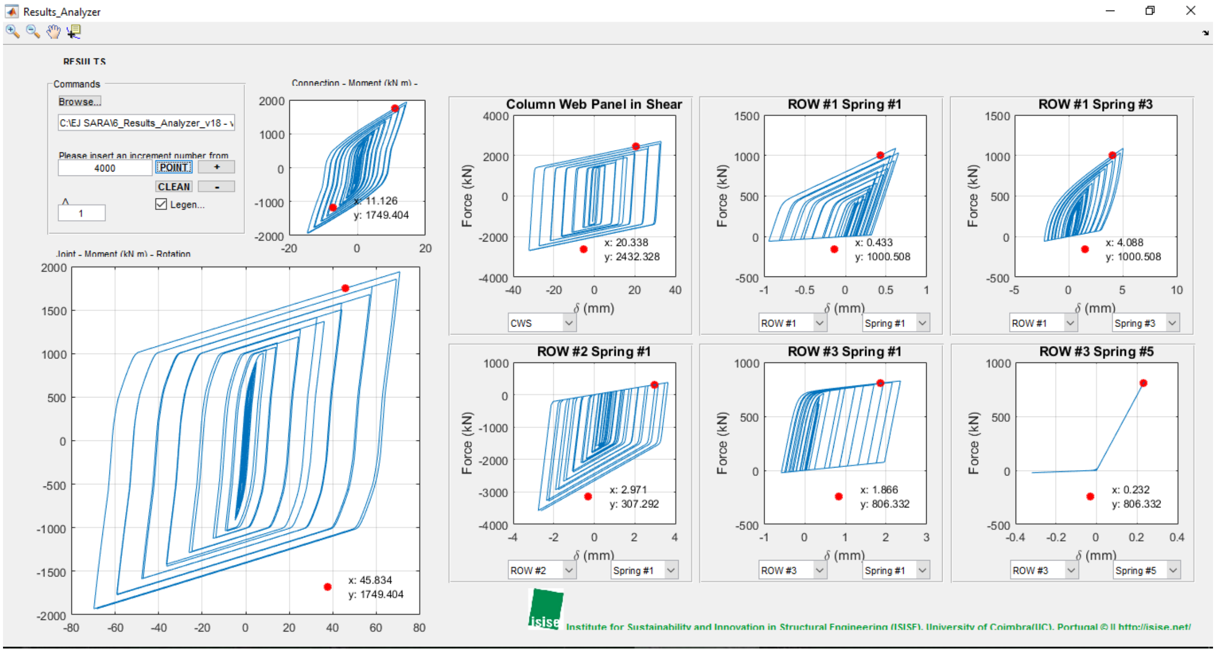
Results_Analyzer

Browse...: C:\EJ SARA\6_Results_Analyzer_v18 - v

Please insert an increment number from: 4000

Δ: 1

☑ Legen...

Figure 7.10 – Results Analyser.

7.5. Concluding remarks

Chapter 7 was dedicated to description of the computational implementation of the CCM. The computer software developed, UCyclic, was written in MATLAB (MathWorks, 2019) and its application to a specific SBCJs is demonstrated in the next chapter.

8 ILUSTRATIVE EXAMPLE

8.1. Introduction

In this chapter the previous tools and procedures are applied to a SBCJ configuration to illustrate the accuracy and versatility of the CCM and its computational implementation.

A double extended end-plate SBCJ configuration studied in the framework of the European pre-qualification research project EQUALJOINTS (Landolfo, 2017a) was selected.

A refined 3D FE model using the software ABAQUS, previously calibrated with experimental tests results, was used to characterize the joint components according to Augusto *et al.* procedure (Augusto *et al.*, 2016; Augusto, 2017).

The illustrative example presented in this chapter follows the CCM proposed in Chapter 6 and the computational implementation described in Chapter 7 .

8.2. Joint description

The specimen considered is the E3-TB-E-M3_ts0 (Augusto *et al.*, 2016; Augusto, 2017), see Figure 8.1(a), where an IPE600 beam is connected to a HEB500 column through a double extended end-plate (25 mm thickness) joint without stiffeners, with six bolt rows with M36 (10.9) bolts. Steel grade S355 was used for all elements.

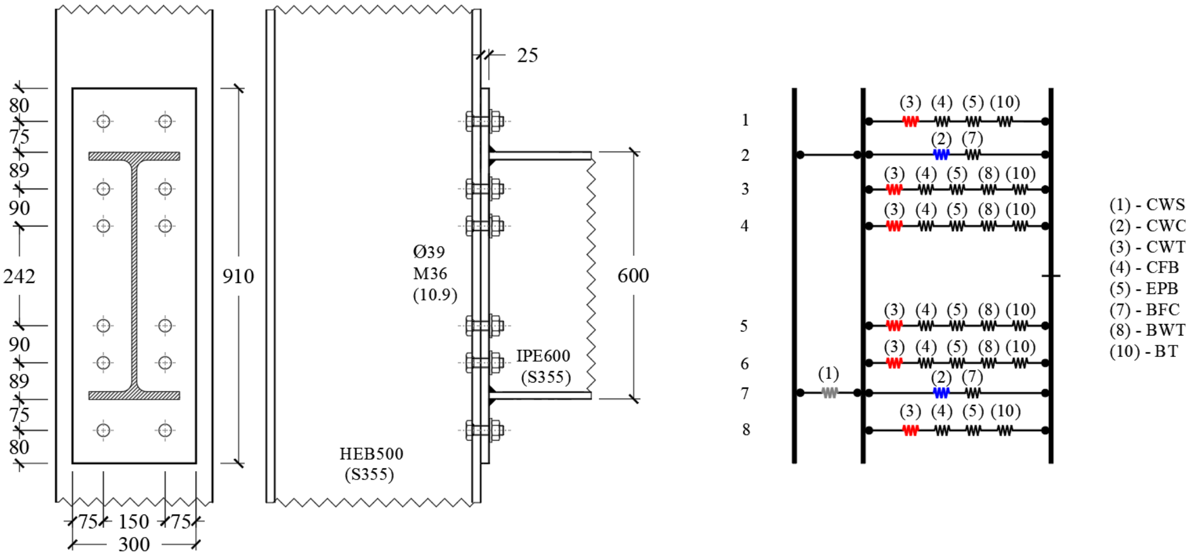

(a) (b)

Figure 8.1 – Joint E3-TB-E-M3_ts0: (a) geometrical sketch of the joint and (b) model assembly (Augusto *et al.*, 2016; Augusto, 2017).

A refined 3D FEM model using the software ABAQUS (ABAQUS, 2014c) was developed (Augusto, 2017), and, in this application example, a comparison of the results from UCyclic and ABAQUS is presented. The following steps are successively addressed:

1) identification and classification of components;
2) computation of the strength F and the initial stiffness K of each component according to EN 1993-1-8;
3) extraction of the cyclic behaviour of the joint components from the refined 3D FEM model;
4) computation of the MRA model parameters using CurveFitting module;
5) computation of the cyclic behaviour of the joint using CompModel Calculator module.

8.3. Identification and classification of components

Based on EN 1993-1-8 (CEN, 2005c), the following components were considered relevant and included in the mechanical model: column web panel in shear (CWS); column web in compression (CWC); column web in tension (CWT); column flange in bending (CFB); end-plate in bending (EPB); beam flange in compression (BFC); beam web in tension (BWT) and bolts in tension (BT).

Figure 8.1(b) shows the CCM used both for moth monotonic and cyclic analysis. Due to the double symmetry of the joint, the hogging and sagging bending moment behaviour is identical.

For the numerical simulation, the following assumptions were considered according to a previously analysis performed in ABAQUS (Augusto *et al.*, 2016; Augusto, 2017).

(i) dissipative components

The CWS, CWC, CWT, CFB and EPB were classified as dissipative. CWS is active for both hogging and sagging moments, so the mechanical behaviour tension-compression was assigned to it. CWC is only active in compression and thus the compression-only behaviour was assigned to it. The remaining components are only active in tension thus the tension-only behaviour was assigned to all of them. The current version of UCyclic does not account the T-stub decoupled component model, therefore, the CFB and EPB are considered as tension-only components.

(ii) non-dissipative components

BT, BFC, BWT and all components in row 4 and 5 (numbering according to Figure 8.1(b)) were classified as non-dissipative and thus bi-linear behaviour was assigned to them.

8.4. Mechanical characteristics of components according to EC3-1-8

The design resistance F_{Rd} and the stiffness coefficient k (and the corresponding initial stiffness K) for each component according to EC3-1-8 (CEN, 2005c) are presented in Table 8.1. The value of the initial stiffness was obtained by $K = k \cdot E$, where E is the Young's modulus ($E = 210$ GPa). Owing to the symmetry of the joint, Table 8.1 present only the mechanical properties of the first four rows.

Table 8.1 – EC3-1-8 calculations (joint E3-TB-E-M3_ts0): rows 1 to 3.

row	component	F_{Rd}	k	K
		kN	mm	kN/mm
0	CWS	2071.06	6.20	1302.96
1	CWT	1593.98	5.76	1208.81
1	CFB	1283.30	44.46	9335.91
1	EPB	590.31	6.03	1265.54
1	BT	735.30	16.55	3474.84
2	CWC	1423.28	9.25	1941.93
2	BFC	2682.36	∞	∞
3	CWT	1593.98	3.31	694.104
3	CFB	1283.30	25.53	5360.74
3	EPB	1174.47	13.38	2810.52
3	BWT	2054.92	∞	∞
3	BT	735.30	16.55	3474.84
4	CWT	1593.98	4.32	907.254
4	CFB	1283.30	33.37	7006.95
4	EPB	1140.41	8.71	1829.05
4	BWT	1872.53	∞	∞
4	BT	735.30	16.55	3474.84

8.5. Quasi-static cyclic behaviour

8.5.1. ABAQUS results

The numerical (i) global behaviour – moment-rotation relations of the joint, connection and CWS, and (ii) dissipative components behaviour – force-deformation relations of the dissipative components, were obtained from a refined 3D FEM model developed in ABAQUS (Augusto *et al.*, 2016; Augusto, 2017).

8.5.1.1. Global behaviour

Figure 8.2(a) illustrates the cyclic behaviour of the joint and Figure 8.2(a) illustrates the cyclic behaviour of the connection, while Figure 8.3 depicts the cyclic behaviour of the CWS in terms of (a) moment-rotation curve and (b) force-deformation curve.

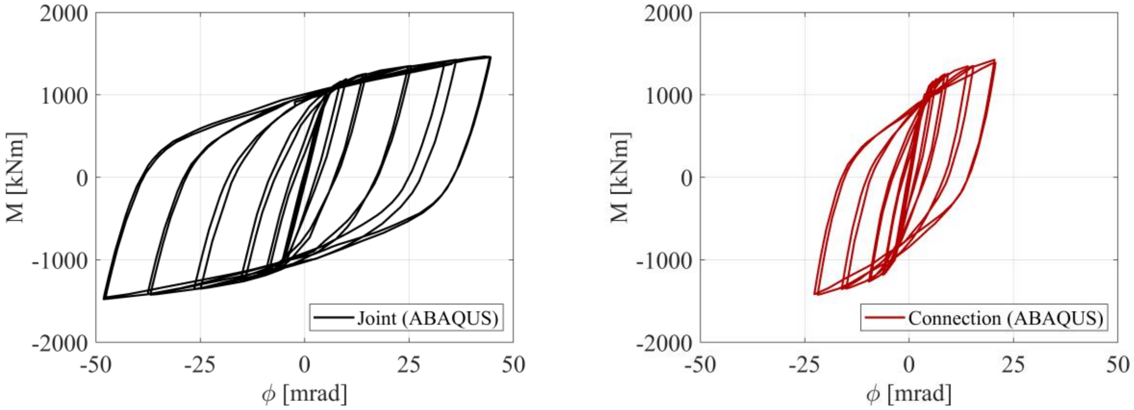

(a) (b)

Figure 8.2 – ABAQUS results (joint E3-TB-E-M3_ts0): (a) joint and (b) connection.

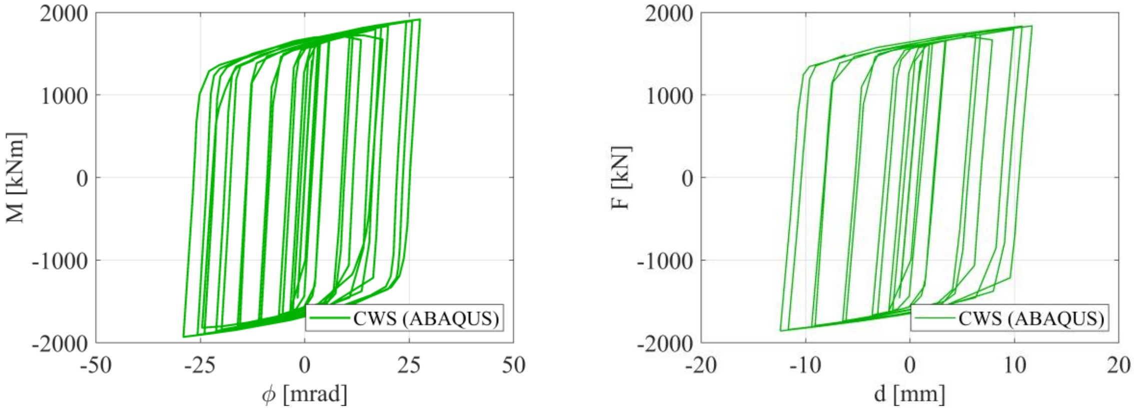

(a) (b)

Figure 8.3 – ABAQUS results (joint E3-TB-E-M3_ts0): CWS (a) moment-rotation and (b) force-deformation.

8.5.1.2. Dissipative components behaviour

Figures 8.4 to 8.7 illustrate the force-deformation curve of the dissipative components. These curves were computed according to the procedure presented in Section 2.8.

Figures 8.4 and 8.5 illustrate the force-deformation curves of the column web in tension (CWT) and in compression (CWC), respectively.

Figure 8.4 shows that, according to the procedure presented in Section 2.8, the component CWT in row 1 and 8 (rows numbering is according to Figure 8.1) show almost no deformation on the tension side.

Figures 8.6 and 8.7 depict the force-deformation curves of the column flange in bending (CFB) and end-plate in bending (EPB), respectively. The component EPB presents deformations two to three times higher than the component CFB.

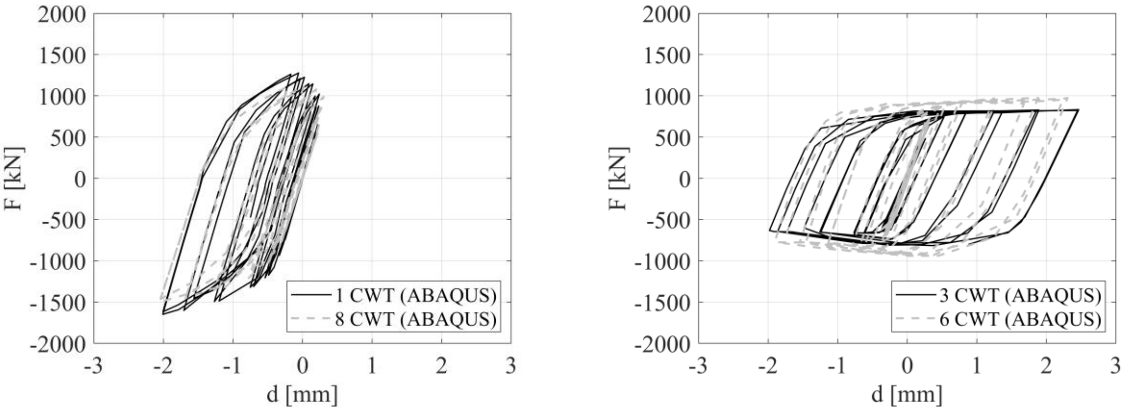

(a) (b)

Figure 8.4 – ABAQUS results (joint E3-TB-E-M3_ts0): CWT in (a) rows 1 and 8 and (b) rows 3 and 6.

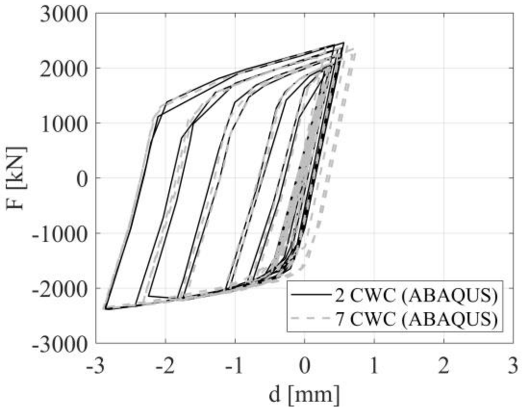

Figure 8.5 – ABAQUS results (joint E3-TB-E-M3_ts0): CWC in rows 2 and 7.

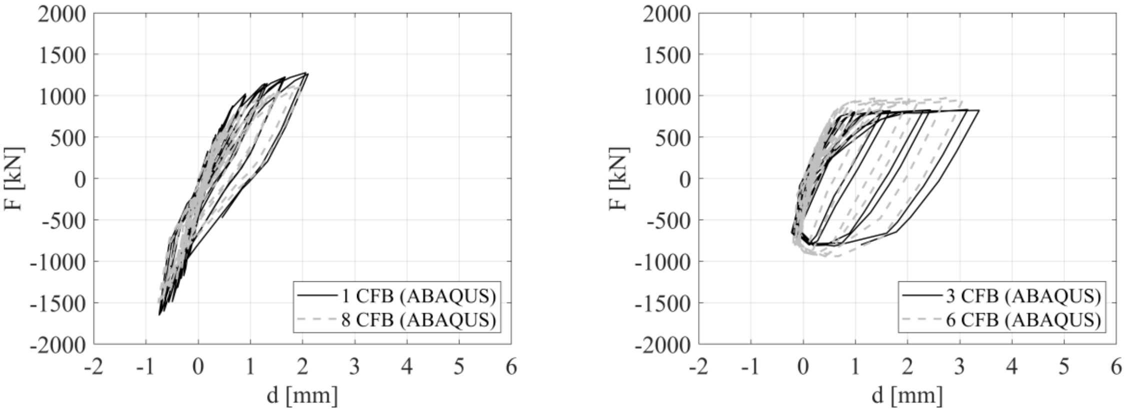

(a) (b)

Figure 8.6 – ABAQUS results (joint E3-TB-E-M3_ts0): CFB in (a) rows 1 and 8 and (b) rows 3 and 6.

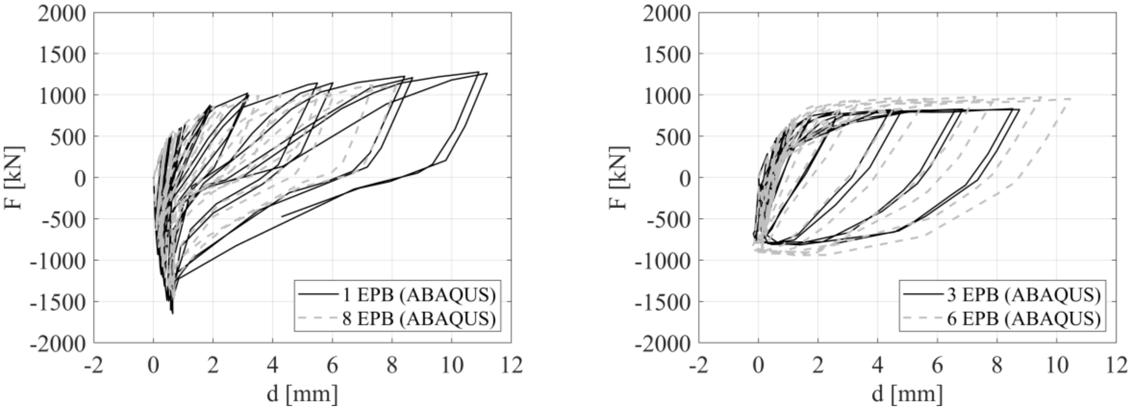

(a) (b)

Figure 8.7 – ABAQUS results (joint E3-TB-E-M3_ts0): EPB in (a) rows 1 and 8 and (b) rows 3 and 6.

8.5.2. Curve fitting

The main parameters for the MRA model (K_0, K_{pl}, F_0 and N) for each dissipative component were computed using the CurveFitting module (the current version does not account for pinching parameters, see Section 7.2) by computing the best fit to the force-deformation behaviour extracted from ABAQUS refined 3D FEM model according to the procedure developed by Augusto *et al.* (2017), see Section 8.5.1.

The curve fitting procedures used were: CFT1 (not imposing any parameter, tension-compression behaviour) and CFT6 (imposing the main four MRA parameters, K_0, K_{pl}, F_0 and N together with a specific mechanical behaviour). The values of K_0 and F_0 to use in CFT6 were either computed according to the EC3-1-8 (CEN, 2005c), or from CFT1 when appropriate, see Table 8.2. The mechanical behaviour assigned in CFT6 (i.e., tension-compression, tension-only or compression-only) was selected as discussed in Section 8.3.

Figures 8.8, 8.9 and 8.11 (CFT1) show some curve fitting results, revealing a good agreement as expected – note that, irrespective of the type of the mechanical behaviour used in the cyclic analysis of the SBCJ, in the curve fitting process (CFT1) the tension-compression behaviour is considered, as the main goal is to extract the four main MRA parameters.

A second analysis was performed in CurveFitting using CFT6, i.e. assigning a mechanical behaviour to each dissipative component and the MRA parameters that best fit to the respective mechanical behaviour (i.e., tension-compression, tension-only or compression-only as defined in Section 8.3), in order to, assess visually the implementation of the mechanical behaviour with the MRA parameters obtained from CFT1 or according to the EC3-1-8 (CEN, 2005c), when appropriate. Within tension-only and compression-only behaviours, two extreme cases of the deformation limit value were assessed: (a) $d_{lim} = \infty$ and (b) $d_{lim} = 0$.

Figures 8.8, 8.10 and 8.12, show the result using CFT6. These figures show that although a good match was found in some cases (e.g. CWS – Figure 8.8(b) – and CWT in row 3 (with $d_{lim} = 0$) – Figure 8.12(a)), other cases show a poor correspondence (e.g. CWT in row 1 (with $d_{lim} = 0$) – Figure 8.10(a)), revealing that the procedure for the extraction of the behaviour of some components from refined 3D FEM models according to Augusto *et al.* (2017) show some disagreement with the mechanical behaviour selected. On the other hand, when assigning $d_{lim} = \infty$, the tension forces in the tension-only behaviour (e.g. CWT in row 1 – Figure 8.10(b) and CWT in row 3 – Figure 8.12(b)) are isolated and accounted for the whole deformation history according to the extraction from the refined 3D FEM models.

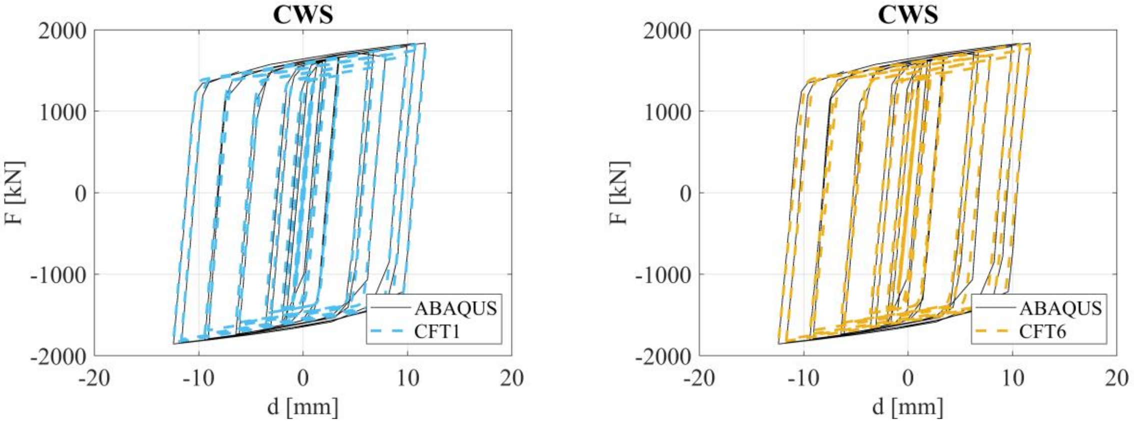

(a) (b)

Figure 8.8 – CurveFitting results (joint E3-TB-E-M3_ts0): CWS.

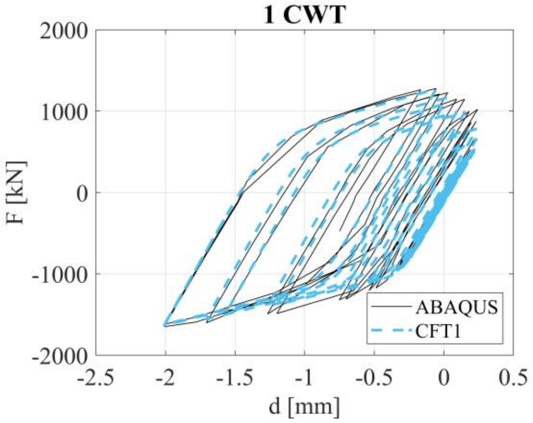

Figure 8.9 – CurveFitting results (joint E3-TB-E-M3_ts0): CWT in row 1.

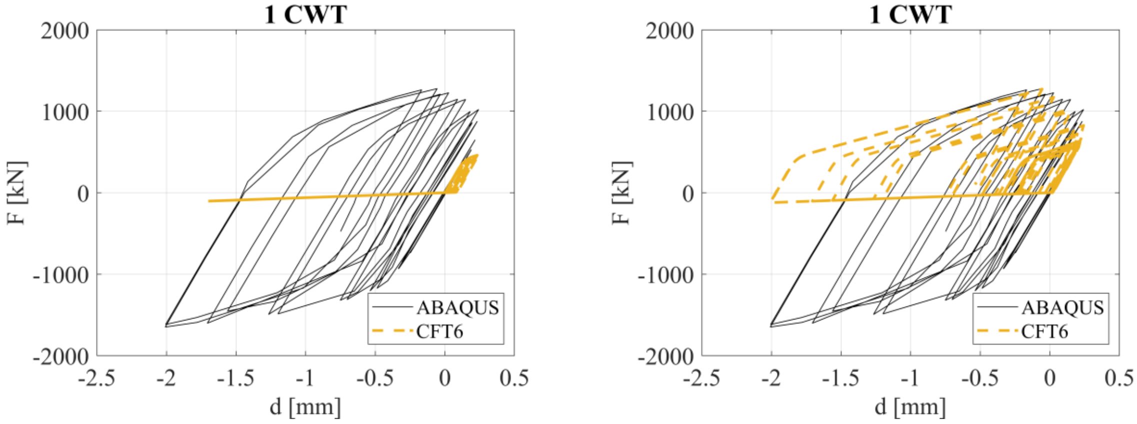

(a) $d_{lim} = 0$ (b) $d_{lim} = \infty$

Figure 8.10 – CurveFitting results (joint E3-TB-E-M3_ts0): CWT in row 1.

Table 8.2 summarizes the final result of the CurveFitting analysis. These parameters are the input data for CompModel Calculator. It shows some disagreement with the mechanical properties computed according to EC3-1-8 (CEN, 2005c) – see Table 8.1, for most components except, in terms of initial stiffness, for CWS, CFB and EPB in row 1.

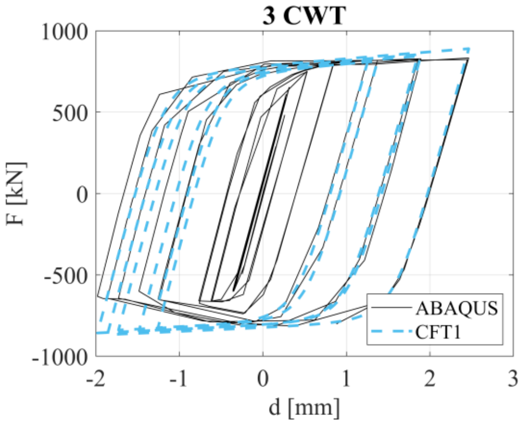

Figure 8.11 – CurveFitting results (joint E3-TB-E-M3_ts0): CWT in row 3.

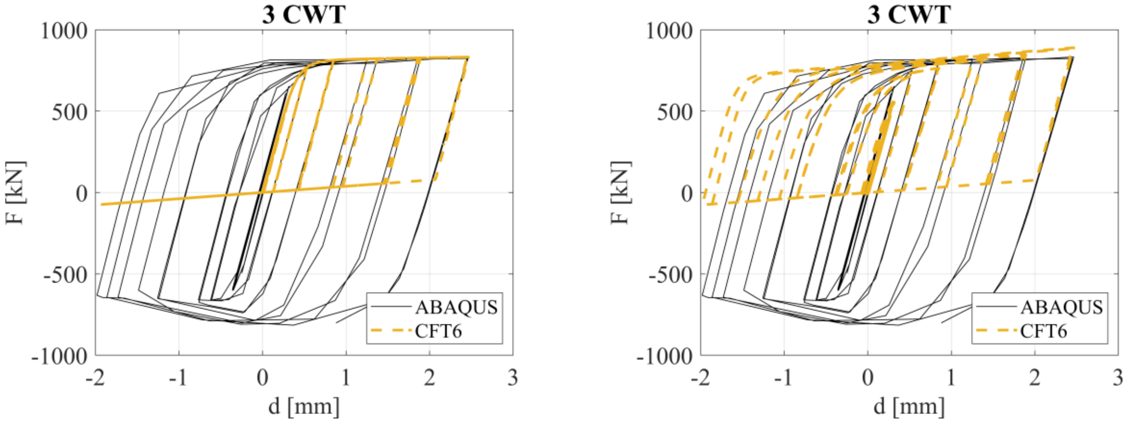

(a) $d_{lim} = 0$ (b) $d_{lim} = \infty$

Figure 8.12 – CurveFitting results (joint E3-TB-E-M3_ts0): CWT in row 3.

8.5.3. CompModel Calculator

8.5.3.1. Introduction

Three analysis were performed to illustrate the importance of assigning suitable mechanical behaviour to these components:

(a) AN1: dissipative components with tension-only or compression-only behaviour, $d_{\text{lim}} = 0$ and $\beta = 2\%$ was assumed;

(b) AN2: similar to AN1 but with strength and stiffness degradation for all dissipative components of row 1 and EPB in row 3;

(c) AN3: similar to AN1 but without imposing a d_{lim}.

AN1 and AN3 represent extreme cases regarding the mechanical behaviours considered: as Figure 8.13 shows with two springs placed in parallel used to model a single spring, assuming compression-only and tension-only mechanical behaviours with $d_{\text{lim}} = 0$ will lead to a poor simulation of the behaviour of the original spring, see Figure 8.13(c), because it will lead to “artificial” pinching. However, in AN3, assuming compression-only and tension-only mechanical behaviours without imposing a d_{lim}, may also lead to a poor simulation of the joint behaviour because the stiffness of the unloading branches will be overestimated and more energy dissipation will be considered. AN2 is present to show the importance of considering the strength/stiffness degradation.

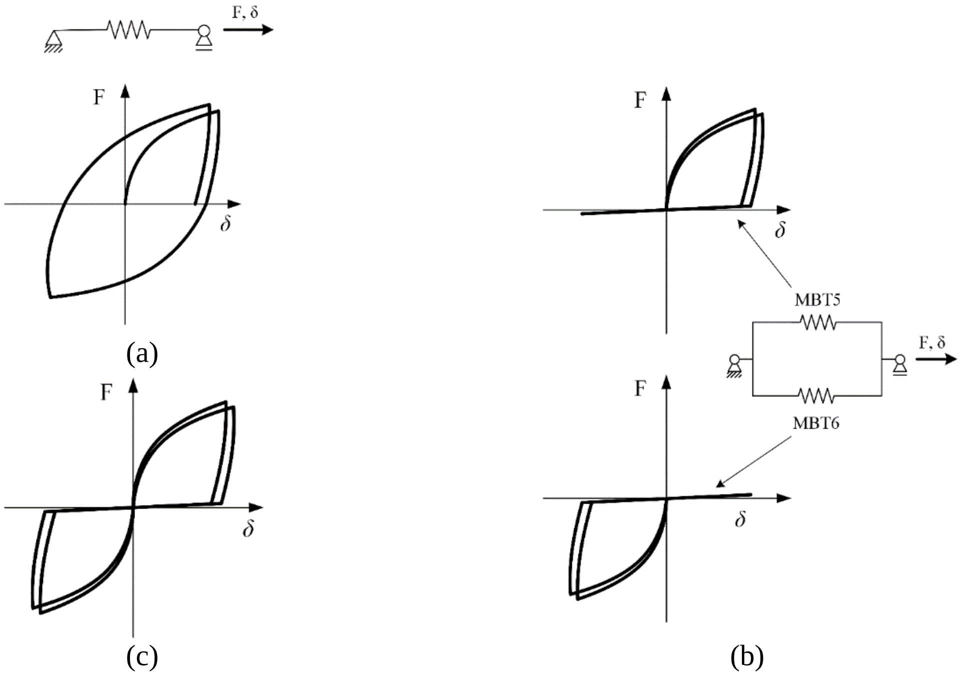

Figure 8.13 – Illustration of the cyclic modelling of the behaviour of one spring making use of two springs in parallel with tension-only and compression-only behaviours.

Table 8.2 shows the full set of parameters required by the MRA models and the mechanical behaviours assigned for each dissipative component used in the analysis performed – the majority of the MRA model parameters were computed as descried in Section 8.5.2. However, when the visual inspection showed that a poor match was found in curve fitting or unreasonable results were found when confronted with EC3-1-8, these parameters were adjusted. The stiffness and strength degradation parameters were assumed according to Nogueiro *et al.* (2006). The current version of the CompModel Calculator does not account for pinching effect.

For the non-dissipative components, a bi-linear behaviour was assumed with elastic stiffness according EN 1993-1-8, see Table 8.3.

Table 8.2 – Input data: dissipative components parameters (CompModel Calculator).

row	name	K_0	K_{pl}	F_0	N	β	d_{lim}*	i_{F}**	i_{K}**
		kN/mm	kN/mm	kN	kN	%	mm	mm	-
0	CWS	1302.95	20.93	1332.07	14.30	-	-	-	-
1	CWT	3025.32	470.83	352.25	6.73	2	0	0.05	0
1	CFB	9335.91	81.10	1212.31	0.75	2	0	0.05	0.05
1	EPB	1265.54	20.70	800.00	1.50	2	0	0.05	0.1
2	CWC	5171.96	88.15	1371.26	14.21	2	0	-	-
3	CWT	1912.60	41.64	704.50	4.86	2	0	-	-
3	CFB	1800.00	18.00	731.70	3.30	2	0	-	-
3	EPB	2500.00	2.30	804.54	1.00	2	0	0	1.5

*AN1 and AN2, **AN2

Table 8.3 – Input data: non-dissipative components parameters (CompModel Calculator).

row	name	$K_{0,T}$	$K_{0,C}$	row	name	$K_{0,T}$	$K_{0,C}$
		kN/mm	kN/mm			kN/mm	kN/mm
2	BFC	200	10000	4	EPB	8.71	8.71
3 and 4	BWT	1000	200	4	CWT	4.32	4.32
1, 3 and 4	BT	16.55	16.55	4	CFB	33.37	33.37

Following, the analysis of the results is done comparing the moment-rotation curves of the joint and the connection and the force-deformation curves of dissipative component from UCyclic with the equivalent results from ABAQUS.

8.5.3.2. Global behaviour

Figure 8.14 shows the bending moment-rotation relation for the beam-to-column joint computed from ABAQUS refined 3D FEM model and with UCyclic showing, in general, a good agreement.

The main disagreement in the moment-rotation curves of the SBCJ for AN1 and AN2, as shown in Figure 8.14(a), is the slope of the unloading branches for a bending moment close to zero for both sagging and hogging moments – the moment-rotation computed with UCyclic for AN1 and AN2 shows high pinching but the bending moment rotation computed with ABAQUS does not. As already explained (Section 8.5.3.1), the difference is mathematically explained by the change of active components: e.g. in AN1 the tension-only mechanical behaviour was assigned for all dissipative components in tension, making-it active only for positive deformations ($d_{\text{lim}} = 0$) – when the internal force approaches zero (close to become inactive), a linear behaviour is assumed with a slope of 2% of the initial stiffness and thus yielding that behaviour – as illustrated previously in Figure 8.13. On the other hand, for AN3, as shown in Figure 8.14(b), an overall better match with the results of ABAQUS was achieved but, also as expected, the unloading branches are stiffer in AN3 than in ABAQUS results leading to a higher energy dissipation.

Figures 8.15 and 8.16 presents the force-deformation curve for CWS and the moment-rotation curve of the connection, both showing good agreement between **UC**yclic and ABAQUS for the initial stiffness, strength and post-limit stiffness. As expected, the differences reported in Figure 8.16 are due to the behaviour assumed for the components in the connection and thus, the trends discussed for the SBCJ behaviour represented in Figure 8.14 are similar to the ones presented in Figure 8.16.

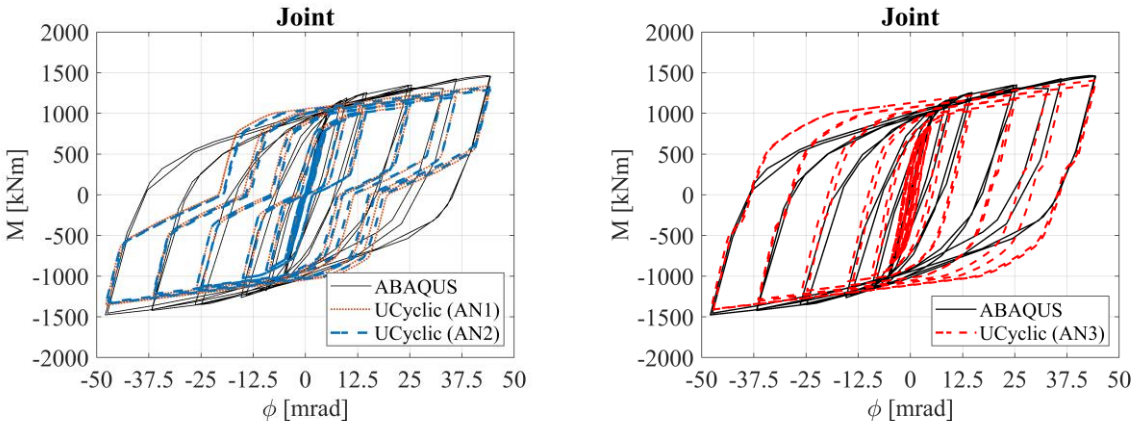

(a) (b)

Figure 8.14 – UCyclic and ABAQUS results (joint E3-TB-E-M3_ts0): joint.

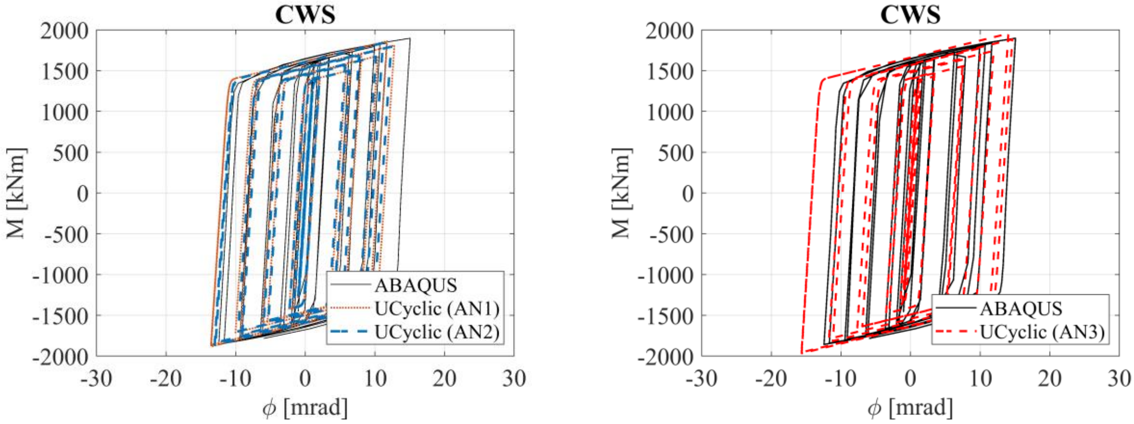

(a) (b)

Figure 8.15 – UCyclic and ABAQUS results (joint E3-TB-E-M3_ts0): CWS.

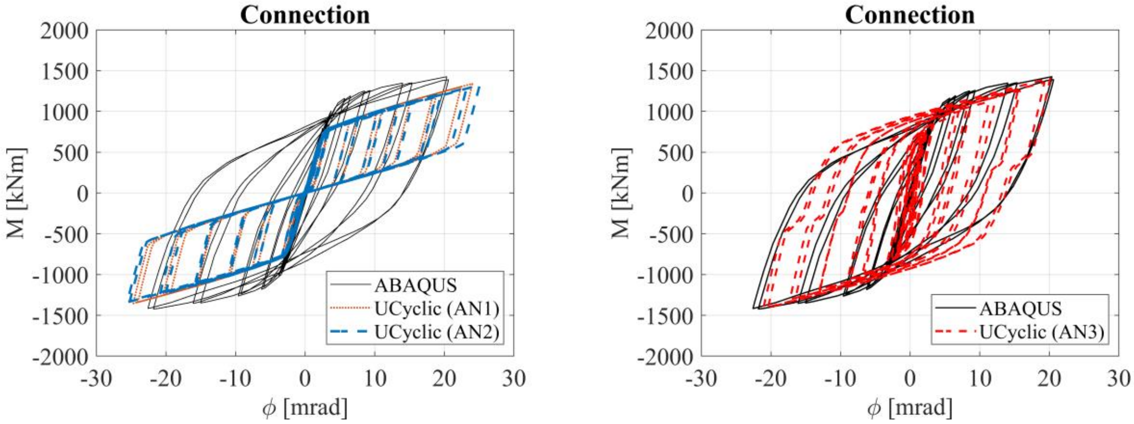

(a) (b)

Figure 8.16 – UCyclic and ABAQUS results (joint E3-TB-E-M3_ts0): connection.

8.5.3.3. Dissipative components

Figures 8.17 to 8.30 show the comparison for the force-deformation relation from ABAQUS and UCyclic of each dissipative component. From these figures the following aspects should be highlighted:

(i) as expected, the results for AN1 and AN2 from UCyclic show that the components CWT, CFB and EPB only carry loads for positive deformation due to the assumption of $d_{\mathrm{lim}} = 0$ in the mechanical behaviour tension-only, however the results extracted from ABAQUS show that these components also carry significative tension forces for negative deformations;

(ii) the results for AN3 from UCyclic show that the tension-only mechanical behaviour accounts for the carrying capacity of CWT, CFB and EPB for negative deformations, however it is clear that these components show distinct behaviour and although some may be carrying tension forces in almost the full range of negative deformations, others do not, e.g. CWT in row 1 (Figure 8.17) carries tension forces in almost the full range of negative deformations but the CFB also in row 1 (Figure 8.18) does not carry tension forces for compression deformations;

(iii) some components that are only relevant (have a contribution for stiffness, strength or deformation capacity) for tension forces for monotonic behaviour are also relevant for compression forces in cyclic conditions, e.g. CFB and EPB (Figures 8.18 and 8.19) and this particular feature of the T-stub was already addressed in Part II of the thesis;

(iv) the post-limit stiffness exhibited in UCyclic by some components is very different of the post-limit stiffness extracted from ABAQUS (e.g. Figure 8.19).

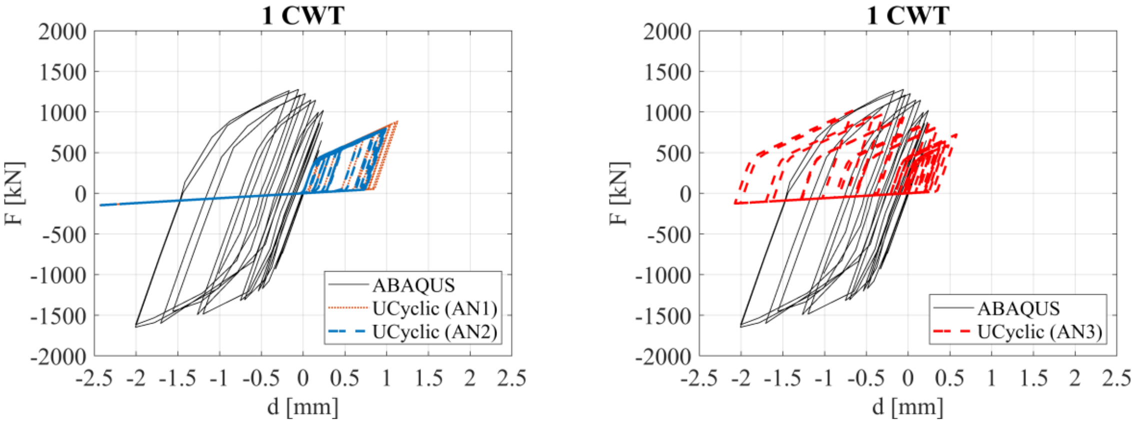

(a) (b)

Figure 8.17 – UCyclic and ABAQUS results (joint E3-TB-E-M3_ts0): CWT in row 1.

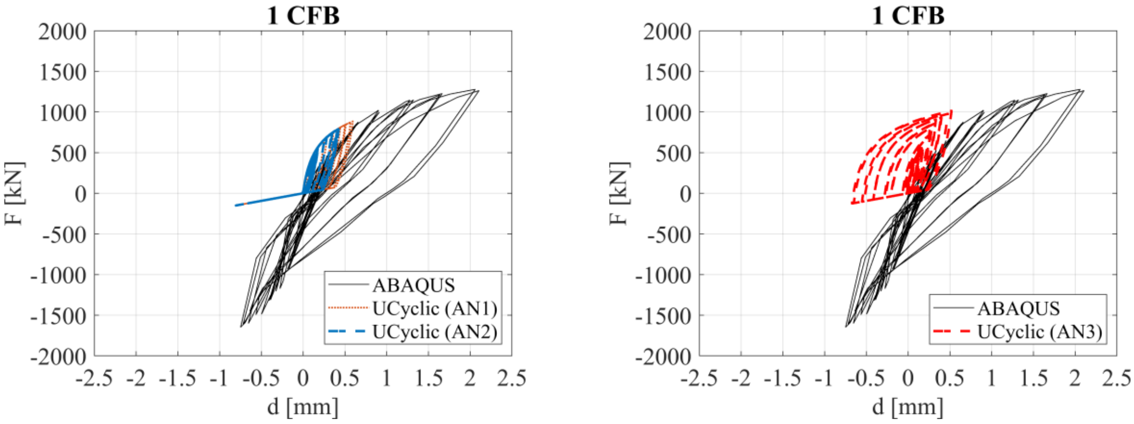

(a) (b)

Figure 8.18 – UCyclic and ABAQUS results (joint E3-TB-E-M3_ts0): CFB in row 1.

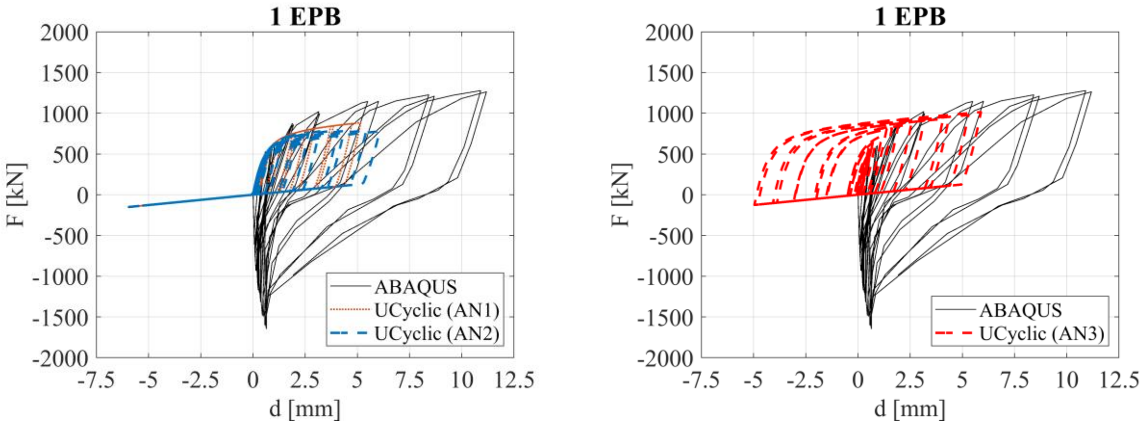

(a) (b)

Figure 8.19 – UCyclic and ABAQUS results (joint E3-TB-E-M3_ts0): EPB in row 1.

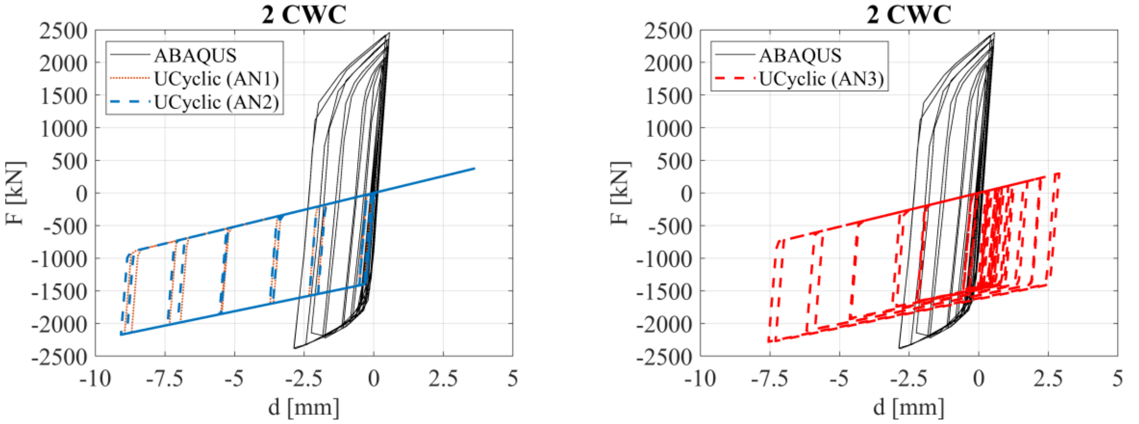

(a) (b)

Figure 8.20 – UCyclic and ABAQUS results (joint E3-TB-E-M3_ts0): CWC in row 2

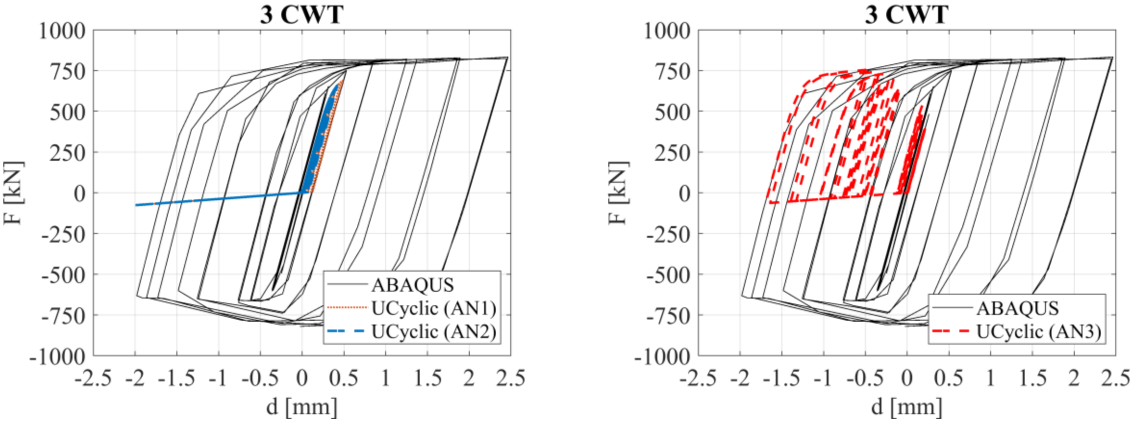

(a) (b)

Figure 8.21 – UCyclic and ABAQUS results (joint E3-TB-E-M3_ts0): CWT in row 3.

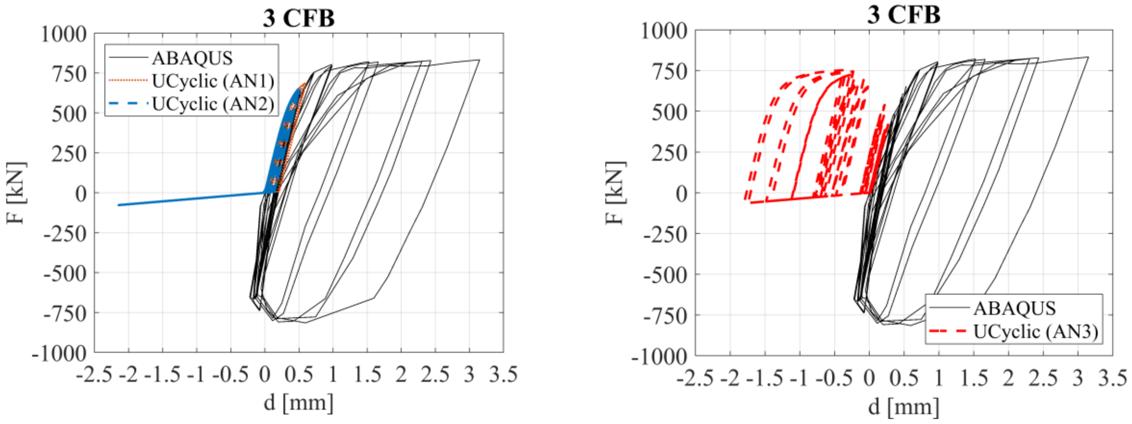

(a) (b)

Figure 8.22 – UCyclic and ABAQUS results (joint E3-TB-E-M3_ts0): CFB in row 3

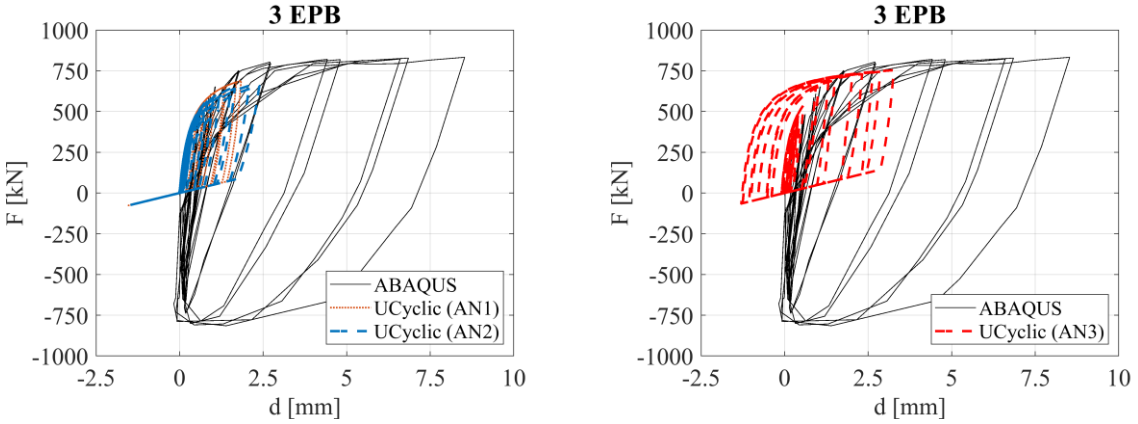

(a) (b)

Figure 8.23 – UCyclic and ABAQUS results (joint E3-TB-E-M3_ts0): EPB in row 3.

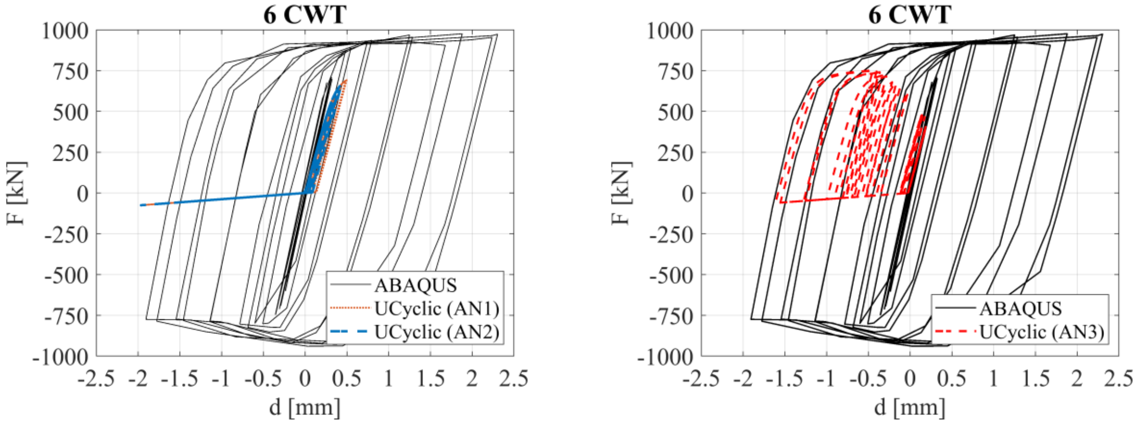

(a) (b)

Figure 8.24 – UCyclic and ABAQUS results (joint E3-TB-E-M3_ts0): CWT in row 6.

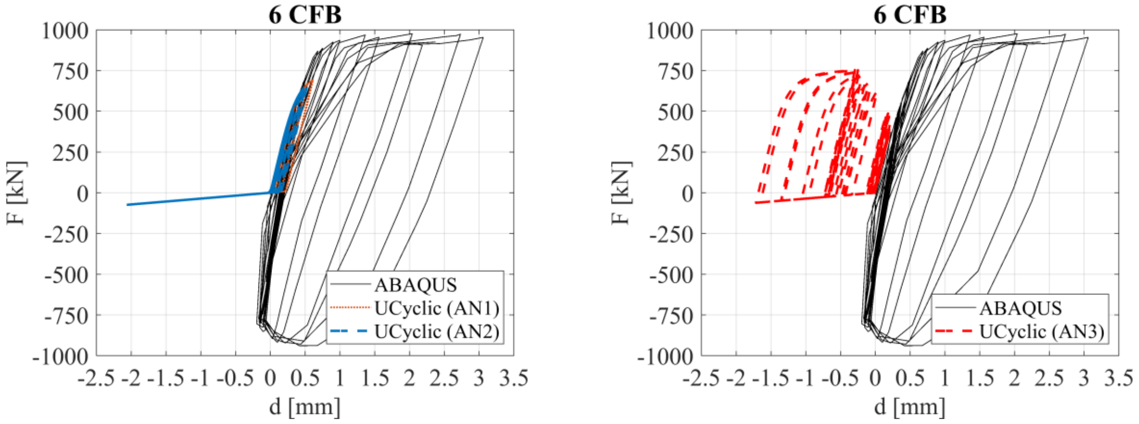

(a) (b)

Figure 8.25 – UCyclic and ABAQUS results (joint E3-TB-E-M3_ts0): CFB in row 6.

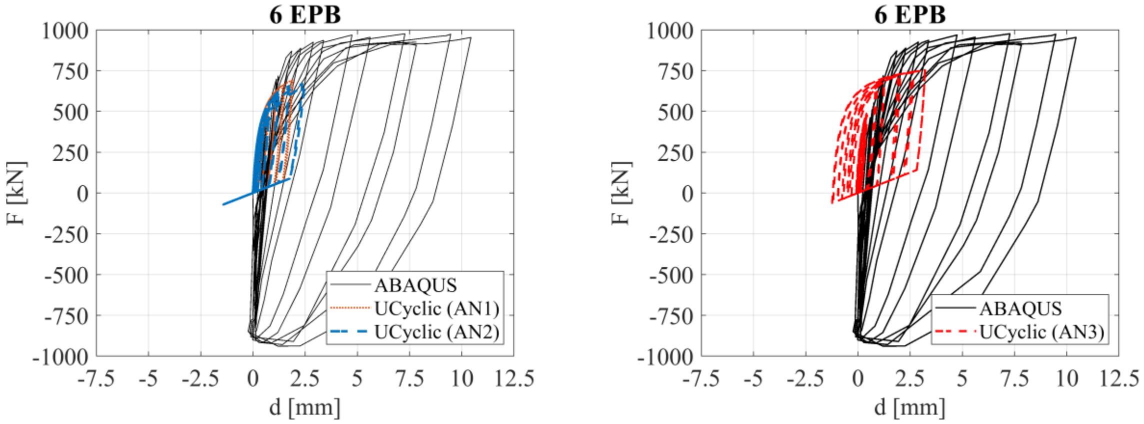

(a) (b)

Figure 8.26 – UCyclic and ABAQUS results (joint E3-TB-E-M3_ts0): EPB in row 6.

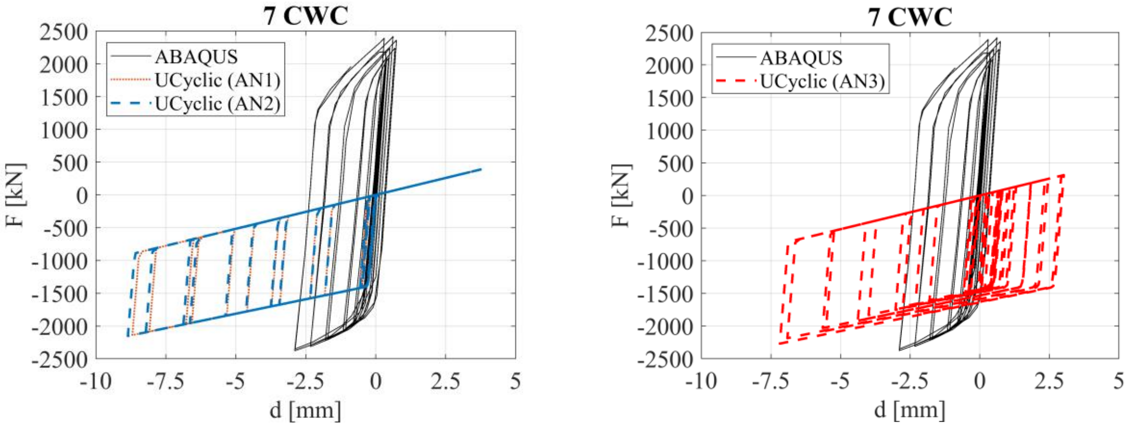

(a) (b)

Figure 8.27 – UCyclic and ABAQUS results (joint E3-TB-E-M3_ts0): CWC in row 7.

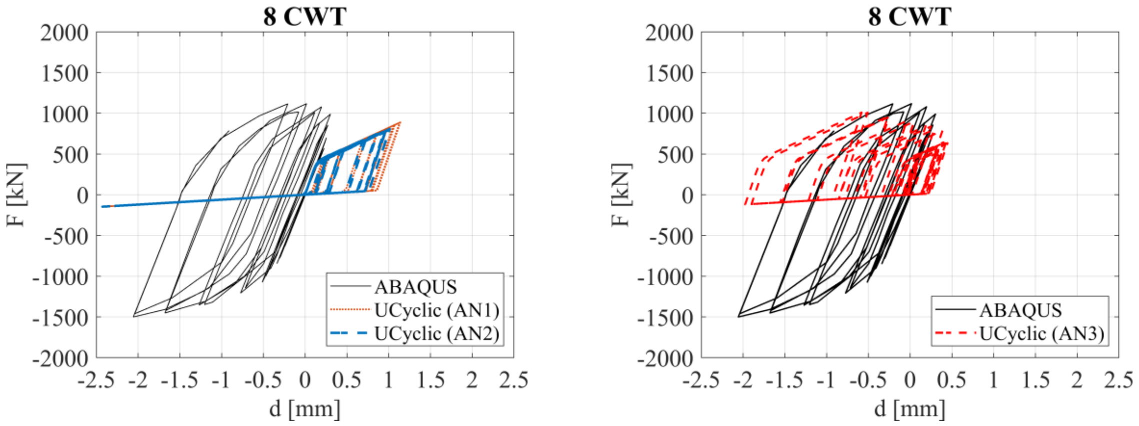

(a) (b)

Figure 8.28 – UCyclic and ABAQUS results (joint E3-TB-E-M3_ts0): CWT in row 8.

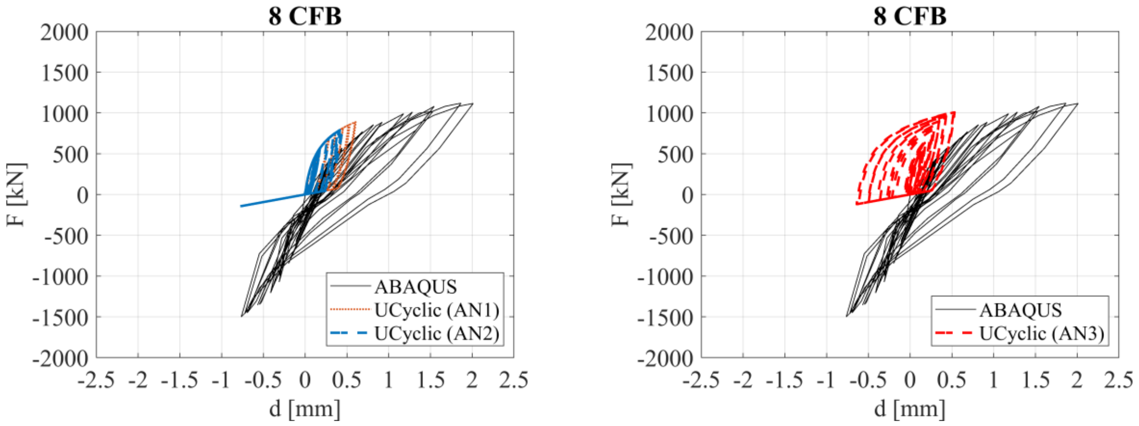

(a) (b)

Figure 8.29 – UCyclic and ABAQUS results (joint E3-TB-E-M3_ts0): CFB in row 8.

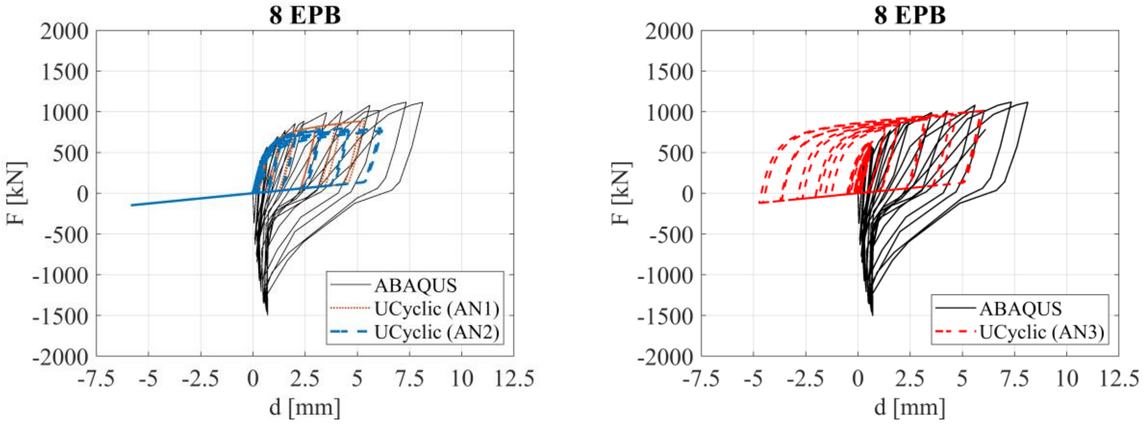

(a) (b)

Figure 8.30 – UCyclic and ABAQUS results (joint E3-TB-E-M3_ts0): EPB in row 8.

8.5.4. ResultsAnalyzer

Figure 8.31 depicts the results of AN1 in terms of force-deformation relations computed with UCyclic for CWT (spring #1), CFB (spring #2) and EPB (spring #3) in row 1, CWC (spring #1) in row 2 and CWT (spring #1) and CFB (spring #2) in row 3 and the bending moment–rotation of the joint and the connection using a screenshot of ResultsAnalyser – the red dot corresponds to the same step in all the graphics.

Figure 7.10 depicts the results of AN3 in terms of force-deformation relations computed with UCyclic for CWS, CWT (spring #1) and EPB (spring #3) in row 1, CWC (spring #1) in row 2 and CWT (spring #1) and BT (spring #5) in row 3 and the bending moment–rotation of the joint and the connection using a screenshot of ResultsAnalyser

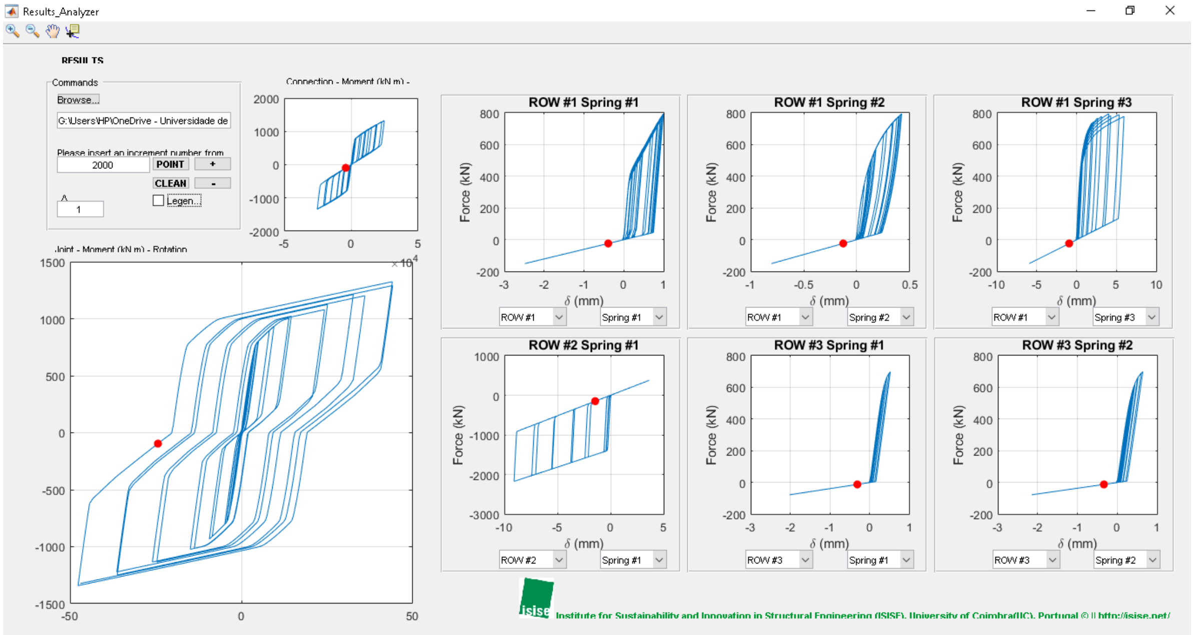

G:\Users\HP\OneDrive - Universidade de

Please insert an increment number from: 2000

Δ: 1

Figure 8.31 – ResultsAnalyser (AN1).

8.6. Concluding remarks

In this chapter the procedures developed in Chapters 6 and 7 were applied to compute the mechanical behaviour to a joint designed according to EN 1993-1-8 (CEN, 2005c). The joint selected was analysed in the scope of the research project EQUALJOINTS (Landolfo, 2017a).

The example illustrates the application of the computer program UCyclic to predict the quasi-static cyclic behaviour of a steel beam-to-column joint. Results from UCyclic are compared in terms of moment-rotation curves of the joint and connection and the force-deformation curves of the dissipative components with the results obtained from a refined 3D FEM model developed in ABAQUS. The comparison showed a good agreement and some expected divergences were found and explained.

The extend of classic component model for quasi-static cyclic conditions is complex, time-consuming and requires several developments. In order to overcome the divergences identified further developments related to the UCyclic tool are required aiming for the (i) the implementation of the decoupled modelling strategy for the CFB and EPB components (T-stub) proposed in Chapter 5 and (ii) additional kinematic constraints of the mechanical model, see the refined component model described in Section 7.3.4 and in Annex D.

Besides the developments in UCyclic, further developments are needed to achieve reliable values for the parameters required for the constitutive models for the components. The strength and stiffness models available in EN 1993-1-8 (CEN, 2005c) are not enough for quasi-static cyclic conditions and do not seem to have the required reliability. Refined 3D FEM models allow to get not only the global behaviour of the joint but also the force-deformation curves of the dissipative components. However, the process of characterizing the mechanical behaviour of components from refined 3D FEM models is complex and requires also some improvements, namely for tension-only or compression-only components.

The results gathered so far allowed not only a deeper insight into the quasi-static cyclic behaviour of SBCJs but also have already proven that CCM provides a reasonable simulation of the joint behaviour for quasi-static cyclic analysis and embodies a clear and powerful tool.

9 CONCLUSIONS AND FUTURE WORK

9.1. Overview

The primary goal of this thesis was to contribute to the development of a method, based on the classic component method, to model and design SBCJs under quasi-static cyclic loading. This goal was pursued by (i) the characterization and modelling of the quasi-static cyclic behaviour of one of the most dissipative components of a SBCJ, i.e. the components that can be modelled through the T-stub analogy, and (ii) the development and implementation of a tool aimed for the assessment of quasi-static cyclic of SBCJs.

The first objective was tackled (i) conducting a test programme on T-stubs under quasi-static cyclic conditions, (ii) evaluating the existing models to characterize the cyclic behaviour of T-stubs and (iii) developing a decoupled component model for the quasi-static cyclic behaviour T-stubs.

The second objective was tackled (i) developing a cyclic component model (CCM), (ii) implementing an incremental-iterative procedure to solve the non-linear system of governing equations of mechanical model underneath the CCM and (iii) illustrating the applicability of the previous tools and methodologies.

9.2. Summary of main contributions

There are some original contributions in this research work that will be summarized in the following paragraphs regarding specifically the components that can be modelled through the T-stubs analogy and the overall SBCJ.

(i) T-stub components related

- a detailed review on the state-of-art of the characterization of the mechanical behaviour of bolted T-stubs under quasi-static cyclic conditions which highlighted the data collection of experimental tests, available analytical models and numerical works on refined 3D FEM models;
- a comprehensive test programme on bolted T-stubs under quasi-static cyclic conditions that yield a database of experimental results on this isolated component; previous research work on coupled rolled T-stubs under variable amplitude cyclic loading is scant in technical literature, see Table 2.2 – Piluso and Rizzano (2008) refer only two test on coupled rolled T-stubs under variable amplitude cyclic loading to validate an analytical methodology; this test programme provided insight into the actual behaviour of this isolated component, failure modes and evolution of mechanical properties throughout the loading history; a quantitative and a qualitative analysis of the T-stub behaviour was performed to provide a better understanding of their quasi-static cyclic behaviour and to identify governing physical phenomena;
- an assessment of the quasi-static cyclic modelling techniques available for T-stubs by using global models; two approaches available in technical literature were assessed and

compared against experimental results in terms of force and energy dissipation: (i) a semi-analytical model (Piluso and Rizzano, 2008) and (ii) a multi-parameter model (MRA model); the set of parameters required by MRA model were calibrated for T-stubs using MultiCal software (Chisari *et al.*, 2017), a curve fitting tool that uses multi-objective optimization managed by Genetic Algorithms;

- development and implementation of a strategy for the quasi-static cyclic modelling of T-stubs by means of a decoupled component model; the rationale for decoupling of the T-stub cyclic behaviour in tension and compression behaviours into separate sub-components was presented and decoupled constitutive relations (tension-only and compression-only) components were developed from adaptation of the MRA model; the decoupled component model for the quasi-static cyclic behaviour of T-stubs (TS-CCM) was validated against experimental results; a sensitivity analysis of the T-stub behaviour computed with the decoupled component model to the MRA parameters and parameter ratios was carried out;

(ii) *cyclic component model for joints related*

- an extensive review on the state-of-art of the characterization of the moment-rotation behaviour of SBCJs under quasi-static cyclic conditions which highlighted the most relevant phenomena and the existing models available for computing their mechanical behaviour;

- an extension of the component method to include quasi-static cyclic loading, called cyclic component method (CCM), to simulate the quasi-static cyclic behaviour of SBCJs.
- the algorithms required to implement the CCM in the software named UCyclic was developed in MATLAB (2019);
- a complete application example of the CCM was presented for an end-plate SBCJ, highlighting the level of accuracy achieved so far in the simulations of the quasi-static cyclic behaviour of joints.

9.3. Summary of main conclusions

Several conclusions drawn from this research work are briefly recalled in the following paragraphs regarding specifically the components that can be modelled through the T-stubs analogy and the overall SBCJ.

(i) T-stub components related

- experimental evidence shows that the quasi-static cyclic behaviour of T-stubs is influenced by the loading protocol (variable or constant amplitude), the presence or not of the bolt preloading and the failure mode;
- the cyclic behaviour of T-stubs is characterized by strong pinching, with higher levels for T-stubs failing according to FM2;

- the MRA model is a versatile model capable of reproducing the complex phenomena observed in T-stubs subjected to quasi-static cyclic loading, in particular the pinching phenomenon and strength and stiffness degradation; however, the MRA model considers the pinching parameters constant throughout the loading history, and the experimental evidence seems to show that these parameters should be dependent of dissipated energy;
- in the scope of the CCM, the decoupling of the cyclic behaviour of the T-stub in tension and compression sub-components is required; the proposed decoupled component model for T-stubs subjected to quasi-static cyclic loading was developed using tension-only and compression-only sub-components with constitutive relations based on the MRA model; the model efficiently reproduces the load reversal and the transition from tension to compression and vice-versa.

(ii) *cyclic component model for joints related*

- the cyclic component method (CCM), developed in the scope of classic component method coded in EC3-1-8 (CEN, 2005c), provides an adequate general basis for the modelling and design of a steel beam-column joints;
- the computational implementation of the CCM (in MATLAB) is a powerful tool, capable of computing the full quasi-static cyclic behaviour of a generic steel beam-column joint;
- the CMM allows a deeper insight into the quasi-static cyclic behaviour of SBCJs and yields good results in terms of global behaviour;

- the models for computing strength and initial stiffness of components provided in EC3-1-8 (CEN, 2005c) may not provide reliable values for the application of CCM; because this is out of scope of the current thesis, all the assessments were conducted based on the component mechanical behaviour extracted from 3D refined FEM models;
- at the current stage, the CCM is able to generate cyclic bending moment-rotation response of steel joints with reasonable accuracy and some required developments were identified, namely, the implementation of the T-stub decoupled component model to account the compression behaviour for positive deformations, i.e. the compression-only behaviour for the CFB and EPB components developed in Chapter 5 ;
- the work performed so far opens the way for the reliable prediction of the quasi-static cyclic mechanical behaviour of steel joints based in the component method.

9.4. Recommendations for future work

The work presented in this thesis lays the foundation for future work on the cyclic component model and to provide a practical tool for the analysis and design SBCJs subjected to quasi-static cyclic loading. However, some aspects of this work still require a more thorough investigation:

- improved procedures for the extraction of the quasi-static cyclic behaviour of components from experimental tests and/or refined 3D FEM models – a reliable and wide data base for mechanical behaviour for each type of component is required for calibration of constitutive models;

- assessment of the suitability of the EC3-1-8 models for the holonomic mechanical behaviour of components for the case of quasi-static loading;
- mechanical-based models for the quasi-static cyclic behaviour of components using as input the mechanical characteristics of steel material and the geometrical characteristics of the components – existing models still depend on many empirical parameters;
- evolution of the pinching level throughout the loading history – existing models tackle pinching parameters as constant, but the experimental evidence seems to show that these parameters should be dependent of dissipated energy;
- calibration and validation the response of the proposed CCM using experimental tests data for a wide and diverse sample of SBCJs until the results of the CCM inspire enough confidence to be used in the current practice;
- develop a user-friendly interface for the software that embodies the CCM.

9.5. Dissemination and publications

The research work described above has been disseminated in several written supports and oral communications, namely:

1) International Journal Papers

Oliveira, Sara; Costa, Ricardo; Santos, Ana Francisca, Simões da Silva, Luís; Harada, Yukihiro; Piluso, Vincenzo. *“A decoupled T-stub component model for the cyclic modelling of* *steel joints"*. Journal of Constructional Steel research, Vol. 209, June 2023. DOI: 10.1016/j.jcsr.2023.108044;

Oliveira, Sara; Costa, Ricardo; Shahbazian, Ashkan; Rebelo, Carlos; Harada, Yukihiro; Simões da Silva, Luís. *"Component-Based Method for Quasi-Static Cyclic Behaviour of Steel Joints"*. Journal of Constructional Steel Research, Vol. 181, June 2021. DOI: 10.1016/j.jcsr.2021.106551;

Simões da Silva, Luís; **Oliveira, Sara**; Costa, Ricardo; Gentili, Filippo. *"Design and Analysis of Steel Structures Considering the 3D Behaviour of the Joints"*. Advanced Steel Construction, Vol. 16, No. 2, pp. 137-145 (2020). DOI: 10.18057/IJASC.2020.16.2.5;

Costa, Ricardo; Valdez, José; **Oliveira, Sara**; Silva, Simões da Silva, Luís; Bayo, Eduardo. *"Experimental behaviour of 3D end-plate beam-to-column bolted steel joints"*. Engineering Structures, Vol. 188, pp. 277-289, June 2019. DOI: 10.1016/j.engstruct.2019.03.017.

2) Conference proceedings

Oliveira, Sara; Costa, Ricardo; Santos, Ana Francisca; Simões da Silva, Luís. "*Modelo de componente desacoplada para T-stubs na modelação cíclica de juntas metálicas*". XIV Congresso de Construção Metálica e Mista, Coimbra, Portugal, November 2023 (*accepted*);

Oliveira, Sara; Costa, Ricardo; Rebelo, Carlos; Simões da Silva, Luís. *"Modelo de componentes cíclico para T-stub"*. 6ª Jornadas Portuguesas de Engenharia de Estruturas (JPEE), Lisboa, Portugal, November 2022;

Oliveira, Sara; Costa, Ricardo; Rebelo, Carlos; Simões da Silva, Luís. *"Avaliação experimental de T-stubs sob carregamento cíclico"*. XIII Congresso de Construção Metálica e Mista, Coimbra, Portugal, November 2021;

Oliveira, Sara; Costa, Ricardo; Rebelo, Carlos; Simões da Silva, Luís. *"Experimental assessment of bolted T-stubs under cyclic loading"*. Eurosteel 2021, Sheffield, England, September 2021. DOI: 10.1002/cepa.1512;

Oliveira, Sara; Costa, Ricardo; Rebelo, Carlos; Simões da Silva, Luís. *"Cyclic behaviour of steel beam-to-column joints and calculation tools"*. Eurosteel 2021, Sheffield, England, September 2021. DOI: 10.1002/cepa.1511;

Oliveira, Sara; Costa, Ricardo; Rebelo, Carlos; Simões da Silva, Luís. *"Ferramentas de cálculo para a previsão do comportamento cíclico de juntas viga-coluna metálicas"*. XII Congresso de Construção Metálica e Mista, Coimbra, Portugal, November 2019;

Oliveira, Sara; Costa, Ricardo; Rebelo, Carlos; Silva, Simões da Silva, Luís. *"Comportamento cíclico de juntas viga-coluna metálicas"*. SÍSMICA 2019 – 11º Congresso Nacional de Sismologia e Engenharia Sísmica, Lisboa, Portugal, April 2019;

Oliveira, Sara; Lemma, Melaku Seyoum; Costa, Ricardo; Rebelo, Carlos; Simões da Silva, Luís. *"Aplicação móvel para o cálculo do comportamento cíclico de juntas viga-coluna metálicas"*. SÍSMICA 2019 – 11º Congresso Nacional de Sismologia e Engenharia Sísmica, Lisboa, Portugal, April 2019;

Oliveira, Sara; Augusto, Hugo; Costa, Ricardo; Rebelo, Carlos; Harada, Yukihiro; Simões da Silva, Luís. *"Implementação computacional de um modelo baseado em componentes para previsão do comportamento cíclico de juntas viga-coluna metálicas"*. XI Congresso de Construção Metálica e Mista, Coimbra, Portugal, November 2017;

Oliveira, Sara; Gentili, Filippo; Shahbazian, Ashkan; Augusto, Hugo; Costa, Ricardo; Rebelo, Carlos; Harada, Yukihiro; Simões da Silva, Luís. *"Assessment of the seismic performance of steel frames using OpenSees"*. OpenSees Days Europe 2017 - 1st European Conference on OpenSees, Porto, Portugal, June 2017.

3) Oral presentations

Sara Oliveira. *"Herramientas de cálculo para uniones precalificadas para sismo"*, Workshop: Estructuras de acero resistentes a sismo – Diseño de uniones precalificadas, Universitat Politècnica de Catalunya (Barcelona, Espanha), 16 May 2019.

Sara Oliveira. *"Modelação analítica do comportamento cíclico de juntas viga-pilar"*, Workshop: Pré-qualificação de juntas viga-pilar metálicas, Tektónica – Feira Internacional da Construção e Obras Públicas (Lisboa, Portugal), 10 May 2019;

Sara Oliveira. "WP4 – EQUALJOINTS Tools, WP5 – Preparation of Workshop Materials and WP6 – Dissemination activities", 4th EQUALJOINTS+ Meeting, Universitatea Politehnica Timisoara, 11 November 2018;

Sara Oliveira. “WP4 – EQUALJOINTS Tools and WP6 – Dissemination activities”, 3rd EQUALJOINTS+ Meeting, Universitat Politècnica de Catalunya, 10 July 2018;

Sara Oliveira. “WP4 – EQUALJOINTS Tools”, 2nd EQUALJOINTS+ Meeting, Università degli Studi di Salerno, 24 January 2018;

REFERENCES

ABAQUS (2014a) *ABAQUS 6.14: Analysis user's guide, Volume III: Materials*. Providence, RI, USA: Dessault Systèmes Simulia Corp.

ABAQUS (2014b) *ABAQUS 6.14: Analysis user's guide, Volume IV: Elements*. Providence, RI, USA: Dassault Systèmes Simulia Corp.

ABAQUS (2014c) *Users, Theory and Scripting manuals*. Providence, RI, USA: ABAUS, Inc., Dassault Systèmes Simulia Corp.

ABAQUS (2022) 'Users, Theory and Scripting manuals, Dassault Systèmes Simulia Corp.' Providence, RI, USA: ABAUS, Inc., Dassault Systèmes Simulia Corp.

Agerskov, H. (1976) 'High-strength bolted connections subjected to prying', *Journal of the Strctural Division*, 102(1), pp. 191–175.

AISC (2005) 'ANSI/AISC 341-05: Seismic Provisions for Structural Steel Buildings', *American Institute of Steel Construction (AISC)*, p. 334.

AISC (2016a) *ANSI/AISC 341-16: Seismic Provisions for Structural Steel Buildings*. Chicago, Illinois, USA: American Institute of Steel Construction.

AISC (2016b) *ANSI/AISC 358-16: Prequalified connections for special and intermediate steel moment frames for seismic applications*. Chicago, Illinois, USA: American Institute of Steel

Construction.

Andrade, T. (2019) *Relevância do pré-esforço dos parafusos no comportamento de ligações metálicas com chapa de extremidade Relevance of bolt preloading in the behaviour of steel connections with end plates*. Universidade de Coimbra.

Ang, K.M. and Morris, G.A. (1984) ‘Analysis of three-dimensional frames with flexible beam–column connections’, *Canadian Journal of Civil Engineering*, 11(2), pp. 245–254. Available at: https://doi.org/10.1139/l84-037.

Augusto, H. (2017) *Characterization of the behaviour of partial-strength joints under cyclic and seismic loading conditions*. University of Coimbra. Available at: http://hdl.handle.net/10316/37035.

Augusto, H., Simões da Silva, L., Rebelo, C. and Castro, J.M. (2016) ‘Characterization of web panel components in double-extended bolted end-plate steel joints’, *Journal of Constructional Steel Research*, 116, pp. 271–293.

Augusto, H., Simões da Silva, L., Rebelo, C. and Castro, J.M. (2017) ‘Cyclic behaviour characterization of web panel components in bolted end-plate steel joints’, *Journal of Constructional Steel Research*, 133, pp. 310–333. Available at: https://doi.org/10.1016/j.jcsr.2017.01.021.

Baber, T.T. and Noori, M.N. (1985) ‘Random vibration of degrading, pinching systems’, *Journal of Engineering Mechanics*, 111(8), pp. 1010–1026.

Baber, T.T. and Noori, M.N. (1986) ‘Modeling general hysteresis behavior and random vibration application’, *Journal of Vibration, Acoustics, Stress, and Reliability in Design*, 108(4), pp. 411–420. Available at: https://doi.org/10.1115/1.3269364.

Baber, T.T. and Wen, Y.-K. (1981) ‘Random Vibration of Hysteretic, Degrading Systems’, *Journal of the Engineering Mechanics Division*, 107(6). Available at: https://doi.org/10.1061/JMCEA3.00027.

Barata, P., Ribeiro, J., Rigueiro, C., Santiago, A. and Rodrigues, J.P. (2014) ‘Assessment of the T-stub joint component at ambient and elevated temperatures’, *Fire Safety Journal*, 70, pp. 1–13. Available at: https://doi.org/10.1016/j.firesaf.2014.08.009.

Bernuzzi, C., Zandonini, R. and Zanon, P. (1996) ‘Experimental analysis and modelling of semi-rigid steel joints under cyclic reversal loading’, *Journal of Constructional Steel Research*, 38(2), pp. 95–123. Available at: https://doi.org/10.1016/0143-974X(96)00013-2.

Bezerra, L.M., Bonilla, J., Freitas, C.S. and Massicotte, B. (2022) ‘Behavior of T-stub steel connections bolted to rigid bases’, *Journal of Constructional Steel Research*, 192(December 2021), p. 107242. Available at: https://doi.org/10.1016/j.jcsr.2022.107242.

Bezerra, L.M., Bonilla, J., Silva, W.A. and Matias, W.T. (2020) ‘Experimental and numerical studies of bolted T-stub steel connection with different flange thicknesses connected to a rigid base’, *Engineering Structures*, 218(May), p. 110770. Available at: https://doi.org/10.1016/j.engstruct.2020.110770.

Borges, L. (2003) *Probabilistic evaluation of the rotation capacity of steel joints*. Universdidade de Coimbra. Available at: https://estudogeral.sib.uc.pt/handle/10316/15652.

Bouc, R. (1967) 'Forced Vibrations of a Mechanical System with Hysteresis', in *Proceedings of the 4th Conference on Non-linear Oscillations*. Prague, p. 315.

BSI (2008) 'BS EN 1090-2: Execution of steel structures and aluminium structures - Part 2: Technical requirements for the execution of steel structures', *British Standards* [Preprint].

Bursi, O.S., Ballerini, M., Nemati, N. and Zandonini, R. (1997) 'Quasi-static monotonic and low-cycle behaviour of steel isolated tee stub connections', in *STESSA '97 - Behaviour of Steel Structures in Seismic Area*. Kyoto, Japan.

Bursi, O.S. and Ferrario, F. (2003) 'Computational models for the low-cycle fatigue behaviour of composite members and joints', *Progress in civil and structural engineering computing, Saxe-Coburg Publications, Stirling,* pp. 119–148. Available at: https://doi.org/10.4203/csets.10.5.

Bursi, O.S., Ferrario, F. and Fontanari, V. (2002) 'Non-linear analysis of the low-cycle fracture behaviour of isolated Tee stub connections', *Computers & Structures,* 80, pp. 2333–2360.

Bursi, O.S. and Jaspart, J.-P. (1997) 'Benchmarks for finite element modelling of bolted steel connections', *Journal of Constructional Steel Research*, 43(1–3), pp. 17–42. Available at: https://doi.org/10.1016/S0143-974X(97)00031-X.

Bursi, O.S. and Jaspart, J.-P. (1998) 'Basic issues in the finite element simulation of extended end plate connections', *Computers and Structures*, 69(3), pp. 361–382. Available at: https://doi.org/10.1016/S0045-7949(98)00136-9.

CEA (2017) 'CAST3M'. France: Commissariat à l'Energie Atomique. Available at: http://www-cast3m.cea.fr.

CEN (2003) 'prEN 1993-1-8 - Eurocode 3: Design of steel structures, Part 1-8: Design of joints', *European Committe for Standardization,* Stage 49 d(May 2003).

CEN (2004) 'EN 1998-1 - Eurocode 8: Design of strcutures for earthquake resistance - Part 1: General rules, seismic actions and rules for buildings', *Comité Européen de Normalisation* [Preprint].

CEN (2005a) 'EN 14399-3: High-strength structural bolting assemblies for preloading - Part 3: System HR - Hexagon bolt and nut assemblies'.

CEN (2005b) 'EN 14399-5: High-strength structural bolting assemblies for preloading - Part 5: Plain washers'.

CEN (2005c) 'EN 1993-1-8 - Eurocode 3: Design of steel structures, Part 1-8: Design of joints', *Comité Européen de Normalisation* [Preprint].

CEN (2005d) 'Eurocode 8: Design of structures for earthquake resistance - Part 1 : General rules, seismic actions and rules for buildings'.

Chen, S., Feng, B., Wang, L., Zhang, Y. and He, J. (2023) 'Effect of stiffeners on mechanical beahvior of T-stubs based on experiment and numerical simulations', *Buildings*, 13. Available at: https://doi.org/doi.org/10.3390/buildings13040986.

Chen, W.-F. and Lui, E.M. (1991) *Stability design of steel frames*. CRC Press.

Chen, Z., Gao, F., Wang, Z., Lin, Q., Huang, S. and Ma, L. (2023) 'Performance of Q690 high-strength steel T-stub under monotonic and cyclic loading', *Engineering Structures*, 277(November 2022). Available at: https://doi.org/10.1016/j.engstruct.2022.115405.

Chisari, C., Francavilla, A.B., Latour, M., Piluso, V., Rizzano, G. and Amadio, C. (2017) 'Critical issues in parameter calibration of cyclic models for steel members', *Engineering Structures*, 132, pp. 123–138.

Coelho, A.M.G., Simões, L. and Bijlaard, F.S.K. (2004) 'Characterization of the Nonlinear Behaviour of Single Bolted T-Stub Connections', (March), pp. 53–64.

Cofie, N.G. and Krawinkler, H. (1985) 'Uniaxial Cyclic Stress-Strain Behavior of Structural Steel', *Journal of Engineering Mechanics*, 111(9), pp. 1105–1120. Available at: https://doi.org/10.1061/(asce)0733-9399(1985)111:9(1105).

Colson, A. and Louveau, J.M. (1983) 'Connections incidence on the inelastic behavior of steel structures', in *Proceedings of Euromech Colloquium*.

Della Corte, G., De Matteis, G. and Landolfo, R. (2000) 'Influence of connection modelling on seismic response of moment resisting steel frames', *Moment resistant connections of steel buildings frames in seismic areas, E. & FN Spon, London*, pp. 485–512.

Cruz, P.J.S., Simões da Silva, L., Rodrigues, D.S. and Simões, R. (1998) ‘Database for the semi-rigid behaviour of beam-to-column connections in seismic regions’, *Journal of Constructional Steel Research,* 46(1–3), pp. 233–234. Available at: https://doi.org/10.1016/S0143-974X(98)80023-0.

D’Aniello, M., Cassiano, D. and Landolfo, R. (2016) ‘Monotonic and cyclic inelastic tensile response of European preloadable gr10.9 bolt assemblies’, *Journal of Constructional Steel Research,* 124, pp. 77–90. Available at: https://doi.org/10.1016/j.jcsr.2016.05.017.

D’Aniello, M., Cassiano, D. and Landolfo, R. (2017) ‘Simplified criteria for finite element modelling of European preloadable bolts’, *Steel and Composite Structures,* 24(6), pp. 643–658. Available at: https://doi.org/10.12989/scs.2017.24.6.643.

D’Aniello, M., Tartaglia, R., Costanzo, S. and Landolfo, R. (2017) ‘Seismic design of extended stiffened end-plate joints in the framework of Eurocodes’, *Journal of Constructional Steel Research,* 128, pp. 512–527. Available at: https://doi.org/10.1016/j.jcsr.2016.09.017.

Deb, K., Pratap, A., Agarwal, S. and Meyarivan, T. (2002) ‘A fast and elitist multiobjective genetic algorithm: NSGA-II’, *IEEE Transactions on Evolutionary Computation,* 6(2), pp. 182–197. Available at: https://doi.org/10.1109/4235.996017.

Dobson, S., Noori, M., Hou, Z., Dimentberg, M. and Baber, T. (1997) ‘Modeling and random vibration analysis of SDOF systems with asymmetric hysteresis’, *International Journal of Non-Linear Mechanics,* 32(4), pp. 669–680. Available at: https://doi.org/10.1016/s0020-7462(96)00090-x.

Douty, R.T. and McGuire, W. (1964) ‘High strength bolted connections with applications to plastic design’, in *7th IABSE Congress*. Rio de Janeiro, Brasil. Available at: http://doi.org/10.5169/seals-7868.

Douty, R.T. and McGuire, W. (1965) ‘High strength moment connections’, *Journal of Strctural Division ASCE*, 91(ST2), pp. 101–128.

Downs, W.M. (2002) *Modeling and Behavior of the Beam/Column Joint Region of Steel Moment Resisting Frames*. Virginia Tech. Available at: http://hdl.handle.net/10919/46198.

Faella, C., Piluso, V. and Rizzano, G. (1998a) ‘Cyclic behaviour of bolted joint components’, *Journal of Constructional Steel Research*, 46(1–3), pp. 433–434.

Faella, C., Piluso, V. and Rizzano, G. (1998b) ‘Experimental analysis of bolted connections: snug versus preloaded bolts’, 124(7), pp. 765–774. Available at: https://doi.org/10.1061/(ASCE)0733-9445(1998)124:7(765).

Faella, C., Piluso, V. and Rizzano, G. (1999) ‘Modelling of the Cyclic Behaviour of Bolted Tee-Stubs’, *Light-Weight Steel and Aluminium Structures*, pp. 539–546. Available at: https://doi.org/10.1016/b978-008043014-0/50165-7.

Faella, C., Piluso, V. and Rizzano, G. (2000) *Structural steel semirigid connections: theory, design and software*. CRC Press.

Faralli, A.C., Latour, M., Tan, P.J., Rizzano, G. and Wrobel, P. (2021) ‘Experimental investigation and modelling of T-stubs undergoing large displacements’, *Journal of*

Constructional Steel Research, 180, p. 106580. Available at: https://doi.org/10.1016/j.jcsr.2021.106580.

Faralli, A.C., Tan, P.J., Latour, M. and Rizzano, G. (2018) 'Finite Element Analysis of Bolted T-Stubs Undergoing Large Displacement: A Preliminary Study', *The Open Construction and Building Technology Journal*, 12(1), pp. 170–176. Available at: https://doi.org/10.2174/1874836801812010170.

FEMA (2000a) 'FEMA-350: Recommended Seismic Design Criteria for New Steel Moment-Frame Buildings'.

FEMA (2000b) 'FEMA-355C: State of the Art Report on Systems Performance of Steel Moment Frames Subject to Earthquake Ground Shaking', *Federal Emergency Management Agency, Washington, DC* [Preprint].

Filippou, F.C., Popov, E.P. and Bertero, V.V. (1983) 'Effects of Bond Deterioration on Hysteretic Behaviour of Reinforced Concrete Joints. Report to the National Science Foundation', *Earthquake Engineering Research Center*, pp. 1–212. Available at: http://www.ce.berkeley.edu/~filippou/Research/Publications/Reports/EERC-83-19.pdf.

Gebbenken, N., Wanzek, T. and Petersen, C. (1997) *Semi-Rigid Connections T-Stub Modelle - Versuchsbericht - Report on Experimental Investigations*. ISSN 1431-1522. München.

Gervásio, H., Simões da Silva, L. and Borges, L. (2004) 'Reliability assessment of the post-limit stiffness and ductility of steel joints', *Journal of Constructional Steel Research*, 60(3–5), pp. 635–648. Available at: https://doi.org/10.1016/S0143-974X(03)00145-7.

Gil-Martín, L.M. and Hernández-Montes, E. (2020) ‘A compact and simpler formulation of the component method for steel connections’, *Journal of Constructional Steel Research*, 164. Available at: https://doi.org/10.1016/j.jcsr.2019.105782.

Girão Coelho, A.M. (2004) *Characterization of the ductility of bolted end plate beam-to-column*. Universidade de Coimbra.

Girão Coelho, A.M., Bijlaard, F.S.K., Gresnigt, N. and Simões da Silva, L. (2004) ‘Experimental assessment of the behaviour of bolted T-stub connections made up of welded plates’, *Journal of Constructional Steel Research*, 60(2), pp. 269–311. Available at: https://doi.org/10.1016/j.jcsr.2003.08.008.

Girão Coelho, A.M., Simões da Silva, L. and Bijlaard, F.S.K. (2006) ‘Finite-Element Modeling of the Nonlinear Behavior of Bolted T-Stub Connections’, *Journal of Structural Engineering*, 132(6), pp. 918–928. Available at: https://doi.org/10.1061/(asce)0733-9445(2006)132:6(918).

Gödrich, L., Wald, F., Kabeláč, J. and Kuříková, M. (2019) ‘Design finite element model of a bolted T-stub connection component’, *Journal of Constructional Steel Research*, 157, pp. 198–206. Available at: https://doi.org/10.1016/j.jcsr.2019.02.031.

Guo, H., Liang, G., Li, Y.L. and Liu, Y. (2017) ‘Q690 high strength steel T-stub tensile behavior: Experimental research and theoretical analysis’, *Journal of Constructional Steel Research*, 139, pp. 473–483. Available at: https://doi.org/10.1016/j.jcsr.2017.10.007.

Hu, J.W., Leon, R.T. and Park, T. (2011) ‘Mechanical modeling of bolted T-stub connections under cyclic loads Part I: Stiffness modeling’, *Journal of Constructional Steel Research*, 67(11), pp. 1710–1718. Available at: https://doi.org/10.1016/j.jcsr.2011.04.009.

Hu, J.W., Leon, R.T. and Park, T. (2012) ‘Mechanical models for the analysis of bolted T-stub connections under cyclic loads’, *Journal of Constructional Steel Research*, 78, pp. 45–57. Available at: https://doi.org/10.1016/j.jcsr.2012.05.011.

Huber, G. and Tschemmernegg, F. (1998) ‘Modelling of Beam-to-Column Joints’, *Journal of Constructional Steel Research*, 45(2), pp. 199–216.

Hutton, D. V. (2003) *Fundamentals of Finite Element Analysis*. New York: McGraw-Hill. Available at: https://doi.org/10.1093/cid/ciq004.

Iannone, F., Latour, M., Piluso, V. and Rizzano, G. (2011) ‘Experimental analysis of bolted steel beam-to-column connections: Component identification’, *Journal of Earthquake Engineering*, 15(2), pp. 214–244. Available at: https://doi.org/10.1080/13632461003695353.

Ibarra, L.F., Medina, R.A. and Krawinkler, H. (2005) ‘Hysteretic models that incorporate strength and stiffness deterioration’, *Earthquake engineering & structural dynamics*, 34(12), pp. 1489–1511. Available at: https://doi.org/10.1002/eqe.495.

ISO (2009) ‘ISO 6892-1: Metallic materials - Tensile testing - Part 1: Method of test at room temperature’.

Jaspart, J.-P. (1991) *Étude de la Semi-Rigidité des Noeuds Poutre-Colonne et son Influence sur* *la Resistence et la Stabilité des Ossatures en Acier*. University of Liège, Belgium.

Jaspart, J.-P. (1997) *Recent advances in the field of joints: Column bases and further configurations for beam to column joints and beam splices*. University of Liège, Belgium.

Jaspart, J.-P. (2000) 'General report: Session on connections', *Journal of Constructional Steel Research*, 55(1–3), pp. 69–89. Available at: https://doi.org/10.1016/S0143-974X(99)00078-4.

Jaspart, J.-P. and Maquoi, R. (1995) 'Effect of bolt preloading on joint behaviour', in *Proc., Steel Struct., Eurosteel '95*, pp. 219–226.

Jaspart, J.-P. and Weynand, K. (2016) *Design of joints in steel and composite structures*. ECCS Press and Ersnest & Sohn.

Kasai, K. and Xu, Y. (2002) 'Experimental study on cyclic inelastic behaviour and low-cycle fatigue of bolted T-stub connections', *Journal of Structural and Construction Engineering (Transactions of AIJ)*, 67(561), pp. 227–235.

Kim, K. and Engelhardt, M.D. (1996) *Development of analytical models for earthquake analysis of steel moment frames*. Berkeley, CA.

Kim, K.D. and Engelhardt, M.D. (2002) 'Monotonic and cyclic loading models for panel zones in steel moment frames', *Journal of Constructional Steel Research*, 58(5), pp. 605–635.

Kishi, N. and Chen, W.-F. (1990) 'Moment-rotation relations of semirigid connections with angles', *Journal of Structural Engineering*, 116(7), pp. 1813–1834.

Krawinkler, H. (1978) ‘Shear in beam-column joints in seismic design of steel frames’, *Engineering Journal*, 15(3), pp. 82–91. Available at: https://www.aisc.org/Shear-in-Beam-Column-Joints-in-Seismic-Design-of-Steel-Frames.

Krawinkler, H., Zohrei, M., Lashkari-Irvani, B., Cofie, N.G. and Hadidi-Tamjed, H. (1983) *Recommendations for Experimental Studies on the Seismic Behavior of Steel Components and Materials, Report - Stanford University, John A. Blume Earthquake Engineering Center*. Stanford, CA.

Krenk, S. (2001) *Mechanics and analysis of beams, columns and cables: A modern introduction to the classic theories*. 2nd edn. Springer.

Krishnamurthy, N. and Graddy, D.E. (1976) ‘Correlation between 2- and 3-dimensional finite element analysis of steel bolted end-plate connections’, *Computers & Structures*, 6(4–5), pp. 38–389. Available at: https://doi.org/https://doi.org/10.1016/0045-7949(76)90016-X.

Kukreti, A.R., Murray, J.M. and Abolmaali, A. (1987) ‘End-plate connections moment-rotation relationship’, *Journal of Constructional Steel Research*, 8, pp. 137–157. Available at: https://doi.org/10.1016/0143-974X(87)90057-5.

Landolfo, R. (2017a) *European pre-qualified steel joints (EQUALJOINTS) - No. RFSR-CT-2013-00021, Final Report*. Brussels, Belgium. Available at: https://doi.org/10.2777/268762.

Landolfo, R. (2017b) *Valorisation of knowledge for European prequalified steel joints (EQUALJOINTS-PLUS) - No. 754048 (2017).*

Landolfo, R. (2022) ‘European seismic prequalification of steel beam-to-column joints: EQUALJOINTS and EQUALJOINTS-Plus projects’, *Journal of Constructional Steel Research*, 192, p. 107238. Available at: https://doi.org/10.1016/j.jcsr.2022.107238.

Landolfo, R., Mazzolani, F.M., Dubina, D., Simões da Silva, L. and D’Aniello, M. (2017) *Design of steel structures for buildings in seismic areas*. ECCS Press/Ersnest & Sohn. Available at: https://doi.org/10.1002/9783433609194.

Latour, M., Piluso, V. and Rizzano, G. (2011) ‘Cyclic modeling of bolted beam-to-column connections: Component approach’, *Journal of Earthquake Engineering*, 15(4), pp. 537–563.

Latour, M. and Rizzano, G. (2012) ‘Experimental behavior and mechanical modeling of dissipative T-stub connections’, *Journal of Structural Engineering*, 138(2), pp. 170–182. Available at: https://doi.org/10.1061/(ASCE)ST.1943-541X.0000435.

Latour, M. and Rizzano, G. (2019) ‘Mechanical modelling of exposed column base plate joints under cyclic loads’, *Journal of Constructional Steel Research*, 162. Available at: https://doi.org/10.1016/j.jcsr.2019.105726.

Latour, M., Rizzano, G., Santiago, A. and Simões da Silva, L. (2014) ‘Experimental analysis and mechanical modeling of T-stubs with four bolts per row’, *Journal of Constructional Steel Research*, 101, pp. 158–174. Available at: https://doi.org/10.1016/j.jcsr.2014.05.004.

Leon, R.T. (1999) *Tests on T-stub connections - SAC phase II-Subtask 7.03 - Design recommendations for T-stub bolted connections*. Georgia. Available at:

http://hdl.handle.net/1853/17756.

Lignos, D. (2008) *Sidesway collapse of deteriorating structural systems under seismic excitations*. Stanford University.

Lignos, D. and Krawinkler, H. (2011) ‘Deterioration modeling of steel components in support of collapse prediction of steel moment frames under earthquake loading’, *Journal of Structural Engineering*, 137(11), pp. 1291–1302. Available at: https://doi.org/10.1061/(ASCE)ST.1943-541X.0000376.

de Lima, L., da Silva, J.G.S., da Silva, J.G.S., Borges, L. and Simões da Silva, L. (2005) ‘Post-limit stiffness prediction of semi-rigid joints using genetic algorithms’, *Latin American Journal of Solids and Structures*, 2(4), pp. 305–320.

de Lima, L., Simões da Silva, L., Vellasco, P.C.G. da S. and de Andrade, S.A.L. (2004) ‘Experimental evaluation of extended endplate beam-to-column joints subjected to bending and axial force’, *Engineering Structures*, 26(10), pp. 1333–1347. Available at: https://doi.org/10.1016/j.engstruct.2004.04.003.

Ling, Y. (1996) ‘Uniaxial True Stress-Strain after Necking’, 5, pp. 37–48.

Liu, X., Hao, Z., Luo, X. and Jin, Z. (2023) ‘Experimental Behavior and Modelling of Steel Bolted T-Stub Connections’, *Buildings*, 13(3). Available at: https://doi.org/10.3390/buildings13030575.

Maggi, Y.I., Gonçalves, R.M., Leon, R.T. and Ribeiro, L.F.L. (2005) ‘Parametric analysis of steel bolted end plate connections using finite element modeling', *Journal of Constructional Steel Research*, 61(5), pp. 689–708. Available at: https://doi.org/10.1016/j.jcsr.2004.12.001.

Mahin, S., Malley, J. and Hamburguer, R. (2002) 'Overview of the FEMA/SAC program for reduction of earthquake hazards in steel moment frame structures', *Journal of Constructional Steel Research*, 58, pp. 511–528.

De Martino, A., Faella, C. and Mazzolani, F.M. (1984) 'Simulation of beam-to-column joint behaviour under cyclic loads', *Construzioni Metalliche*, 6, pp. 346–356.

MathWorks (2019) 'MATLAB (R2019b)'. Natick, Massachusetts, United States: The MathWorks, Inc., p. Natick, Massachusetts, United States.

MATLAB (2015) 'Curve Fitting Toolbox^{TM} User's Guide R2015b'. The MathWorks, Inc., pp. 1–285.

McKenna, F., Fenves, G.L. and Scott, M.H. (2000) 'OpenSEES - Open System for Earthquake Engineering Simulation'. Berkeley, USA: University of California. Available at: http://opensees.berkeley.edu.

Meek, J.L. (1991) *Computer methods in structural analysis*. Edited by Taylor & Francis. CRC Press.

Miner, M.A. (1945) 'Cumulative Damage in Fatigue', *Journal of Applied Mechanics*, 12(3). Available at: https://doi.org/10.1115/1.4009458.

Nemati, N., Le Houedec, D. and Zandonini, R. (2000) ‘Numerical modelling of the cyclic behaviour of the basic components of steel end plate connections’, *Advances in Engineering Software*, 31(11), pp. 837–849. Available at: https://doi.org/10.1016/S0965-9978(00)00046-6.

Nogueiro, P. (2009) *Comportamento Cíclico de Ligações Metálicas*. Universidade de Coimbra.

Nogueiro, P., Simões da Silva, L., Bento, R. and Simões, R. (2005) ‘Numerical implementation and calibration of a hysteretic model with pinching for the cyclic response of steel and composite joints’, in *Proceedings of the Fourth International Conference on Advances in Steel Structures*. Shangai, pp. 767–774.

Nogueiro, P., Simões da Silva, L., Bento, R. and Simões, R. (2007) ‘Numerical Implementation and Calibration of a Hysteretic Model with Pinching for the Cyclic Response of Steel Joints’, *Advanced Steel Construction,* 3(1), pp. 459–484.

Nogueiro, P., Simões, L. and Bento, R. (2006) ‘Numerical Implementation and Calibration of a Hysteretic Model for Cyclic Response of End-Plate Beam-to-Column Steel Joints under Arbitrary Cyclic Loading’, in *Computational Methods in Engineering & Science*. Springer, pp. 230–240. Available at: https://doi.org/10.1007/978-3-540-48260-4_76.

Oliveira, S., Costa, R., Rebelo, C. and Simões da Silva, L. (2021) ‘Experimental assessment of bolted T-stubs under cyclic loading’, *Ce/Papers,* 4(2–4), pp. 1982–1991. Available at: https://doi.org/10.1002/cepa.1512.

Oliveira, S., Costa, R., Santos, A.F. and Simões da Silva, L. (2023) ‘Modelo de componente desacoplada para T-stubs na modelação cíclica de juntas metálicas', in *XIV Congresso de Construção Metálica e Mista*. Coimbra, Portugal: Associação Portuguesa de Construção Metálica e Mista (CMM).

Oliveira, S., Costa, R., Shahbazian, A., Rebelo, C., Harada, Y. and Simões da Silva, L. (2021) 'Component-based method for quasi-static cyclic behaviour of steel joints', *Journal of Constructional Steel Research*, 181, pp. 1–14. Available at: https://doi.org/10.1016/j.jcsr.2021.106551.

Özkılıç, Y.O. (2021) 'The capacities of thin plated stiffened T-stubs', *Journal of Constructional Steel Research*, 186(August). Available at: https://doi.org/10.1016/j.jcsr.2021.106912.

Packer, J.A. and Morris, L.J. (1977) 'Limit State Design Method for the Tension Region of Bolted Beam-Column Connections', *Structural Engineer*, 55(10), pp. 446–458.

Piluso, V., Faella, C. and Rizzano, G. (2001a) 'Ultimate Behavior of Bolted T-Stubs. I: Theoretical Model', *Journal of Strctural Engineering*, 127(6). Available at: https://doi.org/10.1061/(ASCE)0733-9445(2001)127:6(686).

Piluso, V., Faella, C. and Rizzano, G. (2001b) 'Ultimate Behaviour of Bolted T-Stubs. II: Model Validation', *Journal of Structural Engineering*, 127(6). Available at: https://doi.org/10.1061/(ASCE)0733-9445(2001)127:6(694).

Piluso, V. and Rizzano, G. (2008) 'Experimental analysis and modelling of bolted T-stubs under cyclic loads', *Journal of Constructional Steel Research*, 64(6), pp. 655–669. Available at: https://doi.org/10.1016/j.jcsr.2007.12.009.

Ramberg, W. and Osgood, W.R. (1943) ‘Description of stress-strain curves by three parameters’, *National Advisory Committee for Aeronautics* [Preprint], (Technical Note No. 902).

Ribeiro, J., Santiago, A., Rigueiro, C. and Da Silva, L.S. (2015) ‘Analytical model for the response of T-stub joint component under impact loading’, *Journal of Constructional Steel Research*, 106, pp. 23–34. Available at: https://doi.org/10.1016/j.jcsr.2014.11.013.

Richard, R.M. and Abbott, B.J. (1975) ‘Versatile elastic-plastic stress-strain formula’, *Journal of the Engineering Mechanics Division*, 101(4), pp. 511–515.

Sebbagh, H.R., Kerdal, D.E.D., Abidelah, A. and Bouchaïr, A. (2021) ‘T-stubs with two and four bolts under monotonic and cyclic loading’, *Journal of Constructional Steel Research*, 178. Available at: https://doi.org/10.1016/j.jcsr.2020.106486.

SeismoStruct® (2016) ‘SeismoStruct User Manual’. Pavia, Italy: Seismosoft Ltd, p. 427. Available at: https://seismosoft.com/.

Sherbourne, A.N. and Bahaari, M.R. (1994) ‘3D simulation of end-plate bolted connections’, *Journal of Structural Engineering*, 120(11). Available at: https://doi.org/10.1061/(ASCE)0733-9445(1994)120:11(3122).

Shi, G. and Chen, X. (2017) ‘Moment-rotation curves of ultra-large capacity end-plate joints based on component method’, *Journal of Constructional Steel Research*, 128, pp. 451–461.

Available at: https://doi.org/10.1016/j.jcsr.2016.09.012.

Shi, G., Shi, Y., Wang, Y. and Bradford, M.A. (2008) ‘Numerical simulation of steel pretensioned bolted end-plate connections of different types and details’, *Engineering Structures*, 30(10), pp. 2677–2686.

Simões da Silva, L. (2008) ‘Towards a consistent design approach for steel joints under generalized loading’, *Journal of Constructional Steel Research*, 64(9), pp. 1059–1075. Available at: https://doi.org/10.1016/j.jcsr.2008.02.017.

Simões da Silva, L., de Lima, L.R.O., Vellasco, P.C.G.S. and de Andrade, S.A.L. (2004) ‘Behaviour of flush end-plate beam-to-column joints under bending and axial force’, *Steel and Composite Structures*, 4(2), pp. 77–94. Available at: https://doi.org/10.12989/scs.2004.4.2.077.

Simões da Silva, L., Rebelo, C. and Mota, L. (2009) ‘Extension of the component method to end-plate beam-to-column steel joints subjected to seismic loading’, in *Proceedings of CC2009, Trends in Civil and Structural Engineering Computing*. Funchal, Portugal, pp. 1–4. Available at: https://doi.org/10.4203/csets.22.7.

Simões da Silva, L., Santiago, A. and Vila Real, P. (2002) ‘Post-limit stiffness and ductility of end-plate beam-to-column steel joints’, *Computers and Structures*, 80(5–6), pp. 515–531. Available at: https://doi.org/10.1016/S0045-7949(02)00014-7.

Sivaselvan, M. V and Reinhorn, A.M. (2000) ‘Hysteretic models for deteriorating inelastic structures’, *Journal of Engineering Mechanics*, 126(6), pp. 633–640.

Song, J. and Kiureghian, A. (2006) ‘Generalized Bouc-Wen model for highly asymmetric hysteresis’, *Journal of Engineering Mechanics*, 132(610–618). Available at: https://doi.org/10.1061/(ASCE)0733-9399(2006)132:6(610.

Swanson, J.A. (1999) *Characterization of the strength, stiffness, and ductility behavior of T-stub connections*. Georgia Institute of Technology.

Swanson, J.A. and Leon, R.T. (2000) ‘Bolted steel connections: tests on T-stub components’, *Journal of Structural Engineering*, 126(1), pp. 50–56.

Tambá, B. (2020) *Comportamento experimental de T-Stubs sob condições cíclicas*. Universidade de Coimbra.

Tartaglia, R., D’Aniello, M., Rassati, G.A., Swanson, J.A. and Landolfo, R. (2018) ‘Full strength extended stiffened end-plate joints: AISC vs recent European design criteria’, *Engineering Structures*, 159(November 2017), pp. 155–171. Available at: https://doi.org/10.1016/j.engstruct.2017.12.053.

Tartaglia, R., D’Aniello, M. and Zimbru, M. (2020) ‘Experimental and numerical study on the T-Stub behaviour with preloaded bolts under large deformations’, *Structures*, 27(June), pp. 2137–2155. Available at: https://doi.org/10.1016/j.istruc.2020.08.039.

Tschemmernegg, F., Tautschnig, A., Klein, H. and Humer, C. (1987) ‘Zur Nachgiebigkeit von Rahmenknoten–Teil 1’, *Stahlbau*, 56(10), pp. 299–306.

Wen, Y.-K. (1976) ‘Method for random vibration of hysteretic systems’, *Journal of the*

Engineering Mechanics Division, 102(2), pp. 249–263.

Weynand, K., Jaspart, J.-P. and Steenhuis, M. (1995) 'The stiffness model of revised Annex J of Eurocode 3', in *Proceedings of the Third International Workshop on Connections in Steel Structures*. Trento, pp. 441–452. Available at: http://hdl.handle.net/2268/30592.

Wulan, T., Ma, Q., Liu, Z., Liu, M., Song, J., Cai, J. and Wang, P. (2020) 'Experimental study on T-stubs connected by thread-fixed one-side bolts under cyclic load', *Journal of Constructional Steel Research*, 169, p. 106050. Available at: https://doi.org/10.1016/j.jcsr.2020.106050.

Yee, Y.L. and Melchers, R.E. (1986) 'Moment-rotation curves for bolted connections', *Journal of Structural Engineering*, 112(3), pp. 615–635.

Yuan, H.X., Liu, X.H., Liu, J.L. and Theofanous, M. (2021) 'Cyclic behaviour and hysteretic model of austenitic stainless steel bolted T-stubs', *Journal of Constructional Steel Research*, 182. Available at: https://doi.org/10.1016/j.jcsr.2021.106659.

Zandonini, R. and Bursi, O.S. (2002) 'Monotonic and hysteretic behaviour of bolted endplate beam-to-column joints', *Advances in Steel Structures*, 1. Available at: https://doi.org/10.1016/B978-008044017-0/50010-X.

Zhang, Y., Gao, S., Guo, L., Qu, J. and Wang, S. (2022) 'Ultimate tensile behavior of bolted T-stub connections with preload', *Journal of Building Engineering*, 47(November 2021), p. 103833. Available at: https://doi.org/10.1016/j.jobe.2021.103833.

Zhao, M.S., Lee, C.K. and Chiew, S.P. (2016) 'Tensile behavior of high performance structural steel T-stub joints', *Journal of Constructional Steel Research*, 122, pp. 316–325. Available at: https://doi.org/10.1016/j.jcsr.2016.04.001.

Zhao, X., He, S. and Yan, S. (2021) 'Full-range behaviour of T-stubs with various yield line patterns', *Journal of Constructional Steel Research*, 186(May), p. 106919. Available at: https://doi.org/10.1016/j.jcsr.2021.106919.

Zhu, C., Rasmussen, K.J.R. and Yan, S. (2019) 'Generalised component model for structural steel joints', *Journal of Constructional Steel Research*, 153, pp. 330–342. Available at: https://doi.org/10.1016/j.jcsr.2018.10.026.

Zoetemeijer, P. (1974) 'A design method for the tension side of statically loaded, bolted beam-to-column connections', *HERON*, 20(1). Available at: http://resolver.tudelft.nl/uuid:f2dff8e5-dd92-4a3c-89db-c4fa945ea759.

ANNEXES

ANNEX A: COUPON TESTS OF T-STUBS TESTED AT UNIVERSITY OF COIMBRA

A.1 Geometrical properties

The coupons were provided by the factory that produced the T-stubs and were extracted from the flange and web of the T-shaped elements. The cross section of the coupon is rectangular as presented in Figure A-1.

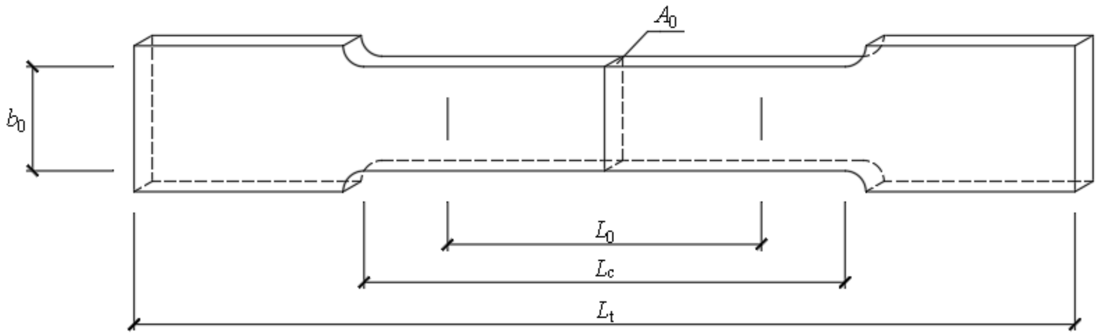

a_0	original thickness of a flat test piece	L_0	original gauge length
b_0	original width of the parallel length of a flat test piece	L_c	parallel length
A_0	original cross-sectional area of the parallel length	L_t	total length of test piece

Figure A-1: Coupon geometry.

A.1.1 Nominal geometrical properties of the coupons

In accordance with clause 6.1.1 of the ISO 6892-1 (ISO, 2009), coupons geometry shows a direct relationship between the original gauge length, L_0, and the original cross-sectional area, S_0, expressed by the following equation

$$L_0 = k\sqrt{S_0} \tag{A-1}$$

where k is a coefficient of proportionality. The internationally adopted value for k is 5.65.

The parallel length of machined test piece, L_c, according to ISO 6892-1 (ISO, 2009) clause D.2.1 b) was

$$L_\mathrm{c} \geq L_0 + 1.5\sqrt{S_0} \tag{A-2}$$

Table A-1 summarizes the nominal geometrical properties of the coupons according to ISO 6892-1 (ISO, 2009). Figure A-2 illustrates the adopted geometry.

Table A-1: Nominal geometrical properties.

coupon		a_0 mm	b_0 mm	S_0 mm^2	L_0 mm	$L_\mathrm{c,min}$ mm	$L_\mathrm{c,adopted}$ mm	L_t mm
A	web	6.5	25	162.5	72.0	91.1	215	450
	flange	10.0	25	250.0	89.3	113.1	215	450
B	web	10.5	25	262.5	91.5	115.8	215	450
	flange	18.0	25	450.0	119.9	151.7	215	450

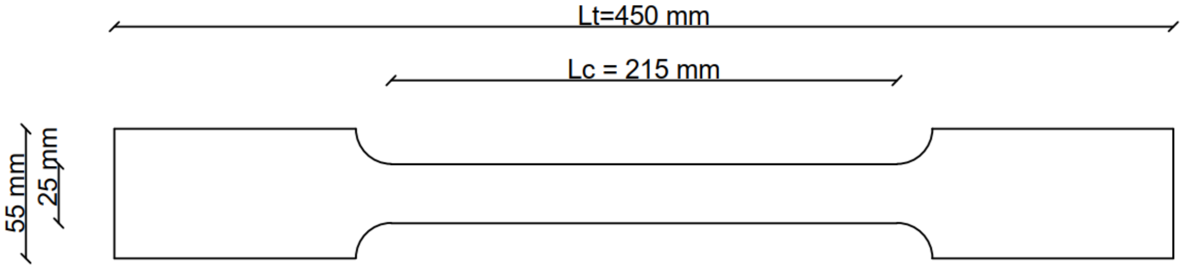

Figure A-2: Coupon adopted geometry.

A.1.2 Measured geometrical properties of the coupons

The original measured cross-sectional area, S_0, was assumed as an average cross-sectional value computed from the measurements of the original thickness, a_0, and the original width, b_0 using multiple measurements. A minimum of three measurements per coupon was performed, as recommended in section 7 of ISO 6892-1 (ISO, 2009), see Table A-2.

Table A-2: Determination of original cross-sectional area.

series	coupon ID	a_{01} mm	a_{02} mm	a_{03} mm	μ_{a_0} mm	b_{01} mm	b_{02} mm	b_{03} mm	μ_{b_0} mm	S_0 mm^2
A web	C01	6.80	6.81	6.82	6.81	24.77	24.80	24.79	24.79	168.80
	C02	6.82	6.76	6.69	6.76	24.89	24.84	24.90	24.88	168.08
	C03	6.75	6.74	6.81	6.77	24.86	24.91	24.92	24.90	168.47
A flange	C04	10.20	9.97	10.05	10.07	24.97	24.99	24.88	24.95	251.30
	C06	8.91	8.92	8.93	8.92	24.83	24.90	24.73	24.82	221.39
	C09	9.99	9.92	9.93	9.95	24.84	24.91	24.96	24.90	247.71
B web	C05	10.49	10.46	10.47	10.47	24.85	24.91	24.83	24.86	260.40
	C07	10.58	10.58	10.58	10.58	24.94	24.94	24.94	24.94	263.87
	C08	10.60	10.63	10.57	10.60	24.97	24.98	24.83	24.93	264.22
B flange	C10	17.40	17.40	17.36	17.39	24.94	24.97	25.20	25.04	435.30
	C11	17.05	17.16	17.27	17.16	24.90	24.95	24.96	24.94	427.91
	C12	17.79	17.81	17.83	17.81	24.98	24.96	24.97	24.97	444.72

A.2 Mechanical properties

A.2.1 Typical stress – strain curve

Figure A-3 depicts the typical stress-strain curve of structural steel, which comprises four regions – linear elastic region, yield plateau, strain hardening region and strain softening after reaching the maximum load – and is characterized by the following properties:

- yield strength $f_y = R_{\mathrm{eH}}$, where R_{eH} is the upper yield strength, i.e. the maximum value of stress prior to the first decrease in force, see Figure A-3;
- yield strain ε_y, where ε_y corresponds to the yield strength f_y;
- ultimate strength $f_u = R_{\mathrm{m}}$, where R_{m} is the tensile strength, i.e. the stress corresponding to the maximum force, F_m, see Figure A-3;
- ultimate strain ε_u, where ε_u corresponds to the ultimate strength f_u.

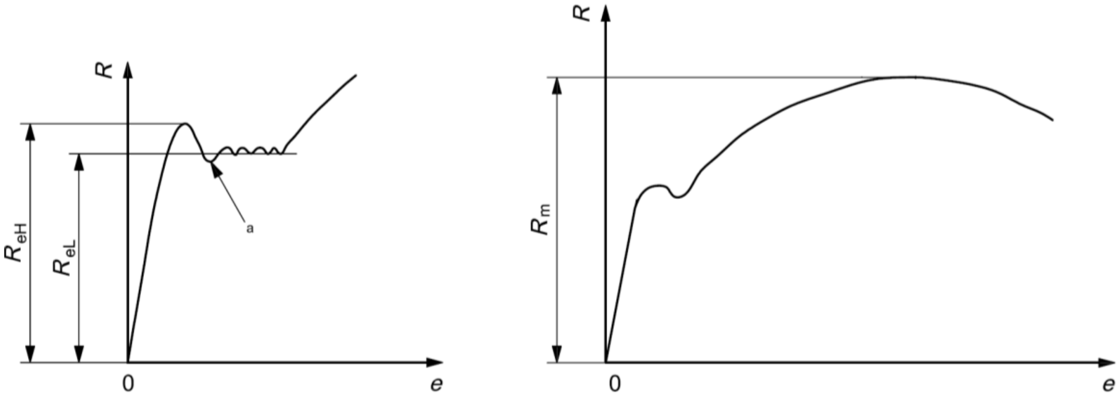

e	strain	R_{eL}	lower yield strength
R	stress	R_m	stress corresponding to the maximum force
R_{eH}	upper yield strength	a	initial transient effect

Figure A-3: Typical stress-strain curve (ISO, 2009).

A.2.2 Test results

The stress is computed as the force per unit area of the cross section, see Eq. (A-3). This stress, defined with reference to the undeformed configuration, i.e. the initial cross sections of the coupons, is called engineering stress, σ_{eng}.

$$\sigma_{eng} = \frac{F}{S_0} \tag{A-3}$$

where F is the force acting perpendicular to the cross section and S_0 is the original cross section area.

Figure A-4 presents the strain-stress curve obtained for each coupon where the strains were measured with electrical and mechanical strain gauges. The four typical regions of the stress-strain curve of structural steel are patent in some cases: linear elastic region, yield plateau, strain hardening region and strain softening after reaching the maximum load. However, in most cases the coupons rupture did not occur within the length monitored by the mechanical strain gauges, which leads to loss of information between the maximum load and the rupture load of the test specimen, and thus it was not possible to obtain the complete curve. Figures A-5 to A-8 illustrate the tensile coupon tests and the respective rupture zone. Table A-3 summarizes the dimensions of the cross-sectional area after fracture.

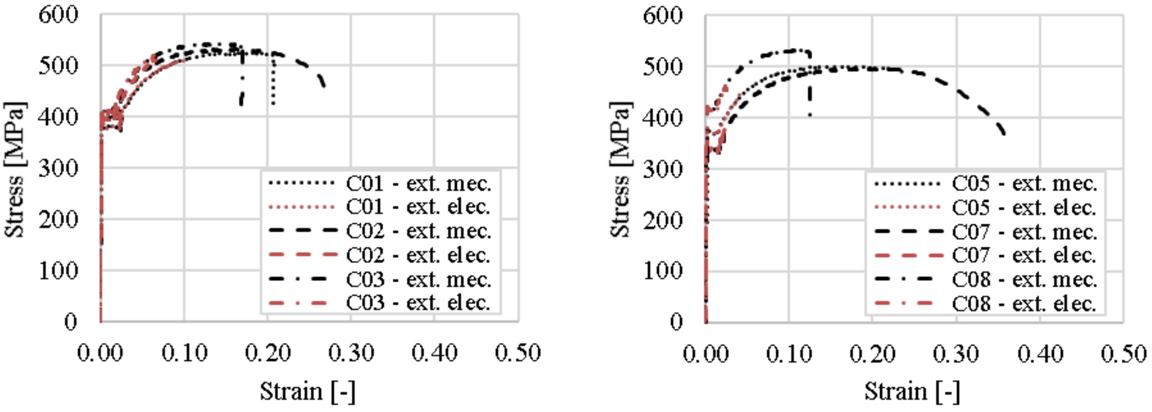

(a) A – web (b) B – web

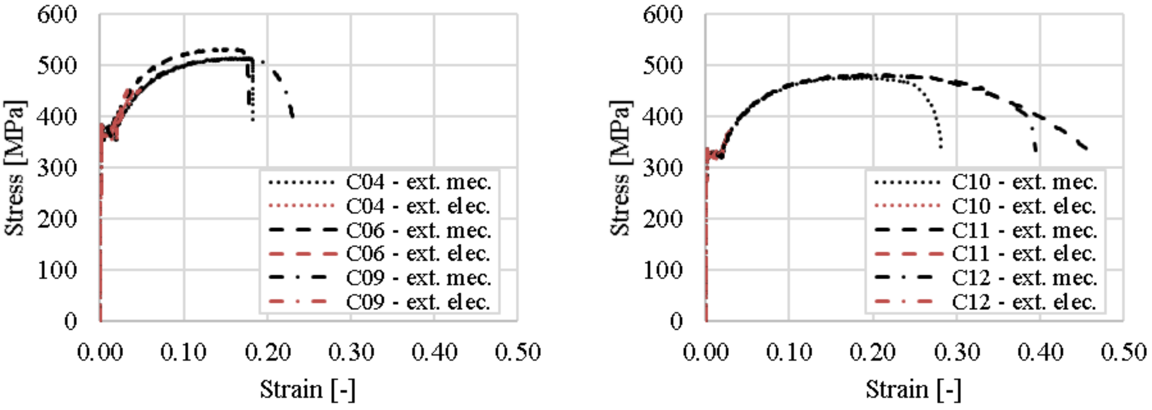

(c) A – flange (d) B – flange

Figure A-4: eng. stress – eng. strain curves (electrical and mechanical strain gauges extensometers).

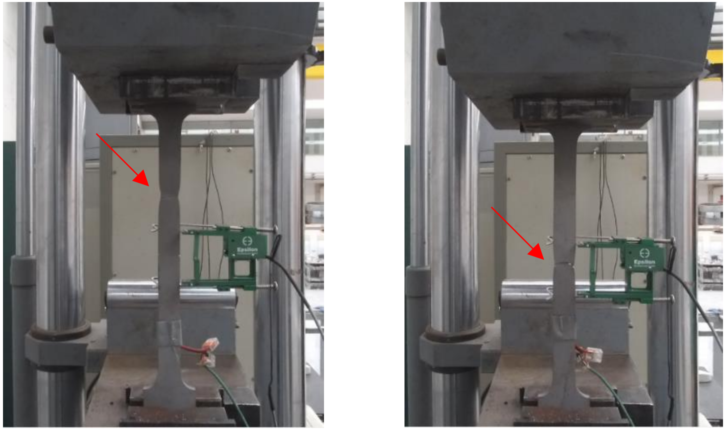

(a) C02 (b) C03

Figure A-5: Tensile tests on coupons of A series – web.

(a) C05 (b) C07 (c) C08

Figure A-6: Tensile tests on coupons of B series – web.

(a) C04 (b) C06 (c) C09

Figure A-7: Tensile tests on coupons of A series – flange.

(a) C10 (b) C11 (c) C12

Figure A-8: Tensile tests on coupons of B series – flange.

Table A-3: Dimensions of the cross-sectional area after fracture.

series	coupon ID	a_f	b_f	S_f
		mm	mm	mm^2
A web	C01	4.36	18.24	79.5
	C02	5.20	20.87	108.5
	C03	4.93	18.46	91.0
A flange	C04	6.66	17.35	115.6
	C06	6.32	17.55	110.9
	C09	6.60	17.38	114.7
B web	C05	6.90	16.69	115.2
	C07	6.10	16.65	101.6
	C08	7.00	17.00	119.0
B flange	C10	10.15	15.36	155.9
	C11	14.44	15.30	220.9
	C12	12.38	17.41	215.5

A.2.3 True stress – true strain curve

As already mentioned, the engineering stress-strain relationship is achieved by dividing the load at any instant by the initial cross area of the coupon. However, when the coupon is tensioned the width and the thickness shorten. Therefore, the actual stress, usually named true stress, is different from the engineering stress, σ_{eng}.

The true stress, σ_{true}, is a more rigorous representation of how the material behaves as it is based on the instantaneous material configuration. If during deformation the volume of the test piece is conserved, the true stress and engineering stress are related by Eq. (A-4) according to Ling (1996)

$$\sigma_{true} = \sigma_{eng}\left(1 + \varepsilon_{eng}\right) \tag{A-4}$$

True strain and engineering strain are also related by Eq. (A-5)

$$\varepsilon_{true} = \ln\left(1 + \varepsilon_{eng}\right) \tag{A-5}$$

regarding the true strain at the rupture load ε_f, it can be evaluated by the relationship

$$\varepsilon_f = \ln\left(\frac{S_0}{S_f}\right) \tag{A-6}$$

where S_0 is the original cross-sectional area of the test specimen and S_f is the minimum cross-sectional area after frature.

Applying the later relations to the experimental results, the true stress – true strain curves were computed and their main characteristics are presented in Table 3.4.

ANNEX B: BEAM MODELS FOR CHARACTERIZATION OF T-STUBS

B.1 Introduction

The evaluation of the initial stiffness of a single T-stub can be done through a beam analogy model in the elastic range making use of the displacement method.

Two beam models are considered: (i) simplified beam model, where the bolt is modelled as a single spring and (ii) refined beam model, where the bolt is modelled as a Winkler foundation, i.e. as an elastic beam resting on deformable foundation. Equations to determine the initial stiffness were driven. In the latter case, the equations my not be suitable for hand calculation, but are useful for programming and performing a quick analysis.

B.2 T-stub beam analogy

Consider a test of two coupled T-stubs where, due to symmetry considerations, only one quarter-model is considered, see Figure B-1. If the three-dimensional effects are not accounted for, the flange of the T-stub can be modelled making use of a 2D beam model.

As for the boundary conditions, the beam model (Figure B-1) is loaded by applying a vertical force $F/2$ to the support which corresponds to the critical section at the flange-to-web connection. The opposite beam tip is modelled with a pinned support to reproduce the effect of the prying forces, Q. The bolt behaviour is incorporated by means of an extensional spring located at the bolt axis (Figure B-1) or an elastic foundation along the bolt diameter (Figure B-4). The mechanical properties of the beam – corresponding to the T-stub flange – can be computed assuming a rectangular cross-section of width b_{eff} – effective width according to EC3-1-8 (CEN, 2005c) – and height equal to the thickness of the flange, t_{f}.

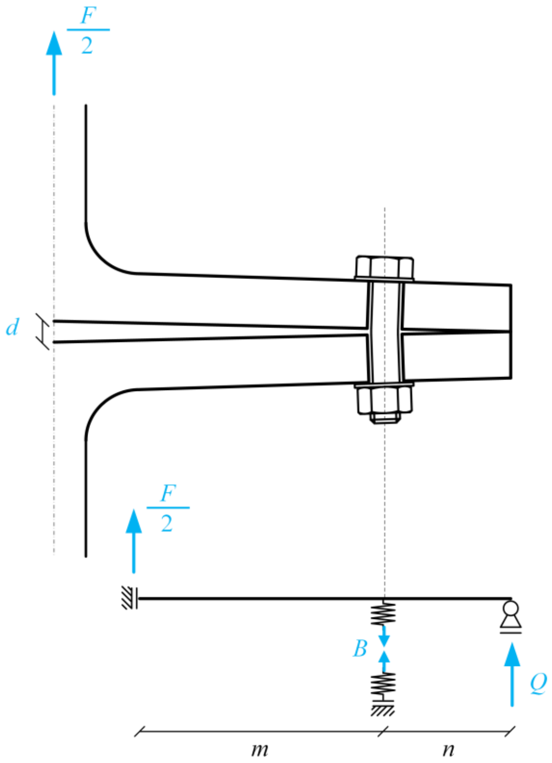

Figure B-1: T-stub beam analogy.

B.3 Simplified beam model

B.3.1 General formulation

The simplified beam model is a two-span beam, comprising two Euler-Bernoulli beam finite elements (roman numerals in Figure B-2). The system is statically indeterminate and can be solved making use of the classical displacements method considering three nodes and the three degrees of freedom (DOF) illustrated in Figure B-2.

The length of the element I and II are equal to the distance between the bolt axis and the location of critical section where plastic hinges can develop (flange-to-web connection), m, and the distance between the prying force and the botl axis n, respectively, which are defined according to EC3.

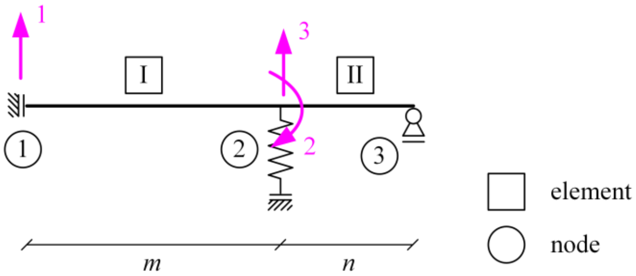

Figure B-2: Simplified beam model (single spring).

Figure B-3 illustrates the deformation modes associated to each unitary generalized nodal displacement to assemble the stiffness matrix $\boldsymbol{K}$ of the simple beam model. To get the elements of the first column of $\boldsymbol{K}$, a vertical unit displacement is applied at the global coordinate 1 ($u_1 = 1$) and the displacements at other coordinates are made zero ($u_2 = u_3 = 0$) by means of ppropriate support conditions, see Figure B-3(a). Restrains are imposed in node 2 so as to get the required deformed condition for the structure. With regard to the second column of $\boldsymbol{K}$, a unit rotation is applied at the global coordinate 2 ($u_2 = 1$) and the vertical displacements at coordinates 1 and 2 are restrained ($u_1 = u_3 = 0$), see Figure B-3(b). Finally, to get the third column of $\boldsymbol{K}$, a vertical unit displacement is applied at coordinate 3 ($u_3 = 1$) and the other displacements are restrained ($u_1 = u_2 = 0$), see Figure B-3(c).

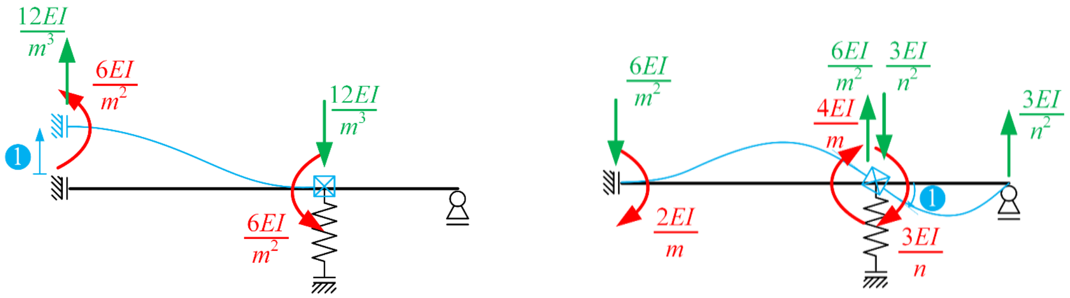

(a) $u_1 = 1$ and $u_i = 0,\ i \neq 1$ (b) $u_2 = 1$ and $u_i = 0,\ i \neq 2$

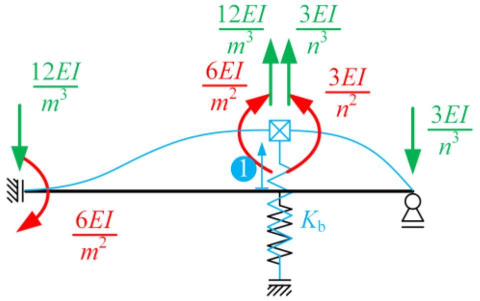

(c) $u_3 = 1$ and $u_i = 0,\ i \neq 3$

Figure B-3: Application of the unitary nodal displacements to simplified beam model.

The equilibrium conditions of the model represented in Figure B-2 can be stated as

$$\boldsymbol{F} = \boldsymbol{K} \cdot \boldsymbol{u} \tag{B-1}$$

where $\boldsymbol{F}$ is the external load vector and $\boldsymbol{u}$ is the vector of nodal displacements.

Governing equations for the beam are thus given by

$$\begin{bmatrix} F \\ 2 \\ 0 \\ 0 \end{bmatrix} = \begin{bmatrix} \frac{12EI}{m^3} & -\frac{6EI}{m^2} & -\frac{12EI}{m^3} \\ -\frac{6EI}{m^2} & \frac{4EI}{m} + \frac{3EI}{n} & \frac{6EI}{m^2} - \frac{3EI}{n^2} \\ -\frac{12EI}{m^3} & \frac{6EI}{m^2} - \frac{3EI}{n^2} & \frac{12EI}{m^3} + \frac{3EI}{n^3} + K_b \end{bmatrix} \cdot \begin{bmatrix} d_1 \\ d_2 \\ d_3 \end{bmatrix} \tag{B-2}$$

Solving Eq. (B-2) in order to the nodal displacements, we get

$$d_1 = \frac{F/2}{6EI} \cdot \frac{K_b \cdot (3m^4n^2 + 4m^3n^3) + 12EI \cdot (m+n)^3}{K_b \cdot (n^3 + 3mn^2) + 3EI} \tag{B-3}$$

$$d_2 = \frac{F/2}{2EI} \cdot \frac{K_b \cdot (m^2n^3) + 3EI(2mn + m^2)}{K_b(n^3 + 3mn^2) + 3EI} \tag{B-4}$$

$$d_3 = \frac{F}{2} \cdot \frac{3m^2n + 6mn^2 + 2n^3}{2K_b(n^3 + 3mn^2) + 3EI} \tag{B-5}$$

The stiffness of the T-stub computed making use of the beam model analogy is then given by Eq. (B-6).

$$K_{beam} = \frac{F/2}{d_1} = 12EI \cdot \frac{2K_b(n^3 + 3mn^2) + 3EI}{2K_b(3m^4n^2 + 4m^3n^3) + 12EI(m+n)^3} \tag{B-6}$$

B.3.2 Simplification according to Jaspart (1991-1997)

Jaspart (1991, 1997) simplified the stiffness calculation for inclusion in EC3 (CEN, 2003). The same simplifications are here employed to achieve the solo stiffness of the flange, i.e. dissociating the bolt deformability from that of the T-stub.

Taking the solution obtained in the previous section, namely Eq. (B-6), and dividing both the numerator and the denominator by K_b

$$K_{beam} = 12EI \cdot \left(\frac{\frac{K_b}{K_b}(n^3 + 3mn^2) + 3\frac{EI}{K_b}}{\frac{K_b}{K_b}(3m^4n^2 + 4m^3n^3) + 12\frac{EI}{K_b}(m+n)^3} \right) \tag{B-7}$$

then

$$K_{beam} = 12EI \cdot \left(\frac{n^3 + 3mn^2 + 3\frac{EI}{K_b}}{3m^4n^2 + 4m^3n^3 + 12\frac{EI}{K_b}(m+n)^3} \right) \tag{B-8}$$

Assuming, as in Figure 2.29, that the bolts are no more deforming in tension, i.e. $A_s \approx \infty$, then

$$K_{beam} = 12EI \cdot \frac{n^3 + 3mn^2}{3m^4n^2 + 4m^3n^3} \tag{B-9}$$

If n is taken as equal to $1.25m$, then

$$K_{beam} = 12EI \cdot \frac{(1.25m)^3 + 3m(1.25m)^2}{3m^4(1.25m)^2 + 4m^3(1.25m)^3} = 12EI \cdot \frac{17}{32m^3} \tag{B-10}$$

Taking $I = b_{\text{eff}}t_{\text{f}}^3/12$, then

$$K_{beam} = 12E\frac{b_{\text{eff}}t_{\text{f}}^3}{12} \cdot \frac{17}{32m^3} = E\frac{17}{32}\frac{b_{\text{eff}}t_{\text{f}}^3}{m^3} \approx E \cdot 0.531\frac{b_{\text{eff}}t_{\text{f}}^3}{m^3} \tag{B-11}$$

With reference to the full T-stub flange, then

$$K_{\mathrm{f}} = 2K_{beam} \approx E \cdot 1.063 \frac{b_{\mathrm{eff}} t_{\mathrm{f}}^3}{m^3} \tag{B-12}$$

Thereby achieving the same result as in Eq. (2.19).

B.4 Refined beam model

The refined beam model is a three-span beam, comprising two Euler-Bernoulli beam elements and a Winkler foundation element (Krenk, 2001) to model de bolt (roman numerals in Figure B-4), The system is statically indeterminate and can be solved making use of the classical displacements method considering four nodes and the five degrees of freedom (DOF) illustrated in Figure B-4.

The length of element II (Winkler foundation element) is equal to the bolt diameter, i.e. $L_2 = d_b$, and the length of the elements I and III are $L_1 = m - d_b/2$ and $L_3 = n - d_b/2$, respectively.

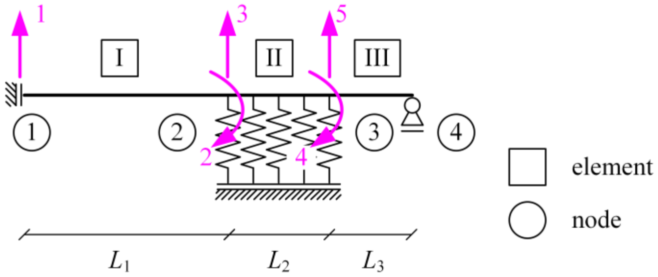

Figure B-4: Refine beam model (Winkler foundation).

Before assemble the stiffness matrix of the refined beam model, the stiffness matrix of a beam on elastic foundation must be driven. Figure B-5 illustrates the Euler-Bernoulli beam resting on a Winkler foundation and the respective independent degrees of freedom.

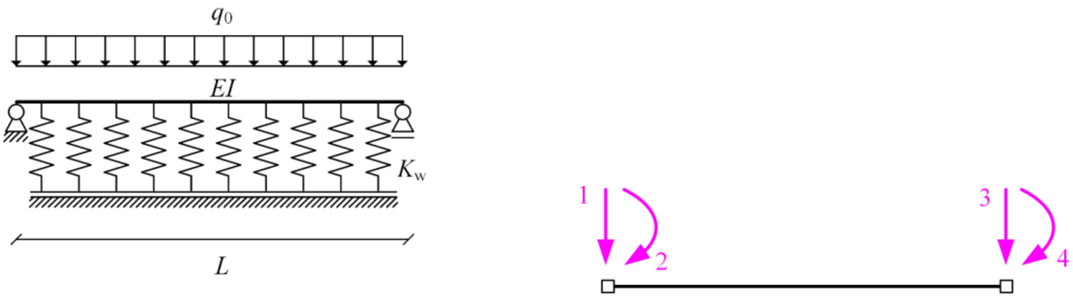

(a) (b)

Figure B-5: (a) Euler-Bernoulli beam resting on a Winkler foundation and (b) beam finite element and independent displacements.

Figure B-6 shows the four basic modes of deformation of a beam element resting on a Winkler foundation.

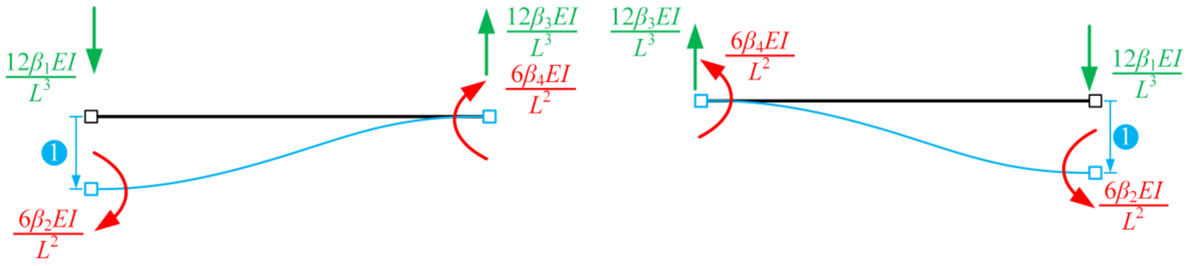

(a) $u_1 = 1$ and $u_i = 0, i \neq 1$ (b) $u_3 = 1$ and $u_i = 0, i \neq 3$

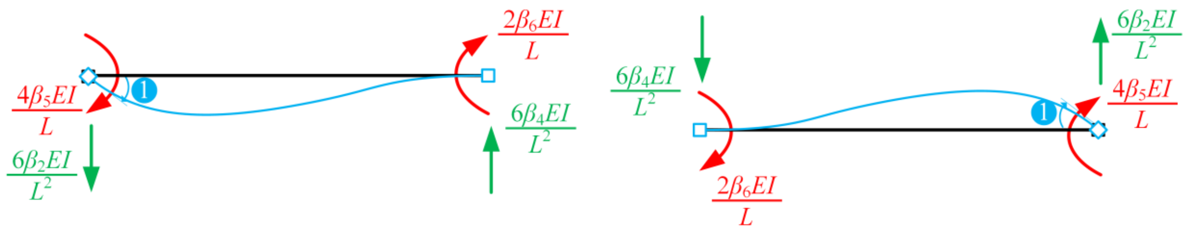

(c) $u_2 = 1$ and $u_i = 0, i \neq 2$ (d) $u_4 = 1$ and $u_i = 0, i \neq 4$

Figure B-6: Application of the unitary nodal displacements to a Euler-Bernoulli beam resting on a Winkler foundation.

The element stiffness matrix of a Euler-Bernoulli beam resting on a Winkler foundation is thus

$$\boldsymbol{K} = \begin{bmatrix} \frac{12\beta_1}{L^3} & \frac{6\beta_2}{L^2} & \frac{-12\beta_3}{L^3} & \frac{6\beta_4}{L^2} \\ \frac{6\beta_2}{L^2} & \frac{4\beta_5}{L} & \frac{-6\beta_4}{L^2} & \frac{2\beta_6}{L} \\ \frac{-12\beta_3}{L^3} & \frac{-6\beta_4}{L^2} & \frac{12\beta_1}{L^3} & \frac{-6\beta_2}{L^2} \\ \frac{6\beta_4}{L^2} & \frac{2\beta_6}{L} & \frac{-6\beta_2}{L^2} & \frac{4\beta_5}{L} \end{bmatrix} \cdot EI \tag{B-13}$$

The stiffness matrix is expressed in terms of dimensionless coefficients β_1 to β_6

$$\beta_1 = \frac{(\alpha L)^3}{3} \frac{\sin(2\alpha L) + \sinh(2\alpha L)}{\cos(2\alpha L) + \cosh(2\alpha L) - 2} \tag{B-14}$$

$$\beta_2 = \frac{(\alpha L)^2}{3} \frac{\cosh(2\alpha L) - \cos(2\alpha L)}{\cos(2\alpha L) + \cosh(2\alpha L) - 2} \tag{B-15}$$

$$\beta_3 = \frac{2(\alpha L)^3}{3} \frac{\sin(\alpha L)\cosh(\alpha L) + \cos(\alpha L)\sinh(\alpha L)}{\cos(2\alpha L) + \cosh(2\alpha L) - 2} \tag{B-16}$$

$$\beta_4 = \frac{4(\alpha L)^2}{3} \frac{\sin(\alpha L)\sinh(\alpha L)}{\cos(2\alpha L) + \cosh(2\alpha L) - 2} \tag{B-17}$$

$$\beta_5 = \frac{\alpha L}{2} \frac{\sinh(2\alpha L) - \sin(2\alpha L)}{\cos(2\alpha L) + \cosh(2\alpha L) - 2} \tag{B-18}$$

$$\beta_6 = 2\alpha L \frac{\sin(\alpha L)\cosh(\alpha L) - \cos(\alpha L)\sinh(\alpha L)}{\cos(2\alpha L) + \cosh(2\alpha L) - 2} \tag{B-19}$$

where $\alpha = \sqrt[4]{K_W/4EI}$, being $K_W = K_b/L$.

Figure B-7 illustrates the deformation modes associated to each unitary nodal displacement to assemble the stiffness matrix $\boldsymbol{K}$ of the refined beam model.

Governing equations for the beam are thus given by

$$\begin{bmatrix} \frac{F}{2} \\ 0 \\ 0 \\ 0 \\ 0 \end{bmatrix} = \begin{bmatrix} \frac{12EI}{L_1^3} & -\frac{6EI}{L_1^2} & -\frac{12EI}{L_1^3} & 0 & 0 \\ -\frac{6EI}{L_1^2} & \frac{4EI}{L_1}+\frac{4\beta_5 EI}{L_2} & \frac{6EI}{L_1^2}-\frac{6\beta_2 EI}{L_2^2} & \frac{2\beta_6 EI}{L_2} & \frac{6\beta_4 EI}{L_2^2} \\ -\frac{12EI}{L_1^3} & \frac{6EI}{L_1^2}-\frac{6\beta_2 EI}{L_2^2} & \frac{12EI}{L_1^3}+\frac{12\beta_1 EI}{L_2^3} & -\frac{6\beta_4 EI}{L_2^2} & -\frac{12\beta_3 EI}{L_2^3} \\ 0 & \frac{2\beta_6 EI}{L_2} & -\frac{6\beta_4 EI}{L_2^2} & \frac{4\beta_5 EI}{L_2}+\frac{3EI}{L_3} & \frac{6\beta_2 EI}{L_2^2}-\frac{3EI}{L_3^2} \\ 0 & \frac{6\beta_4 EI}{L_2^2} & -\frac{12\beta_3 EI}{L_2^3} & \frac{6\beta_2 EI}{L_2^2}-\frac{3EI}{L_3^2} & \frac{12\beta_1 EI}{L_2^3}+\frac{3EI}{L_3^3} \end{bmatrix} \cdot \begin{bmatrix} d_1 \\ d_2 \\ d_3 \\ d_4 \\ d_5 \end{bmatrix} \tag{B-20}$$

The stiffness of the refined beam model is then given by Eq. (B-21).

$$K_{beam} = \frac{F/2}{d_1} \tag{B-21}$$

where d_1 is the solution of the system in Eq. (B-20).

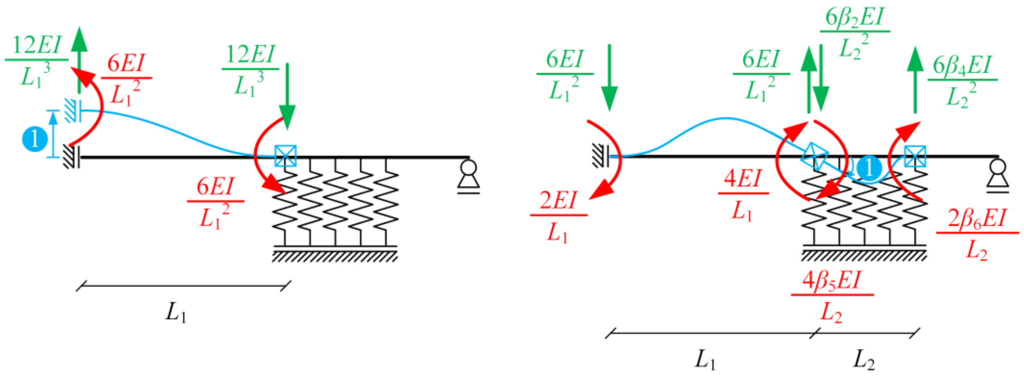

(a) $u_1 = 1$ and $u_i = 0,\ i \neq 1$ (b) $u_2 = 1$ and $u_i = 0,\ i \neq 2$

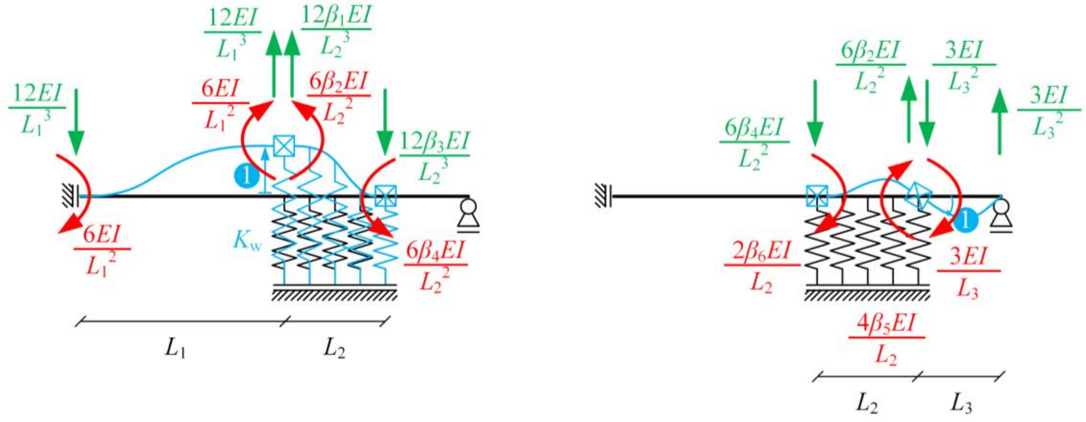

(c) $u_3 = 1$ and $u_i = 0,\ i \neq 3$ (d) $u_4 = 1$ and $u_i = 0,\ i \neq 4$

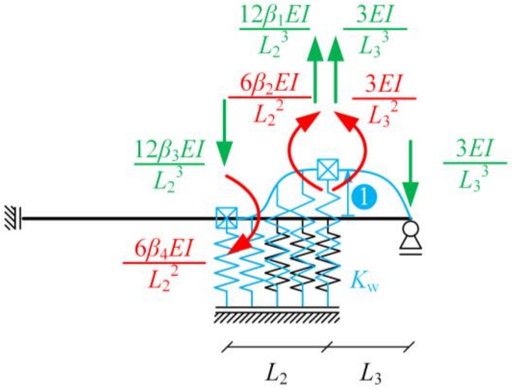

(e) $u_5 = 1$ and $u_i = 0,\ i \neq 5$

Figure B-7: Application of the unitary nodal displacements to the refined beam model.

B.5 Equivalent stiffness

In practice, not all T-stubs connect steel members with the same stiffness – e.g. small beams may be connected to very large and stiff columns – so that the flanges of the two T-elements may be different. Hence, the two following situations may arise: (i) T-stub with two flanges in bending, or (ii) T-stub with only one flange in bending. Whose behaviour is usually assessed experimentally by (i) a coupled T-stub or (ii) a T-stub connected to a rigid support, respectively.

The beam models presented (simple beam model and Winkler beam model in Sections B.3 and B.4, respectively) concern one quarter-model for coupled T-stubs and half-model for T-stubs on rigid support, see Figure B-8. In this regard, the following mechanical characteristics of the flanges and bolts are adopted:

- flange flexural stiffness

$$EI_{\mathrm{f}} = E\,\frac{b_{\mathrm{eff}}t_{\mathrm{f}}^{3}}{12} \tag{B-22}$$

where b_{eff} is the effective width of the T-stub flange for a single bolt row.

- bolt stiffness

$$K_{\mathrm{b}} = E\,\frac{A_s}{L_{\mathrm{b}}^{*}} \tag{B-23}$$

where A_s is tensile stress area of the bolt and L_b^* is the bolt elongation length taken as *coupled T-stub*

$$L_{\mathrm{b}}^{*} = \frac{t_{\mathrm{bh}}/2 + t_{\mathrm{wsh}} + t_{\mathrm{f,u}} + t_{\mathrm{f,l}} + t_{\mathrm{wsh}} + t_{\mathrm{bn}}/2}{2} \tag{B-24}$$

T-stub on rigid support

$$L_{\mathrm{b}}^{*} = \frac{t_{\mathrm{bh}}}{2} + t_{\mathrm{wsh}} + t_{\mathrm{f}} + t_{\mathrm{s}} + t_{\mathrm{wsh}} + \frac{t_{\mathrm{bn}}}{2} \tag{B-25}$$

where t_{bh} is the thickness of the bolt head, t_w is the thickness of the washer, $t_{\mathrm{f,u}}$ and $t_{\mathrm{f,l}}$ is the thickness of the upper and lower T-stub flange, respectively, t_{bn} is the thickness of the bolt nut, t_{f} is the thickness of the T-stub flange, and t_{s} is the thickness of the rigid support.

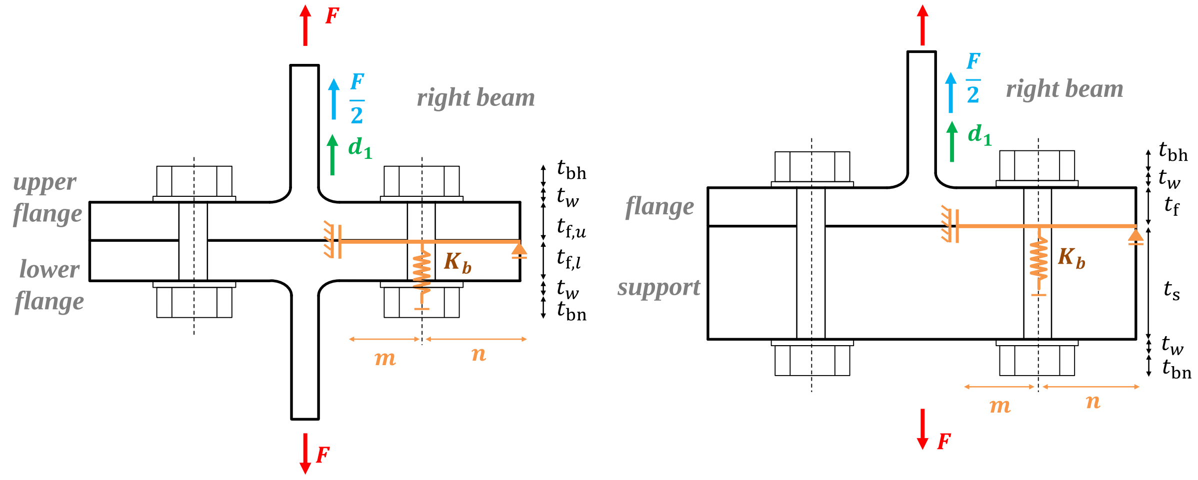

(a) (b)

Figure B-8: Beam model – (a) coupled T-stub and (b) T-stub on rigid support.

In addition, some considerations are required to relate the beam stiffness to the global stiffness of the T-stub (equivalent stiffness) concerning the T-stub set up. Figure B-9 represents the beam model assembly required to compute the equivalent stiffness for the T-stub for both test configurations.

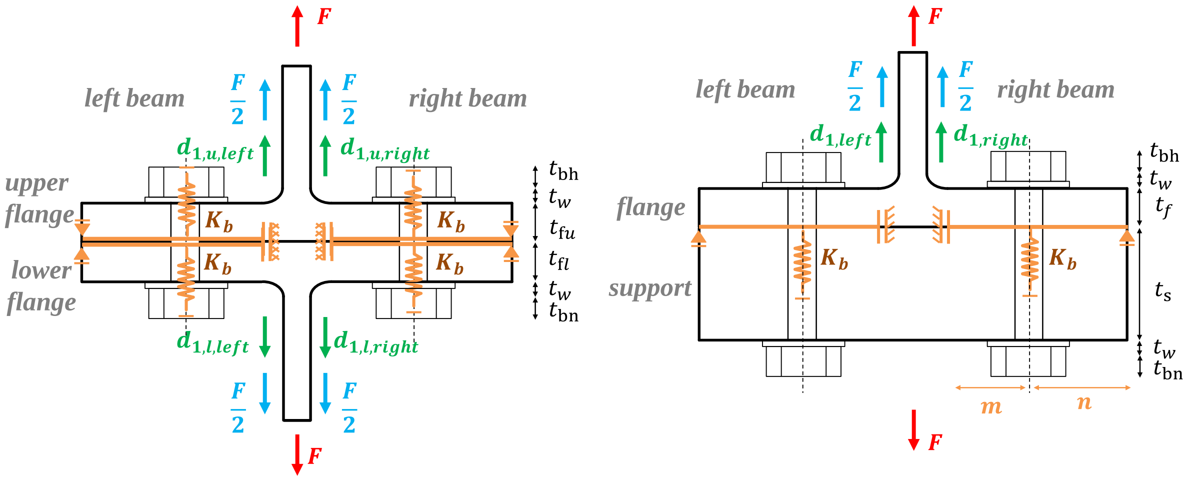

(a) (b)

Figure B-9: Beam model equivalent stiffness – (a) coupled T-stub and (b) T-stub on rigid support.

Regarding the coupled T-stubs (Figure B-9(a)), one beam represents only one quarter of the full test, i.e. it represents half of a flange with half of a bolt. Therefore, four beams need to be considered in order to compute the overall stiffness of the T-stub test: left and right beam of the upper and lower flange. The right and left beam of a flange work in parallel, whereas the upper flange and the lower flange are working in series. Thus, the equivalent stiffness is given by

$$\frac{1}{K_{eq,\mathrm{bm,2T}}} = \frac{1}{K_{beam,\mathrm{u},left} + K_{beam,\mathrm{u},right}} + \frac{1}{K_{beam,\mathrm{l},left} + K_{beam,\mathrm{l},right}} \tag{B-26}$$

Due to symmetry considerations, $K_{beam,\mathrm{u},left} = K_{beam,\mathrm{u},right} = K_{beam,\mathrm{l},left} = K_{beam,\mathrm{l},right}$ and thus, the equivalent stiffness of coupled T-stub is equal to the stiffness of a single beam, i.e.

$$K_{eq,\mathrm{bm,2T}} = K_{beam} \tag{B-27}$$

where K_{beam} is given by Eq. (B-6) or (B-21) if the simple or the refined beam model is adopted, respectively.

On the other hand, one beam represents a half-model for T-stub tested on rigid support, i.e. it represents half of a flange and a full bolt. Therefore, two beams need to be considered in order to compute the overall stiffness of the T-stub test: left and right beam of the flange. The right and left beam of a flange are working in parallel. Thus, the equivalent stiffness is given by

$$\frac{1}{K_{eq,\mathrm{bm,1T}}} = \frac{1}{K_{beam,\mathrm{f},left} + K_{beam,\mathrm{f},right}} \tag{B-28}$$

Due to symmetry considerations, $K_{beam,\mathrm{f},left} = K_{beam,\mathrm{f},right}$ and thus, the equivalent stiffness of a T-stub on rigid support is then double of the stiffness of a single beam model, i.e.

$$K_{eq,\mathrm{bm,1T}} = 2K_{beam} \tag{B-29}$$

ANNEX C: SIMPLIFIED METYHODOLOGIES FOR ASSESSMENT OF THE STIFFNESS OF BOLTED T-STUBS

C.1 Introduction

This annex gives detailed results that were obtained from application of simplified methodologies for assessment of the initial stiffness of single T-stubs, namely (i) EC3-1-8 model, (ii) simplified beam model, see Section B.3, and (ii) refined beam model, see Section B.4. These procedures were used against an extensive database compiled in the course of the current thesis.

C.2 Data collection

Since the 1990’s, some research projects were focused on the monotonic and cyclic behaviour of T-stubs. An extensive literature review of past experimental work, led to database consisting of 15 papers documenting 231 tests, listed in Table C-1, that cover: coupled and rigid support tests set up, welded and rolled compositions, with one and more bolt rows and with or without bolt preloading. From this list, the ones with stiffeners and the ones with insufficient information available were disregarded, resulting in a data collection of 184 specimens.

Table C-1: Data collection – list of experimental tests on T-stubs.

author	experimental campaign		selected		test set up	composition	no of bolt rows	bolt preload.
	LP	no of tests	LP	no of tests				
Bursi and Jaspart (1997)	M	4	M	4	coupled	rolled	2	w/ and w/o
Gebbeken *et al.* (1997)	M	18	M	18	coupled	rolled	2	w/ and w/o
Bursi *et al.* (1997)	M	4	M	-	rigid support	welded	2	w/o
	C	6	C	2				
Kasai and Xu (2002)	M	4	M	4	rigid support	rolled	1	w/ and w/o
	C	38	C	38				
Coelho *et al.* (2004)	M	32	M	25	coupled	welded	2	w/o
Piluso and Rizzano (2008)	M	4	M	3	coupled	rolled and welded	1	w/o
	C	24	C	18				
Barata *et al.* (2014)	M	6	M	6	rigid support	welded	1	w/o
Guo *et al.* (2017)	M	12	M	11	coupled	welded	1 and 2	w/
Andrade (2019)	M	4	M	3	coupled	welded	1	w/ and w/o
Bezerra *et al.* (2020)	M	9	M	3	rigid support	welded	1	w/o
Oliveira *et al.* (2021)	M	4	M	4	coupled	rolled	1	w/ and w/o
	C	8	C	8				
Zhao *et al.* (2021)	M	19	M	10	coupled	welded	1 and 2	w/
Zhang *et al.* (2022)	M	16	M	16	rigid support	welded	2	w/ and w/o
Bezerra *et al.* (2022)	M	12	M	4	rigid support	welded	1 and 3	w/o
Liu *et al.* (2023)	M	7	M	7	coupled	welded	1	w/
	Total	231	Total	184				

C.3 Geometrical and mechanical characteristics of the specimens

The data collection comprises a large variety of T-stub geometric configurations (flange thickness, edge distance, pitch and bolt size) and mechanical properties (European, Chinese and Brazilian steel with grades from S235 up to S690 high strength steel and bolt classes 8.8 and 10.9), giving the opportunity to structure the information according to multiple criteria.

The specimens were grouped according to the test set up (coupled or on rigid support), the composition type (rolled profiles or welded plates) and the presence or not of bolt preloading (with or without bolt preloading). The overall geometrical and mechanical characteristics of the selected specimens are summarized in Tables C-3 to C-9.

Table C-2: Data collection – coupled T-stubs, rolled profiles, without bolt preloading.

author	T-stub ID	loading protocol	beam profile	steel grade		bolts		
				provided	equivalent	no of rows	size and class	preload. level
Bursi and Jaspart (1997)	T1	M	IPE 300	-	-	2	M12 (8.8)	-
	T2	M	HEB 220					
Gebbeken *et al.* (1997)	P1K-1	M	IPE 300	Fe360	S235	2	M16 (10.9)	31.8 kN
	P1K-2	M						35.7 kN
	P1K-3	M						-
	P2K-1	M						36.3 kN
	P2K-2	M						35.3 kN
	P2K-3	M						-
	P3K-1	M						30.4 kN
	P3K-2	M						29.2 kN
	P3K-3	M						-
Oliveira *et al.* (2021)	A2	C	HEA 200	S355	-	1	M20 (10.9)	-
	A4	C						
	A7	M						
	B2	C	HEB 280					
	B1	M						
	B7	C						

Table C-3: Data collection – coupled T-stubs, rolled profiles, with bolt preloading.

author	T-stub ID	loading protocol	beam profile	steel grade		bolts		
				provided	equivalent	no of rows	size and class	preload. level
Bursi and Jaspart (1997)	T1	M	IPE 300	-	-	2	M12 (8.8)	60.7 kN
	T2	M	HEB 220					
Gebbeken *et al.* (1997)	P1V-1	M	IPE 300	Fe360	S235	2	M16 (10.9)	104.9 kN
	P1V-2	M						106.8 kN
	P1V-3	M						-
	P2V-1	M						105.3 kN
	P2V-2	M						104.4 kN
	P2V-3	M						-
	P3V-1	M						111.1 kN
	P3V-2	M						104.3 kN
	P3V-3	M						-
Piluso and Rizzano (2008)	A1	M	HEA 180	Fe430	S275	1	M20 (8.8)	80%
	A2	C						
	A3	C						
	A4	C						
	A5	C						
	A6	C						
	A7	C						
	B1	M	HEB 180					
	B2	C						
	B3	C						
	B4	C						
	B5	C						
	B6	C						
	B7	C						
Oliveira *et al.* (2021)	A1	C	HEA 200	S355	-	1	M20 (10.9)	80%
	A5	M						
	A6	C						
	B3	C	HEB 280					
	B4	M						
	B5	C						

Table C-4: Data collection – coupled T-stubs, welded plates, without bolt preloading.

author	T-stub ID	loading protocol	steel grade		bolts		
			provided	equivalent	no of rows	size and class	preload. level
Coelho *et al.* (2004)	WT1a	M	S355	-	1	M12 (8.8)	-
	WT1b	M	S355	-	1	M12 (8.8)	-
	WT1c	M	S355	-	1	M12 (8.8)	-
	WT1d	M	S355	-	1	M12 (8.8)	-
	WT1e	M	S355	-	1	M12 (8.8)	-
	WT1f	M	S355	-	1	M12 (8.8)	-
	WT1g	M	S355	-	1	M12 (8.8)	-
	WT1h	M	S355	-	1	M12 (8.8)	-
	WT2Aa	M	S355	-	1	M12 (8.8)	-
	WT2Ab	M	S355	-	1	M12 (8.8)	-
	WT2Ba	M	S355	-	1	M12 (8.8)	-
	WT2Bb	M	S355	-	1	M12 (8.8)	-
	WT4Aa	M	S355	-	1	M12 (8.8)	-
	WT4Ab	M	S355	-	1	M12 (8.8)	-
	WT51a	M	S690	-	1	M12 (8.8)	-
	WT51b	M	S690	-	1	M12 (8.8)	-
	WT53C	M	S690	-	1	M12 (8.8)	-
	WT53D	M	S690	-	1	M12 (10.9)	-
	WT53E	M	S690	-	1	M12 (10.9)	-
	WT7_M12	M	S355	-	2	M12 (8.8)	-
	WT7_M16	M	S355	-	2	M16 (8.8)	-
	WT7_M20	M	S355	-	2	M20 (8.8)	-
	WT57_M12	M	S690	-	2	M12 (8.8)	-
	WT57_M16	M	S690	-	2	M16 (8.8)	-
	WT57_M20	M	S690	-	2	M20 (8.8)	-
Andrade (2019)	L1-T20-PE20	M	S355	-	1	M20 (10.9)	20%

Table C-5: Data collection – coupled T-stubs, welded plates, with bolt preloading.

author	T-stub ID	loading protocol	steel grade		bolts		
			provided	equivalent	no of rows	size and class	preload. level
Piluso and Rizzano (2008)	C1	M	Fe430	S275	1	M20 (8.8)	80%
	C2	C					
	C3	C					
	C4	C					
	C5	C					
	C6	C					
	C7	C					
Guo *et al.* (2017)	HWT1	M	Q690D	S690	1	M16 (8.8)	-
	HWT2	M			1	M20 (8.8)	
	HWT3	M			1	M24 (8.8)	
	HWT4	M			1	M16 (10.9)	
	HWT5	M			1	M20 (10.9)	
	HWT6	M			1	M24 (10.9)	
	HWT7	M			1	M20 (8.8)	
	HWT8	M			1	M20 (8.8)	
	HWT9	M			1	M20 (8.8)	
	HWT10	M			1	M20 (8.8)	
	HWT11	M			2	M20 (8.8)	
Andrade (2019)	L1-T20-PE79	M		S355	1	M20 (10.9)	79%
	L1-T15-PE79	M					
Zhao *et al.* (2021)	TS-17.5a-18	M	Q235	S235	1	M18 (8.8)	110 kN
	TS-11.5a-18	M	Q235	S235	1	M18 (8.8)	111 kN
	TS-11.5b-18	M	Q345	-	1	M18 (8.8)	112 kN
	TS-11.5b-20	M	Q345	-	1	M20 (8.8)	143 kN
	TII-9.5a-18	M	Q235	S235	1	M18 (8.8)	110 kN
	TII-9.5b-18	M	Q345	-	1	M18 (8.8)	111 kN
	TII-9.5b-16	M	Q345	-	1	M16 (8.8)	86 kN
	TEG-9.5a-18	M	Q235	S235	2	M18 (8.8)	110 kN
	TEG-9.5b-18	M	Q345	-	2	M18 (8.8)	111 kN
	TEG-9.5b-16	M	Q345	-	2	M16 (8.8)	86 kN
Liu *et al.* (2023)	D14	M	Q355	S355	1	M16 (10.9)	110 kN
	D16	M				M16 (10.9)	110 kN
	D18	M				M16 (10.9)	110 kN
	S90	M				M16 (10.9)	110 kN
	S80	M				M16 (10.9)	110 kN
	M20	M				M20 (10.9)	150 kN
	M24	M				M24 (10.9)	225 kN

Table C-6: Data collection – T-stubs on rigid support, rolled profiles, without bolt preloading.

author	T-stub ID	loading protocol	beam profile	steel grade		bolts		
				provided	equivalent	no of rows	size and class	preload. level
Kasai and Xu (2002)	13	C	-	SS400	S235	1	M24 (10.9)	15%
	15	C					M20 (10.9)	15%

Table C-7: Data collection – T-stubs on rigid support, rolled profiles, with bolt preloading.

author	T-stub ID	Loading protocol	beam profile	steel grade		bolts		
				provided	equivalent	no of rows	size and class	preload. level
Kasai and Xu (2002)	1	C	-	SS400	S235	1	M24 (10.9)	100%
	2	C					M20 (10.9)	100%
	3	C					M24 (10.9)	100%
	4	C					M20 (10.9)	100%
	5	C					M24 (10.9)	100%
	6	C					M20 (10.9)	100%
	7	C					M24 (10.9)	100%
	8	C					M20 (10.9)	100%
	9	C					M24 (10.9)	100%
	10	C					M24 (10.9)	100%
	11	C					M20 (10.9)	100%
	12	C					M20 (10.9)	100%
	14	C					M24 (10.9)	70%
	16	C					M20 (10.9)	70%
	17	M					M24 (10.9)	100%
	18	M					M24 (10.9)	100%
	19	M					M20 (10.9)	100%
	20	M					M20 (10.9)	100%
	21	C					M24 (10.9)	100%
	22	C					M24 (10.9)	100%
	23	C					M24 (10.9)	100%
	24	C					M24 (10.9)	100%
	25	C					M24 (10.9)	100%
	26	C					M24 (10.9)	100%
	27	C					M24 (10.9)	100%
	28	C					M24 (10.9)	100%
	29	C					M24 (10.9)	100%
	30	C					M20 (10.9)	100%
	31	C					M20 (10.9)	100%
	32	C					M20 (10.9)	100%
	33	C					M20 (10.9)	100%
	34	C					M20 (10.9)	100%
	35	C					M20 (10.9)	100%
	36	C					M20 (10.9)	100%
	37	C					M20 (10.9)	100%
	38	C					M20 (10.9)	100%
	39	C					M24 (10.9)	100%
	40	C					M24 (10.9)	100%
	41	C					M24 (10.9)	100%
	42	C					M24 (10.9)	100%

Table C-8: Data collection – T-stubs on rigid support, welded plates, without bolt preloading.

author	T-stub ID	loading protocol	steel grade		bolts		
			provided	equivalent	no of rows	size and class	preload. level
Bursi *et al.* (1997)	TC-2	C	Fe430	S275	2	M20 (8.8)	40%
	TC-3	C					
Barata *et al.* (2014)	T-10-20-1	M	S355	-	1	M20 (8.8)	21%
	T-10-20-2	M				M20 (8.8)	
	T-15-20-1	M				M20 (8.8)	
	T-15-20-2	M				M20 (8.8)	
	T-20-20-1	M				M24 (10.9)	
	T-20-20-2	M				M24 (10.9)	
Bezerra *et al.* (2020)	CD1	M	SAE 1010	S275	1	M12	5 kN
	CD2	M					
	CD3	M					
Zhang *et al.* (2022)	TS0-NP	M	Q235	S235	2	M20 (8.8)	0
	TS1-NP-d24	M				M24 (8.8)	
	TS2-NP-t8	M				M20 (8.8)	
	TS3-NP-t12	M				M20 (8.8)	
	TS4-NP-H70	M				M20 (8.8)	
	TS5-NP-H90	M				M20 (8.8)	
	TS6-NP-L50	M				M20 (8.8)	
	TS7-NP-L60	M				M20 (8.8)	
Bezerra *et al.* (2022)	P1D	M	SAE 1010	S275	1	M12	30 kN
	P2D	M			1		
	P3D	M			1		
	P4D	M			3		

Table C-9: Data collection – T-stubs on rigid support, welded plates, with bolt preloading.

author	T-stub ID	loading protocol	steel grade		bolts		
			provided	equivalent	no of rows	size and class	preload. level
Zhang *et al.* (2022)	TS0-P	M	Q235	S235	2	M20 (8.8)	125 kN
	TS1-P-d24	M				M24 (8.8)	175 kN
	TS2-P-t8	M				M20 (8.8)	125 kN
	TS3-P-t12	M				M20 (8.8)	125 kN
	TS4-P-H70	M				M20 (8.8)	125 kN
	TS5-P-H90	M				M20 (8.8)	125 kN
	TS6-P-L50	M				M20 (8.8)	125 kN
	TS7-P-L60	M				M20 (8.8)	125 kN

C.4 Initial stiffness

Tables C-10 to C-17 compares the initial stiffness predictions (per bolt row) by application of the EC3-1-8 model (CEN, 2005c), the simplified beam model (sbm) and the refined beam model (wbm). Although none of the methods considers in particular the presence of bolt preloading, the assessment of the initial stiffness is performed in separate to assess the impact of neglecting the bolt preloading. The comparison between methods is performed in terms of the ratio of the predicted value and the actual value (experimental results) and assessed through the average ratios of each group. The simple and refined beam model were not employed to Barata *et al.* (2014) and to Zhang *et al.* (2022) in Tables C-16 and C-17 due to insufficient data, namely the thickness of the rigid support, to compute the bolt elongation length.

Table C-10: Initial stiffness per bolt row – coupled T-stubs, rolled profiles, without bolt preloading.

author	T-stub ID	K_{exp} kN/mm	$K_{eq,\mathrm{EC3}}$ kN/mm	$K_{eq,\mathrm{sbm}}$ kN/mm	$K_{eq,\mathrm{wbm}}$ kN/mm	$\frac{K_{eq,\mathrm{EC3}}}{K_{exp}}$	$\frac{K_{eq,\mathrm{sbm}}}{K_{exp}}$	$\frac{K_{eq,\mathrm{wbm}}}{K_{exp}}$
Bursi and Jaspart (1997)	T1	58	147	160	130	2.56	2.78	2.26
	T2	125	360	337	219	2.88	2.70	1.75
Gebbeken *et al.* (1997)	P1K-1	60	120	142	124	2.02	2.39	2.09
	P1K-2	60	124	151	137	2.09	2.53	2.29
	P1K-3	60	122	148	135	2.04	2.48	2.26
	P2K-1	70	225	248	200	3.24	3.57	2.88
	P2K-2	70	219	233	181	3.16	3.35	2.60
	P2K-3	70	220	243	197	3.16	3.50	2.83
	P3K-1	68	183	206	185	2.71	3.05	2.74
	P3K-2	68	187	210	187	2.77	3.11	2.77
	P3K-3	68	186	209	187	2.76	3.10	2.77
Oliveira *et al.* (2021)	A2	41	91	117	120	2.22	2.85	2.91
	A4	42	94	120	122	2.22	2.84	2.89
	A7	37	86	111	114	2.35	3.03	3.13
	B1	70	304	325	256	4.31	4.61	3.64
	B2	98	304	325	255	3.10	3.31	2.60
	B7	106	317	336	263	3.00	3.19	2.49
					μ	2.74	3.08	2.64
					σ	0.57	0.51	0.42

Table C-11: Initial stiffness per bolt row – coupled T-stubs, rolled profiles, with bolt preloading.

author	T-stub ID	K_{exp} kN/mm	$K_{eq,\mathrm{EC3}}$ kN/mm	$K_{eq,\mathrm{sbm}}$ kN/mm	$K_{eq,\mathrm{wbm}}$ kN/mm	$\frac{K_{eq,\mathrm{EC3}}}{K_{exp}}$	$\frac{K_{eq,\mathrm{sbm}}}{K_{exp}}$	$\frac{K_{eq,\mathrm{wbm}}}{K_{exp}}$
Bursi and Jaspart (1997)	T1	120	147	160	130	1.22	1.33	1.08
	T2	285	360	337	219	1.26	1.18	0.77
Gebbeken *et al.* (1997)	P1V-1	70	122	148	135	1.76	2.13	1.94
	P1V-2	70	121	147	134	1.74	2.11	1.93
	P1V-3	70	123	149	136	1.77	2.14	1.95
	P2V-1	87	212	226	176	2.45	2.62	2.04
	P2V-2	87	214	228	178	2.48	2.64	2.05
	P2V-3	87	227	249	201	2.62	2.88	2.32
	P3V-1	90	183	201	171	2.03	2.23	1.90
	P3V-2	90	183	201	171	2.03	2.23	1.90
	P3V-3	90	185	207	186	2.05	2.31	2.06
Piluso and Rizzano (2008)	A1	135	231	265	246	1.72	1.97	1.83
	A2	106	231	265	246	2.18	2.50	2.32
	A3	113	240	273	252	2.12	2.42	2.23
	A4	110	236	270	248	2.15	2.46	2.26
	A5	93	241	274	253	2.60	2.96	2.73
	A6	119	227	260	242	1.91	2.19	2.03
	A7	94	234	268	247	2.48	2.84	2.62
	B1	145	557	552	398	3.84	3.80	2.74
	B2	173	560	554	400	3.24	3.20	2.31
	B3	183	546	543	394	2.99	2.97	2.16
	B4	189	554	549	397	2.94	2.91	2.11
	B5	178	565	558	401	3.18	3.13	2.25
	B6	196	554	550	399	2.82	2.80	2.03
	B7	204	560	554	400	2.75	2.72	1.96
Oliveira *et al.* (2021)	A1	67	84	108	113	1.25	1.62	1.68
	A5	55	86	111	114	1.56	2.03	2.08
	A6	60	86	112	114	1.43	1.86	1.90
	B3	135	311	331	260	2.31	2.46	1.92
	B4	89	328	346	268	3.70	3.91	3.03
	B5	115	305	325	256	2.64	2.82	2.22
					μ	2.30	2.50	2.08
					σ	0.67	0.60	0.42

Table C-12: Initial stiffness per bolt row – coupled T-stubs, welded plates, without bolt preloading.

author	T-stub ID	K_{exp} kN/mm	$K_{eq,\mathrm{EC3}}$ kN/mm	$K_{eq,\mathrm{sbm}}$ kN/mm	$K_{eq,\mathrm{wbm}}$ kN/mm	$\frac{K_{eq,\mathrm{EC3}}}{K_{exp}}$	$\frac{K_{eq,\mathrm{sbm}}}{K_{exp}}$	$\frac{K_{eq,\mathrm{wbm}}}{K_{exp}}$
Coelho *et al.* (2004)	WT1a	48	109	128	112	2.26	2.65	2.33
	WT1b	55	109	128	112	1.98	2.32	2.04
	WT1c	64	109	128	112	1.69	1.98	1.74
	WT1d	60	109	128	112	1.80	2.12	1.86
	WT1e	67	109	128	112	1.62	1.90	1.67
	WT1f	59	109	128	112	1.83	2.15	1.89
	WT1g	69	109	128	112	1.58	1.86	1.63
	WT1h	74	109	128	112	1.48	1.73	1.52
	WT2Aa	64	88	106	95	1.37	1.65	1.48
	WT2Ab	62	88	106	95	1.42	1.72	1.54
	WT2Ba	64	127	146	126	2.00	2.30	1.99
	WT2Bb	80	127	146	126	1.59	1.83	1.58
	WT4Aa	75	172	190	153	2.29	2.53	2.04
	WT4Ab	87	172	190	153	1.98	2.19	1.76
	WT51a	60	92	110	100	1.54	1.85	1.67
	WT51b	62	92	110	100	1.49	1.78	1.61
	WT53C	64	95	113	101	1.48	1.76	1.58
	WT53D	53	97	115	103	1.84	2.18	1.95
	WT53E	65	95	113	101	1.46	1.74	1.56
	WT7_M12	91	169	187	151	1.85	2.05	1.66
	WT7_M16	116	180	211	193	1.55	1.82	1.66
	WT7_M20	138	186	227	233	1.35	1.65	1.70
	WT57_M12	86	152	172	142	1.77	2.00	1.66
	WT57_M16	110	163	195	181	1.48	1.76	1.64
	WT57_M20	151	167	205	216	1.11	1.36	1.43
Andrade (2019)	L1-T20-PE20	1527	1057	1086	716	0.69	0.71	0.47
					μ	1.63	1.91	1.68
					σ	0.33	0.37	0.32

Table C-13: Initial stiffness per bolt row – coupled T-stubs, welded plates, with bolt preloading.

author	T-stub ID	K_{exp} kN/mm	$K_{eq,\mathrm{EC3}}$ kN/mm	$K_{eq,\mathrm{sbm}}$ kN/mm	$K_{eq,\mathrm{wbm}}$ kN/mm	$\frac{K_{eq,\mathrm{EC3}}}{K_{exp}}$	$\frac{K_{eq,\mathrm{sbm}}}{K_{exp}}$	$\frac{K_{eq,\mathrm{wbm}}}{K_{exp}}$
Piluso and Rizzano (2008)	C1	50	117	140	137	2.34	2.80	2.73
	C2	86	106	128	126	1.23	1.49	1.47
	C3	101	104	127	125	1.04	1.26	1.24
	C4	101	105	127	125	1.04	1.26	1.24
	C5	93	109	132	129	1.17	1.42	1.39
	C6	115	105	127	125	0.91	1.10	1.08
	C7	59	103	125	123	1.75	2.13	2.10
Guo *et al.* (2017)	HWT1	68	126	140	132	1.85	2.06	1.94
	HWT2	95	127	146	154	1.33	1.54	1.62
	HWT3	111	131	150	178	1.18	1.36	1.60
	HWT4	83	124	140	132	1.50	1.69	1.59
	HWT5	116	134	146	154	1.15	1.26	1.32
	HWT6	187	130	150	178	0.70	0.80	0.95
	HWT7	50	47	61	66	0.95	1.22	1.32
	HWT8	18	12	19	20	0.69	1.03	1.12
	HWT9	98	122	146	153	1.24	1.49	1.56
	HWT10	103	129	146	153	1.25	1.41	1.49
	HWT11	122	125	146	154	1.02	1.20	1.26
Andrade (2019)	L1-T20-PE79	2857	1057	1087	717	0.37	0.38	0.25
	L1-T15-PE79	990	726	747	503	0.73	0.75	0.51
Zhao *et al.* (2021)	TS-17.5a-18	462	383	384	275	0.83	0.83	0.59
	TS-11.5a-18	119	147	170	155	1.24	1.43	1.31
	TS-11.5b-18	126	147	170	155	1.17	1.35	1.23
	TS-11.5b-20	144	150	175	168	1.04	1.22	1.17
	TII-9.5a-18	77	161	187	170	2.09	2.43	2.20
	TII-9.5b-18	94	161	187	170	1.72	1.99	1.81
	TII-9.5b-16	123	158	181	159	1.29	1.47	1.29
	TEG-9.5a-18	47	122	144	137	2.59	3.07	2.92
	TEG-9.5b-18	59	122	144	137	2.08	2.46	2.34
	TEG-9.5b-16	51	120	140	129	2.35	2.75	2.52
Liu *et al.* (2023)	D14	31	24	33	32	0.76	1.07	1.04
	D16	32	35	47	44	1.08	1.47	1.37
	D18	34	48	64	57	1.41	1.85	1.66
	S90	34	48	61	56	1.41	1.79	1.67
	S80	44	68	80	74	1.53	1.81	1.67
	M20	22	35	49	48	1.61	2.24	2.20
	M24	18	35	50	51	1.96	2.75	2.84
					μ	1.34	1.61	1.56
					σ	0.51	0.62	0.60

Table C-14: Initial stiffness per bolt row – T-stub on rigid support, rolled profiles, without bolt preloading.

author	T-stub ID	K_{exp} kN/mm	$K_{eq,\mathrm{EC3}}$ kN/mm	$K_{eq,\mathrm{sbm}}$ kN/mm	$K_{eq,\mathrm{wbm}}$ kN/mm	$\frac{K_{eq,\mathrm{EC3}}}{K_{exp}}$	$\frac{K_{eq,\mathrm{sbm}}}{K_{exp}}$	$\frac{K_{eq,\mathrm{wbm}}}{K_{exp}}$
Kasai and Xu (2002)	13	123	80	106	56	0.65	0.86	0.46
	15	239	274	280	144	1.15	1.17	0.60
					μ	0.90	1.02	0.53
					σ	0.25	0.15	0.07

Table C-15: Initial stiffness per bolt row – T-stub on rigid support, rolled profiles, with bolt preloading.

author	T-stub ID	K_{exp} kN/mm	$K_{eq,\mathrm{EC3}}$ kN/mm	$K_{eq,\mathrm{sbm}}$ kN/mm	$K_{eq,\mathrm{wbm}}$ kN/mm	$\frac{K_{eq,\mathrm{EC3}}}{K_{exp}}$	$\frac{K_{eq,\mathrm{sbm}}}{K_{exp}}$	$\frac{K_{eq,\mathrm{wbm}}}{K_{exp}}$
Kasai and Xu (2002)	1	328	156	184	99	0.47	0.56	0.30
	2	270	149	166	86	0.55	0.62	0.32
	3	482	296	302	159	0.61	0.63	0.33
	4	410	274	261	134	0.67	0.64	0.33
	5	175	80	106	56	0.46	0.61	0.32
	6	168	79	98	51	0.47	0.58	0.30
	7	293	155	178	93	0.53	0.61	0.32
	8	249	149	158	81	0.60	0.63	0.33
	9	307	156	178	96	0.51	0.58	0.31
	10	332	156	185	99	0.47	0.56	0.30
	11	379	274	245	126	0.72	0.65	0.33
	12	420	274	280	144	0.65	0.67	0.34
	14	169	80	106	56	0.48	0.63	0.33
	16	364	274	261	134	0.75	0.72	0.37
	17	335	156	185	99	0.46	0.55	0.29
	18	172	80	106	56	0.47	0.62	0.33
	19	419	274	280	144	0.65	0.67	0.34
	20	256	149	158	81	0.58	0.62	0.32
	21	335	156	185	99	0.47	0.55	0.30
	22	335	156	185	99	0.46	0.55	0.29
	23	335	156	185	99	0.46	0.55	0.30
	24	340	156	185	99	0.46	0.54	0.29
	25	359	156	185	99	0.43	0.51	0.28
	26	340	156	185	99	0.46	0.54	0.29
	27	172	80	106	56	0.47	0.62	0.33
	28	207	80	106	56	0.39	0.51	0.27
	29	171	80	106	56	0.47	0.62	0.33
	30	417	274	280	144	0.66	0.67	0.35
	31	424	274	280	144	0.65	0.66	0.34
	32	418	274	280	144	0.66	0.67	0.35
	33	420	274	280	144	0.65	0.67	0.34
	34	449	274	280	144	0.61	0.62	0.32
	35	425	274	280	144	0.64	0.66	0.34
	36	250	149	158	81	0.60	0.63	0.33
	37	273	149	158	81	0.55	0.58	0.30
	38	252	149	158	81	0.59	0.63	0.32
	39	94	80	106	56	0.85	1.13	0.60
	40	308	80	106	56	0.26	0.34	0.18
	41	393	80	106	56	0.20	0.27	0.14
	42	736	80	106	56	0.11	0.14	0.08
					μ	0.53	0.59	0.31
					σ	0.14	0.14	0.07

Table C-16: Initial stiffness per bolt row – T-stub on rigid support, welded plates, without bolt preloading.

author	T-stub ID	K_{exp} kN/mm	$K_{eq,\mathrm{EC3}}$ kN/mm	$K_{eq,\mathrm{sbm}}$ kN/mm	$K_{eq,\mathrm{wbm}}$ kN/mm	$\frac{K_{eq,\mathrm{EC3}}}{K_{exp}}$	$\frac{K_{eq,\mathrm{sbm}}}{K_{exp}}$	$\frac{K_{eq,\mathrm{wbm}}}{K_{exp}}$
Bursi *et al.* (1997)	TC-2	697	189	203	109	0.27	0.29	0.16
	TC-3	1502	510	439	225	0.34	0.29	0.15
Barata *et al.* (2014)	T-10-20-1	171	130	-	-	0.76	-	-
	T-10-20-2	179	130	-	-	0.73	-	-
	T-15-20-1	261	336	-	-	1.29	-	-
	T-15-20-2	271	336	-	-	1.24	-	-
	T-20-20-1	729	602	-	-	0.83	-	-
	T-20-20-2	576	602	-	-	1.04	-	-
Bezerra *et al.* (2020)	CD1	19	41	44	23	2.16	2.32	1.21
	CD2	19	63	60	31	3.25	3.10	1.60
	CD3	39	110	92	47	2.83	2.35	1.19
Zhang *et al.* (2022)	TS0-NP	20	14	-	-	0.72	-	-
	TS1-NP-d24	18	21	-	-	1.17	-	-
	TS2-NP-t8	11	15	-	-	1.32	-	-
	TS3-NP-t12	22	14	-	-	0.65	-	-
	TS4-NP-H70	11	14	-	-	1.33	-	-
	TS5-NP-H90	6	14	-	-	2.33	-	-
	TS6-NP-L50	15	14	-	-	0.93	-	-
	TS7-NP-L60	15	14	-	-	0.97	-	-
Bezerra *et al.* (2022)	P1D	33	24	28	16	0.71	0.85	0.47
	P2D	89	78	75	39	0.88	0.84	0.44
	P3D	126	160	143	72	1.28	1.14	0.58
					μ	1.20	1.31	0.68
					σ	0.75	0.97	0.49

Table C-17: Initial stiffness per bolt row – T-stub on rigid support, welded plates, with bolt preloading.

author	T-stub ID	K_{exp} kN/mm	$K_{eq,\mathrm{EC3}}$ kN/mm	$K_{eq,\mathrm{sbm}}$ kN/mm	$K_{eq,\mathrm{wbm}}$ kN/mm	$\frac{K_{eq,\mathrm{EC3}}}{K_{exp}}$	$\frac{K_{eq,\mathrm{sbm}}}{K_{exp}}$	$\frac{K_{eq,\mathrm{wbm}}}{K_{exp}}$
Zhang *et al.* (2022)	TS0-P	24	14	-	-	0.60	-	-
	TS1-P-d24	26	21	-	-	0.79	-	-
	TS2-P-t8	17	15	-	-	0.85	-	-
	TS3-P-t12	27	14	-	-	0.52	-	-
	TS4-P-H70	15	14	-	-	0.93	-	-
	TS5-P-H90	9	14	-	-	1.56	-	-
	TS6-P-L50	17	14	-	-	0.85	-	-
					μ	0.88	-	-
					σ	0.29	-	-

C.5 Discussion

This annex presented systematically the application of several methodologies for the assessment of the initial stiffness of T-stubs. Table C-18 compares the results achieved with different methods from a statistical point of view, in terms of average ratios and standard deviation.

The EC3 results provides an average ratio of 1.89 for coupled T-stub and 0.79 for T-stubs on rigid support. The refined beam model provides better predictions than the simple one with a similar average ratio to EC3 for coupled T-stubs of 1.90, bust worsen for T-stubs on rigid support with an average ratio of 0.39. The results show that the three approaches yield excessive errors and high discrepancies.

Table C-18: Initial stiffness – summary of results.

test set up	composition	bolt preloading	no of T-stubs	$\frac{K_{eq,\mathrm{EC3}}}{K_{exp}}$		$\frac{K_{eq,\mathrm{sbm}}}{K_{exp}}$		$\frac{K_{eq,\mathrm{wbm}}}{K_{exp}}$	
				μ	σ	μ	σ	μ	σ
coupled	rolled	w/o	17	2.74	0.57	3.08	0.51	2.64	0.42
		w/	31	2.30	0.67	2.50	0.60	2.08	0.42
	welded	w/o	26	1.63	0.33	1.91	0.37	1.68	0.32
		w/	37	1.34	0.51	1.61	0.62	1.56	0.60
			111	**1.89**	0.75	**2.15**	0.76	**1.90**	0.60
rigid support	rolled	w/o	2	0.90	0.25	1.02	0.15	0.53	0.07
		w/	40	0.53	0.14	0.59	0.14	0.31	0.07
	welded	w/o	23	1.20	0.75	1.31	0.97	0.68	0.49
		w/	8	0.88	0.29	-	-	-	-
			73	**0.79**	0.54	**0.74**	0.51	**0.39**	0.26
		Total	184	**1.45**	0.9	**1.71**	0.95	**1.42**	0.87

ANNEX D: REFINED MECHANICAL MODEL

D.1 Introduction

The components model developed in Part III can be generalized in other to introduce more kinematic constraints through additional rigid elements. In this Annex the mathematic generalization of the model developed in Part III will be presented.

The model in Figure D-1 is assumed to have: v vertical rigid elements leading to $b = v - 1$ blocks, each block has r rows and where each row is assumed to have S_m components plus the CWS (not accounted in one of the rows), leading to $\sum_{t=1}^{b} \sum_{m=1}^{r_t} S_{t,m} + 1$ components, where r_t is the total number of rows in block t – block is defined as a region between two consecutive rigid elements.

The blocks are numbered sequentially from left to right and the components are numbered sequentially per block starting from the top row (row with higher y coordinate) and from left to right (positive sense of x axis) until the bottom row (row with lower y coordinate). The model thus includes n_d nodes (nodes: 1, p, …, n_d plus v generalised nodes: 2, …, $b + 2$). All nodes are restrained against vertical displacement (y displacement) leading to n_f degrees of freedom (DOFs).

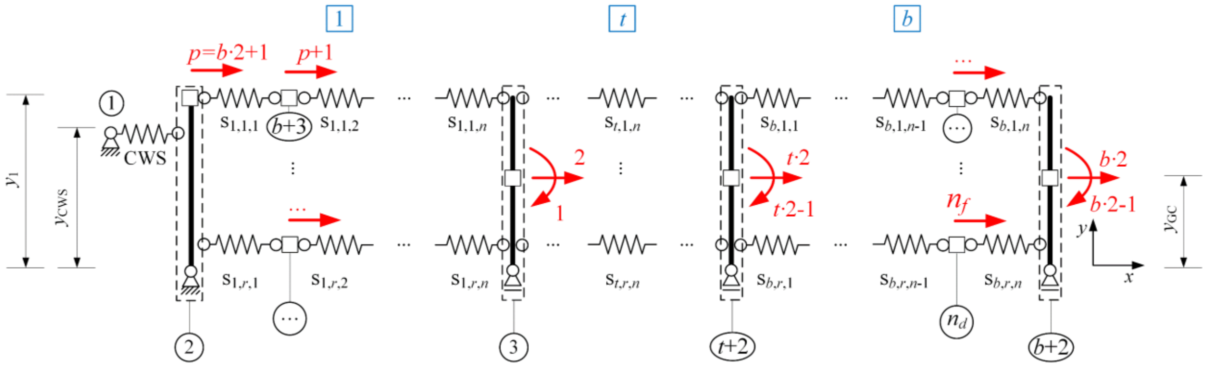

Figure D-1: Generic joint mechanical model, global node numbering, components numbering and global DOFs.

D.2 Global stiffness matrix

The global stiffness matrix of the model will have as many rows and columns as the total number of DOF (n_f). Accordingly, the global stiffness matrix, $\boldsymbol{K}_g$, will be

$$\boldsymbol{K}_g = \begin{bmatrix} K_{1,1} & & & & & & \\ K_{2,1} & K_{2,1} & & & & & \\ K_{3,1} & K_{3,2} & K_{3,3} & & & & \\ \vdots & \vdots & \vdots & \ddots & & & \\ K_{i,1} & K_{2,1} & K_{i,3} & \dots & K_{i,j} & & \\ \vdots & \vdots & \vdots & \vdots & \vdots & \ddots & \\ K_{n_f,1} & K_{n_f,2} & K_{n_f,3} & \dots & K_{n_f,j} & \dots & K_{n_f,n_f} \end{bmatrix} \tag{D-1}$$

According to the model assembly in Figure D-1, the non-null elements of the lower half of the global stiffness matrix can be computed using the following procedure:

1) Assuming that each row has more than one component, the assemblage of the stiffness matrix is as follows for column and line numbers $\leq p$

1.a) rightmost vertical rigid element ($t = b$)

$$K_{t\cdot 2-1,t\cdot 2-1} = \sum_{m=1}^{r_t} \left(\left(y_{t,m} - y_{\mathrm{GC}}\right)^2 \cdot k_{t,m,\mathrm{rightmost}} \right) \tag{D-2}$$

$$K_{t\cdot 2,t\cdot 2-1} = \sum_{m=1}^{r_t} \left(\left(y_{t,m} - y_{\mathrm{GC}}\right) \cdot k_{t,m,\mathrm{rightmost}} \right) \tag{D-3}$$

$$K_{t\cdot 2,t\cdot 2} = \sum_{m=1}^{r_t} k_{t,m,\mathrm{rightmost}} \tag{D-4}$$

1.b) middle vertical rigid elements ($t = 1, \dots, b-1$)

$$\begin{aligned} K_{t\cdot 2-1,t\cdot 2-1} &= \sum_{m=1}^{r_t} \left(\left(y_{t,m} - y_{\mathrm{GC}}\right)^2 \cdot k_{t,m,\mathrm{rightmost}} \right) \\ &\quad + \sum_{m=1}^{r_{t+1}} \left(\left(y_{t+1,m} - y_{\mathrm{GC}}\right)^2 \cdot k_{t+1,m,\mathrm{leftmost}} \right) \end{aligned} \tag{D-5}$$

$$\begin{aligned} K_{t\cdot 2,t\cdot 2-1} &= \sum_{m=1}^{r_t} \left(\left(y_{t,m} - y_{\mathrm{GC}}\right) \cdot k_{t,m,\mathrm{rightmost}} \right) \\ &\quad + \sum_{m=1}^{r_{t+1}} \left(\left(y_{t+1,m} - y_{\mathrm{GC}}\right) \cdot k_{t+1,m,\mathrm{leftmost}} \right) \end{aligned} \tag{D-6}$$

$$K_{t\cdot 2,t\cdot 2} = \sum_{m=1}^{r_t} k_{t,m,\mathrm{rightmost}} + \sum_{m=1}^{r_{t+1}} k_{t+1,m,\mathrm{leftmost}} \tag{D-7}$$

1.c) leftmost vertical rigid element ($t = 1$)

$$K_{p,p} = \frac{1}{y_{t,1}} \cdot \left(\frac{y_{\mathrm{CWS}}}{y_{t,1}}\right)^2 \cdot k_{\mathrm{CWS}} + \frac{1}{y_{t,1}} \cdot \sum_{m=1}^{r_t} \left(\left(\frac{y_{t,m}}{y_{t,1}}\right)^2 \cdot k_{t,m,\mathrm{leftmost}}\right) \tag{D-8}$$

where $y_{t,m}$ is the local y coordinate of the row m in block t, y_{GC} is the y coordinate of the geometric centre of the beam, y_{CWS} is the y coordinate of the CWS component, $k_{t,m,\mathrm{rightmost}}$ and $k_{t,m,\mathrm{leftmost}}$ are the tangent stiffness of the rightmost and of the leftmost component, respectively, of row m in block t.

2) Considering the case where there is only one component in one or more rows, the following assemblage of the stiffness matrix should be considered instead as follows

2.a) rightmost vertical rigid element

2.a.i) mechanical model with more than one block ($t = b$)

$$K_{t\cdot 2-1,(t-1)\cdot 2-1} = -\sum_{m\in E_t}^{r_t} \left(\left(y_{t,m} - y_{\mathrm{GC}}\right)^2 \cdot k_{t,m,\mathrm{single}}\right) \tag{D-9}$$

$$K_{t\cdot 2-1,(t-1)\cdot 2} = -\sum_{m\in E_t}^{r_t} \left(y_{t,m} - y_{\mathrm{GC}}\right) \cdot\ k_{t,m,\mathrm{single}} \tag{D-10}$$

$$\begin{aligned} K_{t\cdot 2-1,t\cdot 2-1} = & \sum_{m\in(\Omega_t - E_t)}^{r_t} \left(\left(y_{t,m} - y_{\mathrm{GC}}\right)^2 \cdot k_{t,m,\mathrm{rightmost}}\right) \\ & + \sum_{m\in E_t}^{r_t} \left(\left(y_{t,m} - y_{\mathrm{GC}}\right)^2 \cdot k_{t,m,\mathrm{single}}\right) \end{aligned} \tag{D-11}$$

$$K_{t\cdot 2,(t-1)\cdot 2-1} = -\sum_{m\in E_t}^{r_t}\left(\left(y_{t,m}-y_{\mathrm{GC}}\right)\cdot k_{t,m,\mathrm{single}}\right) \tag{D-12}$$

$$K_{t\cdot 2,(t-1)\cdot 2} = -\sum_{m\in E_t}^{r_t} k_{t,m,\mathrm{single}} \tag{D-13}$$

$$\begin{aligned} K_{t\cdot 2,t\cdot 2-1} = &\sum_{m\in(\Omega_t-E_t)}^{r_t}\left(\left(y_{t,m}-y_{\mathrm{GC}}\right)\cdot k_{t,m,\mathrm{rightmost}}\right) \\ &+\sum_{m\in E_t}^{r_t}\left(\left(y_{t,m}-y_{\mathrm{GC}}\right)\cdot k_{t,m,\mathrm{single}}\right) \end{aligned} \tag{D-14}$$

$$K_{t\cdot 2,t\cdot 2} = \sum_{m\in(\Omega_t-E_t)}^{r_t} k_{t,m,\mathrm{rightmost}} + \sum_{m\in E_t}^{r_t} k_{t,m,\mathrm{single}} \tag{D-15}$$

where $\Omega_t = \{1,\dots,r_t\}$ is the set of row numbers of block t and $E_t = \{rows\ with\ only\ one\ spring\}$ is the set of row numbers with only one spring in block t.

2.a.ii) mechanical model with only one block ($t = b = 1$)

$$\begin{aligned} K_{t\cdot 2-1,t\cdot 2-1} = &\sum_{m\in(\Omega_t-E_t)}^{r_t}\left(\left(y_{t,m}-y_{\mathrm{GC}}\right)^2\cdot k_{t,m,\mathrm{rightmost}}\right) \\ &+\sum_{m\in E_t}^{r_t}\left(\left(y_{t,m}-y_{\mathrm{GC}}\right)^2\cdot k_{t,m,\mathrm{single}}\right) \end{aligned} \tag{D-16}$$

$$\begin{aligned} K_{t\cdot 2,t\cdot 2-1} = & \sum_{m\in(\Omega_t - E_t)}^{r_t} \left(\left(y_{t,m} - y_{\mathrm{GC}} \right) \cdot k_{t,m,\mathrm{rightmost}} \right) \\ & + \sum_{m\in E_t}^{r_t} \left(\left(y_{t,m} - y_{\mathrm{GC}} \right) \cdot k_{t,m,\mathrm{single}} \right) \end{aligned} \tag{D-17}$$

$$K_{t\cdot 2,t\cdot 2} = \sum_{m\in(\Omega_t - E_t)}^{r_t} k_{t,m,\mathrm{rightmost}} + \sum_{m\in E_t}^{r_t} k_{t,m,\mathrm{single}} \tag{D-18}$$

2.b) middle vertical rigid elements

2.b.i) first block ($t = 1$)

$$\begin{aligned} K_{t\cdot 2-1,t\cdot 2-1} = & \sum_{m\in(\Omega_t - E_t)}^{r_t} \left(\left(y_{t,m} - y_{\mathrm{GC}} \right)^2 \cdot k_{t,m,\mathrm{rightmost}} \right) \\ & + \sum_{m\in E_t}^{r_t} \left(\left(y_{t,m} - y_{\mathrm{GC}} \right)^2 \cdot k_{t,m,\mathrm{single}} \right) \\ & + \sum_{m\in(\Omega_{t+1} - E_{t+1})}^{r_{t+1}} \left(\left(y_{t+1,m} - y_{\mathrm{GC}} \right)^2 \cdot k_{t+1,m,\mathrm{leftmost}} \right) \\ & + \sum_{m\in E_{t+1}}^{r_{t+1}} \left(\left(y_{t+1,m} - y_{\mathrm{GC}} \right)^2 \cdot k_{t+1,m,\mathrm{single}} \right) \end{aligned} \tag{D-19}$$

$$\begin{aligned} K_{t\cdot 2,t\cdot 2-1} = & \sum_{m\in(\Omega_t - E_t)}^{r_t} \left((y_{t,m} - y_{\mathrm{GC}}) \cdot k_{t,m,\mathrm{rightmost}} \right) \\ & + \sum_{m\in E_t}^{r_t} \left((y_{t,m} - y_{\mathrm{GC}}) \cdot k_{t,m,\mathrm{single}} \right) \\ & + \sum_{m\in(\Omega_{t+1} - E_{t+1})}^{r_{t+1}} \left((y_{t+1,m} - y_{\mathrm{GC}}) \cdot k_{t+1,m,\mathrm{leftmost}} \right) \\ & + \sum_{m\in E_{t+1}}^{r_{t+1}} \left((y_{t+1,m} - y_{\mathrm{GC}}) \cdot k_{t+1,m,\mathrm{single}} \right) \end{aligned} \tag{D-20}$$

$$\begin{aligned} K_{t\cdot 2,t\cdot 2} = & \sum_{m\in(\Omega_t - E_t)}^{r_t} k_{t,m,\mathrm{rightmost}} + \sum_{m\in E_t}^{r_t} k_{t,m,\mathrm{single}} + \sum_{m\in(\Omega_{t+1} - E_{t+1})}^{r_{t+1}} k_{t+1,m,\mathrm{rightmost}} \\ & + \sum_{m\in E_{t+1}}^{r_{t+1}} k_{t+1,m,\mathrm{single}} \end{aligned} \tag{D-21}$$

2.b.ii) following blocks ($t = 2, \dots, b-1$)

$$K_{t\cdot 2-1,(t-1)\cdot 2-1} = -\sum_{m\in E_t}^{r_t} \left((y_{t,m} - y_{\mathrm{GC}})^2 \cdot k_{t,m,\mathrm{single}} \right) \tag{D-22}$$

$$K_{t\cdot 2-1,(t-1)\cdot 2} = -\sum_{m\in E_t}^{r_t} (y_{t,m} - y_{\mathrm{GC}}) \cdot k_{t,m,\mathrm{single}} \tag{D-23}$$

$$
\begin{aligned}
K_{t\cdot 2-1,t\cdot 2-1} = & \sum_{m\in(\Omega_t-E_t)}^{r_t} \left(\left(y_{t,m}-y_{\mathrm{GC}}\right)^2\cdot k_{t,m,\mathrm{rightmost}}\right) \\
& + \sum_{m\in E_t}^{r_t} \left(\left(y_{t,m}-y_{\mathrm{GC}}\right)^2\cdot k_{t,m,\mathrm{single}}\right) \\
& + \sum_{m\in(\Omega_{t+1}-E_{t+1})}^{r_{t+1}} \left(\left(y_{t+1,m}-y_{\mathrm{GC}}\right)^2\cdot k_{t+1,m,\mathrm{leftmost}}\right) \\
& + \sum_{m\in E_{t+1}}^{r_{t+1}} \left(\left(y_{t+1,m}-y_{\mathrm{GC}}\right)^2\cdot k_{t+1,m,\mathrm{single}}\right)
\end{aligned}
\tag{D-24}
$$

$$
K_{t\cdot 2,(t-1)\cdot 2-1} = -\sum_{m\in E_t}^{r_t} \left(\left(y_{t,m}-y_{\mathrm{GC}}\right)\cdot k_{t,m,\mathrm{single}}\right)
\tag{D-25}
$$

$$
K_{t\cdot 2,(t-1)\cdot 2} = -\sum_{m\in E_t}^{r_t} k_{t,m,\mathrm{single}}
\tag{D-26}
$$

$$
\begin{aligned}
K_{t\cdot 2,t\cdot 2-1} = & \sum_{m\in(\Omega_t-E_t)}^{r_t} \left(\left(y_{t,m}-y_{\mathrm{GC}}\right)\cdot k_{t,m,\mathrm{rightmost}}\right) \\
& + \sum_{m\in E_t}^{r_t} \left(\left(y_{t,m}-y_{\mathrm{GC}}\right)\cdot k_{t,m,\mathrm{single}}\right) \\
& + \sum_{m\in(\Omega_{t+1}-E_{t+1})}^{r_{t+1}} \left(\left(y_{t+1,m}-y_{\mathrm{GC}}\right)\cdot k_{t+1,m,\mathrm{leftmost}}\right) \\
& + \sum_{m\in E_{t+1}}^{r_{t+1}} \left(\left(y_{t+1,m}-y_{\mathrm{GC}}\right)\cdot k_{t+1,m,\mathrm{single}}\right)
\end{aligned}
\tag{D-27}
$$

$$K_{t\cdot 2,t\cdot 2} = \sum_{m\in(\Omega_t - E_t)}^{r_t} k_{t,m,\mathrm{rightmost}} + \sum_{m\in E_t}^{r_t} k_{t,m,\mathrm{single}} + \sum_{m\in(\Omega_{t+1} - E_{t+1})}^{r_{t+1}} k_{t+1,m,\mathrm{rightmost}} + \sum_{m\in E_{t+1}}^{r_{t+1}} k_{t+1,m,\mathrm{single}} \tag{D-28}$$

2.c) leftmost vertical rigid element ($t = 1$)

$$K_{p,t\cdot 2-1} = -\frac{y_{t,m}}{y_{t,1}} \cdot \sum_{m\in E_t}^{r_t} \left(\left(y_{t,m} - y_{\mathrm{GC}} \right) \cdot k_{t,m,\mathrm{single}} \right) \tag{D-29}$$

$$K_{p,t\cdot 2} = -\frac{y_{t,m}}{y_{t,1}} \cdot \sum_{m\in E_t}^{r_t} k_{t,m,\mathrm{single}} \tag{D-30}$$

$$K_{p,p} = \frac{1}{y_{t,1}} \cdot \left(\frac{y_{\mathrm{CWS}}}{y_{t,1}} \right)^2 \cdot k_{\mathrm{CWS}} + \frac{1}{y_{t,1}} \cdot \sum_{m\in(\Omega_t - E_t)}^{r_t} \left(\left(\frac{y_{t,m}}{y_{t,1}} \right)^2 \cdot k_{t,m,\mathrm{leftmost}} \right) + \frac{1}{y_{t,1}} \cdot \sum_{m\in E_t}^{r_t} \left(\left(\frac{y_{t,m}}{y_{t,1}} \right)^2 \cdot k_{t,m,\mathrm{single}} \right) \tag{D-31}$$

where $k_{t,m,\mathrm{single}}$ is the tangent stiffness of the single component of row m in block t.

3) Remaining rows of $\boldsymbol{K_g}$

3.a) neither to the first nor to the last DOF of the row

$$K_{\mathrm{DOF},\mathrm{DOF}-1} = -k_{t,m,\mathrm{left}} \tag{D-32}$$

$$K_{\mathrm{DOF,DOF}} = k_{t,m,\mathrm{left}} + k_{t,m,\mathrm{right}} \tag{D-33}$$

3.b) last (rightmost) DOF of the row

$$K_{\mathrm{DOF},t\cdot 2-1} = -\left(y_{t,m} - y_{\mathrm{GC}}\right) \cdot k_{t,m,\mathrm{right}} \tag{D-34}$$

$$K_{\mathrm{DOF},t\cdot 2} = -k_{t,m,\mathrm{right}} \tag{D-35}$$

$$K_{\mathrm{DOF,DOF-1}} = -k_{t,m,\mathrm{left}} \tag{D-36}$$

$$K_{\mathrm{DOF,DOF}} = k_{t,m,\mathrm{left}} + k_{t,m,\mathrm{right}} \tag{D-37}$$

$k_{t,m,\mathrm{right}}$ and $k_{t,m,\mathrm{left}}$ are the tangent stiffness of the components which are immediately in the right side of the node where the DOF is assigned respectively, of row m in block t.

3.c) first (leftmost) DOF of the row in the first block ($t = 1$)

$$K_{\mathrm{DOF},p} = -\left(\frac{y_{t,m}}{y_{t,1}}\right) \cdot k_{t,m,\mathrm{left}} \tag{D-38}$$

$$K_{\mathrm{DOF,DOF}} = k_{t,m,\mathrm{left}} + k_{t,m,\mathrm{right}} \tag{D-39}$$

3.d) first (leftmost) DOF of the row in the remaining blocks ($t \neq 1$)

$$K_{\mathrm{DOF},(t-1)\cdot 2-1} = -\left(y_{t,m} - y_{\mathrm{GC}}\right) \cdot k_{t,m,\mathrm{left}} \tag{D-40}$$

$$K_{\mathrm{DOF},(t-1)\cdot 2} = -k_{t,\mathrm{m},\mathrm{left}} \tag{D-41}$$

$$K_{\mathrm{DOF},\mathrm{DOF}} = k_{t,m,\mathrm{left}} + k_{t,m,\mathrm{right}} \tag{D-42}$$

3.e) only DOF of the row in the first block ($t = 1$)

$$K_{\mathrm{DOF},t\cdot 2-1} = -\left(y_{t,m} - y_{\mathrm{GC}}\right) \cdot k_{t,m,\mathrm{right}} \tag{D-43}$$

$$K_{\mathrm{DOF},t\cdot 2} = -k_{t,m,\mathrm{right}} \tag{D-44}$$

$$K_{\mathrm{DOF},p} = -\left(\frac{y_{t,m}}{y_{t,1}}\right) \cdot k_{t,m,\mathrm{left}} \tag{D-45}$$

$$K_{\mathrm{DOF},\mathrm{DOF}} = k_{t,m,\mathrm{left}} + k_{t,m,\mathrm{right}} \tag{D-46}$$

3.f) only DOF of the row in the remaining blocks ($t \neq 1$)

$$K_{\mathrm{DOF},(t-1)\cdot 2-1} = -\left(y_{t,m} - y_{\mathrm{GC}}\right) \cdot k_{t,m,\mathrm{left}} \tag{D-47}$$

$$K_{\mathrm{DOF},(t-1)\cdot 2} = -k_{t,m,\mathrm{left}} \tag{D-48}$$

$$K_{\mathrm{DOF},t\cdot 2-1} = -\left(y_{t,m} - y_{\mathrm{GC}}\right) \cdot k_{t,m,\mathrm{right}} \tag{D-49}$$

$$K_{\mathrm{DOF},t\cdot 2} = -k_{t,m,\mathrm{right}} \tag{D-50}$$

$$K_{\mathrm{DOF,DOF}} = k_{t,m,\mathrm{left}} + k_{t,m,\mathrm{right}} \tag{D-51}$$

The rest of the elements of the global stiffness matrix $\boldsymbol{K_g}$ are equal to zero (null).

D.3 Internal forces vector

To compute the vector of internal forces for increment i and iteration j, $\boldsymbol{IntF}_{\mathrm{DOF}}^{i,j}$, the following procedure was considered:

1) Assuming that each row has more than one component, forces transmitted by the components to the nodes and rigid elements is computed as follows

1.a) rightmost vertical rigid element ($t = b$)

$$IntF_{t\cdot 2-1}^{i,j} = \sum_{m=1}^{r_t} -f_{t,m,\mathrm{rightmost}}^{i,j} \cdot \left(y_{t,m} - y_{\mathrm{GC}}\right) \tag{D-52}$$

$$Int_{t\cdot 2}^{i,j} = \sum_{m=1}^{r_t} -f_{t,m,\mathrm{rightmost}}^{i,j} \tag{D-53}$$

1.b) middle vertical rigid elements ($t = 1, \dots, b-1$)

$$\begin{aligned} IntF_{t\cdot 2-1}^{i,j} = \sum_{m=1}^{r_t} -f_{t,m,\mathrm{rightmost}}^{i,j} \cdot \left(y_{t,m} - y_{\mathrm{GC}}\right) \\ + \sum_{m=1}^{r_{t+1}} f_{t+1,m,\mathrm{leftmost}}^{i,j} \cdot \left(y_{t+1,m} - y_{\mathrm{GC}}\right) \end{aligned} \tag{D-54}$$

$$IntF_{t\cdot 2}^{i,j} = \sum_{m=1}^{r_t} -f_{t,m,\mathrm{rightmost}}^{i,j} + \sum_{m=1}^{r_{t+1}} f_{t+1,m,\mathrm{leftmost}}^{i,j} \tag{D-55}$$

1.c) leftmost vertical rigid element ($t = 1$)

$$IntF_p^{i,j} = -f_{\mathrm{CWS}}^{i,j} \cdot \frac{y_{\mathrm{CWS}}}{y_{t,1}} + \sum_{m=1}^{r_t} f_{t,m,\mathrm{leftmost}}^{i,j} \cdot \frac{y_{t,m}}{y_{t,1}} \tag{D-56}$$

2) remaining DOF

$$IntF_{\mathrm{DOF}}^{i,j} = -f_{t,m,\mathrm{left}}^{i,j} + f_{t,m,\mathrm{right}}^{i,j} \tag{D-57}$$

where $f_{\mathrm{CWS}}^{i,j}$ is the internal force in component column web in shear (CWS), $f_{t,m,\mathrm{rightmost}}^{i,j}$ and $f_{t,m,\mathrm{leftmost}}^{i,j}$ are the internal forces of rightmost and leftmost components in row m of block t, respectively, $f_{t,m,\mathrm{right}}^{i,j}$ and $f_{t,m,\mathrm{left}}^{i,j}$ are the internal forces of components in the left and right side on the node where the DOF, respectively.

2) Considering the case where there is only one component in one or more rows, forces transmitted by the components to the nodes and rigid elements is computed as follows

2.a) rightmost vertical rigid element ($t = b$)

$$\begin{aligned} IntF_{t\cdot 2-1}^{i,j} = & \sum_{m\in(\Omega_t - E_t)}^{r_t} -f_{t,m,\mathrm{rightmost}}^{i,j} \cdot \left(y_{t,m} - y_{\mathrm{GC}}\right) \\ & + \sum_{m\in E_t}^{r_t} -f_{t,m,\mathrm{single}}^{i,j} \cdot \left(y_{t,m} - y_{\mathrm{GC}}\right) \end{aligned} \qquad \text{(D-58)}$$

$$IntF_{t\cdot 2}^{i,j} = \sum_{m\in(\Omega_t - E_t)}^{r_t} -f_{t,m,\mathrm{rightmost}}^{i,j} + \sum_{m\in E_t}^{r_t} -f_{t,m,\mathrm{single}}^{i,j} \qquad \text{(D-59)}$$

2.b) middle vertical rigid elements ($t = 1, \dots, b-1$)

$$\begin{aligned} IntF_{t\cdot 2-1}^{i,j} = & \sum_{m\in(\Omega_t - E_t)}^{r_t} -f_{t,m,\mathrm{rightmost}}^{i,j} \cdot \left(y_{t,m} - y_{\mathrm{GC}}\right) \\ & + \sum_{m\in E_t}^{r_t} -f_{t,m,\mathrm{single}}^{i,j} \cdot \left(y_{t,m} - y_{\mathrm{GC}}\right) \\ & + \sum_{m\in(\Omega_{t+1} - E_{t+1})}^{r_{t+1}} f_{t+1,m,\mathrm{leftmost}}^{i,j} \cdot \left(y_{t+1,m} - y_{\mathrm{GC}}\right) \\ & + \sum_{m\in E_{t+1}}^{r_{t+1}} f_{t+1,m,\mathrm{single}}^{i,j} \cdot \left(y_{t+1,m} - y_{\mathrm{GC}}\right) \end{aligned} \qquad \text{(D-60)}$$

$$\begin{aligned} IntF_{t\cdot 2}^{i,j} = & \sum_{m\in(\Omega_t - E_t)}^{r_t} -f_{t,m,\mathrm{rightmost}}^{i,j} + \sum_{m\in E_t}^{r_t} - f_{t,m,\mathrm{single}}^{i,j} \\ & + \sum_{m\in(\Omega_{t+1} - E_{t+1})}^{r_{t+1}} f_{t+1,m,\mathrm{leftmost}}^{i,j} + \sum_{m\in E_{t+1}}^{r_{t+1}} f_{t+1,m,\mathrm{single}}^{i,j} \end{aligned} \qquad \text{(D-61)}$$

2.c) leftmost vertical rigid element ($t = 1$)

$$IntF_p^{i,j} = -f_{\mathrm{CWS}}^{i,j} \cdot \frac{y_{\mathrm{CWS}}}{y_{t,1}} + \sum_{m\in(\Omega_t - E_t)}^{r_t} f_{t,m,\mathrm{leftmost}}^{i,j} \cdot \frac{y_{t,m}}{y_{t,1}} + \sum_{m\in E_t}^{r_t} f_{t,m,\mathrm{single}}^{i,j} \cdot \frac{y_{t,m}}{y_{t,1}} \qquad \text{(D-62)}$$

2.d) remaining DOF

$$IntF_{\mathrm{DOF}}^{i,j} = -f_{t,m,\mathrm{left}}^{i,j} + f_{t,m,\mathrm{right}}^{i,j} \qquad \text{(D-63)}$$

D.4 Illustrative example

To illustrate the implementation of the above expression, the refined model illustrated in Figure D-2 was selected. The model comprises three blocks and twelve DOFs. Three steps are detailed for illustration: (i) application of the unitary nodal displacements, (ii) computation of the global stiffness matrix and (iii) computation of the internal forces vector.

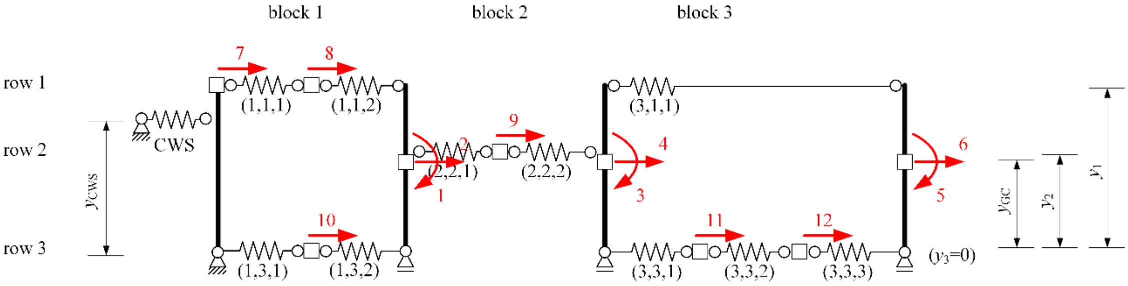

Figure D-2: Illustrative example – refined mechanical model.

D.4.1 Application of the unitary nodal displacements

Figures D-3 and D-4 illustrate the application of the unitary nodal displacements.

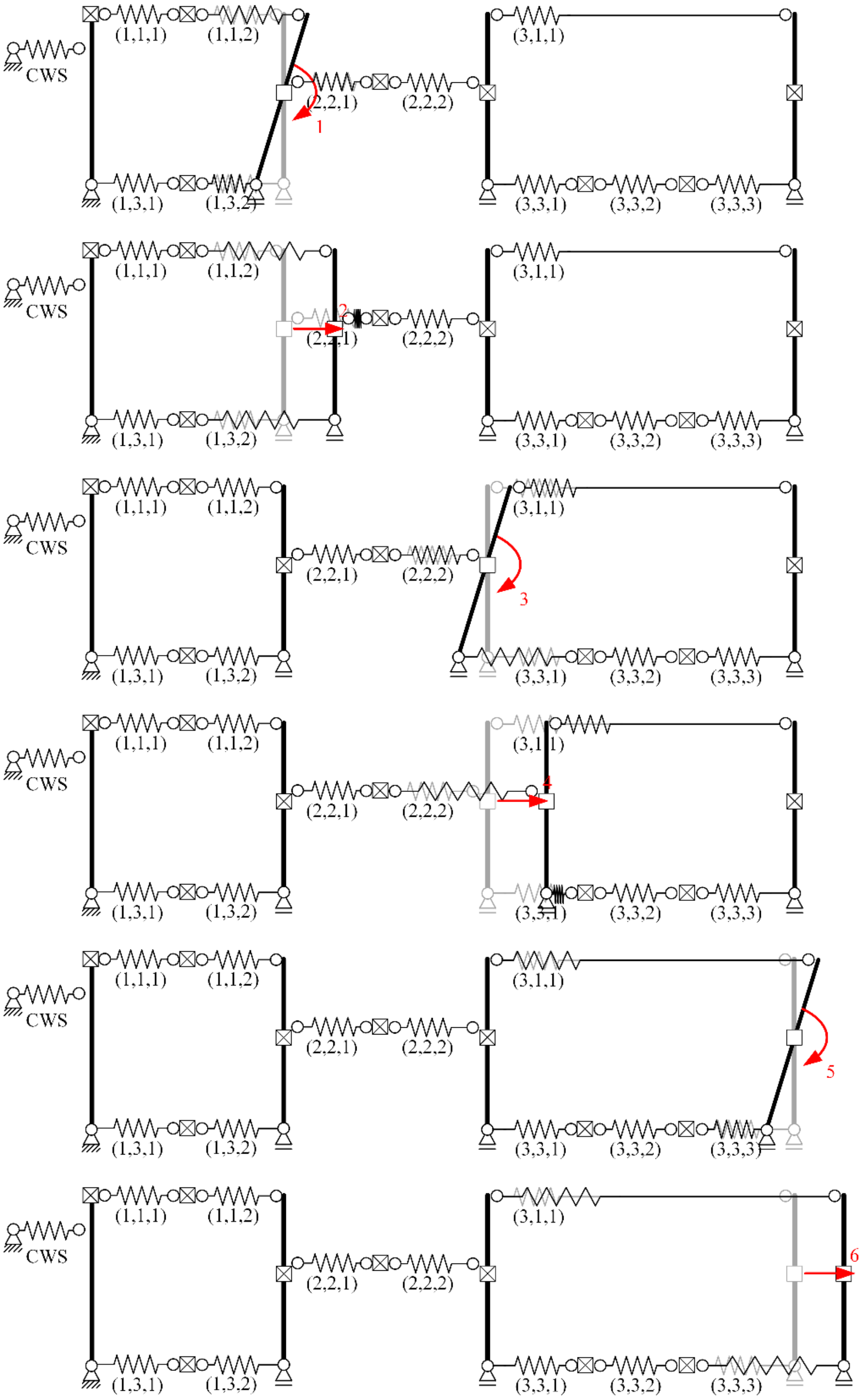

Figure D-3: Application of the unitary nodal displacement (u_1 and u_6).

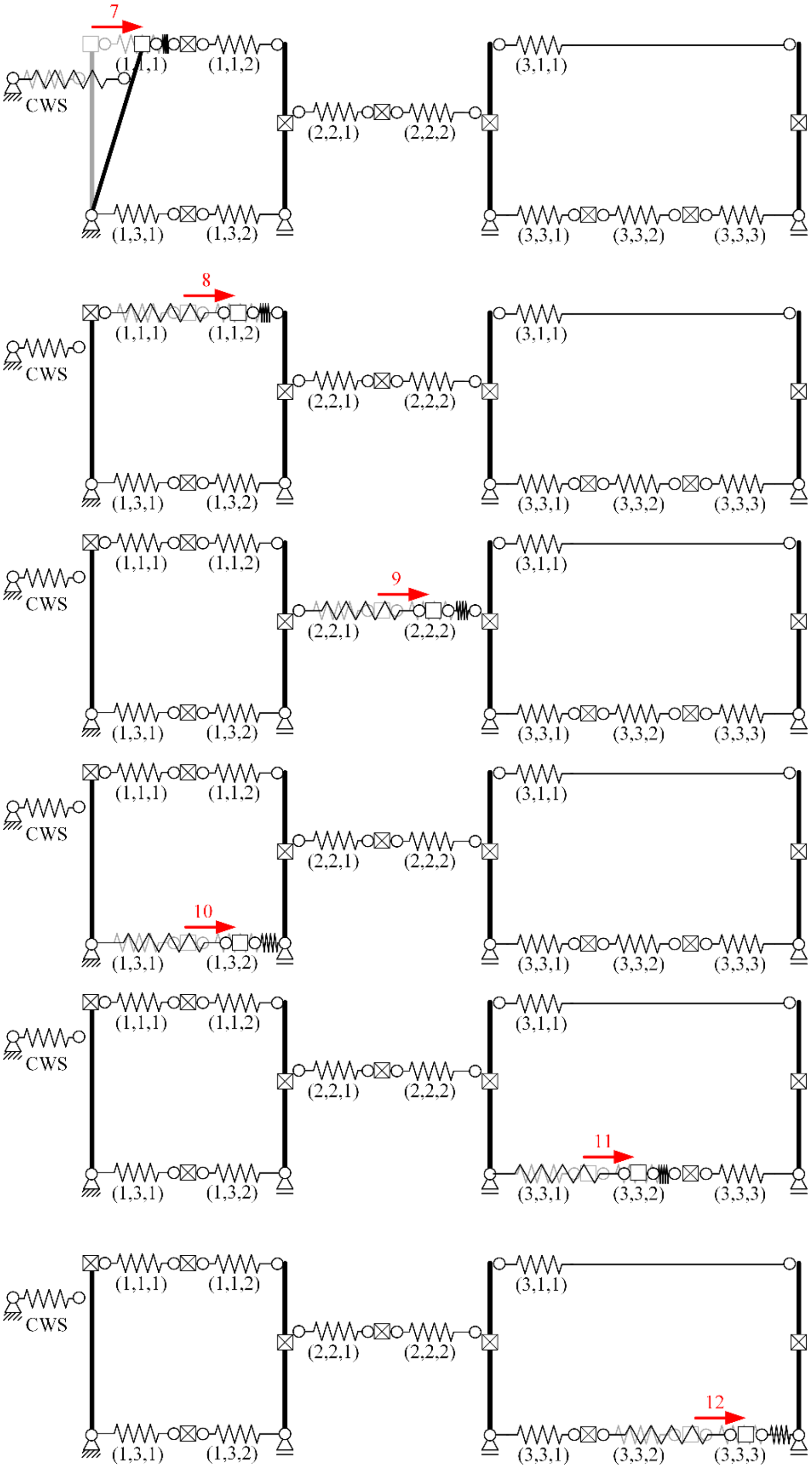

Figure D-4: Application of the unitary nodal displacement (u_7 to u_{12}).

D.4.2 Global stiffness matrix

- DOF 1: bending – middle vertical rigid element ($u = 1$, $t = 1$)

$$K_{t\cdot 2-1,t\cdot 2-1} = \sum_{m=1}^{r_t} \left(\left(y_{t,m} - y_{\mathrm{GC}} \right)^2 \cdot k_{t,m,\mathrm{rightmost}} \right) + \sum_{m=1}^{r_{t+1}} \left(\left(y_{t+1,m} - y_{\mathrm{GC}} \right)^2 \cdot k_{t+1,m,\mathrm{leftmost}} \right)$$

$$K_{1,1} = (y_1 - y_{\mathrm{GC}})^2 \cdot k_{1,1,2} + (y_3 - y_{\mathrm{GC}})^2 \cdot k_{1,3,2} + (y_2 - y_{\mathrm{GC}})^2 \cdot k_{2,2,1}$$

- DOF 2: axial – middle vertical rigid element ($u = 2$, $t = 1$)

$$K_{t\cdot 2,t\cdot 2-1} = \sum_{m=1}^{r_t} \left(\left(y_{t,m} - y_{\mathrm{GC}} \right) \cdot k_{t,m,\mathrm{rightmost}} \right) + \sum_{m=1}^{r_{t+1}} \left(\left(y_{t+1,m} - y_{\mathrm{GC}} \right) \cdot k_{t+1,m,\mathrm{leftmost}} \right)$$

$$K_{2,1} = (y_1 - y_{\mathrm{GC}}) \cdot k_{1,1,2} + (y_3 - y_{\mathrm{GC}}) \cdot k_{1,3,2} + (y_2 - y_{\mathrm{GC}}) \cdot k_{2,2,1}$$

$$K_{t\cdot 2,t\cdot 2} = \sum_{m=1}^{r_t} k_{t,m,\mathrm{rightmost}} + \sum_{m=1}^{r_{t+1}} k_{t+1,m,\mathrm{leftmost}}$$

$$K_{2,2} = k_{1,1,2} + k_{1,3,2} + k_{2,2,1}$$

- DOF 3: bending – middle vertical rigid element ($u = 3$, $t = 2$)

$$K_{3,1} = 0$$

$$K_{3,2} = 0$$

$$K_{t\cdot 2-1,t\cdot 2-1} = \sum_{m\in(\Omega_t-E_t)}^{r_t} \left(\left(y_{t,m}-y_{\mathrm{GC}}\right)^2 \cdot k_{t,m,\mathrm{rightmost}}\right)$$

$$+ \sum_{m\in(\Omega_{t+1}-E_{t+1})}^{r_{t+1}} \left(\left(y_{t+1,m}-y_{\mathrm{GC}}\right)^2 \cdot k_{t+1,m,\mathrm{leftmost}}\right)$$

$$+ \sum_{m\in E_{t+1}}^{r_{t+1}} \left(\left(y_{t+1,m}-y_{\mathrm{GC}}\right)^2 \cdot k_{t+1,m,\mathrm{single}}\right)$$

$$K_{3,3} = (y_2-y_{\mathrm{GC}})^2 \cdot k_{2,2,2} + (y_3-y_{\mathrm{GC}})^2 \cdot k_{3,3,1} + (y_1-y_{\mathrm{GC}})^2 \cdot k_{3,1,1}$$

- DOF 4: axial – middle vertical rigid element ($u = 4$, $t = 2$)

$$K_{4,1} = 0$$

$$K_{4,2} = 0$$

$$K_{t\cdot 2,t\cdot 2-1} = \sum_{m\in(\Omega_t-E_t)}^{r_t} \left(\left(y_{t,m}-y_{\mathrm{GC}}\right) \cdot k_{t,m,\mathrm{rightmost}}\right)$$

$$+ \sum_{m\in(\Omega_{t+1}-E_{t+1})}^{r_{t+1}} \left(\left(y_{t+1,m}-y_{\mathrm{GC}}\right) \cdot k_{t+1,m,\mathrm{leftmost}}\right)$$

$$+ \sum_{m\in E_{t+1}}^{r_{t+1}} \left(\left(y_{t+1,m}-y_{\mathrm{GC}}\right) \cdot k_{t+1,m,\mathrm{single}}\right)$$

$$K_{4,3} = (y_2-y_{\mathrm{GC}}) \cdot k_{2,2,2} + (y_1-y_{\mathrm{GC}}) \cdot k_{3,1,1} + (y_3-y_{\mathrm{GC}}) \cdot k_{3,3,1}$$

$$K_{t\cdot 2,t\cdot 2} = \sum_{m\in(\Omega_t-E_t)}^{r_t} k_{t,m,\mathrm{rightmost}} + \sum_{m\in(\Omega_{t+1}-E_{t+1})}^{r_{t+1}} k_{t+1,m,\mathrm{rightmost}} + \sum_{m\in E_{t+1}}^{r_{t+1}} k_{t+1,m,\mathrm{single}}$$

$$K_{4,4} = k_{2,2,2} + k_{3,3,1} + k_{3,1,1}$$

- DOF 5: bending – rightmost vertical rigid element ($u = 5$, $t = 3$)

$$K_{t\cdot 2-1,(t-1)\cdot 2-1} = -\sum_{m \in E_t}^{r_t} \left(\left(y_{t,m} - y_{\mathrm{GC}} \right)^2 \cdot k_{t,m,\mathrm{single}} \right)$$

$$K_{5,3} = -(y_1 - y_{\mathrm{GC}})^2 \cdot k_{3,1,1}$$

$$K_{t\cdot 2-1,(t-1)\cdot 2} = -\sum_{m \in E_t}^{r_t} \left(y_{t,m} - y_{\mathrm{GC}} \right) \cdot \ k_{t,m,\mathrm{single}}$$

$$K_{5,4} = -(y_1 - y_{\mathrm{GC}}) \cdot k_{3,1,1}$$

$$K_{t\cdot 2-1,t\cdot 2-1} = \sum_{m \in (\Omega_t - E_t)}^{r_t} \left(\left(y_{t,m} - y_{\mathrm{GC}} \right)^2 \cdot k_{t,m,\mathrm{rightmost}} \right) + \sum_{m \in E_t}^{r_t} \left(\left(y_{t,m} - y_{\mathrm{GC}} \right)^2 \cdot k_{t,m,\mathrm{single}} \right)$$

$$K_{5,5} = (y_1 - y_{\mathrm{GC}})^2 \cdot k_{3,1,1} + (y_3 - y_{\mathrm{GC}})^2 \cdot k_{3,3,3}$$

- DOF 6: axial – rightmost vertical rigid element ($u = 6$, $t = 3$)

$$K_{t\cdot 2,(t-1)\cdot 2-1} = -\sum_{m \in E_t}^{r_t} \left(\left(y_{t,m} - y_{\mathrm{GC}} \right) \cdot k_{t,m,\mathrm{single}} \right)$$

$$K_{6,3} = -(y_1 - y_{\mathrm{GC}}) \cdot k_{3,1,1}$$

$$K_{t\cdot 2,(t-1)\cdot 2} = -\sum_{m \in E_t}^{r_t} k_{t,m,\mathrm{single}}$$

$$K_{6,4} = k_{3,1,1}$$

$$K_{t\cdot 2,t\cdot 2-1} = \sum_{m\in(\Omega_t - E_t)}^{r_t} \Big((y_{t,m} - y_{\mathrm{GC}}) \cdot k_{t,m,\mathrm{rightmost}} \Big) + \sum_{m\in E_t}^{r_t} \Big((y_{t,m} - y_{\mathrm{GC}}) \cdot k_{t,m,\mathrm{single}} \Big)$$

$$K_{6,5} = (y_3 - y_{\mathrm{GC}}) \cdot k_{3,3,3} + (y_1 - y_{\mathrm{GC}}) \cdot k_{3,1,1}$$

$$K_{t\cdot 2,t\cdot 2} = \sum_{m\in(\Omega_t - E_t)}^{r_t} k_{t,m,\mathrm{rightmost}} + \sum_{m\in E_t}^{r_t} k_{t,m,\mathrm{single}}$$

$$K_{6,6} = k_{3,3,3} + k_{3,1,1}$$

- DOF 7: rightmost vertical rigid element ($u = 7$, $t = 1$)

$$K_{7,1} = 0$$

$$K_{7,2} = 0$$

$$K_{p,p} = \frac{1}{y_{t,1}} \cdot \left(\frac{y_{\mathrm{CWS}}}{y_{t,1}}\right)^2 \cdot k_{\mathrm{CWS}} + \frac{1}{y_{t,1}} \cdot \sum_{m=1}^{r_t} \left(\left(\frac{y_{t,m}}{y_{t,1}}\right)^2 \cdot k_{t,m,\mathrm{leftmost}} \right)$$

$$K_{7,7} = \frac{1}{y_1} \cdot \left(\frac{y_{\mathrm{CWS}}}{y_1}\right)^2 \cdot k_{\mathrm{CWS}} + \frac{1}{y_1} \cdot \left(\frac{y_1}{y_1}\right)^2 \cdot k_{1,1,1} + \frac{1}{y_1} \cdot \left(\frac{y_3}{y_1}\right)^2 \cdot k_{1,3,1}$$

- DOF 8: last node of row 1 block 1 ($u = 8$, $t = 1$)

$$K_{8,1} = -\big(y_{t,m} - y_{\mathrm{GC}}\big) \cdot k_{t,m,\mathrm{right}} = -(y_1 - y_{\mathrm{GC}}) \cdot k_{1,1,2}$$

$$K_{8,2} = -k_{t,m,\mathrm{right}} = -k_{1,1,2}$$

$$K_{8,7} = -k_{t,m,\mathrm{left}} = -k_{1,1,1}$$

$$K_{8,8} = k_{t,m,\mathrm{left}} + k_{t,m,\mathrm{right}} = k_{1,1,1} + k_{1,1,2}$$

- DOF 9: only node of row 1 block 3 ($u = 9$, $t = 2$)

$$K_{9,1} = -\left(y_{t,m} - y_{\mathrm{GC}}\right) \cdot k_{t,m,\mathrm{left}} = -(y_2 - y_{\mathrm{GC}}) \cdot k_{2,2,1}$$

$$K_{9,\,2} = -k_{t,m,\mathrm{left}} = -k_{2,2,1}$$

$$K_{9,3} = -\left(y_{t,m} - y_{\mathrm{GC}}\right) \cdot k_{t,n,\mathrm{right}} = -(y_2 - y_{\mathrm{GC}}) \cdot k_{2,2,2}$$

$$K_{9,4} = -k_{t,m,\mathrm{right}} = -k_{2,2,2}$$

$$K_{9,9} = k_{t,m,\mathrm{left}} + k_{t,m,\mathrm{right}} = k_{2,2,1} + k_{2,2,2}$$

- DOF 10: last node of row 2 block 2 ($d = 10$, $t = 1$)

$$K_{10,1} = -\left(y_{t,m} - y_{\mathrm{GC}}\right) \cdot k_{t,m,\mathrm{right}} = -(y_3 - y_{\mathrm{GC}}) \cdot k_{1,3,2}$$

$$K_{10,2} = -k_{t,m,\mathrm{right}} = -k_{1,3,2}$$

$$K_{10,7} = -\left(\frac{y_{t,m}}{y_{t,1}}\right) \cdot k_{t,m,\mathrm{left}} = -\left(\frac{y_3}{y_1}\right) \cdot k_{1,3,1}$$

$$K_{10,10} = k_{t,m,\mathrm{left}} + k_{t,m,\mathrm{right}} = k_{1,3,1} + k_{1,3,2}$$

- DOF 11: only node of row 3 block 1 ($u = 11$, $t = 3$)

$$K_{11,\,3} = -\left(y_{t,m} - y_{\mathrm{GC}}\right) \cdot k_{t,m,\mathrm{left}} = -(y_3 - y_{\mathrm{GC}}) \cdot k_{3,3,1}$$

$$K_{11,4} = -k_{t,m,\text{left}} = -k_{3,3,1}$$

$$K_{11,11} = k_{t,m,\text{left}} + k_{t,m,\text{right}} = k_{3,3,1} + k_{3,3,2}$$

- DOF 12: only node of row 3 block 2 ($u = 12$, $t = 3$)

$$K_{12,5} = -\left(y_{t,m} - y_{\text{GC}}\right) \cdot k_{t,m,\text{right}} = -(y_3 - y_{\text{GC}}) \cdot k_{3,3,3}$$

$$K_{12,6} = -k_{t,m,\text{right}} = -k_{3,3,3}$$

$$K_{12,13} = -k_{t,m,\text{left}} = -k_{3,3,2}$$

$$K_{12,12} = k_{t,m,\text{left}} + k_{t,m,\text{right}} = k_{3,3,3} + k_{3,3,2}$$

D.4.3 Internal forces vector

- DOF 1: bending – middle vertical rigid element ($u = 1$, $t = 1$)

$$IntF^{i,j}_{t\cdot 2-1} = \sum_{m=1}^{r_t} -f^{i,j}_{t,m,\text{rightmost}} \cdot \left(y_{t,m} - y_{\text{GC}}\right) + \sum_{m=1}^{r_{t+1}} f^{i,j}_{t+1,m,\text{leftmost}} \cdot \left(y_{t+1,m} - y_{\text{GC}}\right)$$

$$IntF_1 \;= -f_{1,1,2} \cdot (y_1 - y_{\text{GC}}) - f_{1,3,2} \cdot (y_3 - y_{\text{GC}}) + f_{2,2,1} \cdot (y_2 - y_{\text{GC}})$$

- DOF 2: axial – middle vertical rigid element ($u = 2$, $t = 1$)

$$IntF^{i,j}_{t\cdot 2} = \sum_{m=1}^{r_t} -f^{i,j}_{t,m,\text{rightmost}} + \sum_{m=1}^{r_{t+1}} f^{i,j}_{t+1,m,\text{leftmost}}$$

$$Int_2 \;= -f_{1,1,2} - f_{1,3,2} + f_{2,2,1}$$

- DOF 3: bending – middle vertical rigid element ($u = 3, t = 2$)

$$IntF^{i,j}_{t\cdot 2-1} = \sum_{m=1}^{r_t} -f^{i,j}_{t,m,\text{rightmost}} \cdot (y_n - y_{\text{GC}}) + \sum_{m\in(\Omega_{t+1}-E_{t+1})}^{r_{t+1}} f^{i,j}_{t+1,n,\text{leftmost}} \cdot \left(y_{t+1,m} - y_{\text{GC}}\right)$$

$$+ \sum_{m\in E_{t+1}}^{r_t} f^{i,j}_{t+1,m,\text{single}} \cdot \left(y_{t+1,m} - y_{\text{GC}}\right)$$

$$IntF_3 \ = -f_{2,2,2} \cdot (y_2 - y_{\text{GC}}) + f_{3,3,1} \cdot (y_3 - y_{\text{GC}}) + f_{3,1,1} \cdot (y_1 - y_{\text{GC}})$$

- DOF 4: axial – middle vertical rigid element ($u = 4, t = 2$)

$$IntF^{i,j}_{t\cdot 2} = \sum_{m=1}^{r_t} -f^{i,j}_{t,m,\text{rightmost}} + \sum_{m\in(\Omega_{t+1}-E_{t+1})}^{r_{t+1}} f^{i,j}_{t+1,m,\text{leftmost}} + \sum_{m\in E_{t+1}}^{r_{t+1}} f^{i,j}_{t+1,m,\text{single}}$$

$$IntF_4 \ = -f_{2,2,2} + f_{3,3,1} + f_{3,1,1}$$

- DOF 5: bending – rightmost vertical rigid element ($u = 5, t = 3$)

$$IntF^{i,j}_{t\cdot 2-1} = \sum_{m\in(\Omega_t-E_t)}^{r_t} -f^{i,j}_{t,m,\text{rightmost}} \cdot \left(y_{t,m} - y_{\text{GC}}\right) + \sum_{m\in E_t}^{r_t} -f^{i,j}_{t,m,\text{single}} \cdot \left(y_{t,m} - y_{\text{GC}}\right)$$

$$IntF_5 \ = -f_{3,3,3} \cdot (y_3 - y_{\text{GC}}) - f_{3,1,1} \cdot (y_1 - y_{\text{GC}})$$

- DOF 6: axial – rightmost vertical rigid element ($u = 6,\ t = 3$)

$$IntF^{i,j}_{t\cdot 2} = \sum_{m\in(\Omega_t-E_t)}^{r_t} -f^{i,j}_{t,m,\text{rightmost}} + \sum_{m\in E_t}^{r_t} -f^{i,j}_{t,m,\text{single}}$$

$$IntF_6 \ = -f_{3,3,3} - f_{3,1,1}$$

- DOF 7: rightmost vertical rigid element (u= $7,\ t = 1$)

$$IntF_p^{i,j} = -f_{\mathrm{CWS}}^{i,j} \cdot \frac{y_{\mathrm{CWS}}}{y_{t,1}} + \sum_{m=1}^{r_t} f_{t,m,\mathrm{leftmost}}^{i,j} \cdot \frac{y_{t,m}}{y_{t,1}}$$

$$IntF_7^{i,j} = -f_{\mathrm{CWS}} \cdot \frac{y_{\mathrm{CWS}}}{y_1} + f_{1,1,1} \cdot \frac{y_1}{y_1} + f_{1,3,1} \cdot \frac{y_3}{y_1}$$

- DOF 8: last node of row 1 block 1 ($u = 8$, $t = 1$)

$$IntF_8^{i,j} = -f_{t,m,\mathrm{left}}^{i,j} + f_{t,m,\mathrm{right}}^{i,j} = -f_{1,1,1} + f_{1,1,2}$$

- DOF 9: only node of row 1 block 3 ($d = 9$, $t = 2$)

$$IntF_9^{i,j} = -f_{t,m,\mathrm{left}}^{i,j} + f_{t,m,\mathrm{right}}^{i,j} = -f_{2,2,1} + f_{2,2,2}$$

- DOF 10: last node of row 2 block 2 ($u = 10$, $t = 1$)

$$IntF_{10}^{i,j} = -f_{t,m,\mathrm{left}}^{i,j} + f_{t,m,\mathrm{right}}^{i,j} = -f_{1,3,1} + f_{1,3,2}$$

- DOF 11: only node of row 3 block 1 ($d = 11$, $t = 3$)

$$IntF_{11}^{i,j} = -f_{t,m,\mathrm{left}}^{i,j} + f_{t,m,\mathrm{right}}^{i,j} = -f_{3,3,1} + f_{3,3,2}$$

- DOF 12: only node of row 3 block 2 ($d = 12$, $t = 3$)

$$IntF_{12}^{i,j} = -f_{t,m,\mathrm{left}}^{i,j} + f_{t,m,\mathrm{right}}^{i,j} = -f_{3,3,2} + f_{3,3,3}$$